Computational Investigation of Catalytic Reaction Mechanisms

VOM SC SIMTECH UND DER FAKULTÄT CHEMIE
DER UNIVERSITÄT STUTTGART
ZUR ERLANGUNG DER WÜRDE EINES DOKTORS DER
NATURWISSENSCHAFTEN (DR. RER. NAT.) GENEHMIGTE
ABHANDLUNG

Vorgelegt von

Juliane Heitkämper

aus Schwäbisch Hall

Hauptberichter:	Prof. Dr. Johannes Kästner
Mitberichterin:	Prof. Dr. Ainara Nova Flores
Prüfungsvorsitzender:	Prof. Dr. Joris van Slageren
Tag der mündlichen Prüfung:	16. April 2024

Institut für Theoretische Chemie
Universität Stuttgart

2024

Declaration of Authorship

I hereby certify that the dissertation entitled *Computational Investigation of Catalytic Reaction Mechanisms* is entirely my own work except where otherwise indicated. Passages and ideas from other sources have been clearly indicated.

Eidesstattliche Erklärung

Ich versichere, dass ich die vorliegende Arbeit mit dem Titel *Computational Investigation of Catalytic Reaction Mechanisms* selbstständig verfasst und keine anderen als die angegebenen Quellen und Hilfsmmittel benutzt habe. Aus fremden Quellen entnommene Passagen und Gedanken sind als solche kenntlich gemacht.

Name/Name:

Date/Datum:

Sign/Unterschrift: _____

Acknowledgements

Abstract

Due to increasing computing power and efficient numerical algorithms, quantum chemical methods became a powerful tool for studying mechanistic aspects of chemical reactions. Insights on a molecular level enable the understanding of crucial aspects that determine the reactivity of a reaction. However, the difficulties in applying these methods in homogeneous catalysis are manifold. The demand on the quantum chemical calculations and complexity of these large systems is challenging, as well as the interpretation of results.

In this thesis, the reaction mechanisms of three reactions in homogeneous catalysis are explored with quantum chemical methods by investigating the potential-energy landscapes of the full catalytic cycles and applying kinetic modeling. As shown in all three studies, the complex multi-step mechanisms, including short-lived intermediates, and multiple competing processes require the investigation of the full catalytic cycle. This can be efficiently done by examining the energetic span, which is the energy difference between the resting state and the highest transition state within the catalytic cycle. These two states control the efficiency of the catalytic cycle.

First, the quantum chemical study of the coupling reaction between aldehydes with aryl iodides to access secondary alcohols is presented. It is catalyzed by a metal catalyst that combines nickel and a 1,5-diaza-3,7-diphosphacyclooctane ligand. The results contribute to the long-standing cross-coupling debate of whether the catalytically active species is Ni(0). An alternative pathway to the widely accepted Ni(0) mechanism is found, taking shortcuts following the course of Ni(II). Surprisingly, this mechanism also includes an exceptional Ni(0) species. Identifying the energetic span enables exploring its magnitude with different ligands or counter ions. This approach prevents recalculating the whole catalytic cycle and provides a fast approach to understanding the different ligands' experimental performances. The results show that the experimental yields are not a consequence of a lower or higher energetic span but of an interplay between different possible pathways and a side reaction.

Further, the efficient regio- and stereospecific silver-free Pd-catalyzed γ-C(sp^3)-H

alkenylation of (Aza and Oxa) cyclohexylamine with 1-bromoalkenes is studied. A key result from the calculation of the energy landscape is that the mechanism goes through a Pd(II)/Pd(IV) pathway and that the rate-limiting step involves the γ-C(sp^3)-H bond activation and not the Pd(II) oxidative addition. The resting state of the catalytic cycle is the reaction product coordinating to the catalyst. The strong interaction of the palladium center to the double bond within the product results in a stable sink, explaining why alkenylation reactions of this type are very challenging. The calculations show that a pivotal aspect of the reaction is that KOPiv acts as a co-catalyst. By exchanging bromide for pivalate in the resting state lifts its energy, therefore decreasing the energy span. At the same time KBr precipitates, eliminating bromide from the reaction medium and avoiding the use of superstoichiometric silver salt reagents typically used for such reactions. Evaluating the stability of the resting state for different ligands indicates that electron withdrawing or donating groups affect the interaction between the Pd(II) and the double bond within the product. These insights can help to systematically explore the reactant scope.

For the combined quantum chemical and microkinetic study of the asymmetric hydroboration of acetophenone by a cooperative Lewis acid–onium salt catalyst, the energy landscape is calculated to shed light on possible reaction mechanisms and side reactions. Localized intrinsic bond orbitals are conducted to investigate the envisaged dual activation of the catalyst, the influence of present halide ions, and the role of the solvent to activate the catalyst. Additionally, microkinetic modeling is applied, which provides a more comprehensive insight into the reaction system. It accounts for both energetics and concentration effects. Further, it extracts reaction barriers from experimental kinetics data. This approach allows for comparing theory and experiment directly, revealing detailed insight into the elementary steps of the reaction mechanism. For example, replacing iodide by chloride as the counterion of the ammonium salt of the catalyst facilitates the hydride transfer step within the catalytic cycle. However, chloride speeds up the main reaction but simultaneously has the same effect on a side reaction that consumes the product. With this mechanism, consistent free enthalpy barriers for the quantum chemical and kinetic model are gained. Further, a microkinetic sensitivity analysis determines the rate-limiting steps to discuss the states relevant for enantioselectivity.

Zusammenfassung

Aufgrund zunehmender Rechenleistung und effizienter numerischer Algorithmen haben sich quantenchemische Methoden zu einem effektiven Werkzeug für die Untersuchung mechanistischer Aspekte chemischer Reaktionen entwickelt. Einblicke auf molekularer Skala ermöglichen das Verständnis der entscheidenden Aspekte, die die Reaktivität einer Reaktion bestimmen. Die Schwierigkeiten bei der Anwendung dieser Methoden in der homogenen Katalyse sind jedoch vielfältig. Nicht nur die Anforderungen an die quantenchemischen Berechnungen und die Komplexität dieser großen Systeme sind eine Herausforderung, sondern auch die Interpretation der Ergebnisse.

In dieser Arbeit werden die Reaktionsmechanismen von drei Reaktionen in der homogenen Katalyse mit quantenchemischen Methoden erforscht, indem die energetischen Barrieren der vollständigen katalytischen Zyklen untersucht werden. Wie in allen drei Studien gezeigt wird, erfordern die komplexen mehrstufigen Mechanismen, einschließlich kurzlebiger Zwischenprodukte und mehrerer konkurrierender Prozesse, die Untersuchung des gesamten katalytischen Zyklus. Die Ermittlung der Energiedifferenz zwischen dem langlebigsten Intermediat und dem höchsten Übergangszustand innerhalb des katalytischen Zyklus ist eine effiziente Methode, um die Reaktivität des katalytischen Zyklus zu untersuchen.

Zunächst wird die quantenchemische Untersuchung der Kupplungsreaktion zwischen Aldehyden und Aryliodiden zur Bildung sekundärer Alkohole vorgestellt. Sie wird durch einen Metallkomplex katalysiert, der Nickel und einen 1,5-Diaza-3,7-Diphosphacyclooctan-Liganden kombiniert. Die Ergebnisse leisten einen Beitrag zur schon lange andauernden Debatte, ob Kreuzkupplungsreaktionen über katalytisch aktive Ni(0)-Intermediate verlaufen. Es wurde ein alternativer Reaktionspfad zum weithin akzeptierten Ni(0)-Mechanismus gefunden, der diese Spezies vermeidet und direkt über eine Ni(II)-Spezies verläuft. Überraschenderweise enthält dieser Mechanismus auch eine außergewöhnliche Ni(0)-Spezies. Die Identifizierung des ratenbestimmenden Schritts ermöglicht es, diesen mit verschiedenen Liganden oder Gegenionen zu untersuchen. Dieser Ansatz erlaubt es, die Neuberechnung des gesamten katalytischen Zyklus zu vermeiden und bietet einen schnellen Zugang zum Verständnis der experimentellen

Reaktivitäten verschiedener Liganden. Die Ergebnisse zeigen, dass die experimentellen Ausbeuten nicht auf eine niedrigere oder höhere Barriere zurückzuführen sind, sondern auf ein Zusammenspiel zwischen verschiedenen möglichen Reaktionspfaden und einer Nebenreaktion.

Des Weiteren wird die effiziente regio- und stereospezifische, sowie silberfreie Pd-katalysierte γ-C(sp^3)-H-Alkenylierung von Cyclohexylamin mit 1-Bromalkenen untersucht. Eine zentrale Erkenntnis durch die Berechnung der Energielandschaft ist, dass der Mechanismus über einen Pd(II)/Pd(IV)-Reaktionspfad verläuft und dass der geschwindigkeitsbestimmende Schritt die γ-C(sp^3)-H-Bindungsaktivierung und nicht die Pd(II)-oxidative Addition beinhaltet. Ebenso zeigt sich, dass das langlebige Intermediat das Reaktionsprodukt ist, das an den Katalysator koordiniert. Die starke Wechselwirkung des Palladiumzentrums mit der Doppelbindung im Produkt führt zu einem stabilen Komplex. Ein entscheidender Aspekt der Reaktion ist die Funktion von KOPiv als Co-Katalysator, der durch den Austausch von Br gegen OPiv diesen Komplex destabilisiert. Gleichzeitig fällt KBr aus, wodurch Bromid aus dem Reaktionsmedium entfernt wird und die Verwendung von überstöchiometrischen Silbersalzreagenzien, die normalerweise für solche Reaktionen verwendet werden, vermieden werden kann. Da das langlebige Intermediat eine entscheidende Rolle spielt, wird dieser Komplex intensiv untersucht. Der Einflusses von elektronenziehenden oder -schiebenden Gruppen auf die Wechselwirkung zwischen dem Pd(II) und der Doppelbindung im Produkt ermöglicht es, die Erkenntnisse aus den quantenchemischen Berechnungen zu nutzen, um weitere mögliche Reaktanten systematisch zu erforschen.

Für die kombinierte quantenchemische und mikrokinetische Untersuchung der asymmetrischen Hydroborierung von Acetophenon durch einen kooperativen Lewis-Säure–Onium-Salz-Katalysator wird die Energielandschaft berechnet, um Einblicke in mögliche Reaktionsmechanismen und Nebenreaktionen zu erhalten. Lokalisierte *intrinsic bond orbitals* werden herangezogen, um die vorgesehene doppelte Aktivierung des Katalysators, den Einfluss der vorhandenen Halogenidionen und die Aktivierung des Katalysators durch ein Lösungsmittelmolekül, zu untersuchen. Zusätzlich wird eine mikrokinetische Modellierung angewandt, die einen umfassenderen Einblick in das Reaktionssystem ermöglicht. Sie berücksichtigt sowohl energetische als auch Konzentrationseffekte. Außerdem werden Reaktionsbarrieren aus experimentellen Kinetikdaten extrahiert. Ein solcher Ansatz ermöglicht einen direkten Vergleich von Theorie und Experiment und gibt detaillierte Einblicke in die elementaren Schritte des Reaktionsme-

chanismus, z.B. erleichtert das Gegenion des Ammoniumsalzes des Katalysators den Hydridtransferschritt des Reaktionszyklus. Chlorid anstelle von Iodid beschleunigt die Hauptreaktion, hat aber gleichzeitig die gleiche Wirkung auf eine Nebenreaktion, bei der das Produkt verbraucht wird. Mit diesem Mechanismus werden konsistente freie Enthalpiebarrieren für das quantenchemische und kinetische Modell gewonnen. Darüber hinaus enthüllt eine mikrokinetische Sensitivitätsanalyse die ratenlimitierenden Schritte, um die für die Enantioselektivität relevanten Zustände zu diskutieren.

Peer-Reviewed Publications

Peer-reviewed publications included in this thesis:

Paper I:
J. Heitkämper, S. Posada-Pérez, S. Escayola, M. Solà, J. Kästner, and A. Poater: *A Non Expected Alternative Ni(0) Species in the Ni-Catalytic Aldehyde and Alcohol Arylation Reactions Facilitated by a 1,5-Diaza-3,7-diphosphacyclooctane Ligand.* Chemistry: A European Journal **29** (28), e202300193 (2023)
DOI: https://doi.org/10.1002/chem.202300193

Paper II:
K. Gadde*, N. R. Bheemireddy*, J. Heitkämper*, A. Nova, and B. U. W. Maes: *Directed Palladium-Catalyzed γ-C(sp^3)-H Alkenylation of (Aza and Oxa) Cyclohexanamines with Bromoalkenes: Bromide Precipitation as an Alternative for Silver Scavenging.* ACS Catalysis **14** (2), 1157–1172 (2024)
DOI: https://doi.org/10.1021/acscatal.3c04152
* contributed equally to this work

Paper III:
M. Titze, J. Heitkämper, T. Junge, J. Kästner, and R. Peters: *Highly Active Cooperative Lewis Acid–Ammonium Salt Catalyst for the Enantioselective Hydroboration of Ketones.* Angewandte Chemie (International ed. in English) **133** (10), 5604–5613 (2021)
DOI: https://doi.org/10.1002/ange.202012796

Paper IV:
J. Heitkämper, J. Herrmann, M. Titze, S. Bauch, R. Peters, and J. Kästner: *Asymmetric Hydroboration of Ketones by Cooperative Lewis Acid–Onium Salt Catalysis: A Quantum Chemical and Microkinetic Study to Combine Theory and Experiment.* ACS Catalysis **12** (2), 1497–1507 (2022)
DOI: https://doi.org/10.1021/acscatal.1c05440

Peer-reviewed publications not included in this thesis:

1. L. Pfitzer, J. Heitkämper, J. Kästner, and R. Peters: *Use of the N-O bonds in N-mesyloxyamides and -succinimides to get access to 5-alkoxy-3,4-dialkyloxazol-2-ones and 3-heterosubstituted succinimides – a combined experimental and theoretical study.* Synthesis, **55**, 2460-2472 (2023)
   DOI: https://doi.org/10.1055/s-0042-1751447

2. J. Heitkämper, S. Suchaneck, J.G. Concepción, J. Kästner, and G. Molpeceres: *The reactivity of pyridine in cold interstellar environments: The reaction of pyridine with the CN radical.* Frontiers in Astronomy and Space Sciences, **9**, 1020635 (2022)
   DOI: https://doi.org/10.3389/fspas.2022.1020635

3. E. Gougoula, C. Cummings, C. Medcraft, J. Heitkämper, and N. R. Walker: *Microwave Spectra, Molecular Geometries, and Internal Rotation of CH_3 in N-methylimidazole...H_2O and 2-methylimidazole...H_2O Complexes.* Physical Chemistry Chemical Physics, **24**, 12354-12362 (2022)
   DOI: https://doi.org/10.1039/d1cp05526g

4. O. Reckeweg, F. Lissner, J. Heitkämper, J. Kästner, and T. Schleid: *The unexpected crystal structure of thallium(I) tricyanomethanide $Tl[C(CN)_3]$.* Zeitschrift für Naturforschung B, **77** (4-5), 237-243 (2022)
   DOI: https://doi.org/10.1515/znb-2022-0006

5. J. Poater, J. Heitkämper, A. Poater, V. Maraval, and R. Chauvin: *Zwitterionic Aromaticity on Azulene Extrapolated to carbo-Azulene.* European Journal of Organic Chemistry, **46**, 6450–6458 (2021)
   DOI: https://doi.org/10.1002/ejoc.202101228

6. D. Gratzfeld, J. Heitkämper, J. Debailleul, and M. Olzmann: *On the influence of water on urea condensation reactions: a theoretical study.* Zeitschrift für Physikalische Chemie, **234** (7–9), 1311–1327 (2020)
   DOI: https://doi.org/10.1515/zpch-2020-1658

7. E. Gougoula, C. Medcraft, J. Heitkämper, and N. R. Walker: *Barriers to internal rotation in methylimidazole isomers determined by rotational spectroscopy.* The Journal of Chemical Physics, **151**, 144301 (2019)
   DOI: https://doi.org/10.1063/1.5119997

Contents

List of Abbreviations

CREST	Conformer–rotamer ensemble sampling tool
DFT	Density functional theory
GFN2-xTB	Geometry, frequency, noncovalent, extended tight-binding
GGA	Generalised gradient approximation
HF	Hartree-Fock
IAO	Intrinsic atomic orbitals
IBO	Intrinsic bond orbitals
IRC	Intrinsic reaction coordinate
ISM	Interstellar medium
LCAO	Linear combination of atomic orbitals
LDA	Local density approximation
MD	Molecular dynamics
MEP	Minimum energy path
NBO	Natural bond orbitals
NISQ	Noisy intermediate-scale quantum
NLMO	Natural localized molecular orbitals
ODE	Ordinary differential equations
PES	Potential energy surface
QPE	Quantum phase estimation
RCSS	Reaction rate constant scaled sensitivity
RDS	Rate determining step
RRHO	Rigid-rotor-harmonic-oscillator
RRKM	Rice-Ramsperger-Kassel-Marcus
SCF	Self-consistent field
TDI	TOF-determining intermediate
TDTS	TOF-determining transition state
TOF	Turnover frequency
TST	Transition state theory

| **VQE** | Variational quantum eigensolver |
| **ZPE** | Zero-point energy |

1 Introduction

1.1   Computational Homogeneous Catalysis

Catalytic reactions have become an indispensable part of modern society. Being an essential part of many biological functions in living organisms, they became increasingly relevant in the chemical industry to satisfy the growing global demands for fertilizers, fuels, pharmaceuticals, and plastics. Meanwhile, 75% of all chemicals in the chemical industry are produced with the help of catalysts, mainly in the homogeneous or heterogeneous regime. The number raised up to 90% for newly developed processes.[1] In the future, catalytic processes are promising in environmental applications, one of the many possibilities being the production of clean hydrogen with electrocatalysis[2] or conversion of CO_2 into fuels or chemicals.[3]

The final goal of chemists around the world is the predictive discovery of new catalytic reactions, without the need of trial and error experiments. To design catalysts systematically, a detailed understanding of all fundamental reaction steps, their barriers, and kinetic aspects that control the performance of the overall reaction is required. Computational methods based on first-principles electronic structure theory are promising tools to give these insights. They play an increasing role in mechanistic studies of chemical reactions due to faster computers and the development of efficient methods and numerical algorithms to solve the Schrödinger equation. They provide physical insights into the reaction mechanism on a microscopic molecular level. The exploration of the potential energy surface reveals elementary steps and their barriers. Further, the analysis of the electronic structure of the catalyst gives an insight into important aspects like charge distribution and binding energies that drive chemical reactivity.
One example to emphasize the value of quantum chemical calculations is the Grignard reaction, a fundamental reaction to form a carbon-carbon bond taught in every undergraduate chemistry course. The detailed mechanism of this reaction remained unresolved for more than 100 years until, in 2020, a computational study shed light on the multiple coexisting organomagnesium species, competing nucleophilic or radical

reaction paths, and the role of the solvent.[4]

However, computational homogeneous catalysis faces numerous challenges. The limited accuracy of calculations and the intricate interpretation of complex multi-step reactions necessitate a deep understanding of both quantum chemical and kinetic aspects. The present thesis addresses these important considerations through the evaluation of three catalytic reactions as illustrative examples.

1.2   Subject and Outline of the Thesis

In this thesis, computational methods are used to shed light on the reaction mechanism of three homogeneously catalyzed reactions:

A study on the coupling reaction of aldehydes with organohalides, which gives access to secondary alcohols, is presented (**paper I**).[5] The prominent and widely used Grignard reaction synthesizes secondary alcohols via a C-C coupling reaction. The stoichiometric amounts of organomagnesium reagents being used and the necessity of low temperatures due to the reaction's exothermic nature are serious drawbacks. Isbrandt *et al.* developed a new efficient Ni-catalyst with a 1,5-diaza-3,7-diphosphacyclooctane ligand, which mediates the reaction without the use of stoichiometric metal reagents.[6] The present thesis sheds light on the underlying reaction mechanism with an emphasis on the eternal cross-coupling debate of whether the catalytically active species is Ni(0) or the reaction is taking shortcuts following the course of Ni(II). Different competing paths and unwanted side reactions are discovered, and their behavior with different ligands is studied to relate to experimental results. The role of the involved base is also subject to the study.

Following the debate of oxidation states within catalytic cycles, a Pd-catalyzed γ-C(sp^3)-H alkenylation of cyclohexanamines is studied using DFT in close collaboration with experimentalists from the University of Antwerp[i] (**paper II**).[7] Pd-catalyzed C-H bond functionalization reactions are a hot topic as they allow the functionalization of a stable hydrocarbon group under the formation of a new carbon-carbon or carbon-heteroatom bond. However, directed palladium-catalyzed coupling reactions of remote C(sp^3)-H bonds of aliphatic amines with organohalides usually require more reactive

---

[i]Karthik Gadde, Narendraprasad Reddy Bheemireddy, Prof. Dr. Bert Maes, Organic Synthesis (ORSY) group

iodinated reactants and superstoichiometric silver salt reagents, which are known for its role to scavenge halide ions. Bromide reactants and a silver free protocol are desired to optimise cost and resource efficiency.

The mechanism proposed for these reactions typically goes through Pd(II)/Pd(IV) pathways[8] but an alternative Pd(II)/Pd(0) is studied in the present thesis. Also, it is crucial but difficult to predict whether the C-H bond activation or the oxidative addition to Pd(II) would be the rate-limiting step since both steps have been shown to yield relatively high energy barriers.[8,9] The calculation of the full energy landscape for the investigated reaction can reveal the crucial parameters that contribute to the efficiency of the reaction and enables the systematic prediction which reaction conditions can be tuned to achieve better yields or a more sustainable reaction protocol.

The last reaction under study in the present thesis is the asymmetric hydroboration of ketones by a cooperative Lewis acid–onium salt catalyst. The catalyst was designed by collaborating experimentalists from the University of Stuttgart[ii] with dual activation in mind: the aluminum center is supposed to activate the ketone, whereas the onium moiety is thought to activate the borane (**paper III**).[10] Analysis of the electronic structure makes it possible to reveal and quantify this effect. Also, the role of the solvent, which is experimentally found to influence the reaction highly, can be revealed. Microkinetic modeling compares the resulting mechanism and its barriers to experimental kinetic data that experimental collaborators provide (**paper IV**).[11] Extracting barriers by fitting concentration vs. time profiles from the kinetic model to the experimental data allows the comparison of theory and experiment. This is used to find out important details, such as the influence of the solvent, present ions, and side reactions on the overall performance of the reaction.

This thesis is structured as follows: Chapter 2 introduces the basic concepts necessary to study catalytic reactions in homogeneous catalysis from a theoretical perspective. First, aspects concerning the motions of nuclei on the potential energy surface (PES) are reviewed. This is followed by a section on theoretical chemical kinetics, discussing microkinetic modeling and the transition state theory. The following section deals with the electronic structure theory, focusing on density functional theory (DFT) and localization methods to extract chemical information like charge distribution and interaction energies from the wave function. In Chapter 3, scientific results that are the subject of this thesis are presented. Section 3.1 deals with the quantum chemical investigation of

---

[ii]Marvin Titze, Justin Herrmann, Prof. Dr. René Peters, Institute of Organic Chemistry

the full reaction mechanism of Ni-catalytic aldehyde arylation reaction facilitated by a 1,5-diaza-3,7-diphosphacyclooctane ligand and Section 3.2 with the Pd-catalyzed γ-C(sp^3)-H alkenylation of cyclohexanamines with 1-bromoalkenes. Section 3.3 presents the quantum chemical calculations on the hydroboration of ketones catalyzed by a cooperative Lewis acid–onium salt catalyst and the role of the solvent in this reaction system. Based on these results, a more extensive combined quantum chemical and microkinetic study is provided in Section 3.4. The individual papers are contextualized within the broader framework in Chapter 4, where they are accompanied by a discussion within the context of computational homogeneous catalysis. Finally, Chapter 5 summarizes this thesis.

2 Methods

This chapter introduces methods necessary to study chemical reactivity from a theoretical perspective. The focus is set on aspects of theoretical kinetics, which mainly contributed to the developments within this work.

First, the basic principles and properties of the potential energy surface (PES) are explained. The next section introduces chemical kinetics and the basic ideas of microkinetic modeling. Following a macroscopic picture, the reaction rate and rate laws are first discussed. Then, the transition state theory is derived from a microscopic ansatz of kinetics from purely theoretical considerations.

The final section deals with aspects of electronic structure theory relevant to this thesis. Basic principles like the Hartree-Fock (HF) theory, orbitals, basis sets, and the density functional theory (DFT) are reviewed as they are crucial to assess quantum chemical results. In the last section, selected localization methods are presented, which extract chemical information like charge distribution and interaction energies from the wave function.

2.1 Energy Landscape of Chemical Reactions

2.1.1 Potential Energy Surface

Quantum mechanics describes an atom or molecule as a wave function. This function contains all information about the system; thus, all atomic or molecular properties can be derived from it. The references 12–14 give a good introduction to this topic, on which the following section is based.

It is a hitherto unfalsified postulate that the time-independent Schrödinger equation

$$\hat{H}\Psi(x_1, x_2, ..., x_N, R_1, R_2, ..., R_M) = E\Psi(x_1, x_2, ..., x_N, R_1, R_2, ..., R_M) \qquad (2.1)$$

can be used to connect the energy eigenvalue E of a stationary state with a wave function Ψ, which depends on the position of the nucleus R_A and of the electrons x_i. Note that the spin coordinate has been omitted for simplicity. The Hamilton operator $\hat{H}$ contains

all contributions to the total energy of the system, which are the potential energies $\hat{V}$ and kinetic energies $\hat{T}$ of the nuclei N and electrons e:

$$\hat{H} = \hat{V}_{NN} + \hat{V}_{Ne} + \hat{V}_{ee} + \hat{T}_{N} + \hat{T}_{e}. \tag{2.2}$$

However, the solution of the Schrödinger Equation (2.1) is not even possible for simple three-body problems, such as for the simplest possible molecule H_2^+, due to coupled motions of nuclei and electrons. The first step to solving Equation (2.1) is the Born-Oppenheimer approximation. Herein, nuclear and electron motion coupling is eliminated since nuclei move much slower than the electrons. This is because even the lightest nuclei weighs roughly 1800 times more than an electron.[13] Therefore it is assumend that electrons follow the movement of the nuclei instantaneously and electrons are moving in the field of fixed nuclei. The total energy of a system with certain nuclear coordinates using the Born-Oppenheimer approximation is therefore composed of an electronic Hamiltonian operator $\hat{H}_{el}$ and a constant interaction among the nuclei. With the nuclear charge number Z_A and the nabla operator $\nabla = \left(\frac{\partial}{\partial x_1}, \frac{\partial}{\partial x_2}, \cdots \frac{\partial}{\partial x_i} \right)$ the Hamilton operator $\hat{H}_{BO}$ within the Born-Oppenheimer approximation reads

$$\hat{H}_{BO}(R) = \hat{H}_{el}(R) + \sum_{A=1}^{M} \sum_{B>A}^{M} \frac{Z_A Z_B}{|R_A - R_B|}, \tag{2.3}$$

with

$$\hat{H}_{el}(R) = \hat{V}_{Ne} + \hat{V}_{ee} + \hat{T}_{e} = -\sum_{i=1}^{N} \sum_{A=1}^{M} \frac{Z_A}{|x_i - R_A|} + \sum_{i=1}^{N} \sum_{j>i}^{N} \frac{1}{|x_i - x_j|} - \frac{1}{2} \sum_{i=1}^{N} \nabla_i^2. \tag{2.4}$$

Note that atomic units are utilized here and throughout this thesis. The decoupled nuclear dynamics can be described in a separate multidimensional potential energy surface (PES) $E_{BO}(R)$, which is calculated by solving the Schrödinger equation with the Hamilton operator $\hat{H}_{el}$ for different nuclear distances. Methods to calculate the electronic energy $E_{el}(R)$ are explained in Section 2.3.

The PES of a non-linear molecule with M atoms is $3M$-6 dimensional, which makes its calculation even for small molecules impossible. Therefore, only selected points required for the investigation of chemical reactivity are targeted.

There are two types of these points: minima and transition states. Both have in common

that the first derivative, or gradient, is zero. Stable molecular geometries represent energetic minima, as illustrated in Figure 2.1. Chemically they are reactants, products, or intermediates. Mathematically they are characterized by a positive definite Hessian matrix (matrix of second derivatives of the energy). Within the harmonic approximation, vibrational frequencies ν_i of the ith mode can be calculated from the eigenvalues of the mass-weighted Hessian matrix[15,16] $h_{\mathrm{mw},i}$ with the formula

$$\nu_i = \frac{1}{2\pi} \sqrt{h_{\mathrm{mw},i}}. \tag{2.5}$$

The according eigenvectors correspond to the vibrational normal modes. For a positive definite Hessian matrix, all vibrational frequencies are real.

Transition states are maxima along a minimum energy path (MEP) connecting two minima on the PES, which represent the reactant and product (see Figure 2.1). They are first-order saddle points, meaning they are maxima along the reaction coordinate q_1 and minima along all other coordinates. In addition to a vanishing gradient, the indefiniteness of the Hessian matrix is required. A transition state possesses precisely one negative eigenvalue, which according to Equation (2.5), results in an imaginary frequency. The associated eigenvector describes the reaction coordinate. An intrinsic reaction coordinate (IRC) calculation follows this mode in positive and negative directions along the gradient until the next (local) minimum, verifying reactant and product geometries. The concept of a transition state allows studying kinetical aspects theoretically. The energy difference between the transition state and the reactant gives the energy barrier for this reaction step. Further, introducing a dividing surface perpendicular to the reaction coordinate that separates the reactant and product energy surfaces, shown in pink in Figure 2.1, allows evaluating the flux through this surface. As discussed in Section 2.2.2, reaction rate expressions can be derived from this ansatz.

As illustrated in Figure 2.1 it has to be considered that even at absolute zero temperature, molecules retain vibrational motion in their equilibrium structures with coordinates $\mathbf{R}_{\mathrm{min}}$, contributing to the system's internal energy. This zero-point energy (ZPE) is a consequence of the Heisenberg uncertainty principle. Assuming harmonic oscillators, the lowest possible energy E^{ZP} a non-linear quantum system can have is

$$E^{\mathrm{ZP}}(\mathbf{R}_{\mathrm{min}}) = E_{\mathrm{el}}(\mathbf{R}_{\mathrm{min}}) + \frac{1}{2} \sum_{i=1}^{3M-6} h\nu_i, \tag{2.6}$$
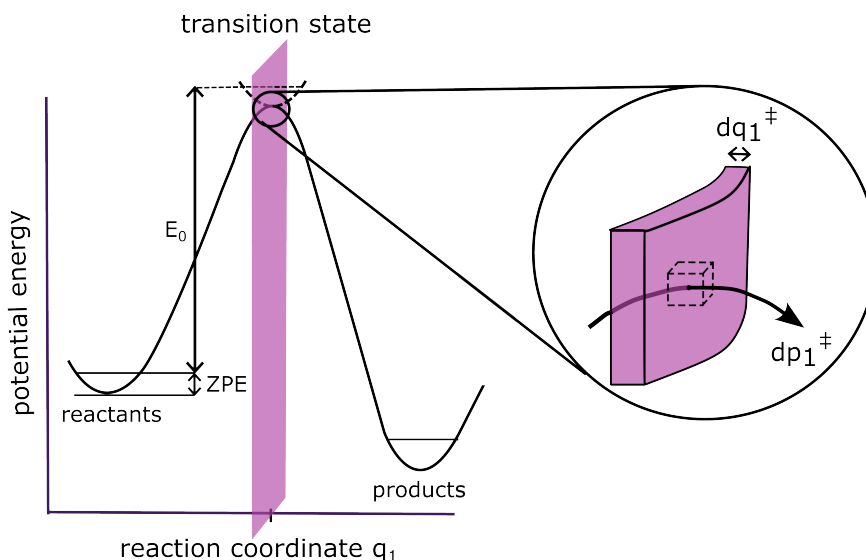
Figure 2.1: Reaction path going from a reactant to a product molecule by passing through a transition state. Shown are also corrections from vibrational zero-point energy (ZPE). The dynamics of the transition state in phase space with the reaction coordinate q_1 and the according momentum p_1 is indicated and the dividing surface drawn in pink.

in which the electronic energy $E_{\mathrm{el}}(\mathbf{R})$ and vibrational modes in the lowest vibrational level are considered. h is the Planck constant and ν_i the frequency of the vibration. The latter is calculated from the Hessian matrix (see Equation (2.5)), which makes its calculation computationally demanding.

However, the energetic landscape does not cover all kinetic information. Considering only energetic information gained from the PES is limiting, as the rate also depends on the concentrations of the involved species. To cover this, kinetic modeling can be applied, which is discussed in Section 2.2.1.

2.1.2 Gibbs Free Energy and Entropy

The goal of computational homogeneous catalysis is to predict chemical reactivity for real-life experiments. So far, theoretical models that describe isolated molecules at zero Kelvin have been discussed. The calculation of this contribution ΔE_{gas} is straightforward with standard *ab-initio* models (see Section 2.3). Additional corrections to account for a finite temperature T, solvation, and other entropic effects are required for a realistic model and comparability with experiments. A better quantity is, therefore, the Gibbs

free energy

$$G(T) = H(T) - T \cdot S(T) \tag{2.7}$$

with the temperature-dependent enthalpy H and entropy S. Statistical thermodynamics, for which all basics are covered in reference 17, can be applied to calculate these quantities. However, a routine method to compute the entropy accurately for large systems does currently not exist.[18,19] Still, in homogeneous catalysis, reaction steps often involve a change of molarity, for which entropy corrections are large in magnitude.[20] The inclusion of entropy is therefore important, as it can change the energy surface qualitatively or affect the agreement with experiments quantitatively. The references 21–23 give a good overview of the current challenges, methods, and their limitations to predict the entropy of large molecules in computational chemistry and reference 20 deals specifically with homogeneous catalysis.

It is common practice to divide the total Gibbs free energy ΔG into four contributions that are computed with different theoretical methods and approaches:[21,23]

$$\Delta G = \Delta E_{\text{gas}} + \Delta G_{\text{thermal}} + \Delta G_{\text{solv}} + \Delta G_{\text{conf}}. \tag{2.8}$$

The first term ΔE_{gas} is the gas phase reaction energy and was already discussed above. $\Delta G_{\text{thermal}}$ is the finite temperature contribution and considers that thermal energy excites translational, rotational, and vibrational modes into higher energy levels, increasing both, the enthalpy and the entropy. The distribution among different excited states is contained in the partition function. However, its calculation in solution is difficult. Typically an ideal gas is assumed, for which expressions of the partition functions can be derived easily. For an ideal gas, the entropy contribution for finite temperature effects can be written as:[17,24]

$$S_{\text{thermal}} = \frac{U}{T} + k_{\text{B}} \ln Q \tag{2.9}$$

with

$$Q = Q_{\text{trans}} Q_{\text{rot}} Q_{\text{vib}}. \tag{2.10}$$

Herein, Q is the canonical partition function and $Q_{\text{trans}}, Q_{\text{rot}}$, and Q_{vib} the canonical partition function for translation, rotation, and vibration, respectively. k_{B} is the Boltzmann constant and U the internal energy of the system. The harmonic oscillator and rigid rotator approximations are usually applied for vibrations and rotations. This is known as the rigid-rotor-harmonic-oscillator (RRHO) approach. Anharmonicities can be partially implied by linear or multi-parametric scaling of the harmonic frequencies.[22] The term ΔG_{solv} in Equation (2.8) is the Gibbs free energy of solvation. In theory,

intensive sampling would be required to capture all possible arrangements of a solute in the solvent. Explicit sampling with *ab-initio* molecular dynamics (MD) is applied in only a few studies[25,26] due to the high computational cost. Most quantum chemical studies in the liquid phase include solvation effects with implicit continuum models, which describe the solvent as a homogeneous, polarisable medium.[27,28] Including this method in single-point calculations, the computed values are hybrid quantities that include solvation entropy by construction as they are gained by integrating over all possible solvent structures.[20]

The last term in Equation (2.8) is the conformational contribution $\Delta G_{\text{conf.}}$[22,23,29] It considers that an ensemble of conformers close in energy is populated statistically, increasing the entropy. Usually, it is neglected due to high computational cost, but this can be an accuracy issue when studying reactions with a significant change of internal degrees of freedom, e.g., ring-opening or -closing reactions.[23]

As a final remark, it is highlighted that the output of conventional quantum chemistry codes gives usually free energies ΔG^{1atm} according to the gas phase standard state of 1 atm. To apply microkinetic modeling, discussed in Section 2.2, free energy barriers with respect to the standard concentration $c_0 =1$ mol l^{-1} have to be used. The choice of the reference state is important because it affects the available volume in the Sackur–Tetrode equation and, with this, the translational entropy.[20,30] Switching the reference states can be done by adding a correction term $RT\ln(c_0 V_m)$ to outputs from quantum chemistry codes. Herein, V_m is the molar volume obtained from the ideal gas law, and R is the ideal gas constant. For bimolecular processes, the free energy in solution ΔG^{1M} results in

$$\Delta G^{\text{1M}} = \Delta G^{\text{1atm}} - RT\ln(c_0 V_m), \qquad (2.11)$$

according to which bimolecular barriers in solution are lowered by about 8 kJ mol^{-1} at room temperature compared to gas phase barriers. This magnitude is not neglectable. Note that unimolecular processes are unaffected.

2.2 Theoretical Chemical Kinetics

2.2.1 Microkinetic Modeling

Reaction kinetics investigates how fast a reaction proceeds. Thus, a key observable is the change of concentrations over time, the reaction rate. In homogeneous catalysis, the overall reaction is usually a sequence of many elementary reaction steps, each with its individual transition state. Revealing non-equilibrium behavior is a powerful tool to get insight into the elementary steps. Analyzing net reaction kinetics requires reasonably good knowledge of the elementary steps involved, which can be studied on a molecular scale using quantum chemistry.

Good textbooks summarizing chemical kinetics are the references 31, 32. Considering a simple bimolecular reaction

$$\nu_a A + \nu_b B \underset{k_{-1}}{\overset{k_1}{\rightleftharpoons}} \nu_g G + \nu_h H \tag{2.12}$$
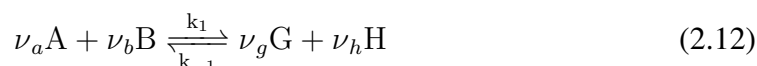
of ν_a molecules of compound A with ν_b molecules of compound B to the products G and H, the reaction rate r is defined as

$$r = -\frac{1}{\nu_a}\frac{d[A]}{dt} = -\frac{1}{\nu_b}\frac{d[B]}{dt} = \frac{1}{\nu_g}\frac{d[G]}{dt} = \frac{1}{\nu_h}\frac{d[H]}{dt}. \tag{2.13}$$

Note that [.] is used to indicate concentrations. For an elementary reaction step, rate expressions can be set up according to

$$r = -k_1 [A]^{\nu_a}[B]^{\nu_b} + k_{-1}[G]^{\nu_g}[H]^{\nu_h}. \tag{2.14}$$

In Equation (2.14), k_1 and k_{-1} are the temperature-dependent reaction rate constants of the forward and backward reaction, respectively. The order $\mathcal{O}$ of the reaction is defined as the sum of the powers, being $\nu_a + \nu_b$ for the forward reaction and $\nu_g + \nu_h$ for the backward reaction. Note that the aforesaid does not hold for reactions that fall into several reaction steps, for which the reaction order is empiric or has to be derived by mechanistical considerations.

For a complex reaction mechanism, Equation (2.13) and Equation (2.14) result in a set of coupled ordinary differential equations (ODE), which can not be solved analytically. Complicated mechanisms can in some cases be simplified by, for example, assuming one compound being present in great excess or applying the steady-state principle. With

such approximations, analytical solutions can be derived for complicated reaction mechanisms.[32]

If direct integration is unfeasible, numerical integration becomes necessary, and microkinetic modeling must be employed. While this methodology is frequently utilized in heterogeneous catalysis,[33–36] it is scarcely applied in homogeneous catalysis.[37,38] The workflow adopted in this thesis, as illustrated in Figure 2.2, proceeds as follows: quantum chemical calculations are performed to give knowledge about the reactions with the lowest barriers, for which rate constants can be calculated using transition state theory (TST) (see Section 2.2.2). All possible reactions are bundled into a reaction mechanism, from which rate laws can be derived using the rules derived above. This mathematical model can be integrated numerically, for example with the $4th$ order Runge-Kutta method.[39,40] From a set of initial concentrations of each compound, the rate constants of each reaction and Equation (2.14), the concentrations can be propagated in small time-steps. The solution is the concentration of each involved species as a function of time. It can be used to predict the behavior of complex reaction systems or to identify critical reaction intermediates and rate-determining elementary reactions. In this thesis, microkinetic modeling is used to extract reaction barriers from experimental data to compare them with quantum chemical results. Therefore, reaction constants, or reaction barriers, are varied to fit the kinetic model to experimental values. The resulting barriers represent an optimized set extracted from the experimental data. It can be directly compared with barriers calculated with quantum chemistry. However, as indicated by the workflow in Figure 2.2, the extracted values are initialized by a guess of the reaction mechanism and the barriers based on the quantum chemical results. The two approaches are, therefore, not completely independent.

The solution of the full kinetic model provides a numerical identification of rate-controlling transition states and intermediates for complex reaction networks involving species with different concentrations. Campbell's concept of rate control has been established as a useful method.[41] As the reaction rate is dependent on both the rate constants (or barriers) and the concentrations, this method offers a more comprehensive analysis compared to considerations based solely on the potential energy surface. It has been applied in many cases for heterogeneous catalysis,[42,43] but applications in homogeneous catalysis[44,45] are less common. Within this concept, a reaction rate constant
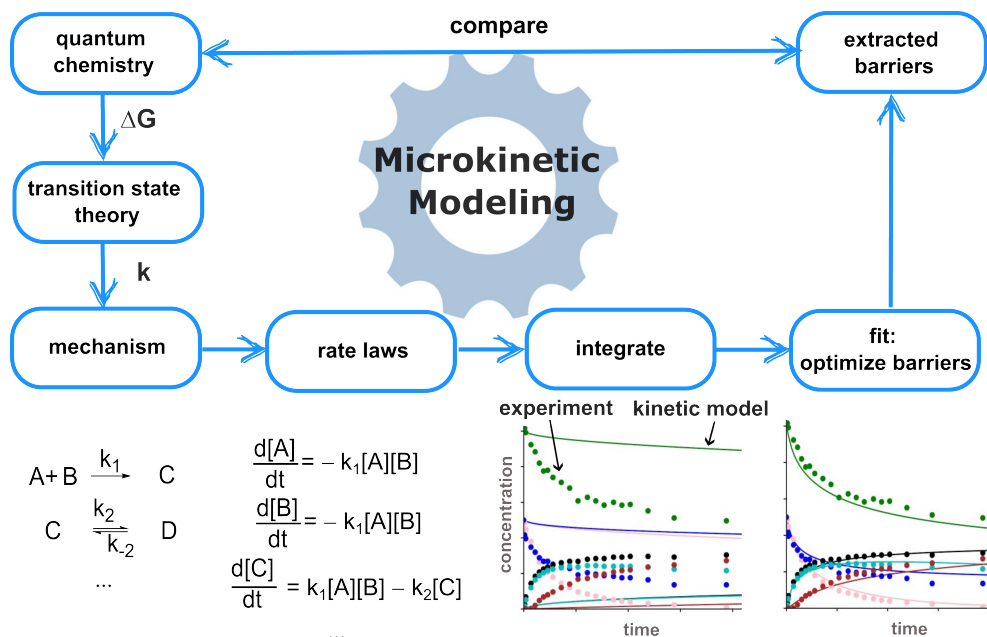
Figure 2.2: Schematic workflow of a microkinetic model.

scaled sensitivity (RCSS) is defined as[44]

$$RCSS_i = \frac{k_i}{r}\left(\frac{\partial r}{\partial k_i}\right)_{k_{j\neq i}}, \tag{2.15}$$

which identifies the few species or barriers that, if slightly changed independently, would speed up the reaction significantly. These species can be revealed, and modification of the catalyst, ligands, or solvent to stabilize or destabilize them can be targeted to improve the reaction systematically. Equation (2.15) quantifies the relative increase (or decrease) in the net reaction rate with a relative increase (or decrease) of the rate constant k_i. Therefore $RCSS_i \in [-1, 1]$ is positive if the reaction rate increases with a higher rate constant (lower barrier) and negative if the reaction slows down for the same scenario. The latter is given for backward reactions or inhibitions. The higher the absolute value of $RCSS_i$, the more it influences the overall rate. For simple reactions, which can be reduced to one RDS, one value is 1, and the rest 0. If the RCSS for a step is 1, a decrease in its barrier by $k_\mathrm{B}T$ would increase the reaction rate by a factor of e.[41] Despite revealing rate-determining steps, $RCSS_i$ is also a measure of the kinetic model's sensitivity. A low value indicates a low sensitivity of the kinetic model towards the barrier i, and it can not be extracted with high accuracy.

Summarizing the aforementioned, calculating the time-dependent concentrations of all

involved species is possible via numerical integration. The last open question is what rate constants k_i to insert in Equation (2.14). This subject is dealt with in the upcoming section, where rate constants are calculated using transition state theory (TST). This method allows the kinetic investigation of large systems, which would need expensive dynamic calculations, by breaking the movements of nuclei down to the problem of finding the transition state and its free energy barrier.

2.2.2   Theory of Reaction Rates

A widely used approach to obtain theoretical absolute reaction rates for bimolecular reactions between molecules A and B in gas and condensed phase is the transition state theory (TST) developed by Eyring, Evans, and Polanyi in 1935.[46–48] Its formulation is based on an existing critical configuration (transition state) on a dividing surface, as discussed in Section 2.1.1, separating the phase space of reactants and products. The dynamics on the PES (Born-Oppenheimer approximation holds) is then evaluated using classical mechanics.[49] Concepts from quantum mechanics and statistical thermodynamics, for example, the calculation of partition functions, are adapted selectively, shaping it into a hybrid theory between dynamics, classical mechanics, quantum mechanics, and statistical thermodynamics. Following the dynamical derivation in reference 32, the reactive flux in phase space, meaning the number of trajectories passing the transition state, is evaluated to arrive at a semi-classical rate expression. This concept is visualized in Figure 2.1.

The first step is to determine the number of activated species that lie in a volume element

$$d\tau = dq_1^\ddagger ... dq_{3M}^\ddagger dp_1^\ddagger ... dp_{3M}^\ddagger. \tag{2.16}$$

on the dividing surface. M is the number of atoms, q are the coordinates, and p the according momenta. q_1 is the reaction coordinate. It can be shown that there are $d\tau / h^{3M}$ states in this volume element.[32] Assuming that the reactants are in thermal equilibrium according to the Boltzmann distribution, and conducting classical statistical mechanics, the relative fraction of reactant species in *one* volume element $d\tau$ on the dividing surface

is given by

$$\frac{dN^{d\tau}}{N_{\mathrm{A}}N_{\mathrm{B}}} = \frac{\exp\left(-\frac{H}{k_{\mathrm{B}}T}\right) dq_1^{\ddagger}...dq_{3M}^{\ddagger}dp_1^{\ddagger}...dp_{3M}^{\ddagger}h^{-3M}}{\int^R \exp\left(-\frac{H}{k_{\mathrm{B}}T}\right) dq_1...dq_{3M}dp_1...dp_{3M}h^{-3M}} \tag{2.17}$$

$$= \frac{\exp\left(-\frac{H}{k_{\mathrm{B}}T}\right) dq_1^{\ddagger}...dq_{3M}^{\ddagger}dp_1^{\ddagger}...dp_{3M}^{\ddagger}h^{-3M}}{Q_{\mathrm{A}}VQ_{\mathrm{B}}V}. \tag{2.18}$$

Herein, N_{A} and N_{B} are the number of molecules and Q_{A} and Q_{B} the partition functions per unit volume V of A and B, respectively. H is the classical Hamiltonian and R denotes that the integral goes over the phase space of the reactant. Equation (2.18) implies that the effective flux goes from reactants to products, and recrossing does not occur. This is a fundamental assumption of the theory and will be elaborated in more detail later. As discussed in reference 32 in great detail, no recrossing results in the transition state being in equilibrium with the reactants, which is the fundamental assumption when deriving TST from a statistical mechanical point of view.

Equation (2.18) is differentiated with respect to time, and the result is integrated over the phase space of the whole dividing surface (only positive values of $p_1^{\ddagger}$ to exclude recrossing). To solve the resulting integrals, the Hamiltonian is separated into energy contributions of the reaction coordinate $H^{\ddagger}$ and the rest of coordinates $H^{\backprime}$. The motion along the reaction coordinate is then described as a translation

$$H = H^{\ddagger} + H^{\backprime} = \frac{(p_1^{\ddagger})^2}{2\mu_1} + H^{\backprime} = \frac{1}{2\mu_1}\left(\mu_1\frac{dq_1^{\ddagger}}{dt}\right)^2 + H^{\backprime}. \tag{2.19}$$

with the reduced mass μ_1. Note that now there are only $3M - 7$ vibrational modes for a non-linear molecule as one vibration along the reaction coordinate was converted into translation. Implementing the aforesaid and integrating over the dividing surface results in

$$\frac{dN}{dt} = \frac{[\mathrm{A}][\mathrm{B}]}{\mu_1 h}\frac{k_{\mathrm{B}}T}{h}\frac{\int \exp\left(-\frac{H^{\backprime}}{k_{\mathrm{B}}T}\right) dq_2^{\ddagger}...dq_{3M}^{\ddagger}dp_2^{\ddagger}...dp_{3M}^{\ddagger}h^{-(3M-1)}}{Q_{\mathrm{A}}Q_{\mathrm{B}}}. \tag{2.20}$$

Using the energy barrier E_0 of the transition state with respect to the reactants, one can rewrite the remaining integral in Equation (2.20) in terms of the partition function $Q^{\ddagger}$ of the transition state for the $3M - 1$ degrees of freedom and a remaining exponential term. Comparing the result with a rate law for a bimolecular reaction (see Equation (2.13) and

Equation (2.14)) gives the famous Eyring equation

$$k = \frac{k_{\mathrm{B}}T}{h} \frac{Q^{\ddagger}}{Q_A Q_B} \exp\left(-\frac{E_0}{k_{\mathrm{B}}T}\right). \tag{2.21}$$

This equation can be multiplied by a transmission coefficient κ to account for tunneling. This goes beyond the scope of this thesis, and the interested reader is referred to reference 50 for an overview of methods and the impact of tunneling in different fields of chemistry.

In homogeneous catalysis, where temperature corrections are of great importance, the thermodynamic form of the Eyring expression

$$k = \frac{k_{\mathrm{B}}T}{h} \exp\left(-\frac{\Delta G_0}{k_{\mathrm{B}}T}\right) \tag{2.22}$$

is used, where ΔG_0 is the difference in standard-state molar free energy between the transition state and the reactants. Note that Equation (2.22) and Equation (2.21) are equivalent considering that $G = -k_{\mathrm{B}}T\ln Q$ holds.[32]

TST would be exact in a classical world without a recrossing of trajectories. The latter limitation overestimates the flux through the transition state because they ignore that trajectories can turn around and move back to the reactant, not leading to any reaction. Therefore, the TST rate can be seen as an upper bound of the rate constant. A refinement of the method emerged with the variational TST (see reference 51 for a recent review). Herein, the dividing surface is shifted along the reaction coordinate to obtain the surface with the minimum rate. However, calculating the flux on various points would need the calculation of the Hessian matrix to calculate partition functions at each of them, which is computationally unfeasible for system sizes studied in the present thesis.

Apart from that, from the derivation above, it becomes clear that a movement of the nuclei according to classical mechanics is assumed. Quantization effects are added through quantum mechanical descriptions of the vibrational partition functions, ending in a semi-classical formulation. It is interesting that a full quantization of the theory faces some fundamental issues as it would need simultaneous knowledge of the reaction coordinate and its momentum to calculate the reactive flux. This would violate the Heisenberg uncertainty principle. Therefore the transition state is not localized.[32] As a result, the reaction coordinate is not separable from the remaining degrees of freedom. This is why a theory derived from classical mechanics is still used until today for the quantum chemical calculation of reaction rates.

The last limitation to be mentioned is the assumption that for multi-step reactions, intermediates are long-lived enough to reach the Boltzmann distribution before the reaction proceeds. However, in homogeneous catalysis, the slow process is usually the passage over the barrier, and compared to this, translational, rotational, and vibrational energy equilibrate on a faster timescale. If the reaction is sufficiently slow, the population deviates only insignificantly from thermal equilibrium.[52]

The transition state theory derived in the previous section holds for a canonical ensemble characterized by uniform temperature and Boltzmann distributed states. The canonical rate constant $k(T)$ can be interpreted as a Boltzmann average of the microcanonical rate constant $k(E)$. With the Boltzmann probability $P(E)$, they can be converted using[32]

$$k(T) = \int_0^\infty k(E)P(E)\mathrm{d}E = \frac{1}{Q_\mathrm{A}} \int_0^\infty k(E)\rho_\mathrm{A}(E)\exp^{-\frac{E}{k_B T}}\mathrm{d}E. \tag{2.23}$$

Herein, Q_A and ρ_A are the partition function and the density of states of the reactant, respectively. The microcanonical rate constant $k(E)$ was historically derived based on the unexpected observation that unimolecular reactions are pressure dependent. Lindemann's explanation is that a key role is an activation event by bimolecular collision.[53] After activation, the molecule can either undergo deactivation or a reaction along a particular mode. If inside the energized molecule, at least a minimum energy E_0 is in a certain critical mode, an immediate reaction will take place along this mode. The according reaction constant is dependent on the available internal energy. The Rice-Ramsperger-Kassel-Marcus (RRKM) theory provides an ansatz to calculate this reaction constant purely using statistical mechanics.[54–57] For a full derivation of the theory, the interested reader is referred to the literature (e.g., references 31, 32). In the present work, a phenomenological introduction to the theory is given: assuming equilibrium between the transition state and reactants allows calculating the probability that at least E_0 is in critical mode. As for TST, it is assumed that the distribution among vibrational energy is way faster than the reaction itself and that, moreover, all internal states are accessible and equally probable. It can then be shown that the microcanonical rate constant is calculated as

$$k(E) = \frac{\sigma}{h}\frac{W^\ddagger(E - E_0)}{\rho_\mathrm{A}(E)} \tag{2.24}$$

with the reaction rate degeneracy σ and the sum of states of the transition state $W^\ddagger(E - E_0)$ above E_0 that is inside the reaction coordinate. Figure 2.3 illustrates the qualitative interpretation of equation 2.24. It shows that there is a statistical population

of all internal states of the reactant A at a fixed energy E, defining the microcanonical ensemble. The energy E of molecule A is redistributed among all active modes with a statistical weight $\rho_A dE$. If the critical mode (with its statistical weight $W^{\ddagger}(E - E_0)$) that leads to the investigated reaction is passed, the minimum energy E_0 has to be located in the reaction coordinate.

In RRKM theory, modes are either active (and can exchange energy freely) or adiabatic
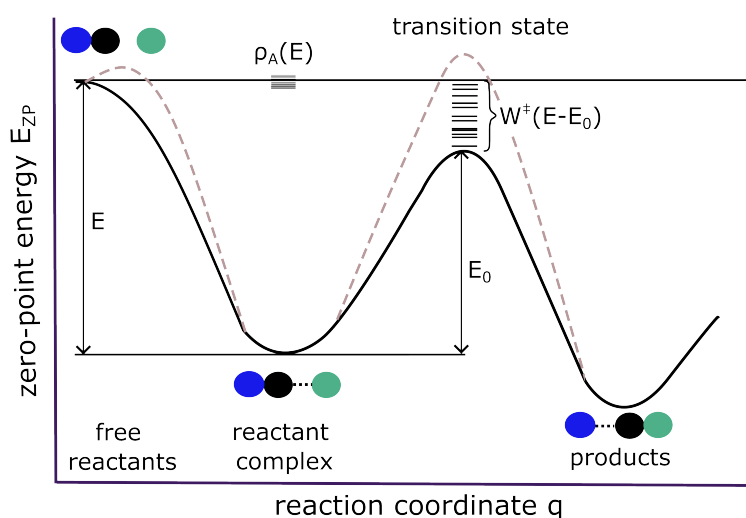
Figure 2.3: Phenemological interpretation of the RRKM theory via the number and density of states at energy E exemplary for an astrochemical reaction. Due to the lack of thermal energy, the dashed gray reaction path is impossible at 0 K without tunneling.

(mode remains in the same quantum number during the reaction). The usual assumption is to treat all vibrational and internal rotational modes as active. A deeper discussion on the treatment of both vibrations and rotations is given in references 32, 58–61.

It can be shown that using Equation (2.23), for high pressures, the RRKM expression turns into the Eyring Equation (2.21).[31,32] This emphasizes the application for low-pressure regimes, for example, in astrochemistry. The chemistry in the interstellar medium (ISM) is unique to what we know from down on Earth as the temperature and particle densities in these regimes are typically very low.[62] In areas with low pressure, no coupling with a bath is given, and the temperature is not well-defined in these regimes. The molecules are described better via a microcanonical over a canonical ensemble, and the RRKM theory is applied.

Due to the lack of thermal energy $k_B T$, only barrierless attacks and submerged barriers are possible (see Figure 2.3). Here, tunneling becomes important, and barriers that can-

not be overcome classically are possibly feasible considering tunneling. Therefore, the sum of states W is corrected according to

$$W_{\text{tun}}(E) = \int_0^{E-E_{R,0}} \rho(E')\kappa(E - E')\mathrm{d}E', \tag{2.25}$$

which counts the number of states below the energy barrier, weighted with a tunneling coefficient κ. For calculating the latter, it is common practice to use a one-dimensional Eckart barrier to avoid the expensive full treatment via instanton theory.[58,63]

In astrochemistry, computational research is crucial as experimental observations are limited due to extreme conditions. The question of which molecules can be formed under these conditions and how is still to be answered by both spectroscopy or quantum chemical simulations.[62] Quantum chemistry can be used, for example, to explain the lack of observations of heterocyclic species in the interstellar medium. These species are of great importance because they can be precursors of biologically relevant molecules such as nucleotides. Reasons for the absence of species in space are manifold, for example, high barriers of formation or fast chemical conversion or destruction. The reactivity of pyridine with the CN radical was studied by the author of this thesis, which is not included in this dissertation. Herein, a combination of quantum chemical calculations and kinetic simulations were applied. The results show that pyridine reacts very fast with CN radicals.[64] This can help the spectroscopic detectability of pyridine, because although pyridine possesses a net dipole moment, the fast addition of a CN group can increase its magnitude. Also, the calculated reaction constants can be used as inputs for astrochemical simulations.

2.3   Electronic Structure Theory

2.3.1   Basic Concepts of Quantum Chemistry

Due to the electron coupling term $\hat{V}_{\text{ee}}$ in Equation (2.4) analytical solutions of the electronic Schrödinger equation (Born-Oppenheimer approximation holds) are only given for systems with a single electron, e.g., the hydrogen atom or H_2^+ molecule. The solution is known as 1s, 2p, 3d, 4f, ... orbitals. For any bigger systems, appropriate numerical approximations have to be found. The references 12–14, used for the following section, provide a comprehensive review of common methods in quantum chemistry.
A suitable ansatz is constructing a trial wave function and optimizing its parameters to

obtain minimal energy. This holds because according to the variational principle, the expectation value of the energy $\langle E \rangle$ of this approximated wave function $\tilde{\Psi}$ is always larger than the true energy E_{exakt}:

$$E_{\text{exakt}} \leq E = \frac{\left\langle \tilde{\Psi} | \hat{H} | \tilde{\Psi} \right\rangle}{\left\langle \tilde{\Psi} | \tilde{\Psi} \right\rangle}. \tag{2.26}$$

A Slater determinant gives a suitable ansatz for an approximate multi-electronic wave function:

$$\tilde{\Psi}(\mathbf{x}_1, \mathbf{x}_2, ..., \mathbf{x}_N) = \frac{1}{\sqrt{N!}} \begin{vmatrix} \chi_1(\mathbf{x}_1) & \chi_2(\mathbf{x}_1) & ... & \chi_N(\mathbf{x}_1) \\ \chi_1(\mathbf{x}_2) & \chi_2(\mathbf{x}_2) & ... & \chi_N(\mathbf{x}_2) \\ \vdots & & & \vdots \\ \chi_1(\mathbf{x}_N) & \chi_2(\mathbf{x}_N) & ... & \chi_N(\mathbf{x}_N) \end{vmatrix}. \tag{2.27}$$

It is built up from N single-electron (spin) orbitals $\chi_k(\mathbf{x}_i)$. It automatically considers the antisymmetry of a wave function with respect to electron interchange required by the Pauli principle. Applying the variational principle to a single Slater determinant and considering the constraint of orthonormal spin orbitals, the Hartree-Fock equations

$$\hat{f}(i)\chi_k(\mathbf{x}_i) = \epsilon_i \chi_k(\mathbf{x}_i) \tag{2.28}$$

with the one-electron Fock-operator

$$\hat{f}(i) = -\frac{1}{2}\nabla_i^2 - \sum_{A=1}^{M} \frac{Z_A}{\mathbf{r}_{iA}} + \hat{\nu}_{\text{HF}}(i) \tag{2.29}$$

are obtained. The potential $\hat{\nu}_{\text{HF}}(i)$ is divided into a classical Coulomb term $\hat{J}$ and a non-classical exchange term $\hat{K}$, which describe the interaction of the electrons j and i. ϵ_i can be physically interpreted as one-electron orbital energy. The N energetically lowest orbitals are occupied, while energetically higher-lying, so-called virtual orbitals remain unoccupied.

In addition to the first two terms in Equation (2.29) of the kinetic energy and the nuclear electron repulsion, it contains the Hartree-Fock potential $\hat{\nu}_{\text{HF}}(i)$. This can be seen as a one-particle operator, substituting the many-body electron-electron repulsion term $\hat{V}_{\text{ee}}$. It describes an average potential experienced by an electron in the averaged field of all other electrons. Within the framework of the Hartree-Fock equations, only

one electron is considered in the averaged field of the others. However, since their properties determine the structure of the Fock operator, the equations can only be solved iteratively. In this self-consistent field (SCF) procedure, starting from an initial estimated set of orbitals, a new set of orbitals is constructed by solving the Hartree-Fock equation, which forms the starting point for a new iteration. This procedure is continued until convergence.

In standard electronic structure methods, the one-electron molecular orbitals χ_k are approximated by a linear combination of atomic orbitals ϕ_ν. Within this linear combination of atomic orbitals (LCAO) ansatz L molecular orbitals are written as

$$\chi_i = \sum_{\nu=1}^{L} c_{\nu i} \phi_\nu \qquad (2.30)$$

where the atomic orbitals are weighted with expansion coefficients $c_{\nu i}$. With this ansatz, the Hartree-Fock equations result in

$$\hat{f}(i) \sum_{\nu=1}^{L} c_{\nu i} \chi_\nu = \epsilon_i \sum_{\nu=1}^{L} c_{\nu i} \chi_\nu \qquad (2.31)$$

and therefore, not the orbitals but rather the expansion coefficients are varied. The molecular orbital coefficients C are obtained by solving the Roothaan-Hall equations

$$FC = SC\epsilon, \qquad (2.32)$$

which can be written in the form of a generalized eigenvalue problem. F is the Fock-Matrix with its matrix elements $F_{\mu\nu} = \left\langle \chi_\nu | \hat{f} | \chi_\mu \right\rangle$ and S the overlap matrix of two basis functions χ_ν and χ_μ with matrix elements $S_{\mu\nu} = \langle \chi_\nu | \chi_\mu \rangle$. ϵ is a diagonal matrix of orbital energies, and C is the matrix of coefficients.

A minimal basis set typically uses a single basis function for each atomic orbital. An increasing number of basis functions per atomic orbital is always accompanied by an increased computational effort. A significant improvement can be achieved by describing the valence orbitals, which mainly define chemical reactivity, with two or more basis functions (split-valence). Additionally, polarisation functions with a higher angular momentum can be included, which better describe anisotropy and, thus, polarities. Without a great loss of accuracy, more easily integrable Gaussian

functions are usually used instead of Slater functions, which leads to a drastic saving in computing time. The latter are closer to the real solution, however, difficulties arise for these functions in the evaluation of multicenter integrals. It is emphasized that basis sets are always finite, and the exact Hartree-Fock energy can only be found for a hypothetical complete set of basis functions.

However, the Hartree-Fock method is an inadequate description of multi-electron systems since the electron-electron interaction is only described by an averaged potential. The missing contribution of the correlation leads to the fact that, according to the variational principle, the Hartree-Fock energy is always slightly higher than the exact energy. The missing energy contribution is termed correlation energy. Post-Hartree-Fock methods like configuration interaction (CI) and coupled cluster (CC) methods that take electron correlation into account were developed. However, they were not used within the work for this thesis and are, therefore, not discussed any further.

2.3.2 Density Functional Theory

DFT has become indispensable for computational homogeneous catalysis. It gives a good compromise between cost and accuracy for big system sizes as correlation is included via parametrized exchange-correlation terms. The fundamental difference of DFT to other quantum chemical methods is the description of electrons in terms of the electron density ρ instead of the wave function Ψ. An advantage is the drastic reduction of the dimensions to be treated. Compared to the wave function with $3N$ spatial (and N spin) coordinates, the electron density only depends on three spatial coordinates. A good introduction for chemists to this method is given by reference 13, which has been used for the following section.

Already in 1927 (at about the same time as the Schrödinger equation and the Hartree approximation), the first attempts by Thomas and Fermi led to a quantum mechanical expression of the kinetic energy of a homogeneous electron gas using the electron density. However, a model of a homogeneous electron gas does not achieve good results for systems with chemical bonds, in which electron density is concentrated between two atoms according to bonding theories. This is why DFT did not receive much attention in quantum chemistry until the first Hohenberg-Kohn theorem was published in 1964. In their contradiction argumentation, Hohenberg and Kohn proved that two different electron densities can never be found for one ground state energy.[65] As a result, a unique

functional maps the electron density bijectively to the ground state energy. In the second theorem, Hohenberg and Kohn also proved that the variation principle applies to the ground state energy with the electron density ρ_0. Therefore, the ground state energy of a quantum mechanical problem can be completely formulated as a function of electron density, and known tools from the Hartree-Fock theory can be applied. The electronic energy E_{DFT} of the ground state is given as

$$E_{\mathrm{DFT}} = E_{\mathrm{DFT}}[\rho] = T_{\mathrm{e}}[\rho] + V_{\mathrm{Ne}}[\rho] + V_{\mathrm{ee}}[\rho] = T_{\mathrm{e}}[\rho] + V_{\mathrm{Ne}}[\rho] + J[\rho] + E_{\mathrm{ncl}}[\rho], \quad (2.33)$$

where the electron-electron interaction is split into a classically known Coulomb part $J[\rho]$ and an unknown non-classical term $E_{\mathrm{ncl}}[\rho]$. The latter contains all quantum mechanical effects, such as self-interaction, exchange, and correlation. However, no sufficiently accurate description could be found for a long time, especially for the kinetic energy of an inhomogeneous electron density. An ansatz by Kohn and Sham introduces a fictitious non-interacting reference system with the same electron density as the real system.[66] By reintroducing a wave function description, the kinetic energy of the non-interacting system can be computed using a single Slater determinant. The remaining contribution to the real kinetic energy caused by correlation is very small. It is merged with the also small but unknown non-classical contributions of V_{ee} into an unknown functional that has to be approximated. Consequently, the wave function and orbitals are restored, and a pure characterization via the electron density is not given anymore. To escape the description of a non-interacting reference system, the external potential V_{S} is chosen such that the same density ρ results for the hypothetical non-interacting (index S) and the real system.

Finally, the total energy in Kohn-Sham DFT E_{KS} is of the form

$$E_{\mathrm{KS}}[\rho] = T_{\mathrm{S}}[\Psi] + J[\rho] + V_{\mathrm{Ne}}[\rho] + V_{\mathrm{XC}}[\rho]. \quad (2.34)$$

All unknown terms are bundled in *one* unknown functional. This exchange-correlation functional

$$V_{\mathrm{XC}}[\rho] = (T[\rho] - T_{\mathrm{S}}[\rho]) + (V_{\mathrm{ee}}[\rho] - J[\rho]) \quad (2.35)$$

contains the correlation energy of the kinetic energy (difference between real and non-interacting system) and the exchange and correlation energy (difference between general electron-electron interaction and Coulomb fraction).

By applying the variational principle to the total energy E_{KS}, the so-called Kohn-Sham equations with the Kohn-Sham orbitals φ_i are found, analogous to the Hartree-Fock

equations (see equation 2.28):

$$\hat{f}_i^{KS} \varphi_i = \epsilon_i \varphi_i \tag{2.36}$$

with the Kohn-Sham operator

$$\hat{f}^{KS} = -\frac{1}{2}\nabla^2 + \hat{V}_S \tag{2.37}$$

and the effective potential

$$\hat{V}_S(\mathbf{r}_i) = \int \frac{\rho(\mathbf{r}_j)}{\mathbf{r}_{ij}}d\mathbf{r}_j + \hat{V}_{XC}(\mathbf{r}_i) - \sum_{A=1}^{M} \frac{Z_A}{\mathbf{r}_{iA}}. \tag{2.38}$$

By resorting partially to wave function-based descriptions, the difference to the Hartree-Fock method lies only in a deviating expression of the effective potential.

A first approach to describe the unknown exchange-correlation functional is given by the local density approximation (LDA) and is based on the assumption of a homogeneous electron gas. However, an LDA functional fails for molecular systems in which the electron density is concentrated between atoms to form bonds. An improvement is given by the generalised gradient approximation (GGA) as its gradient is considered in addition to the electron density at a given point. *meta*-GGA functionals (mGGA) additionally use even higher derivatives of the electron density. Another ansatz is based on the fact that it has been shown that Hartree-Fock methods can describe exchange energies very well but neglect correlation effects. Density functional theory, on the other hand, captures large parts of correlation effects but includes only small contributions of exchange interaction. This opposing trend can be exploited by expressing functionals as a linear combination of both methods and thus using the strengths of both methods.

The challenge is to find an expression for the unknown exchange-correlation functional. With an exact description of it and a complete basis set, an exact solution of the quantum mechanical system would be possible. A weakness of DFT is that, in contrast to post-Hartree-Fock methods, a systematic derivation and improvement of this functional is up to this date hardly possible. Instead, it must be approximated via various models and semi-empirical parameterizations. In turn, the computational results must always be compared to experimental results, and caution is required when choosing the appropriate functional.

In addition, attractive long-range interactions between electrons of different molecules,

so-called dispersion interactions, are not considered. Since the exchange-correlation functional only involves the density or its gradient at the specific site, only short-range correlations between electrons can be well described. Consequently, the method fails, especially for systems with intermolecular hydrogen bonds. It has proven useful to add an empirical correction to common Kohn-Sham functionals to obtain more accurate results for these cases. Grimme decisively influenced this development, and the so-called Grimme dispersion models provide an inexpensive and stable improvement to standard functionals.[67]

2.3.3 From the Wave Function to Chemical Interpretation

The wave function, constructed from molecular orbitals, plays a key role in quantum chemistry. However, canonical orbitals emerging from standard quantum chemistry methods like Kohn-Sham DFT are typically delocalized over the entire molecule. This makes chemical interpretation and relation to qualitative concepts like bonding theories, Lewis structures, oxidation states, and partial charges difficult.

As the energy and properties of a Slater determinant are invariant to unitary rotations, an appropriate unitary transformation, given by a linear combination of delocalized canonical orbitals, can be applied to gain localized molecular orbitals.[68,69] They are localized in a spatial region within the molecule, related to the common concept of bonds or lone pairs. However, there are numerous ways to perform such a unitary transformation, depending on some localization criterion being set.

One widely used set of localized orbitals is natural bond orbitals (NBO).[70,71] Herein, the localization criterion is set so that the localized 1-centre and 2-centre regions of the molecule are maximally occupied. According to the Pauli exclusion principle, the maximum occupancy of an orbital is given by a pair of electrons. Optimizing the occupancy to a value of 2.00 for each orbital closely relates NBOs to a typical Lewis structure picture. The generation of NBOs results in occupied bonding and unoccupied antibonding orbitals. Small occupancies of the latter lead to deviations from the ideal Lewis structure. Donations from Lewis-type occupied orbitals to non-Lewis-type non-occupied acceptor orbitals describe non-covalent corrections to the perfectly localized picture.[72] Non-covalent interactions between, e.g., ligands and a metal center, are very important in homogeneous catalysis and can define the performance of a catalyst. The energy stabilization resulting from such donor-acceptor interactions can be calculated using NBO analysis. To do so, semi-local natural localized molecular orbitals (NLMO)

Ω_i are constructed.[71] They are linear combinations of a major contribution from the parent Lewis-type NBO σ_i and weak contributions from non-Lewis (NL) NBOs σ_j^*:[73]

$$\Omega_i = c_{ii}\sigma_i + \sum_j^{\text{NL}} c_{ji}\sigma_j^* \tag{2.39}$$

The non-covalent contributions to the total energy are typically less than 1% of the covalent contributions. Therefore, deviations from the Lewis structure can be approximated by second-order perturbation theory.[72] However, generally NBO analysis suffers from the drawback of relying on the concept and existence of a Lewis-like bonding pattern for any given molecule.

A more unbiased method suitable for unusual bonding situations is given by intrinsic bond orbitals (IBO).[74] The construction of these orbitals does not rely on the molecule's Lewis structure and is free of empirical input or predefined ideas from bonding theory. Interestingly, bonds and lone pairs, as qualitatively defined within Lewis's theory, emerge naturally from the molecular electronic structure itself.[74] The unbiased approach was used in the literature, for example, to study the stabilizing effects of gold-carbene complexes, revealing the quantitative contributions of σ and π donations of the Au-C bond.[75] Within the present thesis, this analysis has been conducted due to an unusual emerging interaction between chloride and boron.[10,11]

To construct IBOs, an accurate SCF wave function is computed. Then, atomic orbitals are constructed using tabulated free-atom atomic orbitals of standard basis sets. Considering the molecular environment leads to polarized atomic orbitals and orthogonalization to intrinsic atomic orbitals (IAO). They are built such that the sum of all IAOs exactly spans over the molecular orbitals of the accurate SCF wave function. As one IAO can be assigned to one atom, they can be used to calculate atomic properties like partial charges.

To go beyond atomic properties and extract information about molecular bonds, the IAOs are used together with the Pipek-Mezey localization method.[76] This is simply a linear combination of IAOs with the condition of minimizing the number of atoms among which an orbital is centered. This construction allowed the single IBOs to be decomposed into each atom's contributions, which is a useful tool when quantitatively evaluating bonds.

3 Results

3.1 Paper I

A non expected alternative Ni(0) Species in the Ni-Catalytic Aldehyde and Alcohol Arylation Reactions Facilitated by a 1,5-Diaza-3,7-diphosphacyclooctane Ligand

J. Heitkämper, S. Posada-Pérez, S. Escayola, M. Solà, J. Kästner, and A. Poater
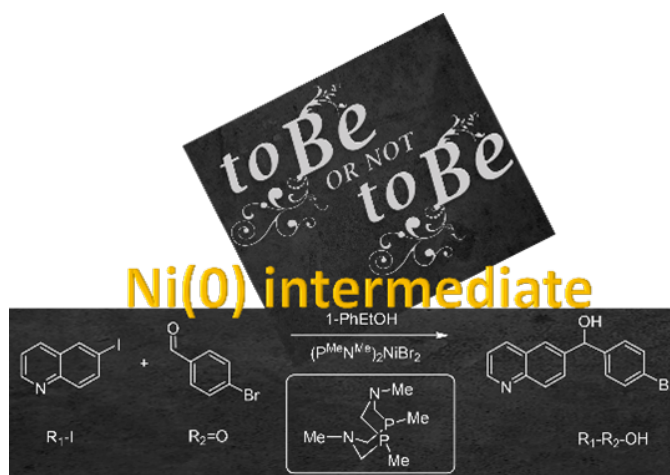
Own contributions:

- all quantum chemical calculations regarding the reaction mechanism (major part), excluding the calculation of oxidation states (minor part)
- preparation of the manuscript together with A. Poater and S. Posada-Pérez

A Non Expected Alternative Ni(0) Species in the Ni-Catalytic Aldehyde and Alcohol Arylation Reactions Facilitated by a 1,5-Diaza-3,7-diphosphacyclooctane Ligand

Juliane Heitkämper,[a, b] Sergio Posada-Pérez,*[b] Sílvia Escayola,[b, c] Miquel Solà,[b] Johannes Kästner,[a] and Albert Poater*[b]

Abstract: For decades there were many attempts to dispense with stoichiometric amounts of metal reagents for the synthesis of secondary alcohols. In 2021, the synthetic results of Newman and collaborators pioneered a synthesis still with metals, but not as reactants. Instead, they serverd as catalytic engines. Here we present a description by means of Density Functional Theory calculations of how this process can occur, and an attempt is made to shed light on the mechanism that facilitates the attainment of secondary alcohols, emphasizing the eternal cross-coupling debate of whether the catalytically active species is Ni(0) or they are really taking shortcuts following the course of Ni(II). Effective Orbital analyses give a clear picture. Furthermore, this paper provides insight not only into the nature of the ligands of the metal catalyst but also the role of the base.

Introduction

The apparent simplicity of the OH functional group that defines the alcohols, and specially its natural origin for the primary alcohols,[1–4] hides somewhat the complexity of the synthesis of secondary and tertiary alcohols. Their importance in drug synthesis[5–8] motivates continued efforts towards improving their synthesis. Among the spectrum of possibilities, the reaction of aldehydes to secondary alcohols with organo-metallic reagents is of vital importance not only academically, but industrially. On the other hand, the formation of C–C bonds, using organomagnesium reagents, or also Grignard reagents, is achieved but only in a stoichiometric way and with a fairly limited variety of functional groups,[9–12] apart from the necessity of low temperatures that are required because of the exothermic nature of the reaction. In order to overcome the limitations of Grignard reagents, an alternative is to replace the organohalides and magnesium metal agents by catalysts. In detail, the Nozaki–Hiyama–Kishi reaction allows the reductive coupling of organohalides and aldehydes by chromium,[13–15] in combination with a nickel catalyst.[16,17] Mechanistically, nickel allows the activation of the carbon-halogen bond and then transmetalates it with chromium, thus generating in situ the nucleophilic species of organochrome. However, the solution is far from definitive since chromium does not act catalytically, although it has been possible to reduce its use.[18–22] Since then, a series of studies made it possible to make a clear evolution to remove chromium. Without these works, our current under-standing of this reaction would not be possible. Cheng and Majumdar first discovered that the Ni/dppe pair could catalyze the reaction, although they needed a stoichiometric amount of Zn,[23] which was required as well by Weix and coworkers, showing that catalysts with N-based ligands such as bipyridine or PyBox, combined with nickel as metal, led to complex secondary alcohols[24] using aryl bromides and aldehydes as reagents. Krische contemporaneously achieved the reduction with sodium formate, therefore in a milder form the combina-tion of reductive coupling and transfer hydrogenation,[25] using a rhodium(I) catalyst and double the amount of aryl iodide to make feasible the arylation of both alkyl like aryl substituted aldehydes, but at high temperature. Continuing with the aim of the synthesis of secondary alcohols, the α-arylation of the primary homologues is in the process of expansion. MacMillan and coworkers, combining nickel and iridium, photochemically achieved this with aliphatic alcohol and aryl bromides.[26] However, the reaction required stoichiometric amounts of Zn.[27–29] This bottleneck, together with the fact that an excess of alcohol was needed, generates undesired ketones as by-products. At that time, nothing had been studied in the

[a] J. Heitkämper, Prof. Dr. J. Kästner
Universität Stuttgart
Institut für Theoretische Chemie
Pfaffenwaldring 55, 70569 Stuttgart (Germany)

[b] J. Heitkämper, Dr. S. Posada-Pérez, S. Escayola, Prof. Dr. M. Solà, Dr. A. Poater
Institut de Química Computacional i Catàlisi and
Departament de Química, Universitat de Girona,
Maria Aurèlia Capmany 69, 17003 Girona, Catalonia (Spain)
E-mail: sergio.posada@udg.edu
        albert.poater@udg.edu
Homepage: http://iqcc.udg.edu/wordpress/portfolio/albert-poater/

[c] S. Escayola
Donostia International Physics Center (DIPC)
Donostia, Euskadi (Spain)

Chemistry–A European Journal

Research Article
doi.org/10.1002/chem.202300193

Chemistry Europe
European Chemical
Societies Publishing

absence of electron-rich heterocycles or benzyl alcohols paving the way to new challenges.

Zhang, Xu, Findlater and collaborators reported an electrochemical arylation capable of interacting with aldehydes and alcohols, but in a very limited way.[30] And more recently, the attempts of Newman and co-workers have followed the same path, with the aim of avoiding the stoichiometric use of any metallic element in the reactions, placing a clear emphasis on the use of Ni(0) as a catalytically active species. Thus, cross-coupling reactions with aldehydes and alcohols as reagents could lead to the synthesis of ketones from aryl triflates with the catalytic framework Ni(0)/triphos.[31] It was proposed that the process took place thanks to the Heck reaction,[32] with β-hydride elimination of an intermediate with the nickel alkoxide ligand that would subsequently give the ketone. Then the goal became more ambitious, and although failed, it happened to reconvert this Ni-alkoxide intermediate to obtain alcohols, in line with other studies that lead to O-arylation,[33] or simply unwanted secondary reactions.[34–36] Another synthetic effort by Newman's group made it possible to overcome these obstacles in reductive arylation and alcohol α-arylation to reach secondary alcohols from the coupling of organohalides without the need for any stoichiometric amount of metal compound. A nickel catalyst with the 1,5-diaza-3,7-diphosphacyclooctane ligand (P_2N_2) was used as a solution,[37,38] which allows not only the cross-coupling of aryl iodides with primary alcohols or aldehydes to obtain secondary benzyl alcohols,[39] but also in an efficient way, to avoid the secondary reactions of Grignard reagents. It was proposed that the mechanism of the reaction under investigation proceeds via a Ni(0) species, despite its relatively expected high instability,[40] extendable especially to palladium, too.[40,41] In the present work, the aldehyde arylation reaction catalyzed by Ni catalyst armed with the P_2N_2 ligand, shown in Figure 1, is studied in terms of Density Functional Theory (DFT) calculations, aiming to reveal the underlying reaction mechanism and conditions that influence it at the molecular level.

Results and Discussion

To reduce the computational cost, we simplified the catalyst by considering methyl groups instead of aryl or cyclohexyl groups on the nitrogen or phosphorus atoms, respectively. However, experiments reported the large influence in the reaction yield of the substituents on the ligand.[39] To systematically investigate this effect, we identified the TOF determining intermediate (TDI) and TOF determining transition state (TDTS) and the
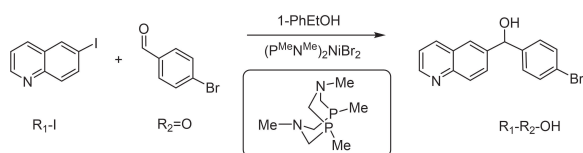
energetic span, according to the energetic span model,[42] using the simplified model system. Then, this energetic span has been recomputed with different substituents on the ligand to explore their influence, by means of the comparison of the energy barrier.

After a careful search of isomers, the most stable conformer of the simplified catalyst is shown in Figure 2a. The simplification by methyl groups becomes a way to reduce the complexity of further isomers with the larger ligands and thus, determine precisely the whole reaction pathway finally locating the right TDI and TDTS. Herein, a hydrogen atom of the methyl group coordinates with the metal center to form an agostic interaction. Apparently, coordination with the nickel center out of the square planar coordination plane has a stabilizing effect. Moreover, when substituting methyl with a bulkier phenyl group, the latter conformation is preferred since the phenyl ring interacts with the metal center. This stabilizing effect was found previously,[43] and is particularly highlighted as it has an influence on the stability of intermediates and transition states, as it will be discussed later. The interaction between the metal and the nearest methyl group is clearly illustrated in Figure 2a, with an activation of the C—H bond up to 1.125 Å, compared to the others of 1.109 Å.

Figure 3 provides an overview of the studied reaction pathways with the corresponding labeling, while Figure 4 shows the analogous energy diagram for the simplified system as well as the structures of the transition states. The reaction mechanism starts with the catalytic active species in the catalytic cycle, **I**, which is generated through an endothermic process from **0**, in which **I** (with $X_1 = Br$) is 10.2 kcal mol^{-1} higher in energy than **0**. To form **I**, the TMP (2,2,6,6-tetramethylpiperidine) and HBr (or HI) are essential. Both acids are very strong and favor the release of protons. The TMP acts as a base, resulting in a very stable TMP···HBr complex shown in Figure 2b. The bond distance of the accepted proton to the nitrogen is of 1.158 Å, very similar to that of the other proton with a bond distance of 1.034 Å. Moreover, the H—Br bond is lengthened to 1.885 Å compared to 1.438 Å in a single HBr molecule. To screen the role of TMP as a base, a discussion of the use of different bases other than TMP is presented later.
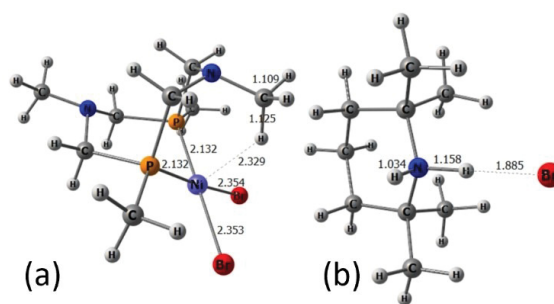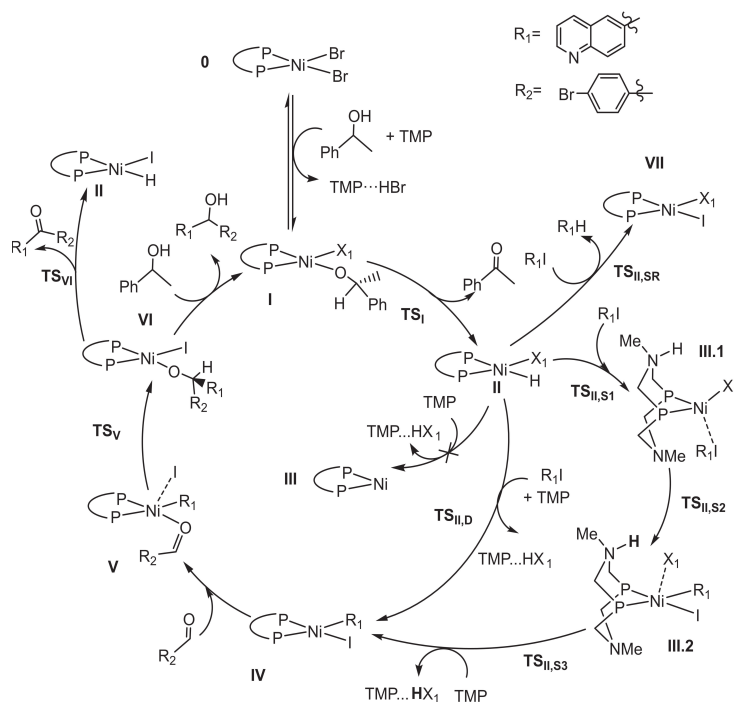

Figure 1. Reaction under investigation in the current study.

Figure 2. (a) The most stable conformer of the simplified catalyst **0** and (b) the formed complex TMP···HBr (selected distances in Å).

Chemistry–A European Journal

Research Article
doi.org/10.1002/chem.202300193

Chemistry
Europe
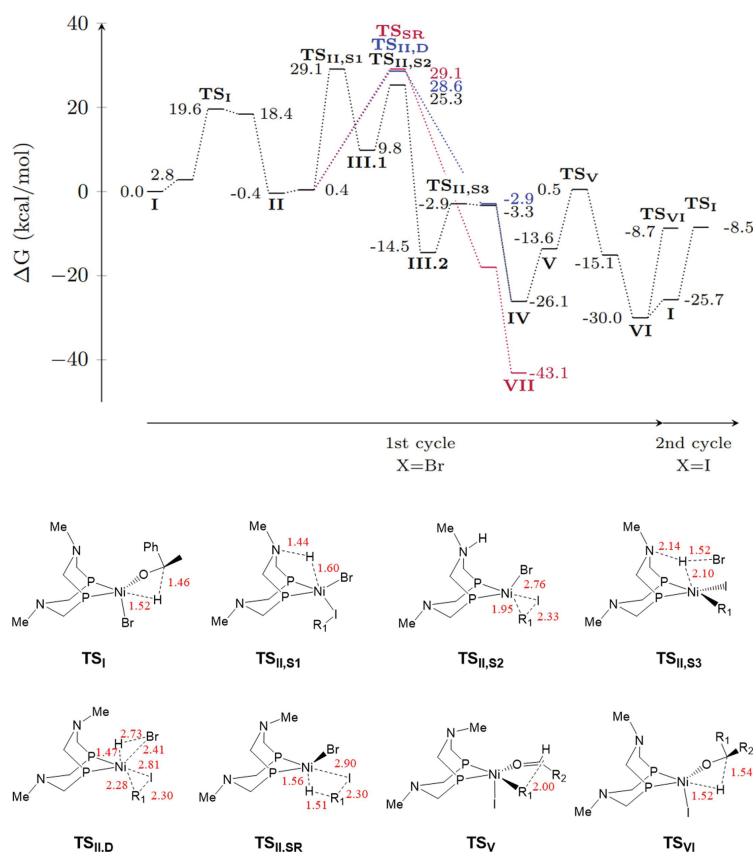European Chemical
Societies Publishing

Figure 3. Reaction mechanism of the aldehyde arylation reaction catalyzed by a nickel center with a 1,5-diaza-3,7-diphosphacyclooctane ligand. $X_1 =$ Br for the first catalytic cycle, but it can be Br or I for the following cycles.

From **I**, a nickel hydride (**II**) is formed via a β-elimination of the alcohol, resulting in the formation of a ketone. To overcome the transition state, **TS$_I$**, 19.6 kcal mol^{-1} are required. In past studies, it was proposed that subsequently the nickel hydride undergoes reductive elimination to form a Ni(0) species **III**.[39] However, it is located thermodynamically 33.1 kcal mol^{-1} above **I** (still disregarding transition states to get there). Thus, it is found to be too high in energy to be formed even at 75 °C. In addition, a possible lower triplet state was ruled out since the triplet spin state is found 19.1 kcal mol^{-1} higher in energy than the singlet ground state. Later we discuss different possibilities for stabilizing intermediate **III**, but first, the path to go directly from **II** to **IV** ruling out the need of a Ni(0) intermediate in between is discussed.

On the one hand, there is a direct reaction pathway in which the Ar–I bond cleaves and both halves coordinate with the nickel center. Simultaneously the H and Br ligands join to form HBr. This step is concerted and possesses a transition state **TS$_{II,D}$** with a relative Gibbs energy of 28.6 kcal mol^{-1}, thus the associated energy barrier is 29.0 kcal mol^{-1} with respect to **II**. On the other hand, an alternative pathway was observed, in which the ligand is actively involved. From the hydride species **II**, **TS$_{II,S1}$** involves the H transfer to the nitrogen atom of the ligand to form **III.1** complex overcoming an energy barrier of 29.5 kcal mol^{-1}. This hydrogen transfer to the ligand was observed in a catalytic hydrogen oxidation mechanism using the same type of ligand.[44] This reaction step is sensitive

depending on the electronic environment of the nitrogen and thus on the substituents at it (see below). This hydrogen transfer step was observed when a R_1-I reactant already coordinates to the Ni center to form a tetrahedrally coordinated complex involving the iodide. Without the R_1-I coordination, structure **III.1** would be 7.6 kcal mol^{-1} higher in energy, so clearly the iodide is coordinated to the nickel center to form a tetrahedrally coordinated nickel complex, which is confirmed by a Mayer Bond Order (MBO)[45] of 0.65 between the iodide and nickel, in accordance with previous results greater than 0.5.[46] In a subsequent step, an oxidative addition process, the R_1-I bond splits to coordinate with the nickel center to form **III.2**, via the transition state **TS$_{II,S2}$** with an energy barrier of 15.5 kcal mol^{-1}. In a final step, the hydrogen is transferred to the bromide ion to release HBr and form **IV** in a fast reaction via **TS$_{II,S3}$** with an energy barrier of 11.6 kcal mol^{-1}.

Apart from the proposed catalytic cycle in Figure 3, alternative steps/pathways were also considered. For instance, from structure **II**, an undesired side reaction of the reactant R_1-I to form the de-halogenated compound R_1-H and **VII** via **TS$_{II,SR}$** was also explored. This side reaction implies an energy barrier of 29.5 kcal mol^{-1} and therefore, it is a competitive pathway. The ratio of rate constants of this side reaction and the main reaction, which is sensitive depending on the substituents on the nitrogen atom, determines the yield of the desired product or the extent of the formation of undesired by-products.

Chemistry–A European Journal

Research Article
doi.org/10.1002/chem.202300193

**Chemistry
Europe**
European Chemical
Societies Publishing

Figure 4. Energy diagram of the investigated reaction mechanism (above) and structures of the transition states (below). Relative Gibbs energies of the stationary points with respect to **I + Reactants**, in kcal mol^{-1}; and selected distances in red are given in Å.

The predicted C–C bond formation between the aldehyde and the R$_1$ group occurs after the aldehyde coordinates to **IV** to form **V**. The energy barrier to obtain the product coordinated to the catalyst (**TS$_V$**) is overall 26.6 kcal mol^{-1}. This step is greatly stabilized by coordinating agents below and above the square plane of the active center. It increases by 4.4 kcal mol^{-1} if the methyl group is not coordinated by a Ni···H interaction,[47] and further decreases by 6.8 kcal mol^{-1} if an ArCF$_3$ ligand is on the nitrogen atom of the ligand instead of a methyl group.

The mechanism is finally completed by the exchange of the product by a 1-PhEtOH molecule to initiate a new catalytic cycle in an endothermic step. However, the whole catalytic pathway is exergonic, since completing the catalytic cycle, the system ends up at **I** again releasing 25.7 kcal mol^{-1}.

According to the energetic span model,[42] intermediate **VI** and **TS$_{II}$** describe the TDI and TDTS of the catalytic cycle and create an energetic span of 32.2 kcal mol^{-1} (see Figure 5a). Even though this energy barrier is remarkable, even at 75 °C, there is the key factor that, after the first catalytic cycle, one iodide is coordinated to the nickel center instead of Br. Therefore, X$_1$ could be iodide instead of bromide in Figure 3, from the second catalytic pathway. Figure 5b shows that this fact has a particular
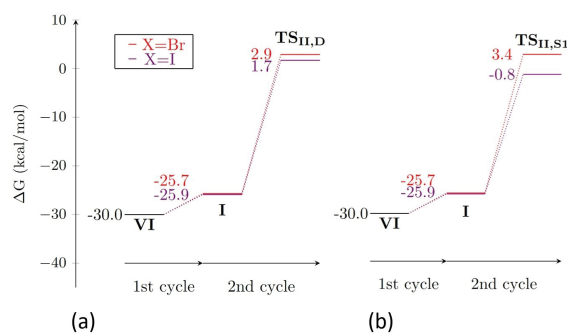
Figure 5. Energetic span for the simplified catalyst with X=Br, I (relative Gibbs energies in kcal mol^{-1} with respect to **I + Reactants**) for (a) the transition state **TS$_{II,D}$** and (b) **TS$_{II,S1}$**.

influence on **TS$_{II,SR}$**, decreasing the energetic span to 28.5 kcal mol^{-1}. Thus, iodide is likely to be part of the active catalyst rather than bromide.

As indicated in Figure 3, from the energy well of the reaction, i.e. intermediate **VI**, it is also conceivable that the

Chemistry–A European Journal

Research Article
doi.org/10.1002/chem.202300193

Chemistry Europe
European Chemical
Societies Publishing

coordinated product alcohol undergoes a β-elimination via **TS$_{VI}$**, which is energetically competitive with a β-elimination of 1-PhEtOH (see Figure 4) via **TS$_I$**. However, a β-elimination of the product is not observed experimentally. A possible explanation is that 1-PhEtOH is present at high concentrations, favoring the reaction rate of the formation of **II**.

Since intermediate **VI** and the following **TS$_{II}$** turned out to dominate the energetic span, these species were recomputed with different ligands to understand the performance of different catalysts. Experimentally it was found that, for example, the use of an P^{Cy}N^{ArCF3} catalyst forms the desired product, while P^{Cy}N^{ArOMe} yields mainly the quinoline side product (**VII**). Therefore, the methyl group interacting with the nickel center was substituted by ArOMe and ArCF$_3$ and the energetic span recomputed. As can be seen in Figure 6, the performance of the catalyst seems to depend on a sensitive interplay between the energy barriers for the side reaction and the desired transition state **TS$_{II}$**. In case of ArOMe (Figure 6b) the side reaction has the same energy barrier as the main reaction, yielding a formation of the side product **VII** in large amount, lowering the yield of the desired product. In case of the ArCF$_3$ the side reaction is slightly higher in energy than the transition state for the main product formation (0.5 kcal mol^{-1}). As known from enantioselective reactions, just 1–2 kcal mol^{-1} are already enough to fully favor one enantiomer over the other and therefore, it is possible that this small energy difference decides over the formation of the main or side product.
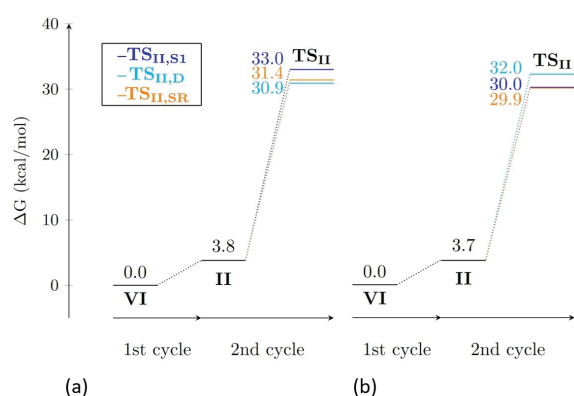
As already discussed, the Ni(0) species **III** is very high in energy. However, there are a few possibilities to stabilize this complex. On the one hand, the coordination of a benzene ring to the metal center is found in the literature to have a stabilizing effect.[48] As can be seen in Figure 7, coordination of a toluene molecule indeed stabilizes intermediate **III** by 23.1 kcal mol^{-1}. Note that in this comparison we added phenyl rings to the nitrogen as they might influence this effect a lot and also not species **I**, but species **0**, was taken as a reference. Coordination of a second ligand in place of toluene further stabilizes **III** (see Figure 7). However, this complex is apparently catalytically inactive since there is no space around the nickel center to coordinate reactants to undergo the catalytic reaction. Separating the second ligand to form **III** in order to make space for catalysis would end in a too high energy barrier to be overcome. A discussion on the Ni(0) species **III.1** is provided later.

Experimentally it was found that the choice of the base has a great influence on the reaction. The use of TMP as a base was critical and with other common bases or additives like pyridine, triethylamine (NEt$_3$) or K$_3$PO$_4$ no reaction was observed.[39] As shown in Figure 8, DFT calculations show that pyridine or phosphoric acid coordinate stronger to the nickel centre than PhEtOH, therefore inhibiting the reaction by preventing the formation of **I**. For complexes with sterically hindered bases like NEt$_3$ or TMP (with similar pk$_a$ values of 10.8 and 11.1 respectively) no analogous square planar coordination was found. As shown in Figure 9, for the example of TMP, the bromide and TMP coordinate above and below the plane, resulting in a less stable species than **I**. Therefore, they do not inhibit the reaction. However, this argument does not explain why TMP outperforms NEt$_3$. It is possible that NEt$_3$, as the bulkiest base, is sterically very demanding, hindering the trimolecular reaction from **0** to **I** in which the catalyst, alcohol and base needs to be in close proximity. Unfortunately, it is barely possible to study such processes from a computational point of view. Nevertheless, DFT calculations allow to lead to

Figure 6. Energetic span using (a) the P^{Cy}N^{ArCF3} catalyst and (b) the P^{Cy}N^{ArOMe} catalyst for X=I (relative Gibbs energies in kcal mol^{-1} with respect to **VI**).
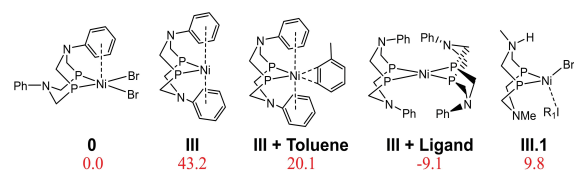
Figure 7. Stabilization of intermediate **III** by toluene, a second ligand or intramolecular deprotonation of the Ni-hydride to make anionic Ni(0)-Br and a protonated amine (relative energy values in kcal mol^{-1}).
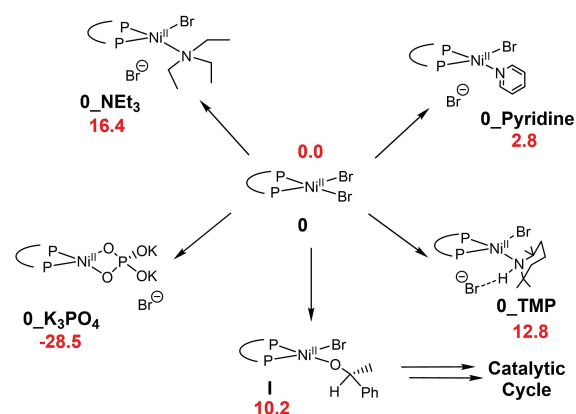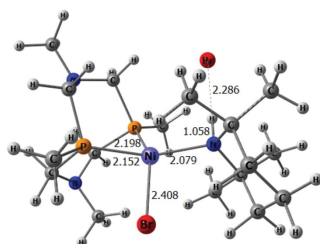
Figure 8. Relative Gibbs energies for the coordination of different bases to the metal centre with respect to **0**, in kcal mol^{-1}.

Chemistry–A European Journal

Research Article
doi.org/10.1002/chem.202300193

Chemistry
Europe

European Chemical
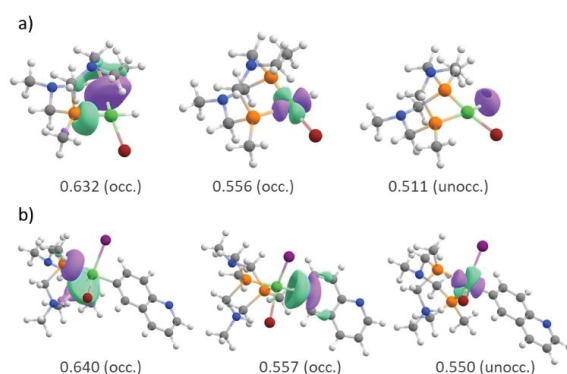Societies Publishing

Figure 9. Coordination of TMP to the catalyst (selected distances indicated in Å).

this conclusion and a potential precipitation of a salt when adding TMP in the crude is a plausible explanation.

To further explore the nature of the reaction intermediates, a summary of the effective oxidation state (EOS) results for intermediate **II**, **III.1**, **III.2**, and **III** is shown in Table 1 (see

Table 1. Occupation number of last occupied and first unoccupied EFOs and Effective Oxidation State (EOS) of each fragment within the system and global reliability index R (%) for intermediates **II**, **III.1**, **III.2** and **III**.

	Fragment	Last occ. EFO	First unocc. EFO	Ox. State	R [%]
II	M (Ni)	**0.556**	0.194	0	54.5
	X_1 (Br)	0.724	0.017	−1	
	H	0.000	**0.511**	+1	
	P-Ligand	0.632	0.104	0	
III	M (Ni)	0.814	**0.233**	0	91.1
	P-Ligand	**0.644**	0.146	0	
III.1	M (Ni)	0.673	0.175	0	54.6
	X (I)	0.881	**0.458**	+1	
	X (Br)	0.795	0.012	−1	
	R_1	**0.504**	0.282	−1	
	P-Ligand-H	0.740	0.146	+1	
III.2	M (Ni)	0.844	**0.550**	+2	52.7
	X (I)	0.687	0.015	−1	
	X (Br)	0.802	0.013	−1	
	R_1	**0.577**	0.053	−1	
	P-Ligand-H	0.640	0.152	+1	

a)

0.632 (occ.)   0.556 (occ.)   0.511 (unocc.)

b)

0.640 (occ.)   0.557 (occ.)   0.550 (unocc.)

Figure 10. EFOs with occupation numbers between 0.450 and 0.650 in intermediate a) **II** and b) **III.2**. The orbitals are visualized with an isocontour of 0.05 (with the exception of H orbital, where an isocontour of 0.1 was used).

Table S1 in the Supporting Information for detailed information on other intermediates),[49] to provide information about the oxidation state of Ni. From the EOS results, we can observe that intermediate **III** is a Ni(0) species (R > 90%), and the same oxidation state holds when changing the phosphine ligand, including coordination of an explicit solvent molecule or adding a second phosphine ligand unit. For the rest of the intermediates, the assignation of the oxidation state is less clear (R < 55%). In most of the cases (intermediates **0**, **I**, **III.2**, **IV**, **V**, and **VI**), the last electron pair to be assigned is located on an effective fragment orbital (EFO) of the phosphine ligand, which gets a global oxidation state of 0, leaving an oxidized Ni center with an OS of +2.[50,51] There are some exceptions, intermediates **II** and **III.1**, which have an OS of 0 on the Ni atom. In the case of intermediate **II**, the last occupied EFO is located on the Ni and the first unoccupied EFO is located on the H atom (see Figure 10), which gets an oxidation state of +1. Nevertheless, one has to note that in this case, the populations of the frontier EFOs are very close, 0.556 for the last occupied and 0.511 for the first unoccupied EFO, so the actual OS of the Ni may lay in between 0 and +2. Then, for intermediate **III.1**, the assignation of an OS of 0 to the Ni center is more clear (the last occupied EFO located on the Ni fragment has a significant occupation of 0.673) and the low value of R is only due to our fragment selection since the last-assigned electron pair, disputed between R_1 (OS of −1) and I (OS of 1), should be assigned to R_1 +I considered as a single fragment. Having revealed the OS of 0 for this species, we added it to the row of Ni(0) complexes in Figure 7.

Mechanistically, from the point of view of the oxidation state, we start the catalytic cycle with an Ni(II) species that gets partially reduced with the formation of **II**, and it could become clearly Ni(0) after the release of the ketone and the decoordination of the Br (formation of **III**). However, as stated above, this is not affordable thermodynamically. From intermediate **II** a second reaction can take place when R_1I is inserted on this intermediate leading to the formation of **III.1** which is also a Ni(0) species, in agreement with past work of Borys and Hevia,[52] Newman and coworkers,[39,53] and previously with palladium by Amatore and Jutand.[54] Then, the metal center is oxidized back to Ni(II) with the formation of **III.2**. Both reaction paths converge to intermediate **IV** that latter evolves to **V** and **VI**, these last three intermediates are all Ni(II) species. These bidirectional changes from Ni(II) to Ni(0), with Ni(I) in between, have also been exposed very recently with great potential for cross-coupling reactions by Doyle and coworkers,[55] but we have not characterized any Ni(I) species,[56] and it is ruled out from the current study.

Conclusion

We have reported DFT studies of a catalytic method to access secondary alcohols from aryl iodides. This reaction is catalyzed by a metal catalyst that combines nickel and a 1,5-diaza-3,7-diphosphacyclooctane ligand. Even though and in line with cross-coupling reactions, the presence of a Ni(0) intermediate is

Chemistry–A European Journal

Research Article
doi.org/10.1002/chem.202300193

Chemistry Europe
European Chemical
Societies Publishing

considered throughout the reaction mechanism, here it must be discarded apparently. Instead an alternative proposal is announced, with a catalytic pathway that alternatively changes the halide lowering the kinetic cost of the catalysis. Unexpectedly, this alternative mechanism also includes Ni(0) intermediates. The mechanistic study also describes that electron-donating groups on the aryl ligands bonded to the metal enhance the catalytic activity, as well as unveils the role of the base, indispensable for the reaction. Unfortunately, our computational study does not provide a complete understanding of the nature of the base. Thus, there are still mechanistic points at the root of the experiments that need to be further studied computationally,[39] for example to explain why, with pyridine as a base, the alcohol is not obtained but quinoline and residually the ketone product.

Computational Details

DFT calculations have been performed with the Gaussian16 program package.[57] Geometry optimizations and subsequent frequency calculations were performed with the BP86 functional, i.e. the gradient generalized approximation (GGA) functional of Becke and Perdew,[58] adding D3(BJ) dispersion corrections,[59] and using the def2-SVP basis set.[60] All minima were verified to possess only real frequencies and transition structures only a single mode with imaginary frequency. The Gibbs energies were calculated at 348.15 K and are presented according to a liquid phase reference state. At converged geometries, the electronic energies were calculated using the B3LYP functional, i.e. the hybrid GGA functional of Becke, Lee, Yang, and Parr,[61] and the def2-TZVP basis set. The solvent effects were accounted for with the Polarizable Continuum Model (PCM),[62] using toluene as a solvent. Numerical integration was carried out on an ultrafine grid. All calculations were performed for singlet spin states, verifying that the triplet state was not accessible in any case. Reported Gibbs energies are electronic energies obtained at the B3LYP–D3(BJ)/def2-TZVP(Toluene)//BP86-D3(BJ)/def2SVP level of theory with added ZPEs, thermal corrections and entropy contributions to the Gibbs energy obtained at the BP86/def2-SVP level. Conformational searches have been carried out with the crest tool,[63] to account for the conformational complexity of the system.

The characterization of the Ni oxidation state has been done by means of the EOS analysis with the APOST-3D program.[64] The EOS and partial atomic charges have been computed at the BP86-D3BJ/def2-SVP level of theory (same as geometry optimization) using the topological fuzzy Voronoi cells (TFVC) 3D-space partitioning and a 40 × 146 atomic grid for numerical integration. Together with the EOS results we have analyzed the corresponding EFOs and their occupations in the cases were low values or the reliability index (R < 55%) were found. The R (%) index is obtained from the relative occupation of the frontier EFOs, and measures how close is the OS assignation to the actual electron distribution.

Acknowledgements

Conflict of Interest

There are no conflicts of interest to declare.

Data Availability Statement

The data that support the findings of this study are available in the supplementary material of this article.

Keywords: DFT calculations · Ni(0) · nickel · reaction mechanism · secondary alcohol

[1] G. C. Chinchen, P. J. Denny, J. R. Jennings, M. S. Spencer, K. C. Waugh, *Appl. Catal.* **1988**, *36(C)*, 1–65.
[2] J. M. Marchetti, V. U. Miguel, A. F. Errazu, *Renewable Sustainable Energy Rev.* **2007**, *11*, 1300–1311.
[3] H. Valera, A. K. Agarwal, Methanol as an Alternative Fuel for Diesel Engines, Energy, Environment, and Sustainability. In Methanol and the Alternate Fuel Economy. A. K. Agarwal, A. Gautam, N. Sharma, A. P. Singh (eds). Springer, Singapore, **2019**, 9–33.
[4] C. Jin, M. Yao, H. Liu, C.-F. F. Lee, J. Ji, *Renewable Sustainable Energy Rev.* **2011**, *15*, 4080–4106.
[5] S. K. Sythana, P. R. Bhagat, *J. Indian Chem. Soc.* **2015**, *92*, 563–565.
[6] W. Song, K. Dong, M. Li, *Org. Lett.* **2020**, *22*, 371–375.
[7] B. Krasniqi, K. Geerts, W. Dehaen, *J. Org. Chem.* **2019**, *84*, 5027–5034.
[8] C.-M. Hong, F.-F. Zou, X. Zhuang, Z. Luo, Z.-Q. Liu, L.-Q. Ren, Q.-H. Li, T.-L. Liu, *Org. Chem. Front.* **2022**, *9*, 299–304.
[9] V. C. Grignard, C. R. Hebd, *Séances Acad. Sci.* **1900**, *130*, 1322–1324.
[10] A. Krasovskiy, P. A. Knochel, *Angew. Chem. Int. Ed.* **2004**, *43*, 3333–3336; *Angew. Chem.* **2004**, *116*, 3396–3399.
[11] D. Seyferth, *Organometallics* **2009**, *28*, 1598–1605.
[12] M. J. Pedersen, T. Skovby, M. J. Mealy, K. Dam-Johansen, S. Kiil, *Org. Process Res. Dev.* **2018**, *22*, 228–235.
[13] T. Takai, M. Tagashira, T. Kuroda, K. Oshima, K. Utimoto, H. Nozaki, *J. Am. Chem. Soc.* **1986**, *108*, 6048–6050.
[14] A. Fürstner, *Chem. Rev.* **1999**, *99*, 991–1046.
[15] K. Namba, Y. Kishi, *Org. Lett.* **2004**, *6*, 5031–5033.
[16] Y. Okude, S. Hirano, T. Hiyama, H. Nozaki, *J. Am. Chem. Soc.* **1977**, *99*, 3179–3181.
[17] H. Jin, J. Uenishi, W. J. Christ, Y. Kishi, *J. Am. Chem. Soc.* **1986**, *108*, 5644–5646.
[18] A. Fürstner, N. Shi, *J. Am. Chem. Soc.* **1996**, *118*, 12349–12357.
[19] M. Durandetti, J. Périchon, J.-Y. Nédélec, *Tetrahedron Lett.* **1999**, *40*, 9009–9013.
[20] W. Harnying, A. Kaiser, A. Klein, A. Berkessel, *Chem. Eur. J.* **2011**, *17*, 4765–4773.
[21] A. Gil, F. Albericio, M. Álvarez, *Chem. Rev.* **2017**, *117*, 8420–8446.
[22] Y. Gao, D. E. Hill, W. Hao, B. J. McNicholas, J. C. Vantourout, R. G. Hadt, S. E. Reisman, D. G. Blackmond, P. S. Baran, *J. Am. Chem. Soc.* **2021**, *143*, 9478–9488.
[23] K. K. Majumdar, C.-H. Cheng, *Org. Lett.* **2000**, *2*, 2295–2298.

Chemistry–A European Journal

Research Article
doi.org/10.1002/chem.202300193

Chemistry Europe
European Chemical
Societies Publishing

[24] K. J. Garcia, M. M. Gilbert, D. J. Weix, *J. Am. Chem. Soc.* **2019**, *141*, 1823–1827.

[25] C. G. Santana, M. J. Krische, *ACS Catal.* **2021**, *11*, 5572–5585.

[26] J. Twilton, M. Christensen, D. A. DiRocco, R. T. Ruck, I. W. Davies, D. W. C. MacMillan, *Angew. Chem. Int. Ed.* **2018**, *57*, 5369–5373; *Angew. Chem.* **2018**, *130*, 5467–5471.

[27] C. Heinz, J. P. Lutz, E. M. Simmons, M. M. Miller, W. R. Ewing, A. G. Doyle, *J. Am. Chem. Soc.* **2018**, *140*, 2292–2300.

[28] H. Lyu, I. Kevlishvili, X. Yu, P. Liu, G. Dong, *Science* **2021**, *372*, 175–182.

[29] J. Liao, C. H. Basch, M. E. Hoerrner, M. R. Talley, B. P. Boscoe, J. W. Tucker, M. R. Garnsey, M. P. Watson, *Org. Lett.* **2019**, *21*, 2941–2946.

[30] S. Zhang, L. Li, J. Li, J. Shi, K. Xu, W. Gao, L. Zong, G. Li, M. Findlater, *Angew. Chem. Int. Ed.* **2021**, *60*, 7275–7282; *Angew. Chem.* **2021**, *133*, 7351–7358.

[31] a) J. K. Vandavasi, X. Hua, H. B. Halima, S. G. Newman, *Angew. Chem. Int. Ed.* **2017**, *56*, 15441–15445; *Angew. Chem.* **2017**, *129*, 15643–15647; b) J. K. Vandavasi, S. G. Newman, *Synlett* **2018**, *29*, 2081; c) T. Verheyen, L. van Turnhout, J. K. Vandavasi, E. S. Isbrandt, W. M. De Borggraeve, S. G. Newman, *J. Am. Chem. Soc.* **2019**, *141*, 6869–6874.

[32] a) R. F. Heck, *Org. React.* **1982**, *27*, 345–390; b) W. Cabri, I. Candiani, *Acc. Chem. Res.* **1995**, *28*, 2–7; c) T. M. Gøgsig, J. Kleimark, S. O. Nilsson Lill, S. Korsager, A. T. Lindhardt, P.-O. Norrby, T. Skrydstrup, *J. Am. Chem. Soc.* **2012**, *134*, 443–452; d) J.-H. Bian, W.-Y. Tong, C. E. Pitsch, Y.-B. Wu, X. Wang, *Dalton Trans.* **2021**, *50*, 2654–2662.

[33] P. M. MacQueen, J. P. Tassone, C. Diaz, M. Stradiotto, *J. Am. Chem. Soc.* **2018**, *140*, 5023–5027.

[34] M. Zembayashi, K. Tamao, J. Yoshida, M. Kumada, *Tetrahedron Lett.* **1977**, *18*, 4089–4091.

[35] M. Sakai, M.-S. Lee, K. Yamaguchi, Y. Kawai, K. Sasaki, Y. Sakakibara, *Bull. Chem. Soc. Jpn.* **1992**, *65*, 1739–1740.

[36] C. Desmarets, S. Kuhl, R. Schneider, Y. Fort, *Organometallics* **2002**, *21*, 1554–1559.

[37] a) J. Y. Yang, S. Chen, W. G. Dougherty, W. S. Kassel, R. M. Bullock, D. L. DuBois, S. Raugei, R. Rousseau, M. Dupuis, M. R. DuBois, *Chem. Commun.* **2010**, *46*, 8618–8620; b) D. L. DuBois, R. M. Bullock, *Eur. J. Inorg. Chem.* **2011**, *2011*, 1017–1027; c) U. J. Kilgore, M. P. Stewart, M. L. Helm, W. G. Dougherty, W. S. Kassel, M. R. DuBois, D. L. DuBois, R. M. Bullock, *Inorg. Chem.* **2011**, *50*, 10908–10918; d) T. Liu, D. L. DuBois, M. R. Bullock, *Nat. Chem.* **2013**, *5*, 228–233; e) A. K. Das, M. H. Engelhard, M. R. Bullock, J. A. S. Roberts, *Inorg. Chem.* **2014**, *53*, 6875–6885; f) R. M. Bullock, M. L. Helm, *Acc. Chem. Res.* **2015**, *48*, 2017–2026; g) B. R. Galan, J. Schöffel, J. C. Linehan, C. Seu, A. M. Appel, J. A. S. Roberts, M. L. Helm, U. J. Kilgore, J. Y. Yang, D. L. DuBois, C. P. Kubiak, *J. Am. Chem. Soc.* **2011**, *133*, 12767–12779; h) U. H. Kilgore, J. A. S. Roberts, D. H. Pool, A. M. Appel, M. P. Stewart, M. R. DuBois, W. M. Dougherty, W. S. Kassel, R. M. Bullock, D. L. DuBois, *J. Am. Chem. Soc.* **2011**, *133*, 5861–5872; i) A. M. Appel, D. H. Pool, M. O'Hagan, W. J. Shaw, J. Y. Yang, M. R. DuBois, D. L. DuBois, M. R. Bullock, *ACS Catal.* **2011**, *1*, 777–785; j) J. M. Stubbs, R. J. Hazlehurst, P. D. Boyle, J. M. Blacquiere, *Organometallics* **2017**, *36*, 1692–1698.

[38] a) C. S. Seu, D. Ung, M. D. Doud, C. E. Moore, A. L. Rheingold, C. P. Kubiak, *Organometallics* **2013**, *32*, 4556–4563; b) I. Strelnik, I. Dayanova, E. Musina, A. Karasik, O. Sinyashin, *Phosphor. Sulfur Silicon Relat. Elem.* **2016**, *191*, 1515–1517; c) Y. S. Spiridonova, I. D. Strelnik, E. I. Musina, E. Hey-Hawkins, I. A. Litvinov, A. A. Karasik, *Russ. J. Coord. Chem.* **2020**, *46*, 477–484; d) Y. S. Spiridonova, Y. A. Nikolaeva, A. S. Balueva, E. I. Musina, I. A. Litvinov, I. D. Strelnik, V. V. Khrizanforova, Y. G. Budnikova, A. A. Karasik, *Molecules* **2020**, *25*, 3775; e) A. A. Karasik, R. N. Naumov, O. G. Sinyashin, G. P. Belov, H. V. Novikova, P. Lönnecke, E. Hey-Hawkins, *Dalton Trans.* **2003**, 2209–2214.

[39] E. S. Isbrandt, A. Nasim, K. Zhao, S. G. Newman, *J. Am. Chem. Soc.* **2021**, *143*, 14646–14656.

[40] G. Magi Meconi, S. V. C. Vummaleti, J. A. Luque-Urrutia, P. Belanzoni, S. P. Nolan, H. Jacobsen, L. Cavallo, M. Solà, A. Poater, *Organometallics* **2017**, *36*, 2088–2095.

[41] a) G. Li, T. Zhou, A. Poater, L. Cavallo, S. P. Nolan, M. Szostak, *Catal. Sci. Technol.* **2020**, *10*, 710–716; b) M. C. D'Alterio, È. Casals-Cruañas, N. V. Tzouras, G. Talarico, S. P. Nolan, A. Poater, *Chem. Eur. J.* **2021**, *27*, 13481–13493; c) S. Yang, T. Zhou, A. Poater, L. Cavallo, S. P. Nolan, M. Szostak, *Catal. Sci. Technol.* **2021**, *11*, 3189–3197.

[42] S. Kozuch, S. Shaik, *Acc. Chem. Res.* **2011**, *44*, 101–110.

[43] D. E. Chapple, P. D. Boyle, J. M. Blacquiere, *ChemCatChem* **2021**, *13*, 3789–3800.

[44] J. Y. Yang, S. Chen, W. G. Dougherty, W. S. Kassel, R. Morris Bullock, D. L. DuBois, S. Raugei, R. Rousseau, M. Dupuis, M. Rakowski DuBois, *Chem. Commun.* **2010**, *46*, 8618–8620.

[45] a) I. Mayer, *Chem. Phys. Lett.* **1983**, *97*, 270–274; b) A. Poater, A. Gallegos Saliner, M. Solà, L. Cavallo, A. P. Worth, *Expert Opin. Drug Delivery* **2010**, *7*, 295–305.

[46] a) A. Vidal-López, S. Posada-Pérez, M. Solà, V. D'Elia, A. Poater, *Green Chem. Eng.* **2022**, *3*, 180–187; b) S. Arayachukiat, P. Yingcharoen, S. V. C. Vummaleti, L. Cavallo, A. Poater, V. D'Elia, *J. Mol. Catal.* **2017**, *443*, 280–285; c) A. Poater, S. V. C. Vummaleti, E. Pump, L. Cavallo, *Dalton Trans.* **2014**, *43*, 11216–11220; d) S. Karimi, N. Bahri-Laleh, S. Sadjadi, G. Pareras, M. Nekoomanesh-Haghighi, A. Poater, *J. Ind. Eng. Chem.* **2021**, *97*, 44–451; e) A. Hanifpour, N. Bahri-Laleh, M. Nekoomanesh-Haghighi, A. Poater, *Appl. Organomet. Chem.* **2021**, *35*, e6227; f) M. Tabrizi, S. Sadjadi, G. Pareras, M. Nekoomanesh-Haghighi, N. Bahri-Laleh, A. Poater, *J. Colloid Interface Sci.* **2021**, *581*, 939–953; g) M. Tomasini, L. Caporaso, J. Trouvé, J. Poater, R. Gramage-Doria, A. Poater, *Chem. Eur. J.* **2022**, *28*, e202201970; h) A. Poater, S. Moradell, E. Pinilla, J. Poater, M. Solà, M. A. Martínez, A. Llobet, *Dalton Trans.* **2006**, 1188–1196.

[47] a) S. Posada-Pérez, S. Escayola, J. Poater, M. Solà, A. Poater, *Dalton Trans.* **2022**, *51*, 12585–12595; b) F. Bru, M. Lesieur, A. Poater, A. M. Z. Slawin, L. Cavallo, C. S. J. Cazin, *Chem. Eur. J.* **2022**, *28*, e202201917.

[48] C.-L. Ji, P.-P. Xie, X. Hong, *Molecules* **2018**, *23*, 2681.

[49] G. Skara, M. Gimferrer, F. De Proft, P. Salvador, B. Pinter, *Inorg. Chem.* **2016**, *55*, 2185–2199.

[50] J. Poater, M. Gimferrer, A. Poater, *Inorg. Chem.* **2018**, *57*, 698–6990.

[51] M. Gimferrer, P. Salvador, A. Poater, *Organometallics* **2019**, *38*, 4585–4592.

[52] A. M. Borys, E. Hevia, *Angew. Chem. Int. Ed.* **2021**, *60*, 24659–24667; *Angew. Chem.* **2021**, *133*, 24864–24872.

[53] A. Nasim, G. T. Thomas, J. S. Ovens, S. G. Newman, *Org. Lett.* **2022**, *24*, 7232–7236.

[54] C. Amatore, A. Jutand, *Acc. Chem. Res.* **2000**, *33*, 314–321.

[55] S. H. Newman-Stonebraker, J. Y. Wang, P. D. Jeffrey, A. G. Doyle, *J. Am. Chem. Soc.* **2022**, *144*, 19635–19648.

[56] S. I. Ting, W. L. Williams, A. G. Doyle, *J. Am. Chem. Soc.* **2022**, *144*, 5575–5582.

[57] Gaussian 16, Revision C.01, M. J. Frisch, G. W. Trucks, H. B. Schlegel, G. E. Scuseria, M. A. Robb, J. R. Cheeseman, G. Scalmani, V. Barone, G. A. Petersson, H. Nakatsuji, X. Li, M. Caricato, A. V. Marenich, J. Bloino, B. G. Janesko, R. Gomperts, B. Mennucci, H. P. Hratchian, J. V. Ortiz, A. F. Izmaylov, J. L. Sonnenberg, J. Williams-Young, F. Ding, F. Lipparini, F. Egidi, J. Goings, B. Peng, A. Petrone, T. Henderson, D. Ranasinghe, V. G. Zakrzewski, J. Gao, N. Rega, G. Zheng, W. Liang, M. Hada, M. Ehara, K. Toyota, R. Fukuda, J. Hasegawa, M. Ishida, T. Nakajima, Y. Honda, O. Kitao, H. Nakai, T. Vreven, K. Throssell, J. A. Montgomery, Jr., J. E. Peralta, F. Ogliaro, M. J. Bearpark, J. J. Heyd, E. N. Brothers, K. N. Kudin, V. N. Staroverov, T. A. Keith, R. Kobayashi, J. Normand, K. Raghavachari, A. P. Rendell, J. C. Burant, S. S. Iyengar, J. Tomasi, M. Cossi, J. M. Millam, M. Klene, C. Adamo, R. Cammi, J. W. Ochterski, R. L. Martin, K. Morokuma, O. Farkas, J. B. Foresman, and D. J. Fox, Gaussian, Inc., Wallingford CT, **2016**.

[58] a) A. D. Becke, *Phys. Rev. A* **1988**, *38*, 3098–3100; b) J. P. Perdew, *Phys. Rev. B* **1986**, *33*, 8822–8824.

[59] a) S. Grimme, J. Antony, S. Ehrlich, H. Krieg, *J. Chem. Phys.* **2010**, *132*, 154104; b) S. Grimme, S. Ehrlich, L. Goerigk, *J. Comput. Chem.* **2011**, *32*, 1456–1465; c) S. Grimme, *Wiley Interdisc. Rev.: Comput. Mol. Sci.* **2011**, *1*, 21–228.

[60] a) F. Weigend, R. Ahlrichs, *Phys. Chem. Chem. Phys.* **2005**, *7*, 3297–3305; b) F. Weigend, *Phys. Chem. Chem. Phys.* **2006**, *8*, 1057–1065.

[61] a) A. D. Becke, *J. Chem. Phys.* **1993**, *98*, 5648–5652; b) C. Lee, W. Yang, R. G. Parr, *Phys. Rev. B* **1988**, *37*, 785–789; c) P. J. Stephens, F. J. Devlin, C. F. Chabalowski, M. J. Frisch, *J. Phys. Chem.* **1994**, *98*, 11623–11627.

[62] a) V. Barone, M. Cossi, *J. Phys. Chem. A* **1998**, *102*, 1995–2001; b) J. Tomasi, M. Persico, *Chem. Rev.* **1994**, *94*, 2027–2094; c) M. Cossi, N. Rega, G. Scalmani, V. Barone, *J. Comput. Chem.* **2003**, *24*, 669–681.

[63] P. Pracht, F. Bohle, S. Grimme, *Phys. Chem. Chem. Phys.* **2020**, *22*, 7169–7192.

[64] a) P. Salvador, E. Ramos-Cordoba, M. Gimferrer, M. Montilla, APOST-3D Program; Universitat de Girona: Girona, Spain, **2020**; b) E. Ramos-Cordoba, P. Salvador, I. Mayer, *J. Chem. Phys.* **2013**, *138*, 214107.

3.2 Paper II

Directed Palladium-Catalyzed γ-C(sp^3)-H Alkenylation of (Aza and Oxa) Cyclohexanamines with Bromoalkenes: Bromide Precipitation as an Alternative for Silver Scavenging

K. Gadde*, N. R. Bheemireddy*, J. Heitkämper*, A. Nova, and B. U. W. Maes
*authors have contributed equally

Own contributions:

- all quantum chemical calculations (equal contribution with experimental part)
- preparation of the manuscript together with A. Nova Flores, K. Gadde, and B. Maes
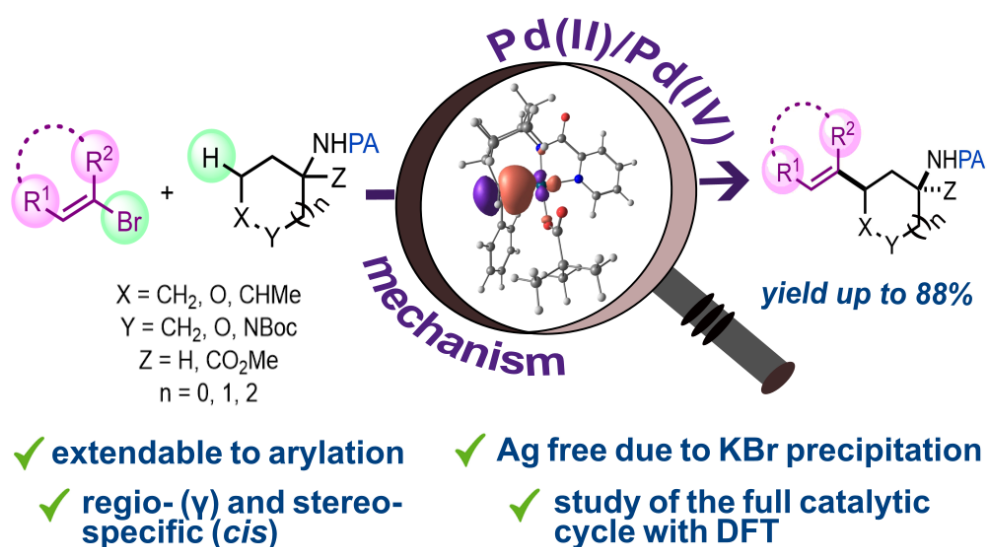
Research Article

Directed Palladium-Catalyzed γ-C(sp^3)−H Alkenylation of (Aza and Oxa) Cyclohexanamines with Bromoalkenes: Bromide Precipitation as an Alternative to Silver Scavenging

Karthik Gadde,[£] Narendraprasad Reddy Bheemireddy,[£] Juliane Heitkämper,[£] Ainara Nova,* and Bert U. W. Maes*

Read Online

ACCESS | Metrics & More | Article Recommendations | SI Supporting Information

ABSTRACT: Directed palladium-catalyzed coupling of remote C(sp^3)−H bonds of aliphatic amines with organohalides is a powerful synthetic tool. However, these reactions still possess limitations with respect to cost and resource efficiency, requiring more reactive iodinated reactants and superstoichiometric silver salt reagents. In this work, an efficient regio- and stereospecific silver-free Pd-catalyzed γ-C(sp^3)−H alkenylation of cyclohexanamines and heterocyclic analogues with bromoalkenes is reported, which can also be applied on five- and seven-membered rings. DFT methods revealed that the oxidative addition of the organobromide to Pd(II) is not the rate-limiting step but rather γ-C(sp^3)−H bond activation in the substrate. The lowest energy complex in the catalytic cycle is a Pd(II)-Br complex coordinated with the reaction product (η^2-alkene and a bidentate directing group). The stability of this complex defines the overall energy span of the reaction. Co-catalyst KOPiv plays a pivotal role by exchanging bromide for pivalate in the complex, via precipitation of the KBr coproduct. This removal of bromide from the reaction media decreases the energy span, avoiding the use of superstoichiometric silver salt reagents and allowing decoordination of the reaction product. In addition, pivalate facilitates the C(sp^3)−H bond activation in the substrate once another substrate molecule is coordinated. The reaction conditions could be directly applied for (hetero)arylation given the weaker coordination of the reaction product, featuring a (hetero)aryl versus alkenyl and change in resting state. The picolinoyl directing group can be removed via amide esterification.

KEYWORDS: C−H activation, alkenylation, directing group, palladium catalysis, computational chemistry
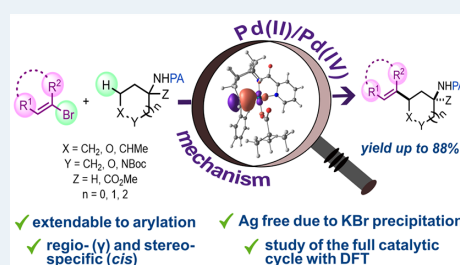
INTRODUCTION

In the past two decades, Pd-catalyzed C−H bond functionalization reactions have emerged as a novel tool for the formation of carbon−carbon and carbon-heteroatom bonds bringing potential advantages concerning step economy and waste reduction for organic synthesis.[1] In particular, the regioselective functionalization of C(sp^2)−H bonds of arenes and heteroarenes has been extensively developed and widely adopted by synthetic organic chemists, whereas the corresponding selective functionalization of C(sp^3)−H bonds of alkanes has, in comparison, been far less studied. In recent years, the Pd-catalyzed methodologies with the assistance of transition metal coordinating directing groups have shown tremendous progress toward the functionalization of remote (β, γ, or δ) C(sp^3)−H bonds, including aspects of regio- and stereoselectivity.[1a−f] Remarkably, among the various organohalide electrophiles used alkenyl halides have rarely been reported as reactants.[2−4] Moreover, these remote alkenylations of C(sp^3)−H bonds all require superstoichiometric halide scavenging of silver reagents. With one exception,[3e] using a (E)-β-bromostyrene, these are all limited to alkenyl iodides,

which are more expensive and less available than the corresponding bromides.[1f]

Aliphatic amines are found in chemical, pharmaceutical, textile, cosmetic, and metal industries. These chemicals are used as intermediates, solvents, rubber accelerators, catalysts, emulsifiers, synthetic cutting fluids, corrosion inhibitors, and flotation agents.[5] Considering their importance, the direct transformation of aliphatic amines via directed Pd-catalyzed C(sp^3)−H bond functionalization has been studied over the past decade.[6] In particular, the easily removable and reusable picolinamide directing group is one of the powerful tools to achieve selective remote C(sp^3)−H bond functionalization. In 2005, Daugulis and co-workers reported picolinamide directing group assisted Pd-catalyzed γ-C(sp^3)−H arylation in aliphatic
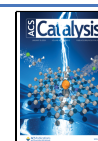
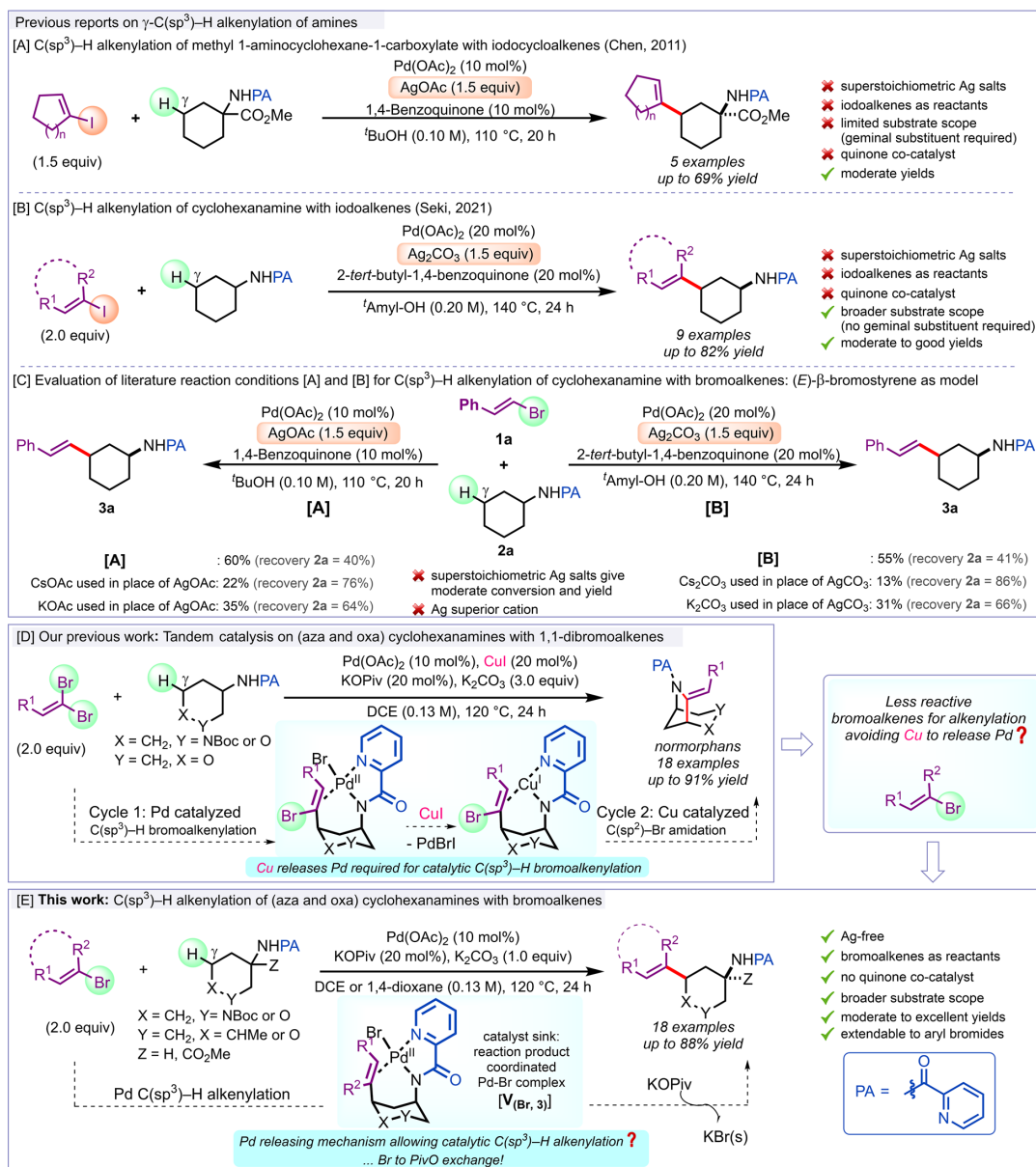**Scheme 1. Pd-Catalyzed γ-alkenylation of Cyclohexanamines Equipped with a Directing Group: State-of-the-Art Iodoalkenes (A, B), Application of the State-of-the-Art Conditions on Bromoalkenes (C), Our Previous Work with 1,1-Dibromoalkenes (D), and This Work with Bromoalkenes (E)**


amines with aryl iodides.[7] Since then, various functionalizations at remote sites in aliphatic amines have been reported, mainly using iodinated electrophiles, with methyl preference (concerted Pd–C bond formation: 1° > 2° > 3° alkyl-H).[8] Among these, the more difficult remote C(sp³)−H methylene bonds of cycloalkanamines are scarcely explored.[6] Remarkably, for the γ-C(sp³)−H alkenylation of cycloalkanamines, only two methods have been reported so far (Scheme 1).[2] The first method reported by Chen and co-workers is a Pd-catalyzed γ-C(sp³)−H alkenylation of methyl 1-picolinoylaminocyclohex-

ane-1-carboxylate, which employs cycloalkenyl iodides as alkenyl coupling partners and silver acetate reagent (Scheme 1A).[2a] The second method, reported by Seki and Takahashi, discloses a Pd-catalyzed γ-C(sp³)−H alkenylation of *N*-picolinoylcyclohexanamine employing alkenyl iodides as reactant and silver carbonate reagent (Scheme 1B).[2b] Both approaches are limited to alkenyl iodides as coupling partners and require a superstoichiometric silver salt reagent. Clearly, new and efficient silver-free reaction conditions are required based on alkenyl bromides. We recently developed a Pd and

Cu tandem catalytic process toward bridged bicyclic nitrogen scaffolds synthesis involving a Pd-catalyzed γ-C(sp^3)-bromoalkenylation of N-picolinoylcyclohexanamine with 1,1-dibromoalkene, followed by a consecutive intramolecular Cu-catalyzed amidation of the 1-bromo-1-alkenylated intermediate.[9] Remarkably, the CuI required for the amidation step was shown to promote the Pd-catalyzed γ-C(sp^3)-bromoalkenylation step of the tandem process by releasing intermediate product (i.e., 1-bromo-1-alkenylated) from the Pd catalyst via exchange with Cu (Scheme 1D). We disclose in this work γ-C(sp^3)−H alkenylation of N-picolinoylcyclohexanamines with less reactive 1-bromoalkenes, lacking the geminal bromine atom under silver- and copper-free conditions relying on another Pd releasing mechanism (Scheme 1E).

The motivation to replace silver or cesium salts in state-of-the-art C−H functionalization protocols is based on price and the weight of the concomitant waste produced (Supporting Information, Sections S4 and S5). The abundance of metals in Earth's crust is generally reflected in the price of their corresponding inorganic salts (Figure 1 and Supporting
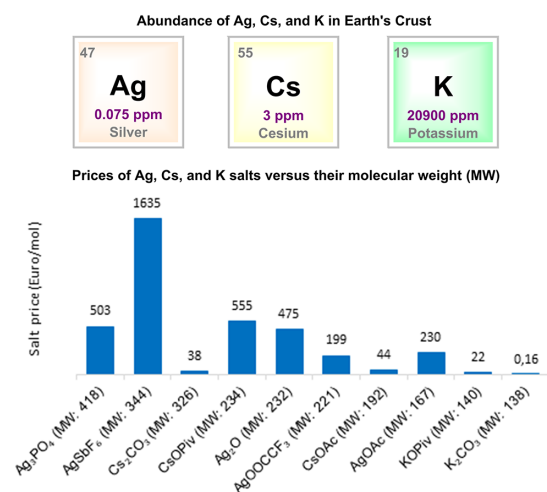
Figure 1. Prices of Common Reagents and the cation abundances of their reagents in Earth's Crust. MW = molecular weight.

Information Section S6.2), and the higher molecular weight of the metal, the more waste (in g) is produced. Based on both

factors, potassium salts are preferred over silver and cesium salts.

In order to rationalize why no Ag salts are required in our alkenylation protocol, the reaction mechanism of the γ-C(sp^3)−H functionalizations with organobromides was studied by using DFT calculations. Besides alkenyl bromide, aryl bromide was selected as a comparison. The catalytic cycle proposed for the Pd(II) catalyzed C−H functionalization reactions with electrophilic coupling partners typically goes through Pd(II)/Pd(IV) pathways.[6] Previous computational studies on these reactions have focused on the mechanism of the C−H bond activation step and other selected reaction steps to address aspects like stereoselectivity,[10] the formation of crucial off-cycle Pd species,[11] or competitive β-hydride elimination reactions.[12] However, few computational studies have looked at the full catalytic cycle, and these studies involve C(sp^2)−H bonds[10f,13] or the use of organoiodide reactants.[11,14] In the case of C(sp^3)−H and organobromide coupling partners, it is difficult to predict whether the C−H bond activation or the organobromide addition to Pd(II) would be the rate limiting step.[6a,15] In this work, we disclose that for γ-C(sp^3)−H functionalization of cyclohexanamines with alkenyl bromides, the C−H bond activation involves the highest energy barrier. The lowest energy complex in the catalytic cycle is a Pd(II)-Br complex coordinated to the reaction product [$\mathbf{V_{(Br,3)}}$]. For strongly coordinating reaction products containing a C=C bond and directing group, this resting state complex $\mathbf{V_{(Br,3)}}$ becomes a catalyst sink and a limiting factor for the turnover of the C(sp^3)−H functionalization reaction, requiring an effective transformation into a more reactive Pd complex.

■ RESULTS AND DISCUSSION

C(sp^3)−H Alkenylation of (Aza- and Oxa-) Cyclohexanamines with Bromoalkenes. We began our investigation of the γ-C(sp^3)−H alkenylation of cyclohexanamines with N-picolinoylcyclohexanamine (**2a**) and (E)-β-bromostyrene (**1a**) as model coupling partners. When we applied the two sets of conditions reported for the γ-C(sp^3)−H alkenylation of N-picolinoylcyclohexanamine with iodoalkenes on the model system, moderate conversion (∼60%) and product yields (55−60%) were obtained (Scheme 1C, and Supporting Information Section S2). Furthermore, when we replaced silver salts with either cesium or potassium salts, lower conversion and product yields were obtained in accordance with the superior halide scavenging role of silver (Scheme 1C).[1g,h] When applying our

Table 1. Reaction Optimization on the Model Reaction of (E)-β-Bromostyrene (1a) with N-Picolinoylcyclohexanamine (2a)
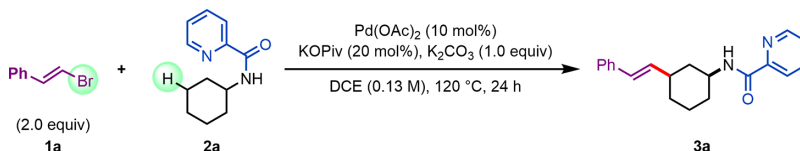
entry	deviation from standard conditions	reaction time, h	recovery of 2a, %[a]	yield of 3a, %[a]
1	with 20 mol % CuI	24	14	79
2	none	24	11 (9)[b]	89 (86)[b]
3	absence of KOPiv	24	55	45
4	absence of K$_2$CO$_3$	24	78	11
5	(E)-β-iodostyrene used in place of 1a	24	1 (1)[b]	98 (94)[b]

[a]^{1}H NMR yield. cis major compound see Supporting Information Table S3−S4. [b]Isolated yield.

Scheme 2. Scope of the Diastereoselective Pd-Catalyzed γ-C(sp³)−H Alkenylation with Bromoalkenes[a]
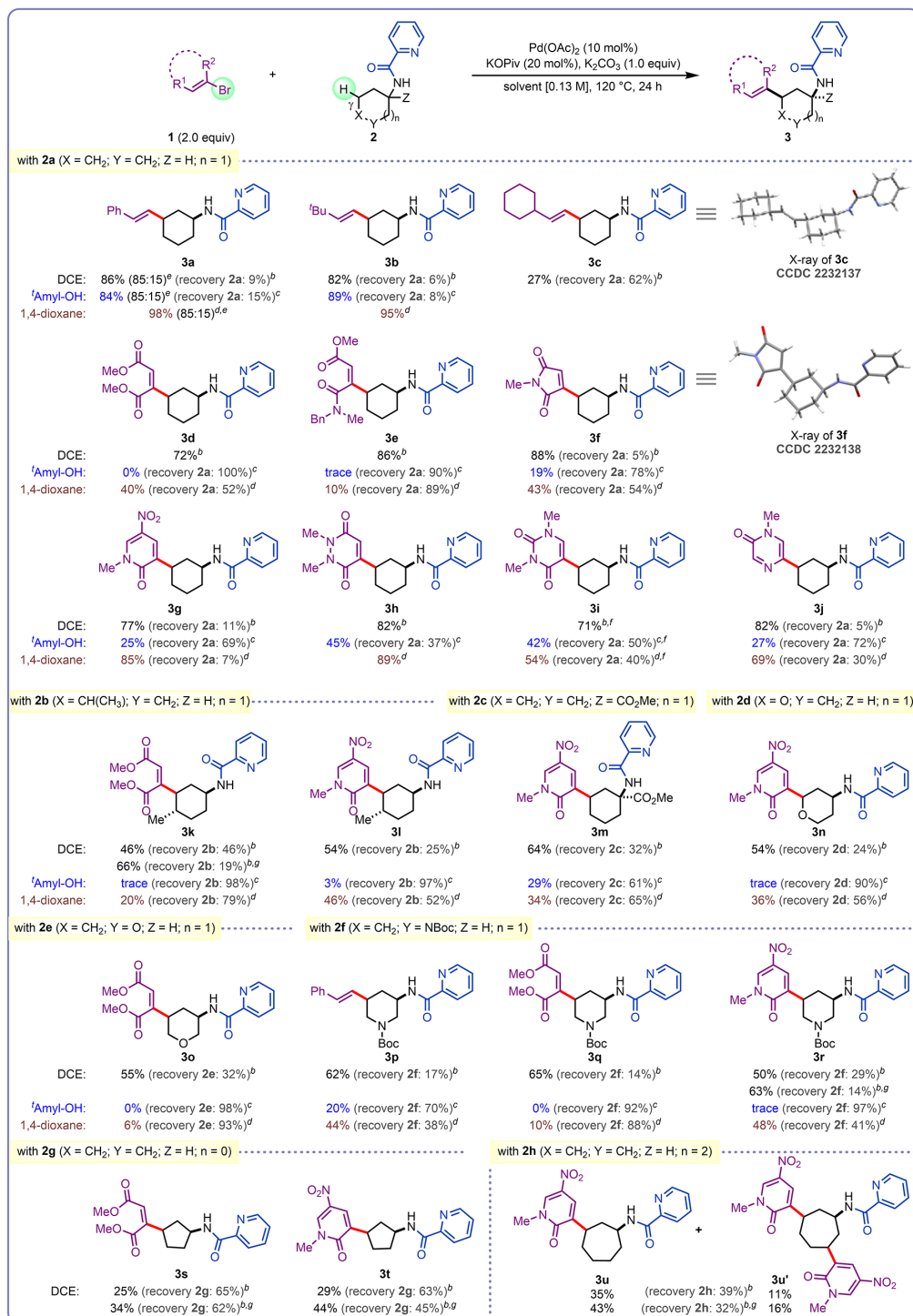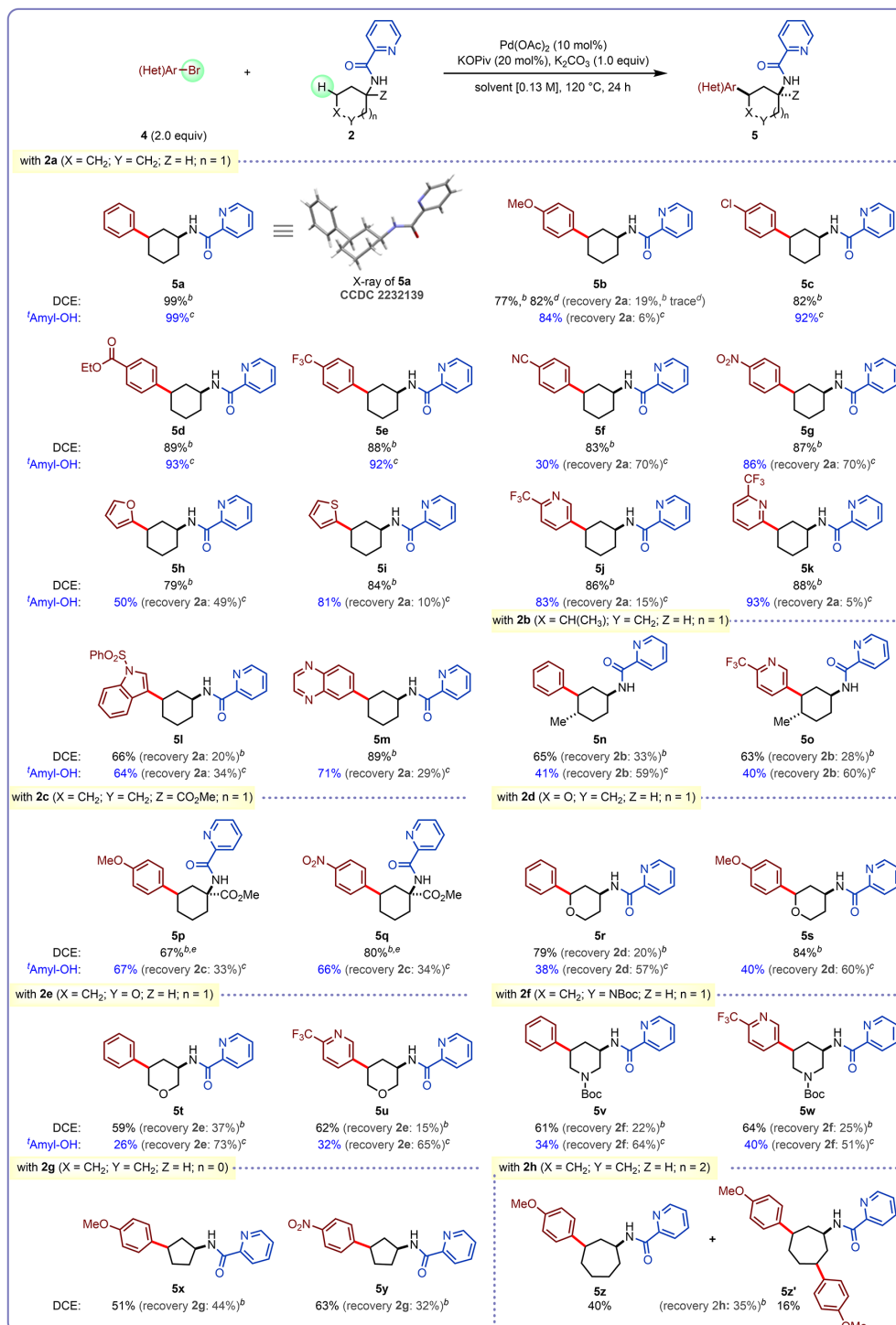

[a]Full *cis* diastereoselectivity except for **3a**. When no recovery of **2** is indicated, it was <5%. [b]1,2-Dichloroethane used as solvent. Isolated yields. [c]*tert*-Amyl alcohol used as solvent. ¹H NMR yields. [d]1,4-Dioxane used as solvent. ¹H NMR yields. [e]*Cis/trans* ratio. [f]5.0 equiv of bromoalkene was used. [g]20 mol % Pd(OAc)₂ was used.

previously reported reaction conditions optimized for β,β-bromostyrene as the electrophile, in the framework of the tandem protocol toward normorphans (Scheme 1D), the targeted γ-alkenylated cyclohexanamine, i.e., 3-(2-phenyl-ethenyl)-N-picolinoylcyclohexanamine (3a) was obtained in 79% yield with 14% recovery of 2a (Table 1, entry 1).[9] 1a lacks a bromine atom versus β,β-bromostyrene and is, therefore, less reactive versus oxidative addition. When omitting catalytic CuI, a better mass balance and 89% 3a was obtained (Table 1, entry 2), indicating an inhibiting rather than a promoting role for this additive when only C−H alkenylation is involved and no tandem bromoalkenylation−amidation reaction. Deviation from these conditions indicated which parameters are crucial in the γ-alkenylation process (Table 1, and Supporting Information Section S3). Omitting the additive KOPiv or performing the reaction in the absence of K_2CO_3 furnished conversions of less than 50% and low yields of 3a, 45 and 11%, respectively (Table 1, entries 3 and 4). The use of (E)-β-iodostyrene (1aa) in place of (E)-β-bromostyrene yielded the desired product 3a in 98% yield (entry 5), also without using silver additives which are required with iodinated coupling partners (Scheme 1A,B).

Encouraged by the outcome of the γ-C(sp^3)−H alkenylation of 2a with (E)-β-bromostyrene (1a), we next evaluated the bromoalkene scope with more challenging coupling partners 1, which are not styrene based (Scheme 2). Interestingly, aliphatic bromoalkenes (E)-1-bromo-3,3-dimethylbut-1-ene (1b) and (E)-(2-bromovinyl)cyclohexane (1c) provided the desired reaction products. While the former gave 94% conversion of 2a and 82% yield of 3b, the latter gave 27% 3c and 62% recovered 2a. Esters and amide conjugated with the double bond were well tolerated as illustrated with coupling partners dimethyl 2-bromomaleate (1d) and methyl (E)-4-[benzyl(methyl)amino]-3-bromo-4-oxobut-2-enoate (1e), providing high yields of 3d and 3e, in 72 and 86%, respectively. The double bond can also be included in an imide, as shown by the efficient coupling with 3-bromo-1-methyl-1H-pyrrole-2,5-dione (1f). Interestingly, azinones [3-bromo-1-methyl-5-nitropyridin-2(1H)-one (1g)] as well as diazinones [4-bromo-1,2-dimethyl-1,2-dihydropyridazine-3,6-dione (1h), 5-bromo-1,3-dimethyluracil (1i), and 5-bromo-1-methylpyrazin-2(1H)-one (1j)] proved also suitable coupling partners with 2a, and the desired corresponding alkenylated products 3g, 3h, 3i, and 3j were obtained in high yields. The cyclohexanamine can also be substituted in the position next to the methylene, as exemplified by the reaction of trans-4-methyl-N-picolinoylcyclohexanamine (trans-2b) with 1d and 1g, delivering the alkenylated product 3k and 3l in moderate yields (46 and 54%, respectively) without altering the reaction conditions. Unnatural amino acid ester 2c reacted with bromopyridin-2(1H)-one 1g, delivering alkenylated product 3m in 64% yield. To our delight, also oxa- and aza- analogues of cyclohexanamines, i.e., N-picolinoyltetrahydro-2H-pyran-4-amine (2d), N-picolinoyltetrahydro-2H-pyran-3-amine (2e), and 1-Boc-N-picolinoyl-piperidin-3-amine (2f), provided target compounds under the standard reaction conditions, further supporting its generality. The reaction of 2d with bromopyridin-2(1H)-one 1g furnished the corresponding desired product 3n in 54% yield. The reaction of 2e with 2-bromomaleate 1d also gave the corresponding desired product
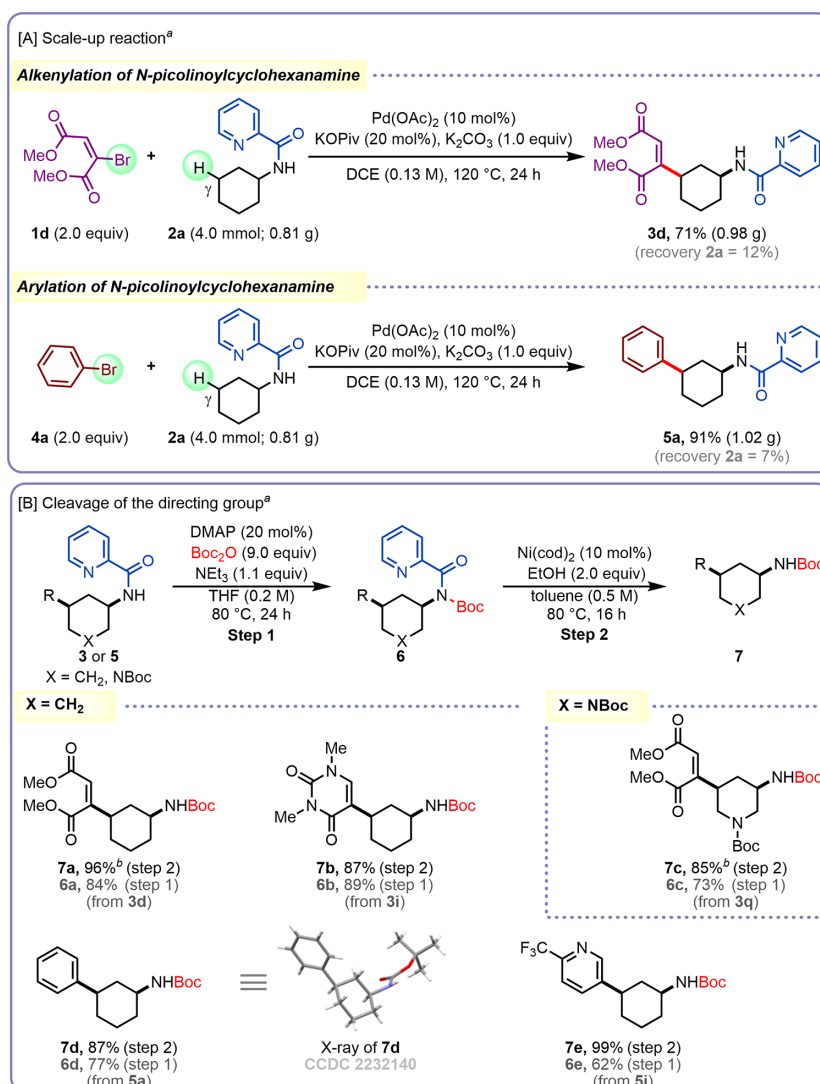
3o in 55% yield. Starting material 2f reacted with bromostyrene 1a, bromomaleate 1d, and bromopyridin-2(1H)-one 1g, affording the desired alkenylated products 3p, 3q, and 3r in 62, 65, and 50% yields, respectively. With these challenging substituted and heterocyclic substrates,[16] starting materials 2b−f were easily recycled under the standard conditions. However, the mass balances were high, indicating the high chemoselectivity of the reaction. Alternative solvents were also studied. t-Amyl alcohol generally proved to be a poor solvent, particularly for alkenylation reactions featuring heteroatom containing 2 and/or 1 (Scheme 2). Interestingly, 1,4-dioxane gave better results with the exception of the diester (1d) or mixed ester/amide (1e) of bromomaleic acid as reactants providing poor yields of the corresponding reaction products. Bromo(di)azinones 1g−j performed equally well in comparison to DCE though with challenging substrates 2 (C-substituted and aza- and oxa cyclohexanamines, 2b−f) with lower conversions and yields. This methodology could also be extended to five- and seven-membered cycloalkanamine substrates, without adaptation of the reaction conditions, as exemplified by the reaction of N-picolinoylcyclopentanamine (2g) with 1d and 1g, and the reaction of N-picolinoylcyclo-heptanamine (2h) with 1g under standard conditions, giving the desired alkenylation products 3s, 3t, and 3u in moderate yields (Scheme 2). Interestingly, in the case of seven-membered cyclic amine substrate 2h under these conditions, 11% of dialkenylation product 3u′ was isolated which was never detected on other substrates 2. For the different substrates (trans-2b, 2f, 2g, 2h) an example with moderate conversion with bromoalkene 1d and/or 1g was selected and repeated with a double loading of Pd(OAc)$_2$ (20 mol %). However, the yields of 3k, 3r, 3s, 3t, and 3u were only slightly improved (8−20% yields).

C(sp^3)−H Arylation of (Aza- and Oxa-) Cyclohexan-amines with (Hetero)aryl Bromides. Inspired by the results with bromo(di)azinones, we wondered whether the reaction conditions could also allow γ-C(sp^3)−H arylation of the same substrates (2) employing aryl bromides (4) rather than bromoalkenes (1) as a coupling partner (Scheme 3). We reasoned that the incorporation of the double bond into an aromatic system will impact the energy of several steps in the reaction mechanisms and therefore provide a good comparison for the DFT studies (vide infra). Gratifyingly, bromobenzene (4a) reacted with N-picolinoylcyclohexanamine (2a) under our reaction conditions without any alteration, providing 99% 3-phenyl-N-picolinoylcyclohexanamine (5a). Interestingly, aryl bromides bearing both electron-donating [i.e., methoxy (4b)] and electron-withdrawing [chloro (4c), ester (4d), trifluor-omethyl (4e), cyano (4f), and nitro (4g)] groups were also compatible under the standard reaction conditions providing the corresponding γ-C(sp^3)−H arylated products 5b−5g in 77−89% yield. In addition, heteroaryl bromides such as 2-bromofuran (4h), 2-bromothiophene (4i), 5-bromo-2-(trifluoromethyl)pyridine (4j), regioisomeric 2-bromo-6-(trifluoromethyl)pyridine (4k), 3-bromo-1-(phenylsulfonyl)-1H-indole (4l), and 6-bromoquinoxaline (4m) also provided good to excellent yields of the corresponding arylation products (5h in 79%, 5i in 84%, 5j in 86%, 5k in 88%, 5l in 66%, and 5m in 89% isolated yield). The cyclohexanamine can also be substituted in the position next to the methylene, as

Scheme 3. Scope of the Diastereoselective Pd-Catalyzed γ-C(sp³)−H (Hetero)arylation with (Hetero)aryl Bromides[a]

[a]Full *cis* diastereoselectivity. When no recovery of **2** is indicated, it was <5%. [b]1,2-Dichloroethane used as solvent. Isolated yields. [c]*tert*-Amyl alcohol used as solvent. ¹H NMR yields. [d]4.0 equiv of aryl bromide was used. [e]10−15% 3,5-diarylated compound isolated.

Scheme 4. (A) Gram-Scale Reaction and (B) Cleavage of the Picolinoyl Directing Group

[A] Scale-up reaction[a]

Alkenylation of N-picolinoylcyclohexanamine

1d (2.0 equiv) + 2a (4.0 mmol; 0.81 g)
Pd(OAc)₂ (10 mol%), KOPiv (20 mol%), K₂CO₃ (1.0 equiv), DCE (0.13 M), 120 °C, 24 h
→ 3d, 71% (0.98 g) (recovery 2a = 12%)

Arylation of N-picolinoylcyclohexanamine

4a (2.0 equiv) + 2a (4.0 mmol; 0.81 g)
Pd(OAc)₂ (10 mol%), KOPiv (20 mol%), K₂CO₃ (1.0 equiv), DCE (0.13 M), 120 °C, 24 h
→ 5a, 91% (1.02 g) (recovery 2a = 7%)

[B] Cleavage of the directing group[a]

3 or 5, X = CH₂, NBoc
Step 1: DMAP (20 mol%), Boc₂O (9.0 equiv), NEt₃ (1.1 equiv), THF (0.2 M), 80 °C, 24 h
→ 6
Step 2: Ni(cod)₂ (10 mol%), EtOH (2.0 equiv), toluene (0.5 M), 80 °C, 16 h
→ 7

X = CH₂

7a, 96%[b] (step 2); 6a, 84% (step 1) (from 3d)
7b, 87% (step 2); 6b, 89% (step 1) (from 3i)
7d, 87% (step 2); 6d, 77% (step 1) (from 5a)
X-ray of 7d, CCDC 2232140

X = NBoc

7c, 85%[b] (step 2); 6c, 73% (step 1) (from 3q)
7e, 99% (step 2); 6e, 62% (step 1) (from 5j)

[a]Isolated yield. [b]MeOH (5.0 equiv) was used in place of EtOH (2.0 equiv). DMAP = 4-dimethylaminopyridine.

exemplified by the reaction of *trans*-4-methyl-*N*-picolinoylcyclohexanamine (*trans*-2b) with bromobenzene (4a) and 5-bromo-2-(trifluoromethyl)pyridine (4j), delivering the arylated products 5n and 5o in moderate yields (65 and 63%, respectively). Unnatural amino acid ester 2c performed similarly as 2a in an arylation with 1-bromo-4-methoxybenzene (4b) and 1-bromo-4-nitrobenzene (4g) providing the desired products 5p and 5q in good yields. Remarkably, in this case a low percentage (10−15%) of 3,5-diarylation was also observed, which was never detected on other substrates 2. Notably, also heterocyclic analogues of cyclohexanamine can be applied without altering the standard conditions. The reaction of bromobenzene (4a) and 4-bromoanisole (4b) with *N*-picolinoyltetrahydro-2*H*-pyran-4-amine (2d) delivered the corresponding (hetero)arylated products 5r and 5s in excellent yields. The reaction of regioisomeric *N*-picolinoyltetrahydro-

2*H*-pyran-3-amine (2e) with bromobenzene (4a) and 5-bromo-2-(trifluoromethyl)pyridine (4j) delivered the corresponding arylated products 5t and 5u in good yields, though with some remaining substrate. Aza analogue 1-Boc-*N*-picolinoylpiperidin-3-amine (2f) performed equally well (5v and 5w in 61 and 64% yields, respectively). Alternative solvents were also studied. *t*-Amyl alcohol generally proved to be a good solvent with some exceptions (5f, 5h, and 5m), though lower conversions than in DCE were obtained for challenging substrates 2 (C-substituted and aza and oxa cyclohexanamines, 2b−f). When five- and seven-membered cycloalkanamine substrates 2g and 2h were subjected to the standard reaction conditions, the desired arylation products 5x, 5y, and 5z were obtained in moderate yields (Scheme 3). However, in the case of *N*-picolinoylcycloheptanamine substrate 2h under these conditions, 16% of diarylation

Scheme 5. Control Reactions to Support the Catalytic Cycle: (A) Kinetic Isotope Effect (KIE); (B) Pd Catalyst Inhibition by Product 3; (C) Salt Solubility; (D) Addition of Bu₄NBr
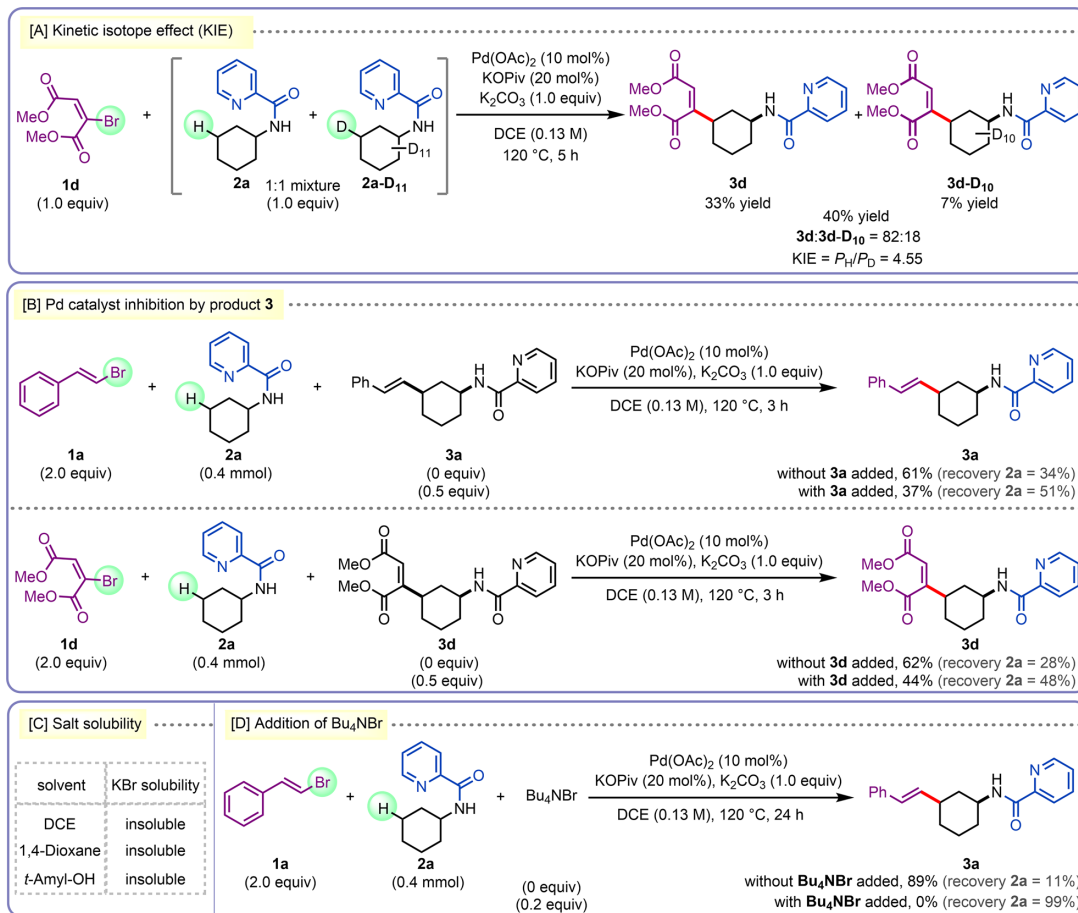
product **5z′** was isolated in addition to the monoarylation product **5z**. This is similar to what was observed in the γ-C(sp³)−H alkenylation (*vide supra*).
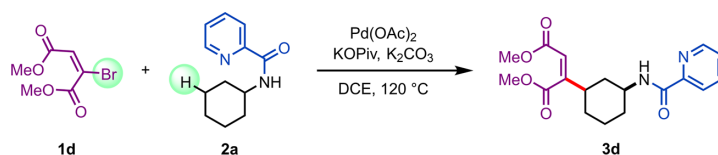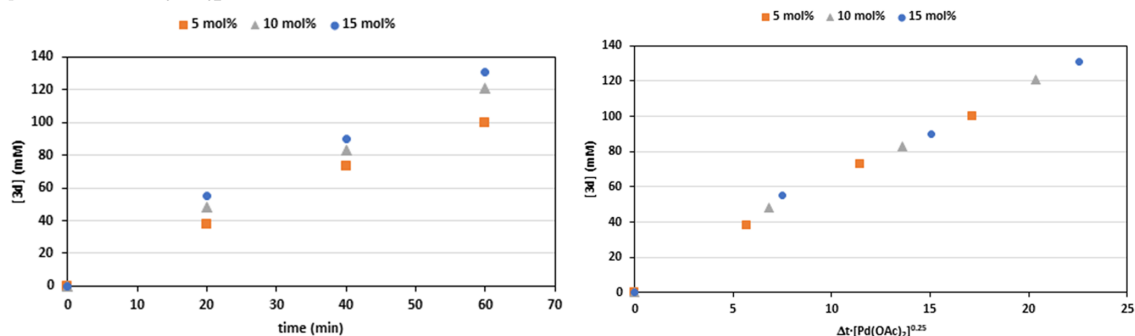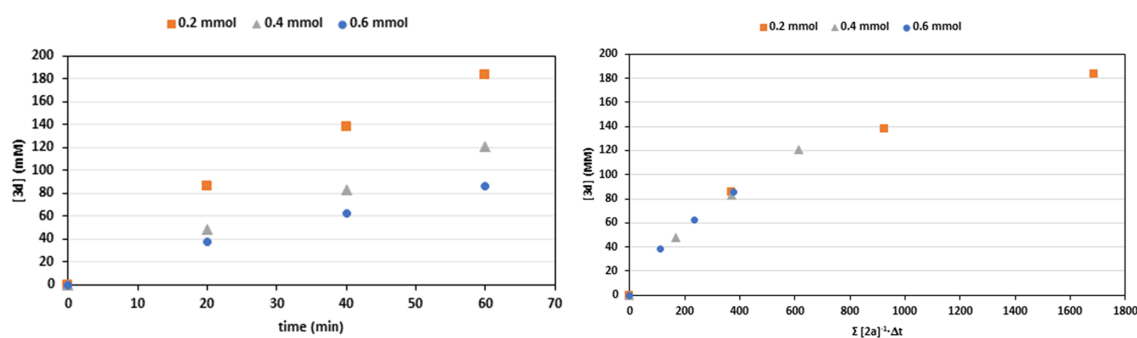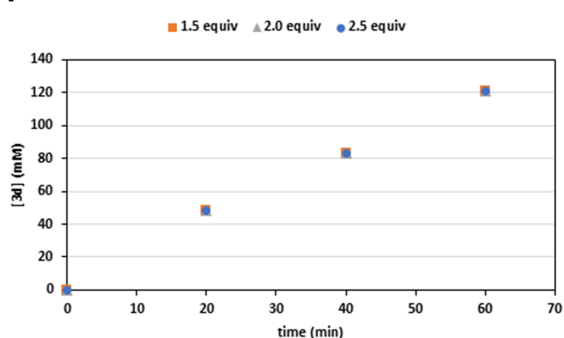
Diastereoselectivity. Full *cis*-diastereoselectivity was obtained in all of the γ-C(sp³)−H alkenylation (**3**) and arylation (**5**) reactions imposed by the reaction mechanism of the C−H activation step (*vide supra*) with the exception of 3-(2-phenylethenyl)-*N*-picolinoylcyclohexanamine (**3a**). By subjecting reaction product **3a** to the same reaction conditions of the functionalization, we could prove that this is a Pd-catalyzed postisomerization of the *cis* diastereoisomer as the *cis:trans* ratio changed from 87:13 to 76:24 (Supporting Information, Scheme S4). This is presumably due to the activated nature of the cinnamyl moiety. Also, the double bond geometry of reactants **1** was fully retained in all of the reaction products **3**.

Reaction Scalability and Removal of the Directing Group. Scale-up experiments were performed for showcasing the scalability of our alkenylation and arylation methods (Scheme 4A). Scaling up the reaction 10-fold to 4 mmol of *N*-picolinoylcyclohexanamine (**2a**) with coupling partners dimethyl 2-bromomaleate (**1d**) and bromobenzene (**4a**) delivered the desired products **3d** and **5a** in 71 and 91% yields, respectively. Next, we focused our attention on the

removal of the picolinoyl directing group. In this regard, we applied our previously developed two-step method for the cleavage of the picolinamide directing group *via N*-Boc activation followed by Ni-catalyzed esterification with alcohol on both alkenylated (**3d**, **3i**, and **3q**) and arylated (**5a** and **5j**) products (Scheme 4B).[17,18] Boc activation of **3** and **5** with (Boc)₂O in THF at 80 °C for 24 h gave the resulting Boc products **6** in good to excellent isolated yields. Next, these Boc-protected picolinamides were treated with Ni(cod)₂ (10 mol %) and ethanol (2.0 equiv) in toluene at 80 °C for 16 h, which delivered the corresponding Boc protected amines **7** in excellent isolated yields. In the case of alkenylated substrates derived from dimethyl bromomaleate, methanol (5.0 equiv) is used instead of ethanol to avoid the transesterification in the resulting reaction products.

Study of the Reaction Mechanism. To gain insight into the reaction mechanism, the kinetic isotope effect (KIE) was determined. A competitive experiment with equimolar amounts of *N*-picolinoylcyclohexanamine (**2a**) and **2a-D₁₁** in a reaction with dimethyl 2-bromomaleate (**1d**) gave a KIE value of 4.55, which suggests that the C(sp³)−H bond cleavage is the rate-determining step in this reaction (Scheme 5A and Supporting Information Section S9). Furthermore, kinetic

Figure 2. Use of VTNA to determine the reaction order in $Pd(OAc)_2$, amide **2a**, and bromoalkene **1a**. The profiles obtained under standard conditions are represented by gray triangles. Left column: concentration of product **3d** as a function of time using different initial concentrations of (A) $Pd(OAc)_2$, (B) amide **2a**, and (C) bromoalkene **1d**. Right column: concentration profiles of **3d** after time scale normalization for a 0.25 order in (A) $Pd(OAc)_2$, for a −1 order in (B) amide **2a**, and for a zero order in (C) bromoalkene **1d**. Reaction conditions: (a) **2a** (0.4 mmol), bromoalkene **1d** (0.8 mmol), $Pd(OAc)_2$ (0.02−0.06 mmol), KOPiv (0.08 mmol), K_2CO_3 (0.4 mmol), DCE (3 mL), 120 °C; (b) **2a** (0.2−0.6 mmol), bromoalkene **1d** (0.8 mmol), $Pd(OAc)_2$ (0.04 mmol), KOPiv (0.08 mmol), K_2CO_3 (0.4 mmol), DCE (3 mL), 120 °C; (c) **2a** (0.4 mmol), bromoalkene **1d** (0.6−1.0 mmol), $Pd(OAc)_2$ (0.04 mmol), KOPiv (0.08 mmol), K_2CO_3 (0.4 mmol), DCE (3 mL), 120 °C. Each data point corresponds to a discrete reaction.

analysis of the same reaction using variable time normalization analysis (VTNA)[14e,19] revealed a 0.25 order in $Pd(OAc)_2$, a −1

order in amide **2a**, and a zero-order in bromoalkene **1d** (Figure 2 and Supporting Information Section S10). To rationalize the
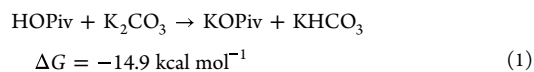
Scheme 6. Computed Reaction Mechanism for the γ-C(sp³)−H Alkenylation of *N*-Picolinoylcyclohexanamine (2a) with (*E*)-β-bromostyrene (1a) as the Model Reaction Studied by DFT
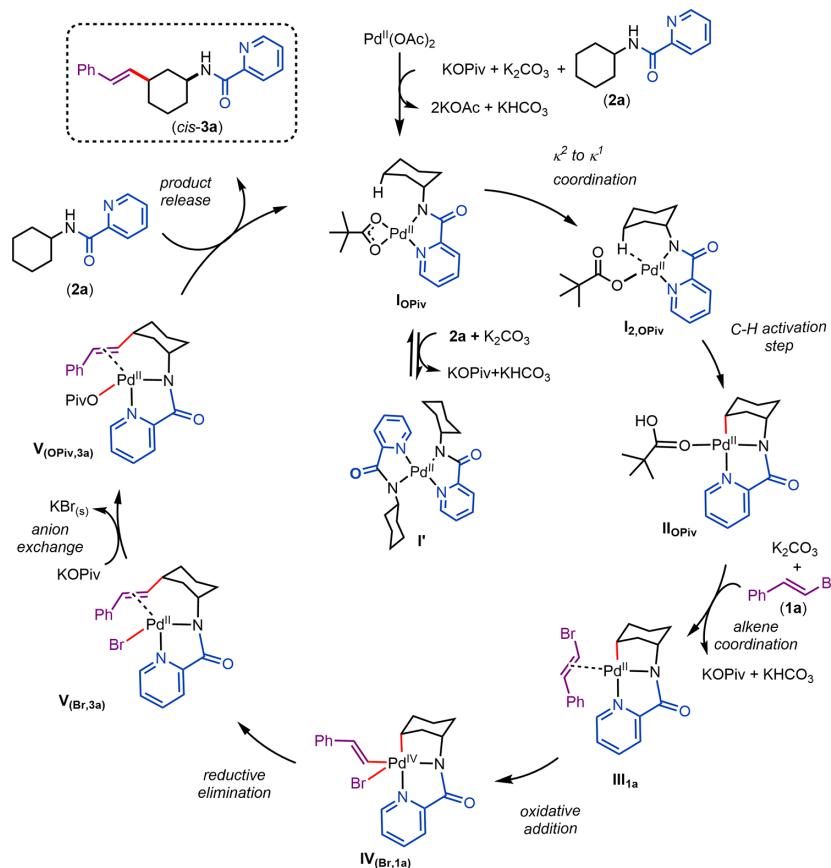
KIE and kinetic results, the reaction mechanism of the Pd-catalyzed γ-C(sp³)−H alkenylation of cyclohexanamines was also investigated computationally through density functional theory (DFT, M06-D3/def2-SVP//def2-TZVP, SMD)[20] calculations using (*E*)-β-bromostyrene (**1a**) and *N*-picolinoylcyclohexanamine (**2a**) as model reactants.

Catalytic Cycle. The reaction mechanism of the entire catalytic cycle and the corresponding Gibbs free energy profile diagram are shown in Scheme 6 and Figure 3, respectively. A possible Pd(0)/Pd(II) pathway was studied but disregarded due to high energy barriers (Supporting Information Scheme S8). In the first step of the reaction mechanism, the catalyst precursor Pd(OAc)₂ is transformed into the catalytically active Pd(II) species **I$_{OPiv}$** by reaction with the substrate *N*-picolinoylcyclohexanamine (**2a**), KOPiv and K₂CO₃, which are present in larger concentrations than the released KOAc. This step is a highly exergonic process with $\Delta G = -31.0$ kcal mol⁻¹, suggesting a strong interaction of Pd(II) with reactant **2a**. The coordination and deprotonation of a second substrate molecule yielding **I′** and byproducts KOPiv and KHCO₃ is also exergonic, but in a lower extent ($\Delta G = -8.6$ kcal mol⁻¹). This species **I′** is in equilibrium with the catalytically active **I$_{OPiv}$** complex, which explains the order −1 in substrate obtained experimentally. It is important to notice that these reactions (formation of **I$_{OPiv}$** and **I′** from Pd^{II}(OAc)₂), and

others described later, are highly driven by the deprotonation of the HOPiv byproduct by K₂CO₃ as shown in eq 1, which will be highly influenced by the solubility of the involved salts. The absence of this deprotonation reaction would make the formation of **I′** from **I$_{OPiv}$** endergonic by 6.3 kcal mol⁻¹.

$$\text{HOPiv} + \text{K}_2\text{CO}_3 \rightarrow \text{KOPiv} + \text{KHCO}_3$$

$$\Delta G = -14.9 \text{ kcal mol}^{-1} \qquad (1)$$

Following the formation of **I$_{OPiv}$**, the C(sp³)−H bond of the coordinated substrate is broken via a concerted metalation deprotonation (CMD) pathway, consistent with previous mechanistic studies providing **II$_{OPiv}$**.[21] In this step, the proton is transferred to the coordinated pivalate, via a six-membered ring transition state **TSI$_{OPiv}$**, which has an energy of 25.1 kcal mol⁻¹ above **I$_{OPiv}$**, and 33.7 kcal mol⁻¹ above **I′**. The latter energy barrier is *ca* 1 kcal mol⁻¹ higher than expected for the experimental conditions, which is reasonable considering the errors associated with DFT and omitting solubility issues. The transformation goes via a Pd(II) C−H agostic intermediate **I$_{2,OPiv}$**, allowed by a change in the pivalate coordination from κ² to κ¹. As a consequence of the agostic interaction, the C(sp³)−H bond distance increases from 1.10 (in **I$_{OPiv}$**) to 1.14 Å (in **I$_{2,OPiv}$**), facilitating subsequent C−H bond cleavage. Next, the substitution of the protonated pivalic acid (HOPiv) in **II$_{OPiv}$** by

Figure 3. Energy diagram for the γ-C(sp^3)−H alkenylation of *N*-picolinoylcyclohexanamine (**2a**) with (*E*)-β-bromostyrene (**1a**) as a model reaction studied by DFT.
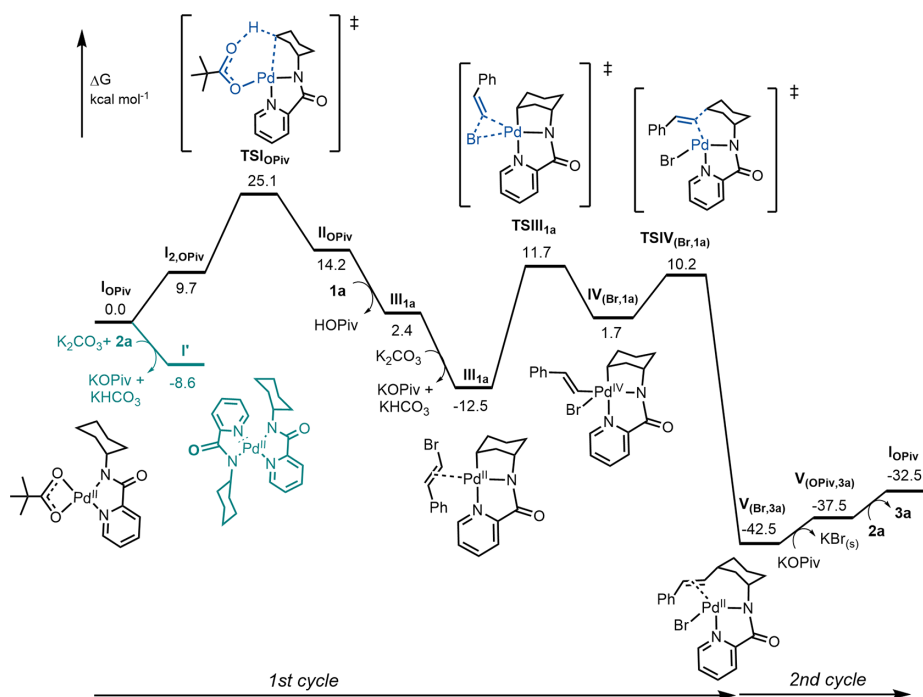
(*E*)-β-bromostyrene (**1a**) and HOPiv deprotonation by K$_2$CO$_3$ is highly exergonic ($\Delta G = -26.7$ kcal mol^{-1}, see also eq 1) yielding η^2-alkene coordinated intermediate **III$_{1a}$**. This reaction makes the overall C−H bond activation an irreversible process, in line with the KIE observed. In a subsequent oxidative addition, the palladium center is oxidized from Pd(II) to Pd(IV) with an activation barrier of 24.2 kcal mol^{-1}, yielding **IV$_{(Br,1a)}$**. Generally, Pd(IV) intermediates are highly unstable compared to Pd(II). However, the strong σ donation of the amide ligand to the palladium center stabilizes the Pd(IV) species.[22] This effect is consistent with the large stabilization energy (SE = 117.5 kcal mol^{-1}) obtained for this interaction as determined by natural bond orbital (NBO) analysis.[23] For comparison, the SE for the σ donation of pyridine to Pd(IV) was found to be 38.1 kcal mol^{-1} (Supporting Information Figure S3). The insertion of bromoalkene **1a** into the Pd−C(sp^3) bond[24] was also investigated as an alternative pathway to the oxidative addition. However, the transition state associated with this pathway (**TSIII$_{Ins}$**) is 10.4 kcal mol^{-1} higher in energy than **TSIII$_{1a}$** (Supporting Information Figure S5B) ruling this possibility out. In a subsequent reaction step, the C−C bond formation takes place via reductive elimination yielding **V$_{(Br,3a)}$**, in which the oxidation state of palladium is reduced to +2. This step is expected to be fast (activation barrier of 8.5 kcal mol^{-1}), and highly exergonic ($\Delta G = -44.2$ kcal mol^{-1}). The high stability of **V$_{(Br,3a)}$** turns this intermediate into the resting state of the catalytic cycle. As shown in Figure 3, going back to **I$_{OPiv}$** by product **3a** release and formation of KBr costs 10.0 kcal mol^{-1}, which results in an overall energy span[25] of 35.1 kcal mol^{-1}, which is too high to be overcome at 120 °C. However, we found KBr is insoluble in DCE (Scheme 5C, Supporting

Information, Section 7). This drives the reaction toward **V$_{(OPiv,3a)}$**, hereby decreasing the energetic span to 30.1 kcal mol^{-1}, which is reasonable under the experimental conditions. These results suggest that both the solvent and the KOPiv additive play a crucial role in this reaction: the solvent by removing the bromide anions by precipitation of KBr and the pivalate by destabilizing the Pd resting state (**V$_{Br,3a}$** to **V$_{OPiv,3a}$**), hereby decreasing the overall energy barrier for the C−H bond cleavage. This rationalizes why alkenylation reactions are particularly challenging to develop and alkenyl halides have rarely been reported as reactants and required silver halide scavengers. While KBr is not soluble in DCE, *t*-amyl alcohol, and 1,4-dioxane (Scheme 5C, Supporting Information Section S7) therefore potentially suitable solvents for the crucial Br exchange in **V$_{(Br,3)}$** by OPiv, DCE proved to be a more general solvent (Scheme 2). Likely, the lack of specific interactions (no Lewis basicity and hydrogen bonding) and high solvating ability of DCE are responsible.

Effect of Anion X on the C(sp^3)−H Bond Activation Step. The proton transfer in the CMD mechanism of the C(sp^3)−H activation can involve different anions than pivalate (OPiv) present in the KOPiv additive, i.e., acetate (OAc), bicarbonate (HCO$_3$), and bromide (Br) also present in the reaction mixture. Acetate was considered as it appears in the Pd(OAc)$_2$ precatalyst added. Bicarbonate is formed in the reaction, considering that K$_2$CO$_3$ is the stoichiometric base used. Bromide is the leaving group of electrophile **1a**. Interestingly, also bromide can induce the C(sp^3)−H activation,[2ff,26] forming HBr. In Figure 4, an overview of the energy diagram of this step is given. In agreement with the literature,[26] the energetic span **V$_{(X,3a)}$** → **TSI$_X$** is highest for X = Br with 38.8 kcal mol^{-1} so this pathway will certainly not play a role here.
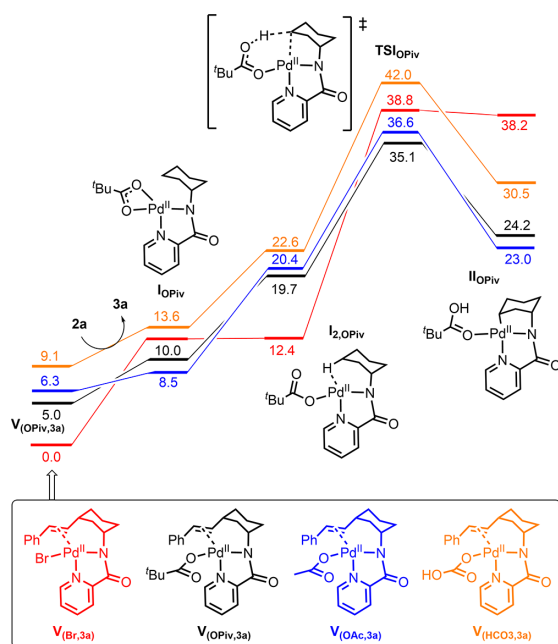
Figure 4. Effect of anion for Pd(II) in the Gibbs free energy profile for the C(sp^3)−H activation in *N*-picolinoylcyclohexanamine (**2a**). Gibbs free energies in kcal mol^{-1}.

However, with X = HCO$_3$ the energetic span decreases to 32.9 kcal mol^{-1} and further decreases to around 30 kcal mol^{-1} for X = OPiv, OAc. These results indicate that carboxylates are required to destabilize the bromide complex **V$_{(Br,3a)}$** besides their role in the C(sp^3)−H activation mechanism. In accordance with this, when the KOPiv additive was omitted in the *γ*-C(sp^3)−H alkenylation of *N*-picolinoylcyclohexanamine (**2a**) with (*E*)-*β*-bromostyrene (**1a**), the yield dropped from 89 to 45% (Table 1, entries 2 and 3). Moreover, addition of 20 mol % Bu$_4$NBr completely blocked catalysis as pivalate coordination to Pd(II) is blocked (Scheme 5D).

Effect of the Electrophile RX on the Oxidative Addition and Catalyst Resting State. The energy profile depicted in Figure 3 shows that for the reactants (*E*)-*β*-bromostyrene (**1a**) and *N*-picolinoylcyclohexanamine (**2a**), the highest energy barrier of the catalytic cycle corresponds to the C(sp^3)−H bond activation step. Therefore, the oxidative addition of (*E*)-*β*-bromostyrene to Pd(II), which has an energy barrier of 24.2 kcal mol^{-1}, is not a rate limiting factor in accordance with the experimental zero-order of the reaction in **1a**. As expected, the energy barrier for the oxidative addition with (*E*)-*β*-iodostyrene (**1aa**) is significantly lower (18.6 kcal mol^{-1}) (Figure 5). The fact that the oxidative addition is not rate limiting suggests that all RX compounds react equally fast (assuming equal insolubility of KI and KBr affecting the **V$_{(X,3a)}$** to **V$_{(OPiv,3a)}$** equilibrium in DCE) as the energetic span determined by the resting state **V$_{(OPiv,3a)}$** and the C(sp^3)−H bond activation step is independent of the halide ion (Supporting Information Figure S5A). In accordance with this, the reaction performed with (*E*)-*β*-iodostyrene (**1aa**) gave a similar result as with (*E*)-*β*-bromostyrene (**1a**) (Table 1, entries 2 and 5).

The oxidative addition energy barrier was also calculated for other bromoalkenes (Figure 5). (2,2-Dibromoethenyl)benzene (**8a**)[9] features a lower barrier than **1a** in accordance with the additional geminal bromine atom. With (*E*)-(2-bromovinyl)-cyclohexane (**1c**) the energy increases versus **1a** based on the removal of the activating phenyl. Finally, bromobenzene (**4a**) shows the lowest energy value (16.2 kcal mol^{-1}) which is also still lower than the C(sp^3)−H bond activation barrier, indicating that the oxidative addition is not a limiting factor.

Stability of the Resting State V$_{(OPiv,3)}$ Featuring Different 3-Alkenyl-N-picolinoylcyclohexanamine Products (3). Besides anion X, the electrophile has an influence on the stability of the catalyst's resting state. Therefore, the effect of the double bond in the C3-substituent of the coordinated reaction product **3** in **V$_{(Br,3)}$** has been investigated in more detail. Replacing the ethylene Ph substituent in **V$_{(Br,3a)}$** by Cy **V$_{(Br,3c)}$** decreases the energy of the resting state by 3.9 kcal/mol^{-1}, while changing Ph by ^{t}Bu does not have an impact on the energy of the resting state **V$_{(Br,3b)}$** (Scheme 7). With ethenyl conjugated to phenyl (**V$_{(Br,3a)}$**), the electron density at the double bond is lower than that with the alkyl substituent Cy (**V$_{(Br,3c)}$**). This difference results in a weaker η^2 interaction between Pd(II) and the double bond. Consequently, the resting state **V$_{(Br,3c)}$** is stabilized compared to **V$_{(Br,3a)}$** and the energetic span versus **TSI$_{OPiv}$** increases. A ^{t}Bu is also an electron donating group but its sterics significantly weakens the η^2 interaction in **V$_{(Br,3b)}$**. This counterbalancing effect brings it to the same energy level of a Ph substituent (**V$_{(Br,3b)}$** versus **V$_{(Br,3a)}$** is 0.9 kcal mol^{-1}). Consistently, the trend in stability of **V$_{(Br,3)}$** with Cy, Ph and ^{t}Bu substituents correlates well with the π-donation and back-donation interactions between the ethenyl C=C bond and the Pd d$_{x^2-y^2}$ orbital (Supporting Information Table S11). These DFT results are in accordance with the experimental results, where for **3c** (R = Cy), the starting material **2a** was recovered in 62%, while for **3a** (R = Ph) and **3b** (R = ^{t}Bu), high yields and high conversions of substrate **2a** were observed in 24 h (Scheme 7). When 50 mol % of reaction product **3a** was added to the model reaction of **1a** and **2a**, the conversion to and yield of **3a** in 3 h dropped significantly (Scheme 5B). A higher concentration of **3a** inhibits catalysis by hampering the decomplexation of **3a** from **V$_{(Br,3a)}$** via **V$_{(OPiv,3a)}$**. This is required to allow subsequent complexation of substrate **2a**, hereby providing starting complex **I$_{OPiv}$** for another catalytic cycle in accordance to the computed mechanism (Scheme 6). A similar observation was made when adding 50 mol % of **3d** to the reaction of **1d** and **2a** (Scheme 5B). These inhibitions rationalize the experimental order of 0.25 for the reaction in Pd(OAc)$_2$.

Catalyst Resting State for C(sp^3)−H Arylation versus Alkenylation. With 3-phenylated product **5a**, the weaker coordination of the aromatic ring compared with the η^2 double bond in 3-alkenylated products **3** lifts the energy of **V$_{(Br,5a)}$** versus **V$_{(Br,3a)}$** by 16.3 kcal mol^{-1} (Figure 5). This result implies that **V$_{(Br,5a)}$** is not the resting state in the arylation reaction but rather **I′**, with a slightly decreased energetic span with rate limiting **TSI$_{OPiv}$** (33.9 for **5a** versus 35.2 for **3a**) kcal mol^{-1} (Figure 5). As observed for **3a**, the bromide complex **V$_{(Br,5a)}$** is more stable (2.3 kcal mol^{-1}) than the pivalate **V$_{(OPiv,5a)}$**. The similar overall energy span for arylation justifies why the reaction conditions developed for alkenylation could be applied to arylation without further modification (Scheme 3). However, alkenylation is a much more difficult reaction. A higher conversion of substrate **2a** means a higher concen-
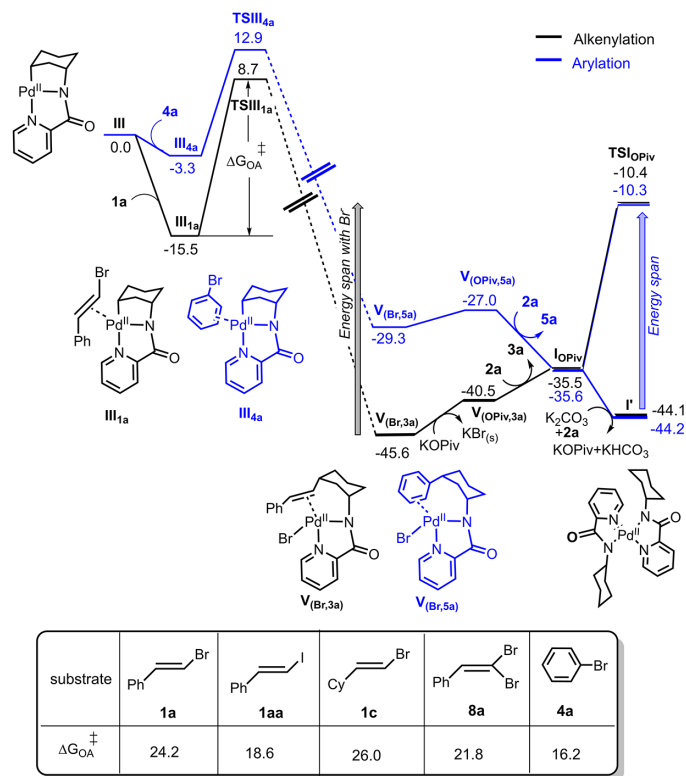
Figure 5. Energy diagram for the alkenylation reaction with reactant **1a** (black) and the arylation reaction with reactant **4a** (blue). Barriers for the oxidative addition step, $\Delta G^{\ddagger}$, for different electrophiles and halide leaving groups are also shown. Gibbs free energies in kcal mol^{-1}.

Scheme 7. Effect of C3-Substituent in Product 3/5 on the Stability of $V_{(Br,3/5)}$ and $V_{(OPiv,3/5)}$ (Gibbs Free Energies in kcal mol^{-1})
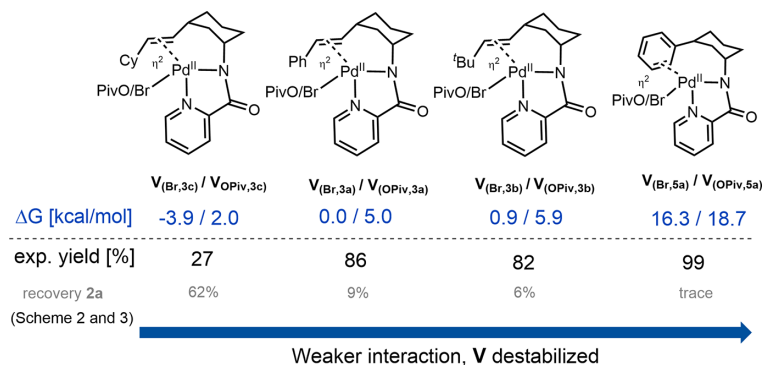
tration of reaction product **3a**, making its release of the resting state $V_{(Br,3a)}$ progressively more difficult. On the contrary, in arylation a higher conversion of substrate **2a** means a lower concentration of **2a**, promoting I_{OPiv} versus resting state I', hereby making the reaction easier.

■ **CONCLUSIONS**

In summary, we have developed an efficient Pd-catalyzed reaction for the γ-C(sp^3)−H alkenylation of cyclohexanamines, employing a picolinoylamine bidentate directing group with

readily available alkenyl bromide coupling partners under silver-free conditions. Even very challenging heterocyclic substrates (piperidinamine and tetrahydro-2H-pyranamine) were compatible. The method exhibits a broad alkenyl reactant scope with excellent functional group tolerance and regio- and stereospecificity. The underlying reaction mechanism has been studied experimentally by using kinetics and a KIE, and theoretically by density functional theory. The calculations show that the reaction follows a Pd(II)/Pd(IV) pathway in which the transition state of the C(sp^3)−H activation occurs

through a CMD mechanism. Interestingly, the oxidative addition to form a Pd(IV) species is not rate-determining. The overall energy barrier is determined by the $C(sp^3)-H$ activation and the reaction product formed in the catalytic cycle, which strongly coordinates to the palladium center. Addition of a catalytic amount of KOPiv is beneficial for the conversion of substrate, resulting in substantially higher product yield. The additive is involved in the C−H activation mechanism, i.e., CMD, as well as in the anion exchange in the catalyst resting state $V_{(Br,3)}$ providing a more reactive pivalate complex $V_{(OPiv,3)}$. This endergonic step only proceeds efficiently by precipitation of KBr and hence the importance of the reaction solvent. Precipitation makes the use of superstoichiometric metal reagents redundant. Insights into the electronic structure of $V_{(Br,3)}$ revealed that alkenyl groups featuring electron-withdrawing substituents leads to a weaker η^2 interaction between π of alkene of the reaction product **3** and the Pd(II). Consequently, the resting state $V_{(Br,3)}$ is destabilized and the overall barrier decreases allowing easier decomplexation of the reaction product **3** via $V_{(OPiv,3)}$. Electron donating substituents therefore provide poorer conversion. This trend matches the experimental performance of the different alkene substituents. **I′**, formed by coordination of a second substrate molecule to I_{OPiv} and deprotonation, is higher in energy than $V_{(Br,3)}$. However, it can become the resting state of the catalytic cycle with weaker Pd(II) coordinating electrophiles, such as the arene of product **5**. The slightly lower overall energy span (TSI_{OPiv} - **I′** versus TSI_{OPiv} - $V_{(Br,3)}$) rationalizes why our developed method is also effective for the γ-$C(sp^3)-H$ arylation involving (hetero)aryl bromides. Here $V_{(Br,5)}$ does not act as a resting state and both $V_{(Br,5)}$ and $V_{(OPiv,5)}$ are substantially higher in energy based on a weaker coordination of the arene of product **5** to Pd(II), resulting in another catalyst resting state (**I′**). Nevertheless, γ-$C(sp^3)-H$ arylation is a much easier reaction than γ-$C(sp^3)-H$ alkenylation when considering concentrations. After all, a higher conversion of substrate **2** favors I_{OPiv} versus **I′**, while at this higher conversion, there is more reaction product **3/5** present, favoring $V_{(Br,3/5)}$ versus I_{OPiv}. The difference in the resting state, i.e., **I′** for arylation versus $V_{(Br,3)}$ for alkenylation, therefore directly determines performance as the former complex is not affected by product coordination while the latter is.

■ ASSOCIATED CONTENT

ⓢ Supporting Information

The Supporting Information is available free of charge at https://pubs.acs.org/doi/10.1021/acscatal.3c04152.

> Detailed optimization data, experimental procedures, characterization data, and copies of NMR spectra of all compounds, DFT computations, and crystallographic data (PDF)

Accession Codes

CCDC 2232137 (for **3c**), 2232138 (for **3f**), 2232139 (for **5a**), 2232140 (for **7d**) contain the supplementary crystallographic data for this paper. These data are provided free of charge by contacting the Cambridge Crystallographic Data Centre.

■ AUTHOR INFORMATION

Corresponding Authors

Ainara Nova − *Department of Chemistry, Hylleraas Centre for Quantum Molecular Sciences and Centre for Materials Science and Nanotechnology, University of Oslo, N-0315 Oslo, Norway*; Email: a.n.flores@kjemi.uio.no

Bert U. W. Maes − *Division of Organic Synthesis, Department of Chemistry, University of Antwerp, B-2020 Antwerp, Belgium*; ◉ orcid.org/0000-0003-0431-7606; Email: bert.maes@uantwerpen.be

Authors

Karthik Gadde − *Division of Organic Synthesis, Department of Chemistry, University of Antwerp, B-2020 Antwerp, Belgium*; ◉ orcid.org/0000-0001-6624-4129

Narendraprasad Reddy Bheemireddy − *Division of Organic Synthesis, Department of Chemistry, University of Antwerp, B-2020 Antwerp, Belgium*

Juliane Heitkämper − *Department of Chemistry, Hylleraas Centre for Quantum Molecular Sciences and Centre for Materials Science and Nanotechnology, University of Oslo, N-0315 Oslo, Norway; Institute for Theoretical Chemistry, University of Stuttgart, D-70569 Stuttgart, Germany*

Complete contact information is available at:
https://pubs.acs.org/10.1021/acscatal.3c04152

Author Contributions

£K.G., N.R.B., and J.H. contributed equally to this work.

Notes

The authors declare no competing financial interest.

■ ACKNOWLEDGMENTS

■ REFERENCES

(1) For selected reviews, see: (a) Sambiagio, C.; Schönbauer, D.; Blieck, R.; Dao-Huy, T.; Pototschnig, G.; Schaaf, P.; Wiesinger, T.; Zia, M. F.; Wencel-Delord, J.; Besset, T.; Maes, B. U. W.; Schnürch, M. A Comprehensive Overview of Directing Groups Applied in Metal-Catalysed C−H Functionalisation Chemistry. *Chem. Soc. Rev.* **2018**, *47*, 6603−6743. (b) Rej, S.; Ano, Y.; Chatani, N. Bidentate Directing Groups: An Efficient Tool in C−H Bond Functionalization Chemistry for the Expedient Construction of C−C Bonds. *Chem. Rev.* **2020**, *120*, 1788−1887. (c) Liu, B.; Romine, A. M.; Rubel, C. Z.; Engle, K. M.; Shi, B.-F. Transition-Metal-Catalyzed, Coordination-Assisted Functionalization of Nonactivated $C(sp^3)-H$ Bonds. *Chem. Rev.* **2021**, *121*, 14957−15074. (d) Jacob, C.; Maes, B. U. W.; Evano, G. Transient Directing Groups in Metal−Organic Cooperative Catalysis. *Chem.—Eur. J.* **2021**, *27*, 13899−13952. (e) Sen, S.; Das, J.; Maiti, D. Strategies to Transform Remote $C(sp^3)$-H Bonds of Amino Acid Derivatives. *Tetrahedron Chem.* **2022**, *1*, No. 100005. (f) Ali, W.; Prakash, G.; Maiti, D. Recent Development in Transition Metal-Catalysed C−H Olefination. *Chem. Sci.* **2021**, *12*, 2735−2759.

(g) Bhattacharya, T.; Dutta, S.; Maiti, D. Deciphering the Role of Silver in Palladium-Catalyzed C−H Functionalizations. *ACS Catal.* **2021**, *11*, 9702−9714. (h) Mondal, A.; van Gemmeren, M. Silver-Free C−H Activation: Strategic Approaches towards Realizing the Full Potential of C−H Activation in Sustainable Organic Synthesis. *Angew. Chem., Int. Ed.* **2022**, *61*, No. e202210825.

(2) Remote-C(sp³)−H alkenylation of alkanamines with alkenyl iodides: (a) He, G.; Chen, G. A Practical Strategy for the Structural Diversification of Aliphatic Scaffolds through the Palladium-Catalyzed Picolinamide-Directed Remote Functionalization of Unactivated C(sp³)−H Bonds. *Angew. Chem., Int. Ed.* **2011**, *50*, 5192−5196. (b) Seki, A.; Takahashi, Y. Pd-Catalyzed Methylene γ-C(sp³)−H Alkenylation of *N*-picolinoylcycloalkylamines with Alkenyl Iodides Promoted by 2-*tert*-Butyl-1,4-benzoquinone. *Tetrahedron Lett.* **2021**, *74*, No. 153130.

(3) Remote-C(sp³)−H alkenylation of carbonyl compounds (carboxylic acids and ketones) with alkenyl iodides: (a) Gutekunst, W. R.; Gianatassio, R.; Baran, P. S. Sequential Csp³−H Arylation and Olefination: Total Synthesis of the Proposed Structure of Pipercyclobutanamide A. *Angew. Chem., Int. Ed.* **2012**, *51*, 7507−7510. (b) Gutekunst, W. R.; Baran, P. S. Applications of C−H Functionalization Logic to Cyclobutane Synthesis. *J. Org. Chem.* **2014**, *79*, 2430−2452. (c) Wang, B.; Lu, C.; Zhang, S.-Y.; He, G.; Nack, W. A.; Chen, G. Palladium-Catalyzed Stereoretentive Olefination of Unactivated C(sp³)−H Bonds with Vinyl Iodides at Room Temperature: Synthesis of β-Vinyl α-Amino Acids. *Org. Lett.* **2014**, *16*, 6260−6263. (d) Shan, G.; Huang, G.; Rao, Y. Palladium-Catalyzed Unactivated β-Methylene C(sp³)−H Bond Alkenylation of Aliphatic Amides and its Application in a Sequential C(sp³)−H/C(sp²)−H Bond Alkenylation. *Org. Biomol. Chem.* **2015**, *13*, 697−701. (e) Zhang, Y.-F.; Zhao, H.-W.; Wang, H.; Wei, J.-B.; Shi, Z.-J. Readily Removable Directing Group Assisted Chemo- and Regioselective C(sp³)−H Activation by Palladium Catalysis. *Angew. Chem., Int. Ed.* **2015**, *54*, 13686−13690. (f) Chapman, L. M.; Beck, J. C.; Wu, L.; Reisman, S. E. Enantioselective Total Synthesis of (+)-Psiguadial B. *J. Am. Chem. Soc.* **2016**, *138*, 9803−9806. (g) Thrimurtulu, N.; Khan, S.; Maity, S.; Volla, C. M. R.; Maiti, D. Palladium Catalyzed Direct Aliphatic γC(sp³)−H Alkenylation with Alkenes and Alkenyl Iodides. *Chem. Commun.* **2017**, *53*, 12457−12460. (h) Wu, Q.-F.; Shen, P.-X.; He, J.; Wang, X.-B.; Zhang, F.; Shao, Q.; Zhu, R.-Y.; Mapelli, C.; Qiao, J. X.; Poss, M. A.; Yu, J.-Q. Formation of α-Chiral Centers by Asymmetric β-C(sp³)−H Arylation, Alkenylation, and Alkynylation. *Science* **2017**, *355*, 499−503. (i) Zhu, R.-Y.; Li, Z.-Q.; Park, H. S.; Senanayake, C. H.; Yu, J.-Q. Ligand-Enabled γ-C(sp³)−H Activation of Ketones. *J. Am. Chem. Soc.* **2018**, *140*, 3564−3568. (j) Wang, Q.-F.; Wang, X.-B.; Shen, P.-X.; Yu, J.-Q. Enantioselective C−H Arylation and Vinylation of Cyclobutyl Carboxylic Amides. *ACS Catal.* **2018**, *8*, 2577−2581. (k) Minami, T.; Fukuda, K.; Hoshiya, N.; Fukuda, H.; Watanabe, M.; Shuto, S. Synthesis of Enantiomerically Pure 1,2,3-Trisubstituted Cyclopropane Nucleosides Using Pd-Catalyzed Substitution via Directing Group-Mediated C(sp³)−H Activation as a Key Step. *Org. Lett.* **2019**, *21*, 656−659. (l) Liu, Y.; Wang, Y.; Dai, W.; Huang, W.; Li, Y.; Liu, L. Palladium-Catalysed C(sp³)−H Glycosylation for the Synthesis of C-Alkyl Glycoamino Acids. *Angew. Chem., Int. Ed.* **2020**, *59*, 3491−3494.

(4) Activated alkenes have been used in oxidative alkenylation: (a) Park, H.; Li, Y.; Yu, J.-Q. Utilizing Carbonyl Coordination of Native Amides for Palladium-Catalyzed C(sp³)−H Olefination. *Angew. Chem., Int. Ed.* **2019**, *58*, 11424−11428. (b) Zhuang, Z.; Yu, J.-Q. Pd(II)-Catalyzed Enantioselective γ-C(sp³)−H Functionalizations of Free Cyclopropylmethylamines. *J. Am. Chem. Soc.* **2020**, *142*, 12015−12019. (c) Bhattacharya, T.; Baroliya, P. K.; Al-Thabaiti, S. A.; Maiti, D. Simplifying the Synthesis of Nonproteinogenic Amino Acids via Palladium-Catalyzed δ-Methyl C−H Olefination of Aliphatic Amines and Amino Acids. *JACS Au* **2023**, *3*, 1975−1983. (d) Das, J.; Pal, T.; Ali, W.; Sahoo, S. R.; Maiti, D. Pd-Catalyzed Dual-γ-1,1-C(sp³)−H Activation of Free Aliphatic Acids with Allyl−O Moieties. *ACS Catal.* **2022**, *12*, 11169−11176. (e) see reference 3g.

(5) Ricci, A.; Bernardi, L. *Methodologies in Amine Synthesis: Challenges and Applications*. Wiley: Weinheim, 2021.

(6) For selected reviews, see: (a) He, C.; Whitehurst, W. G.; Gaunt, M. J. Palladium-Catalyzed C(sp³)−H Bond Functionalization of Aliphatic Amines. *Chem.* **2019**, *5*, 1031−1058. (b) Trowbridge, A.; Walton, S. M.; Gaunt, M. J. New Strategies for the Transition-Metal Catalyzed Synthesis of Aliphatic Amines. *Chem. Rev.* **2020**, *120*, 2613−2692.

(7) Zaitsev, V. G.; Shabashov, D.; Daugulis, O. Highly Regioselective Arylation of sp³ C−H Bonds Catalyzed by Palladium Acetate. *J. Am. Chem. Soc.* **2005**, *127*, 13154−13155.

(8) Hartwig, J. F.; Larsen, M. A. Undirected, Homogeneous C−H Bond Functionalization: Challenges and Opportunities. *ACS Cent. Sci.* **2016**, *2*, 281−292.

(9) Biswas, S.; Van Steijvoort, B. F.; Waeterschoot, M.; Bheemireddy, N. R.; Evano, G.; Maes, B. U. W. Expedient Synthesis of Bridged Bicyclic Nitrogen Scaffolds via Orthogonal Tandem Catalysis. *Angew. Chem., Int. Ed.* **2021**, *60*, 21988−21996.

(10) (a) Giri, R.; Lan, Y.; Liu, P.; Houk, K. N.; Yu, J.-Q. Understanding Reactivity and Stereoselectivity in Palladium-Catalyzed Diastereoselective sp³ C−H Bond Activation: Intermediate Characterization and Computational Studies. *J. Am. Chem. Soc.* **2012**, *134*, 14118−14126. (b) Yang, Y.-F.; Hong, X.; Yu, J.-Q.; Houk, K. N. Experimental−Computational Synergy for Selective Pd(II)-Catalyzed C−H Activation of Aryl and Alkyl Groups. *Acc. Chem. Res.* **2017**, *50*, 2853−2860. (c) Rodrigalvarez, J.; Reeve, L. A.; Miró, J.; Gaunt, M. J. Pd(II)-Catalyzed Enantioselective C(sp³)−H Arylation of Cyclopropanes and Cyclobutanes Guided by Tertiary Alkylamines. *J. Am. Chem. Soc.* **2022**, *144*, 3939−3948. (d) Hao, W.; Bay, K. L.; Harris, C. F.; King, D. S.; Guzei, I. A.; Aristov, M. M.; Zhuang, Z.; Plata, R. E.; Hill, D. E.; Houk, K. N.; Berry, J. F.; Yu, J.-Q.; Blackmond, D. G. Probing Catalyst Speciation in Pd-MPAAM-Catalyzed Enantioselective C(sp³)−H Arylation: Catalyst Improvement via Destabilization of Off-Cycle Species. *ACS Catal.* **2021**, *11*, 11040−11048. (e) Melot, R.; Zuccarello, M.; Cavalli, D.; Niggli, N.; Devereux, M.; Bürgi, T.; Baudoin, O. Palladium(0)-Catalyzed Enantioselective Intramolecular Arylation of Enantiotopic Secondary C−H Bonds. *Angew. Chem., Int. Ed.* **2021**, *60*, 7245−7250. (f) Zhang, H.; Wang, H.-Y.; Luo, Y.; Chen, C.; Cao, Y.; Chen, P.; Guo, Y.-L.; Lan, Y.; Liu, G. Regioselective Palladium-Catalyzed C-H Bond Trifluoroethylation of Indoles: Exploration and Mechanistic Insight. *ACS Catal.* **2018**, *8*, 2173−2180. (g) Romero, E. A.; Chen, G.; Gembicky, M.; Jazzar, R.; Yu, J.-Q.; Bertrand, G. Understanding the Activity and Enantioselectivity of Acetyl-Protected Aminoethyl Quinoline Ligands in Palladium-Catalyzed β-C(sp³)−H Bond Arylation Reactions. *J. Am. Chem. Soc.* **2019**, *141*, 16726−16733. (h) Ghouilem, J.; Tran, C.; Grimblat, N.; Retailleau, P.; Alami, M.; Gandon, V.; Messaoudi, S. Diastereoselective Pd-Catalyzed Anomeric C(sp³)−H Activation: Synthesis of α-(Hetero)aryl C-Glycosides. *ACS Catal.* **2021**, *11*, 1818−1826.

(11) Smalley, A. P.; Gaunt, M. J. Mechanistic Insights into the Palladium-Catalyzed Aziridination of Aliphatic Amines by C−H Activation. *J. Am. Chem. Soc.* **2015**, *137*, 10632−10641.

(12) Rodrigalvarez, J.; Nappi, M.; Azuma, H.; Flodén, N. J.; Burns, M. E.; Gaunt, M. J. Catalytic C(sp³)−H Bond Activation in Tertiary Alkylamines. *Nat. Chem.* **2020**, *12*, 76−81.

(13) Lian, B.; Zhang, L.; Chass, G. A.; Fang, D.-C. Pd(OAc)₂-Catalyzed C−H Activation/C−O Cyclization: Mechanism, Role of Oxidant-Probed by Density Functional Theory. *J. Org. Chem.* **2013**, *78*, 8376−8385.

(14) (a) Provencher, P. A.; Hoskin, J. F.; Wong, J. J.; Chen, X.; Yu, J.-Q.; Houk, K. N.; Sorensen, E. J. Pd(II)-Catalyzed Synthesis of Benzocyclobutenes by β-Methylene-Selective C(sp³)−H Arylation with a Transient Directing Group. *J. Am. Chem. Soc.* **2021**, *143*, 20035−20041. (b) Ha, H.; Choi, H. J.; Park, H.; Gwon, Y.; Lee, J.; Kwak, J.; Kim, M.; Jung, B. Pd-Catalyzed Regio- and Stereoselective sp³ C−H Arylation of Primary Aliphatic Amines: Mechanistic Studies and Synthetic Applications. *Eur. J. Org. Chem.* **2021**, *2021*, 1136−1145. (c) Martínez-Mingo, M.; García-Viada, A.; Alonso, I.; Rodríguez, N.; Gómez Arrayás, R.; Carretero, J. C. Overcoming the

Necessity of γ-Substitution in δ-C(sp^3)−H Arylation: Pd-Catalyzed Derivatization of α-Amino Acids. *ACS Catal.* **2021**, *11*, 5310−5317. (d) Yang, Y.-F.; Chen, G.; Hong, X.; Yu, J.-Q.; Houk, K. N. The Origins of Dramatic Differences in Five-Membered vs Six-Membered Chelation of Pd(II) on Efficiency of C(sp^3)−H Bond Activation. *J. Am. Chem. Soc.* **2017**, *139*, 8514−8521. (e) Antermite, D.; White, A. J. P.; Casarrubios, L.; Bull, J. A. On the Mechanism and Selectivity of Palladium-Catalyzed C(sp^3)−H Arylation of Pyrrolidines and Piperidines at Unactivated C4 Positions: Discovery of an Improved Dimethylaminoquinoline Amide Directing Group. *ACS Catal.* **2023**, *13*, 9597−9615.

(15) Bonney, K. J.; Schoenebeck, F. Experiment and Computation: A Combined Approach to Study the Reactivity of Palladium Complexes in Oxidation States 0 to IV. *Chem. Soc. Rev.* **2014**, *43*, 6609−6638.

(16) For reviews and book chapters on C(sp^3)−H functionalization in saturated heterocycles, see: (a) Mitchell, E. A.; Peschiulli, A.; Lefevre, N.; Meerpoel, L.; Maes, B. U. W. Direct α-Functionalization of Saturated Cyclic Amines. *Chem.—Eur. J.* **2012**, *18*, 10092−10142. (b) Liu, G.-Q.; Opatz, T., Recent Advances in the Synthesis of Piperidines: Functionalization of Preexisting Ring Systems. In *Advances in Heterocyclclic Chemistry.*, Scriven, E. F. V.; Ramsden, C. A., Eds.: 2018; Vol. *125*, pp 107−234 DOI: 10.1016/bs.aihch.2017.10.001. (c) Antermite, D.; Bull, J. A. Transition Metal-Catalyzed Directed C(sp^3)−H Functionalization of Saturated Heterocycles. *Synthesis* **2019**, *51*, 3171−3204. (d) Dutta, S.; Li, B.; Rickertsen, D. R. L.; Valles, D. A.; Seidel, D. C−H Bond Functionalization of Amines: A Graphical Overview of Diverse Methods. *SynOpen* **2021**, *05*, 173−228. (e) Piticari, A.-S.; Larionova, N.; Bull, J. A., C−H Functionalization of Saturated Heterocycles Beyond the C2 Position. In *Transition-Metal-Catalyzed C-H Functionalization of Heterocyles*, Punniyamurthy, T.; Kumar, A., Eds.: Wiley, 2023; pp 567−607 DOI: 10.1002/9781119774167.ch13.

(17) (a) Biswas, S.; Bheemireddy, N. R.; Bal, M.; Van Steijvoort, B. F.; Maes, B. U. W. Directed C−H Functionalization Reactions with a Picolinamide Directing Group: Ni-Catalyzed Cleavage and Byproduct Recycling. *J. Org. Chem.* **2019**, *84*, 13112−13123. (b) Van Steijvoort, B. F.; Kaval, N.; Kulago, A. A.; Maes, B. U. W. Remote Functionalization: Palladium-Catalyzed C5(sp^3)-H Arylation of 1-Boc-3-aminopiperidine through the Use of a Bidentate Directing Group. *ACS Catal.* **2016**, *6*, 4486−4490.

(18) For a review, see: Gao, P.; Rahman, M. M.; Zamalloa, A.; Feliciano, J.; Szostak, M. Classes of Amides that Undergo Selective N−C Amide Bond Activation: The Emergence of Ground-State Destabilization. *J. Org. Chem.* **2023**, *88*, 13371−13391.

(19) (a) Burés, J. A Simple Graphical Method to Determine the Order in Catalyst. *Angew. Chem., Int. Ed.* **2016**, *55*, 2028−2031. (b) Burés, J. Variable Time Normalization Analysis: General Graphical Elucidation of Reaction Orders from Concentration Profiles. *Angew. Chem., Int. Ed.* **2016**, *55*, 16084−16087. (c) Nielsen, C. D. T.; Burés, J. Visual kinetic analysis. *Chem. Sci.* **2019**, *10*, 348−353.

(20) Zhao, Y.; Truhlar, D. G. The M06 Suite of Density Functionals for Main Group Thermochemistry, Thermochemical Kinetics, Noncovalent Interactions, Excited States, and Transition Elements: Two New Functionals and Systematic Testing of Four M06-Class Functionals and 12 other Functionals. *Theor. Chem. Acc.* **2008**, *120*, 215−241.

(21) (a) Alharis, R. A.; McMullin, C. L.; Davies, D. L.; Singh, K.; Macgregor, S. A. The Importance of Kinetic and Thermodynamic Control when Assessing Mechanisms of Carboxylate-Assisted C−H Activation. *J. Am. Chem. Soc.* **2019**, *141*, 8896−8906. (b) Altus, K. M.; Love, J. A. The Continuum of Carbon−Hydrogen (C−H) Activation Mechanisms and Terminology. *Commun. Chem.* **2021**, *4*, 173. (c) Balcells, D.; Clot, E.; Eisenstein, O. C−H Bond Activation in Transition Metal Species from a Computational Perspective. *Chem. Rev.* **2010**, *110*, 749−823. (d) Davies, D. L.; Macgregor, S. A.; McMullin, C. L. Computational Studies of Carboxylate-Assisted C−H Activation and Functionalization at Group 8−10 Transition Metal

Centers. *Chem. Rev.* **2017**, *117*, 8649−8709. (e) Ghosh, S.; Shilpa, S.; Athira, C.; Sunoj, R. B. Role of Additives in Transition Metal Catalyzed C−H Bond Activation Reactions: A Computational Perspective. *Top. Catal.* **2022**, *65*, 141−164. (f) Boutadla, Y.; Davies, D. L.; Macgregor, S. A.; Poblador-Bahamonde, A. I. Mechanisms of C−H Bond Activation: Rich Synergy between Computation and Experiment. *Dalton Trans.* **2009**, 5820−5831.

(22) Topczewski, J. J.; Sanford, M. S. Carbon−Hydrogen (C−H) Bond Activation at Pd^{IV}: A Frontier in C−H Functionalization Catalysis. *Chem. Sci.* **2015**, *6*, 70−76.

(23) Reed, A. E.; Curtiss, L. A.; Weinhold, F. Intermolecular Interactions from a Natural Bond Orbital, Donor-Acceptor Viewpoint. *Chem. Rev.* **1988**, *88*, 899−926.

(24) Zaitsev, V. G.; Daugulis, O. Catalytic Coupling of Haloolefins with Anilides. *J. Am. Chem. Soc.* **2005**, *127*, 4156−4157.

(25) Kozuch, S.; Shaik, S. How to Conceptualize Catalytic Cycles? The Energetic Span Model. *Acc. Chem. Res.* **2011**, *44*, 101−110.

(26) García-Cuadrado, D.; de Mendoza, P.; Braga, A. A. C.; Maseras, F.; Echavarren, A. M. Proton-Abstraction Mechanism in the Palladium-Catalyzed Intramolecular Arylation: Substituent Effects. *J. Am. Chem. Soc.* **2007**, *129*, 6880−6886.

3.3 Paper III

Highly Active Cooperative Lewis Acid–Ammonium Salt Catalyst for the Enantioselective Hydroboration of Ketones

M. Titze, J. Heitkämper, T. Junge, J. Kästner, and R. Peters
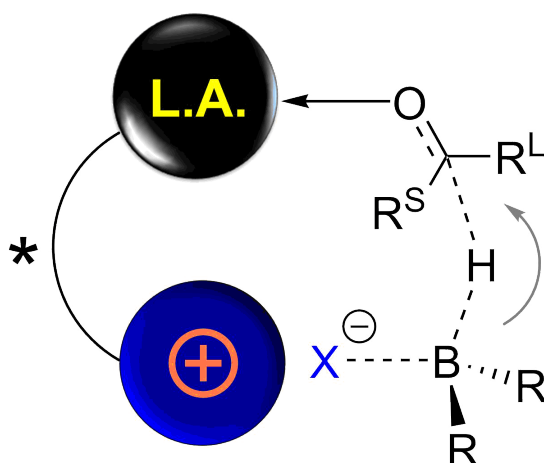
Own contributions:

- all quantum chemical calculations (minor part of the manuscript)
- preparation of the computational part of the manuscript (minor part) with J. Kästner

Check for updates

Cooperative Catalysis

Highly Active Cooperative Lewis Acid—Ammonium Salt Catalyst for the Enantioselective Hydroboration of Ketones

Marvin Titze, Juliane Heitkämper, Thorsten Junge, Johannes Kästner* and René Peters*

Abstract: *Enantiopure secondary alcohols are fundamental high-value synthetic building blocks. One of the most attractive ways to get access to this compound class is the catalytic hydroboration. We describe a new concept for this reaction type that allowed for exceptional catalytic turnover numbers (up to 15 400), which were increased by around 1.5–3 orders of magnitude compared to the most active catalysts previously reported. In our concept an aprotic ammonium halide moiety cooperates with an oxophilic Lewis acid within the same catalyst molecule. Control experiments reveal that both catalytic centers are essential for the observed activity. Kinetic, spectroscopic and computational studies show that the hydride transfer is rate limiting and proceeds via a concerted mechanism, in which hydride at Boron is continuously displaced by iodide, reminiscent to an S_N2 reaction. The catalyst, which is accessible in high yields in few steps, was found to be stable during catalysis, readily recyclable and could be reused 10 times still efficiently working.*

Introduction

Catalytic enantioselective reductions of ketones are among the most important asymmetric reactions owing to the significance of enantiopure secondary alcohols as building blocks for the synthesis of bioactive compounds.[1] An attractive class of catalytic asymmetric reductions is the hydroboration which has been described using various catalyst types.[2,3] A number of them furnished products with high enantioselectivities. Probably the most popular method of this type is the Corey-Bakshi-Shibata (CBS) reduction of ketones which uses readily available oxazaborolidine catalysts and H_3B*L (L = THF, DMS) as stoichiometric reducing agent and is applicable to a broad substrate range.[4] However,

despite the great progress achieved with a number of previously reported catalyst concepts, a current limitation still is that highly active catalysts allowing for turnover numbers (TONs) > 500—while still acting highly enantioselectively—remained elusive.

Some years ago we introduced the concept of asymmetric bifunctional Lewis acid/aprotic onium salt catalysis and since then this concept has demonstrated its potential in various reaction classes such as [2+2] cycloadditions,[5] S_N reactions[6] and 1,2-additions.[7] The synthetic transformations investigated were either previously not viable or not very efficient in terms of catalytic activity. Herein we report that this concept allows for extraordinary catalytic activity combined with high enantioselectivity in the hydroboration of ketones, allowing for TONs up to 15 400, being equivalent to an increase of activity of about 1.5 to > 3 orders of magnitude compared to the most efficient asymmetric hydroboration catalysts. Our development was driven by the idea that a Lewis acidic oxophilic metal center could activate a ketone substrate, whereas a borane reagent might be activated by an appended ammonium halide moiety via a boron/halide interaction (Scheme 1). The activated borane would thus be quasi-intramolecularly directed towards the ketone. This simultaneous activation of both reactants was considered as promising tool to attain high catalytic activity,[8–10] while the reactants were expected to be precisely spatially preorganizable within the chiral environment of the bifunctional active site thus enabling high levels of enantioselectivity.
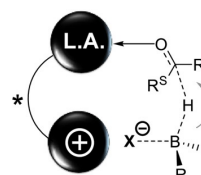
Scheme 1. Visualization of the concept of bifunctional Lewis Acid (L.A.)—ammonium salt catalyzed enantioselective hydroboration of ketones.

Results and Discussion

Development and Optimization Studies

As model reaction the hydroboration of acetophenone **1a** by pinacolborane (HBPin) was studied at 25°C using Al catalyst **C1** (Table 1).[11] Initial experiments conducted in CH_2Cl_2 proceeded disappointingly, because only traces of racemic product were formed like in entry 1.[12] A subsequent solvent screening (Supporting Information) not only revealed an accelerating effect by THF, but also allowed for high enantioselectivity (entry 2). The use of pure THF was more efficient than a mixture of THF and CH_2Cl_2 (entry 3). The use

[*] M. Sc. M. Titze, M. Sc. T. Junge, Prof. Dr. R. Peters
Universität Stuttgart, Institut für Organische Chemie
Pfaffenwaldring 55, 70569 Stuttgart (Germany)
E-Mail: rene.peters@oc.uni-stuttgart.de

M. Sc. J. Heitkämper, Prof. Dr. J. Kästner
Universität Stuttgart, Institut für Theoretische Chemie
Pfaffenwaldring 55, 70569 Stuttgart (Germany)
E-Mail: kaestner@theochem.uni-stuttgart.de

Supporting information and the ORCID identification number(s) for the author(s) of this article can be found under:
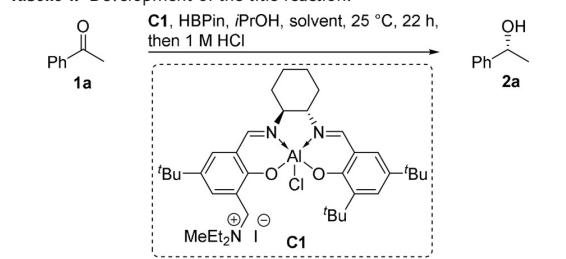https://doi.org/10.1002/anie.202012796.

Tabelle 1: Development of the title reaction.

#	C1 [mol%]	solvent	[1a] [mol/L]	HBPin [equiv]	iPrOH [equiv]	yield[a] [%]	ee[b] [%]	TON
1	5	CH₂Cl₂	0.14	1.0	–	2	2	0.4
2	5	THF	0.14	1.0	–	24	94	4.8
3	5	CH₂Cl₂/ THF (2:1)	0.14	1.0	–	16	93	3.2
4	5	THF	0.14	1.0	1.0	52	92	10.4
5	5	THF	0.14	2.0	1.0	72	92	14.4
6	0.5	THF	1.0	2.0	1.0	99	95	198
7	0.05	THF	1.0	2.0	1.0	99	97	1980
8	0.05	THF	1.0	1.0	1.0	84	93	1680
9	0.01	THF	1.0	2.0	1.0	93	92	9300
10	0.005	THF	1.6	2.0	1.0	77	91	15400
11	0.005	THF	neat	2.0	1.0	72	91	14400

[a] Yield determined by ¹H-NMR of the crude product using an internal standard. [b] Enantiomeric excess determined by GC.

of other common hydroboration agents led to inferior results (Supporting Information).

Continuous reaction monitoring by ¹H-NMR under the conditions of entry 2 revealed that the free alcohol **2a** is generated as catalytic intermediate, which is subsequently borylated. This implicated that a proton source is required for catalytic turnover. In the initial studies residual water was probably the proton source. Various (sub)stoichiometric proton sources were evaluated identifying *i*PrOH as the most efficient one of those examined (see Supporting Information). By this the yield was strongly improved (entry 4). Additional improvements were achieved by an excess of HBPin (entry 5) and an increased concentration. This allowed to significantly reduce the catalyst loading to technically interesting values (entries 6–11). With 0.05 mol% of **C1** an *ee* of 97% in combination with a nearly quantitative product yield was attained (entry 7).[13] However, under these optimized conditions, attractive results were also attained with just one equivalent of HBPin (entry 8). Also, with as little as 0.01 and 0.005 mol% **C1**—that is, 100 ppm and 50 ppm catalyst, respectively—high *ee* values (92% and 91%) and good yields (93% and 77%) were noticed (entries 9 & 10), corresponding to TONs of 9300 and 15400, respectively. These values are substantially higher than for all previously reported highly enantioselective catalysts in this reaction type.[2] The reaction was also performed under neat conditions and similar results were attained (entry 11).

Reaction Scope

The reaction conditions of Table 1/entry 7 were then applied to different prochiral ketones (Table 2). *Ortho-*, *meta-* and *para-*chloro substituted aryl rings within alkyl aryl

Tabelle 2: Investigation of different ketone substrates 1.[a,b]

[a] Yields of isolated products. [b] The enantiomeric excess was determined by HPLC or GC. [c] 0.1 mol% of **C1** were used. [d] 0.2 mol% of **C1** were used. [e] 0.5 mol% of **C1** were used. [f] 1.0 mol% of **C1** were used. [g] Basic work-up using sat. NaHCO₃. [h] Neutral work-up using water.

ketones were all well tolerated and provided **2b–2d**. Next to other σ-acceptors like *p*-fluoro (→ **2e**) and π-acceptors like *p*-nitro (→ **2f**), *p*-cyano (→ **2g**), a *p*-methylester (→ **2h**) and a *p*-dimethylamide group (→ **2i**), also σ-donors like *p*-methyl (→ **2j**) as well as π-donors like *p*-methoxy (→ **2k**) and even unprotected *p*-amino (→ **2l**) were well accepted on the aromatic moieties. In case of **2k** a basic reaction work-up was required to avoid racemization of the product. Chemoselectivity problems were not found with functional groups that are also susceptible to reductions. In addition, extended π-systems such as 2-naphthyl (→ **2m**) were successfully used. Next to methyl ketones, other alkyl ketones (→ **2n–2r**) as well as heteroaryl ketones (→ **2s** & **2t**) were accommodated and allowed for good to high enantioselectivity.

Noteworthy is also that dialkyl ketones can be efficiently used, if the difference of the steric demand of both residues is sufficiently large. **2u** was thus formed in almost quantitative yield with 98 % *ee*. Like expected with decreasing size difference the enantioselectivity decreased (→ **2v** & **2w**). A similar effect was observed for enones like shown for **2x**, **2y** and **2z**. The latter has been reported as intermediate toward a number of carotenoid-derived odorants and bioactive terpenes including α-damascone.[14]

Upscaling and Catalyst Recycling

The model reaction was also investigated on a gram scale (Table 3). With 0.05 mol % of catalyst and around 1 g of substrate, the product was formed with high yield (97 %) and enantioselectivity (*ee* = 96 %, entry 1). To enforce a quantitative yield, a reaction on 10 g scale was run with prolonged reaction time and provided excellent results (entry 2). A gram scale experiment was also performed employing only 0.02 mol % of catalyst (entry 3). Also in this case, a quantitative yield (TON 4950) and high enantioselectivity were attained (*ee* = 96 %). These results demonstrate the practical utility of this method.

In addition, the possibility to recycle the catalyst was examined (Scheme 2). In total 11 runs were conducted. Taking advantage of the ammonium salt moiety within the catalyst, *n*-pentane was added to the reaction mixture after 22 h in order to precipitate **C1**, which was then washed, dried under high vacuum, and reused. For the first 9 runs, nearly quantitative yields were achieved. The *ee* slowly dropped

Tabelle 3: Scale-up results.

#	scale **1a** [g] ([mmol])	**C1** [mol %]	*t* [d]	yield[a] [%]	amount **2a** [g]	*ee*[b] [%]	TON
1	1.00 (8.35)	0.05	1	97	0.99	96	1860
2	1.00 (8.35)	0.02	4.5	99	1.01	96	4950
3	10.03 (83.50)	0.05	4.5	99	10.14	95	1980

[a] Yield of isolated product. [b] Enantiomeric excess determined by GC.

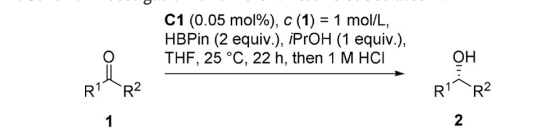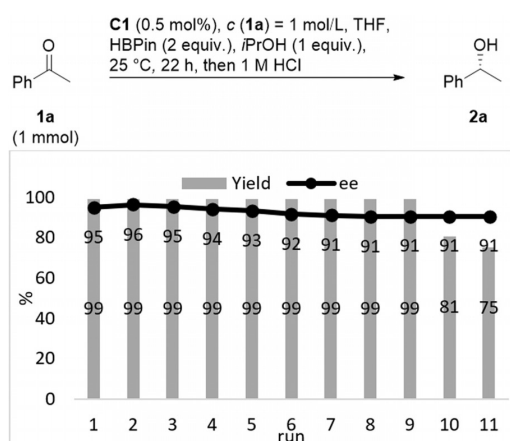**Scheme 2.** Catalyst recycling studies. Yield determined by ¹H-NMR of the crude product using an internal standard. Enantiomeric excess determined by GC.

from 95 to 91 %. Starting from the tenth run, the yield started to decrease (81 % for run 10, 75 % for run 11). Nevertheless, the enantiomeric excess stayed above 90 %. Albeit these results have not been optimized regarding the catalyst reisolation, they show that **C1** is remarkably stable during the reaction and also during recovery thus further increasing the practicality of the title reaction.

Mechanistic Studies
a) Control Experiments

To learn more about the role and impact of the catalytically relevant groups in **C1**, experiments with several control catalyst systems were conducted. Regarding the Lewis acidic center, catalysts with different anionic ligands were investigated (Table 4). Next to **C1** bearing a chloride ligand also the corresponding fluoride (**C2**) and methyl (**C3**) containing complexes were employed. It was found that **C1** was significantly more efficient regarding productivity and enantioselectivity. In particular **C3** was found to be a poor catalyst. In combination with the solvent effect, an explanation of the exceptionally high activity of **C1** might be that the catalytically active species makes use of a cationic Al center by displacing the metal bound chloride with THF (see also DFT calculations below). Cationic Al salen and salphen catalysts lacking an ammonium functional group and bearing two coordinating THF molecules at the Al center were previously reported and structurally characterized by Coates et al.[15] Because the Al−F bond in **C2** is much stronger than the Al−Cl bond,[7] the generation of the cationic species is less favored. In addition, neither Me in **C3**, nor the isopropoxide formed by protonation of **C3** with isopropanol are expected to readily form a cationic Al center.

Upon treatment of **C1** with an excess of HBPin, in situ recorded IR, ¹H-NMR and UV/Vis spectra did not result in significant changes. A similar result was also found for

Tabelle 4: Comparison of anionic ligands at the Al center.

C (0.05 mol%), c (**1a**) = 1 mol/L, THF, HBPin (2 equiv.), iPrOH (1 equiv.), 25 °C, 22 h, then 1 M HCl

C1: X = Cl
C2: X = F
C3: X = Me

#	C	yield[a] [%]	ee[b] [%]
1	**C1**	99	97
2	**C2**	42	80
3	**C3**	14	27

[a] Yield determined by ¹H-NMR of the crude product using an internal standard. [b] The enantiomeric excess was determined by GC.

catalyst treatment with *i*PrOH in UV/Vis experiments (Supporting Information). The formation of significant amounts of Al-H or Al-O*i*Pr species thus seems unlikely.

To learn more about the importance of the ammonium halide moiety, different sets of experiments were performed. In the initial set, various tetrabutylammonium salts were examined as catalysts to study the effect of the anion. Using the conditions of Table 1, entry 7, but in the absence of a catalyst, racemic product was formed in 13 % yield after 22 h at 25 °C (Table 5, entry 1). Employing different halide salts, catalytic activity increased with increasing size and thus higher polarizability of the anion (entries 3–5). In contrast to this trend, the highest activity was found with fluoride. However, we found that treatment of HBPin with TBAF results in partial formation of BF₃ and TBA[B(Pin)₂]. This outcome was confirmed by X-ray crystal structure analysis (see Supporting Information).[16,17] BF₃ might thus act as a Lewis acid cocatalyst which increases the catalytic activity.

Tabelle 5: Control experiments with TBAX salts.

TBAX, c (**1a**) = 1 mol/L, THF, HBPin (2 equiv.), iPrOH (1 equiv.), 25 °C, 22 h, then 1 M HCl

#	TBAX, X =	TBAX [mol %]	yield[a] [%]
1	—[b]	–	13
2	F	1	99
3	Cl	1	37
4	Br	1	55
5	OTf	1	38
6	I	1	81
7	I	0.05	37

[a] Yield determined by ¹H-NMR of the crude product using an internal standard. [b] No catalyst was used.

A lower yield was found for less nucleophilic anions like triflate. Decreasing the TBAI loading from 1.0 to 0.05 mol % resulted in decreased activity. These results demonstrate that ammonium halides have a catalytic activity in the reduction. Nevertheless, with TBAI the catalytic activity is significantly lower than for catalyst **C1** also bearing an iodide counterion (compare Table 5, entry 6 to Table 1, entry 6–9). This confirms the importance of the Lewis acidic Al center.

The interaction between halide ions and the boron center -maybe resulting in a more pronounced hydride character of HBPin- was studied by ¹H-NMR (for details see the Supporting Information). The methyl signal of the pinacolate framework was used as probe, because the hydride signal itself was quite broad. For the same reason, also ¹¹B-NMR was not employed. By adding the corresponding TBA halide salt (1 equiv) to HBPin in DCM-d₂ at 25 °C, the signals were slightly upfield-shifted, arguably as a result of a higher electron density at the B center. The softer the halide ion, the smaller should be the interaction with the relatively hard B center. According to these expectations the highest shift was found for chloride. However, the observed effect is small (around 0.05 ppm), probably due to the remote position of the investigated Me group.

Using 0.5 equiv of TBACl, there was no second signal for free HBPin, but the observed shift was smaller pointing to a dynamic behaviour for the chloride coordination. Also at −20 °C there was a single signal, but the observed shift was larger, pointing to more halide adduct in the equilibrium.

In addition, we investigated the variation of the ammonium counterion in the bifunctional complexes under the optimized conditions (Table 6). **C1** (entry 1) offered the best productivity for this catalyst series. Using **C1-Br** and **C1-Cl** bearing bromide and chloride counterions, respectively, the product yields were reduced by around 30 %. Using a „non"-nucleophilic ion the productivity was further decreased but remained noticeable. This seems contra-intuitive, but might

Tabelle 6: Study of the impact of different counterions in catalysts **C1**.

C1 (0.05 mol%), c (**1a**) = 1 mol/L, THF, HBPin (2 equiv.), iPrOH (1 equiv.), 25 °C, 22 h, then 1 M HCl

C1:   Y = I
C1-Br: Y = Br
C1-Cl: Y = Cl
C1-PF₆: Y = PF₆

#	Catalyst	yield[a] [%]	ee[b] [%]%
1	**C1**	99	97
2	**C1-Br**	69	95
3	**C1-Cl**	67	93
4[c]	**C1-PF₆**	57	92

[a] Yield determined by ¹H-NMR of the crude product using an internal standard. [b] The enantiomeric excess was determined by GC. [c] The corresponding triethylammonium salt was used as the catalyst.
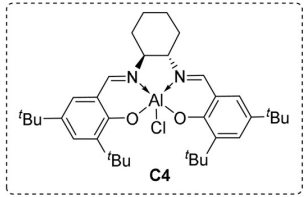
be explained by the generation of a cationic Al center thus releasing a nucleophilic chloride, while the non-nucleophilic anion is not expected to strongly interact with the cationic Al center.

Since the catalytic activity employing the different halide ions is not in agreement with the proposed binding tendencies of chloride, bromide and iodide to HBPin, it seems that the formation of an anionic halide/HBPin adduct intermediate cannot account for the catalytic activity differences. DFT calculations disclosed below suggest that interaction of the halide anion with the B center and the transfer of the hydride to the carbonyl group is a concerted process, reminiscent to an S_N2 reaction thus continuously displacing hydride by halide. Formation of an anionic intermediate is thus not necessary. Like in an S_N2 reaction, polarizability is a decisive factor (see also Figure 5).

Additional control experiments were performed with the widely used salen catalyst **C4**[18] (Table 7). As shown in entry 1, in the absence of any catalyst and *i*PrOH, only traces of product were formed. In the presence of *i*PrOH (1 equiv), the yield raised to 13% (entry 2). The same conditions, but using 0.05 mol% of catalyst **C4**, 16% of **2a** were formed with an *ee* of 72% (entry 3). With 0.005 mol%, 13% of product were obtained (entry 4) with an *ee* of 49%, probably because the background reaction gained importance (compare to entry 2). These experiments show that catalyst **C4** lacking an internal ammonium moiety is significantly less active and acts less enantioselectively than the bifunctional catalyst **C1**. **C4** is also less active than TBAI (0.05 mol%, entry 5). With the binary system of **C4** and TBAI (entry 6), results became slightly better as compared to the use of **C4** only (entry 3). Nevertheless, the productivity was lower than with the TBAI alone (entry 5). These results show that the bifunctional catalyst is substantially more efficient than monofunctional Lewis acid or ammonium catalysts and the corresponding binary catalyst system, probably as result of an intramolecular double activation pathway.

Tabelle 7: Control experiments with catalyst **C4**.

#	**C4** [mol%]	TBAI [mol%]	*i*PrOH [equiv]	yield[a] [%]	*ee*[b] [%]
1	0	0	0	2	–
2	0	0	1	13	–
3	0.050	0	1	16	72
4	0.005	0	1	13	49
5	0	0.05	1	37	–
6	0.050	0.05	1	25	74

[a] Yield determined by ^{1}H-NMR of the crude product using an internal standard. [b] The enantiomeric excess was determined by GC.

b) Kinetic Investigations

Reaction monitoring and kinetic investigations were performed via ^{1}H-NMR spectroscopy in THF-d$_8$ at 25°C using 0.1 mol% of **C1** (for details of the kinetic studies see the Supporting Information).

Catalyst robustness and a possible product inhibition were investigated by Blackmond's *Reaction Progress Kinetic Analysis* (RPKA) „*same excess*" protocol.[19] Three experiments were performed using different initial concentrations (Table 8, Figure 1).[20]

The decay of the concentration of **1a** over the course of the reaction is shown. Experiment 1 (Table 8) serves as reference reaction. In experiment 2 the starting concentration of **1a** corresponded to that of the reference reaction experiment when the latter had reached 50% conversion.[19] A time shift shows that in experiment 2 the reaction proceeded slower than in experiment 1. In a further experiment 3 the starting point of experiment 2 was used except that 50 mol% of product **2a** was added, because in reference experiment 1 also 50% product were present after 50% conversion. The good overlay of the reaction profiles of experiment 1 and 3 and the acceleration of experiment 3 compared to experiment 2 demonstrate two things:

1) There is apparently no significant catalyst decomposition taking place, because otherwise the reaction rate of experiment 2 and 3 should be higher than that of experiment 1.

Tabelle 8: Initial reaction conditions for the RPKA „same excess" experiments.

Exp.	[**1a**] [mol L^{-1}]	[HBPin] [mol L^{-1}]	[*i*PrOH] [mol L^{-1}]	[**2a**] [mol L^{-1}]
1	0.84	1.68	0.84	0
2	0.42	1.26	0.42	0
3	0.42	1.26	0.42	0.42
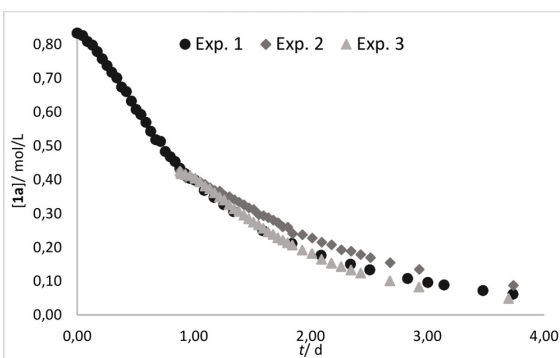
Figure 1. Reaction profiles of **1a** using Blackmond's „same excess" protocol under the conditions of Table 8.[19]

© 2020 The Authors. Angewandte Chemie published by Wiley-VCH GmbH

2) As the reaction rate of experiment 3 is higher than that of experiment 2, the product **2a** has an accelerating effect. It is likely that **2a** also acts as a proton source to release the product (see below).

The empirical rate law was determined by the *Variable Time Normalization Analysis* (VTNA) described by Burés.[21] Again, the model reaction of **1a** was examined at 25°C in THF-d$_8$ using catalyst **C1**. Six reactions with different initial concentrations of **1a**, **C1**, HBPin, *i*PrOH and **2a** were used monitoring the concentration of all reagents (for details see the Supporting Information).

The best fit for the normalization of the time scale axis was achieved for the following empirical rate:

$$r = k_{obs} \, [\mathbf{C1}]^{1.00} \, [\mathbf{1a}]^{1.00} \, [HBPin]^{0.52} \, [i\text{PrOH}]^{0.37} \, [\mathbf{2a}]^{0.31}. \qquad (1)$$

The reaction rate thus follows a first order kinetic dependence for catalyst **C1**[22] and the substrate **1a**, whereas for HBPin, *i*PrOH and **2a** orders between 0 and 1 were found.[23] The first order kinetic in catalyst indicates that a single catalyst molecule is probably involved in the turnover-limiting step. To probe this interpretation we took account of a non-linear effect.[24] As expected, a linear correlation between catalyst *ee* and product *ee* values were found thus confirming this claim (see Supporting Information).

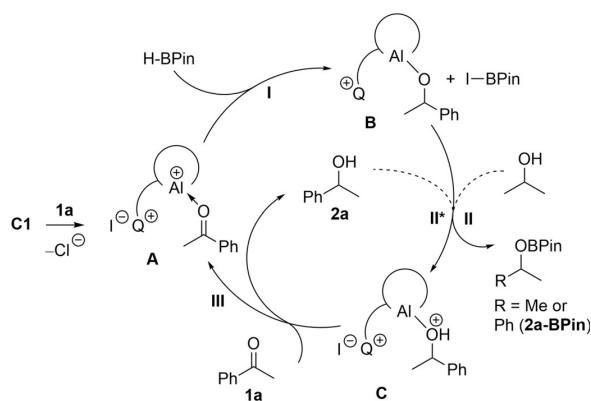As both alcohols accelerate the reaction, they are likely to cause the protonation step during the catalytic reaction. By the concentration profiles of **1a** and the corresponding boric-acid esters **2a-BPin** and *i***PrO-BPin** this assumption is reinforced (see Supporting Information). There is also an uncatalyzed side reaction taking place, in which HBPin reacts with *i*PrOH to form the corresponding boric acid ester, which constantly reduces the concentration of both *i*PrOH and HBPin. This event thus slows down the overall reaction progress.

Based on the described experimental results, we propose the simplified catalytic cycle described in Scheme 3. Acetophenone **1a** is expected to coordinate to the Lewis acidic aluminum center, which is suggested to be cationic in THF in the catalytically most active form **A** in agreement with studies of Coates and the above described solvent effect.[15] A cationic Al complex lacking the coordinated ketone substrate was indeed detected by ESI mass spectrometry using catalyst reisolated after a catalytic run. Moreover, our DFT studies presented below show that the activation barrier is significantly lower with a cationic compared to a neutral Al center. The iodide counterion of **A** (alternatively a released chloride ion) could activate and direct HBPin quasi-intramolecularly towards the keto moiety to generate Al-alcoholate **B** and IBPin (alternatively ClBPin). Protonation of **B** by *i*PrOH could release alcohol **2a**, whereas the generated isopropanolate could be trapped by IBPin (alternatively ClBPin). Upon accumulation of **2a**, it can also serve as proton source like *i*PrOH to release more of **2a**, while itself being transformed to the final boric ester product **2a-BPin**. Coordination of another acetophenone molecule would close the catalytic cycle.

c) Computational Investigations

To gain more insight into the reaction mechanism, the reduction of **1a** with HBPin was investigated by density functional theory (DFT) at the M06-2X/def2-TZVP level of theory on M06-2X/def2-SVP geometries with solvent effects accounted for by the conductor-like screening model (COS-MO, see Computational Details). The catalytic mechanism with **C1$_S$** ($_S$ for simplified) was studied, where the two *t*Bu groups of **C1** in *para*-position to the oxygen were removed to simplify the model.

The quantum chemical investigations predict a mechanism proposed in Figure 3. It turns out that step **I**, in which the hydride of the borane is transferred to the ketone and the borane binds to the free iodide, is rate determining. With the Al-Cl catalyst **C1$_S$**, this step has a barrier of 102 kJ mol^{-1}, which is too high to explain the observed kinetics. Thus, **C1** is not expected to be the active catalytic species. In agreement with the experimental finding that THF is required for the reaction to proceed, we found that a replacement of the chloride by THF is necessary to form an active catalyst **C1$^+$**. Figure 2 shows a simplified geometry of this complex (**C1$_{ss}^+$**), where the *t*Bu groups and the onium moiety are removed ($_{ss}$ for twice simplified). The exchange releases the chloride, which could subsequently also take over the role of the nucleophilic iodide in the catalytic cycle. This explains that some activity was observed with **C4**, lacking the onium moiety and the iodide, as well as catalyst systems with „non"-nucleophilic ions like **C1-PF$_6$**.

Scheme 3. Proposed simplified catalytic cycle.
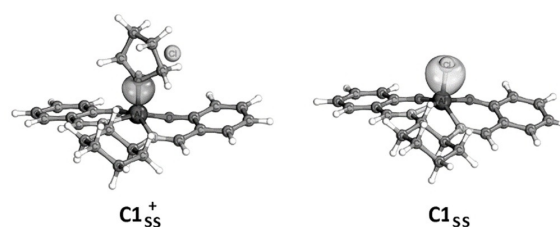
Figure 2. The binding IBO for [**C1$_{ss}^+$**]Cl$^-$ (left) and **C1$_{ss}$** (right). For a color Figure see the Supporting Information.

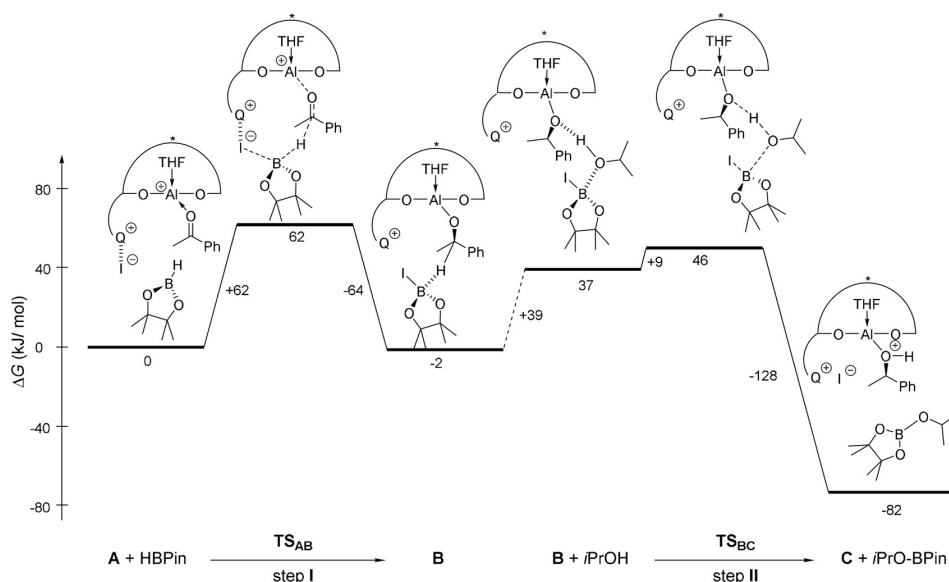The reaction barrier with the THF-activated catalyst **C1$_s$$^+$** is significantly lowered to 62 kJ mol^{-1}. It should be noted that according to DFT, **C1$_s$** is lower in energy by 20 kJ mol^{-1} than **C1$_s$$^+$**. However, the high excess of the solvent shifts the equilibrium towards the active form.

To explain the observed reactivity, structurally simplified complexes of the active (**C1$_{ss}$$^+$**) and the original (**C1$_{ss}$**) catalyst (see Figure 2) were investigated with the help of DFT and Intrinsic Bond Orbitals (IBOs) (see Computational Details). IBOs are helpful to interpret quantum chemical calculations, as they often provide chemically meaningful orbitals.

For **C1$_{ss}$$^+$**, the bond length Al-O (THF) was 1.87 Å. The localized IBO, which is responsible for this bond, is located at aluminum by only 12 % of its charge. In **C1$_{ss}$** the corresponding Al-Cl bond length is 2.17 Å. In this case 19 % of the bond charge is located at aluminum. As a consequence, the aluminum center carries a higher partial charge (IBO charge) of +1.19 in **C1$_{ss}$$^+$** than in **C1$_{ss}$** (+1.08). Therefore, as expected the Lewis acidity of the aluminum is increased by the exchange of chloride with THF.

The resulting mechanism with **C1$_s$$^+$** and its energetics are illustrated in Figure 3. The structures of the respective transition states can be found in Figure 4. We provide the energies for the unimolecular steps only, since the free-energy of association is rather ill-defined at our level of treatment of the solvation (COSMO) and in any case depends on the concentration of the reaction partners.

As already mentioned, step **I** from **A** to **B** represents the rate determining step of the catalytic mechanism with a barrier of 62 kJ mol^{-1}. It describes the carbonyl reduction via a hydride transfer from the borane to the electrophilic center of the ketone, which is activated by the Lewis-acidic

Figure 4. Geometries of the transition states obtained by DFT. Lengths of the bonds that are formed or broken during the transition are given in Å. For a color Figure see the Supporting Information.

aluminum. In a concerted reaction the borane simultaneously binds to the free iodide.

An electronic effect of the iodide on the borane was also studied. The B-I distance in **A** (before the bond formation) is 3.56 Å and decreases to 2.45 Å in **TS$_{AB}$** and further to 2.14 Å once the B−I bond is formed in **B**. An analysis of the IBOs reveals that there already is a slight interaction between the iodide and the borane in **A**. Figure 5 shows that the electron density of one IBO, that relates to the free electron pair at the iodide, is polarized towards the borane. The role of the iodide, through the help of the onium moiety, is not only to be in the proximity of the HBPin to act as a binding partner as soon as the hydride is transferred, but might also push electron density towards the borane activating the hydride.

Figure 3. Details of the catalytic steps as obtained from DFT with relative free-energy profile of the reaction steps A → B (step **I**) and B + *i*PrOH → C (step **II**). Dashed lines represent bimolecular steps.

Figure 5. IBOs that relate to the p electron pairs of the iodide in **A**. Two electron pairs have two equally sized lobes (one of them is shown on the left) and one is polarized towards the borane (right). For a color Figure see the Supporting Information.

As the enantioselectivity is here defined in the rate determining step, the formation of the enantiomer with minor yield is also studied. It yields a barrier of 74 kJ mol^{-1}. The enantiomeric excess can be calculated based on these results to be 98% which is in very good agreement with the measured *ee* value of 97%.

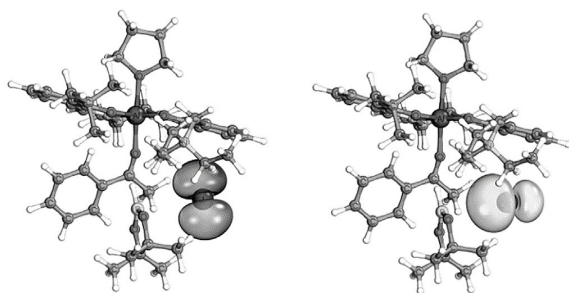In step **II** an *i*PrOH molecule is added (**B** + *i*PrOH) and the alcoholate that is coordinated to the aluminum center is protonated. As a consequence, the Al−O bond length increases from 1.80 Å to 2.00 Å.

The step possesses an early transition state with a small barrier of 8 kJ mol^{-1}. To confirm the experimentally found kinetics, where the product alcohol takes over the role of a protonating agent during the course of the reaction, step **II** was also investigated with the product alcohol **2a** instead of *i*PrOH. Apart from slightly more steric hindrance the reaction is qualitatively the same. The barrier increases to 16 kJ mol^{-1} but is still very small. When *i*PrOH is consumed in the course of the reaction and the concentration of the product alcohol increases, it is likely that the latter will be the more and more dominating proton source.

To estimate the reliability of the DFT results, single point calculations have been repeated with the functionals TPSS and PBE0 (see Supporting Information). They result in overall smaller barriers but the conclusions drawn from DFT are unaltered.

Conclusion

In summary, we have reported a concept for the catalytic asymmetric hydroboration of ketones, which allows for extraordinarily high turnover numbers (up to 15 400) that are around 1.5–3 orders of magnitude higher than with the most efficient catalysts previously reported. The chiral secondary alcohols—high-value-added products—were typically formed with high yields and high enantioselectivity. In our concept an aprotic ammonium halide moiety and an oxophilic Lewis acid work in concert and cooperate with each other within the same catalyst molecule. This was confirmed by a number of control experiments showing that both catalytic centers are indispensable for the observed activity.

Moreover, kinetic, spectroscopic and computational studies revealed that the hydride transfer is most likely rate limiting. According to our calculations, it proceeds via a concerted mechanism, in which hydride is continuously displaced by iodide at the B center, reminiscent to an S$_N$2 reaction. Simultaneously, the hydride attacks the ketone, which is activated by a cationic Al^{III} center. Further practical value is added by the fact that the catalyst, which is readily accessible in high yields in few steps, is stable during catalysis and readily recyclable by taking advantage of the ammonium salt moiety. This allowed to reuse the catalyst 10 times, while still efficiently working.

Computational Details

Molecular geometries were optimized with the DL-FIND[25] optimization library in Chemshell.[26] The density functional theory (DFT) calculations were performed with the Turbomole V 7.0.1 and V 7.4.1 program package[27] using (DFT) with the M06-2X functional[28] and the def2-SVP basis set.[29] Frequencies were calculated at the same level of theory. Numerical integration was carried out on a m4 grid and SCF energies were converged for an energy difference of less than 10^{-8} atomic units. All transition structures were verified to possess only a single mode with imaginary frequency. IRC (internal reaction coordinate) calculations starting from the transition structures were performed and verified the reactants and products. The free energy G was calculated at 298.15 K within the RRHO (rigid rotor harmonic oscillator) approximation. Vibrational frequencies less than 100 cm^{-1} were raised to this threshold. At fixed geometries, the energy was calculated using the def2-TZVP basis set[29] and the solvent effects were accounted for with the conductor-like screening model (COSMO)[30] using a dielectric constant of $\varepsilon = 7.39$ for THF at 298.15 K. For the atomic radii in the cavity the default values for COSMO were used. Intrinsic bond orbitals (IBOs)[31] were calculated based on orbitals of M06-2X/def2-TZVP level of theory with exponent 2 in the localization method. The visualization of the IBOs was realized using the IboView program by Knizia (http://www.iboview.org/).

Acknowledgements

Conflict of interest

The authors declare no conflict of interest.

Stichwörter: ammonium salts · asymmetric catalysis · chiral alcohols · cooperative catalysis · hydroboration

[1] a) R. Noyori, T. Ohkuma, *Angew. Chem. Int. Ed.* **2001**, *40*, 40–73; *Angew. Chem.* **2001**, *113*, 40–75; b) R. Noyori, M. Koizumi, D. Ishii, T. Ohkuma, *Pure Appl. Chem.* **2001**, *73*, 227–232; c) T. Ohkuma, M. Kitamura, R. Noyori, *New Frontiers in Asymmetric Catalysis*, Wiley, Hoboken, **2006**, pp. 1–32; d) M. Zaidlewicz, M. M. Pakulski in *Science of Synthesis Stereoselective Synthesis*, *Vol. 2* (Eds.: J. G. De Vries, G. A. Molander, P. A. Evans), Thieme, Stuttgart, **2011**, pp. 59–131; e) N. Arai, T. Ohkuma in *Science of Synthesis Stereoselective Synthesis, Vol. 2* (Eds.: J. G. De Vries, G. A. Molander, P. A. Evans), Thieme, Stuttgart, **2011**, pp. 9–57; f) H. Gröger, S. Borchert, M. Krausser, W. Hummel in *Encyclopedia of Industrial Biotechnology, Vol. 3* (Ed.: M. C. Flickinger), Wiley, Hoboken, **2010**, pp. 2094–2110; g) V. S. Shende, P. Singh, B. M. Bhanage, *Catal. Sci. Technol.* **2018**, *8*, 955–969; h) Z. H. Yang, R. Zeng, G. Yang, Y. Wang, L. Z. Li, Z. S. Lv, M. Yao, B. Lai, *J. Ind. Microbiol. Biotechnol.* **2008**, *35*, 1047–1051; i) B. S. Chen, F. Z. Ribeiro de Souza, *RSC Adv.* **2019**, *9*, 2102–2115.

[2] Reviews: a) B. T. Cho, *Chem. Soc. Rev.* **2009**, *38*, 443–452; b) M. L. Shegavi, S. K. Bose, *Catal. Sci. Technol.* **2019**, *9*, 3307–3336; see also: c) H. C. Brown, P. V. Ramachandran, *Acc. Chem. Res.* **1992**, *25*, 16–24; d) P. V. Ramachandran, H. C. Brown, *ACS Symposium Series, Vol. 641*, ACS Publications, Washington, **1996**, pp. 84–97.

[3] Reviews on boron chemistry: a) P. Kaur, G. Khatik, S. Nayak, *Curr. Org. Synth.* **2016**, *14*, 665–682; b) D. G. Hall in *Boronic Acids: Preparation and Applications in Organic Synthesis and Medicine*, Wiley-VCH, Weinheim, **2006**, pp. 1–99; c) H. Defrancesco, J. Dudley, A. Coca, *ACS Symp. Ser.* **2016**, *1236*, 1–25.

[4] a) E. J. Corey, C. J. Helal, *Angew. Chem. Int. Ed.* **1998**, *37*, 1986–2012; *Angew. Chem.* **1998**, *110*, 2092–2118; for highly enantioselective hydroborations using HBPin, see: b) J. Guo, J. Chen, Z. Lu, *Chem. Commun.* **2015**, *51*, 5725–5727; c) V. Vasilenko, C. K. Blasius, H. Wadepohl, L. H. Gade, *Angew. Chem. Int. Ed.* **2017**, *56*, 8393–8397; *Angew. Chem.* **2017**, *129*, 8513–8517; d) C. K. Blasius, V. Vasilenko, L. H. Gade, *Angew. Chem. Int. Ed.* **2018**, *57*, 10231–10235; *Angew. Chem.* **2018**, *130*, 10388–10392; e) V. Vasilenko, C. K. Blasius, L. H. Gade, *J. Am. Chem. Soc.* **2018**, *140*, 9244–9254; f) M. Magre, B. Maity, A. Falconnet, L. Cavallo, M. Rueping, *Angew. Chem. Int. Ed.* **2019**, *58*, 7025–7029; *Angew. Chem.* **2019**, *131*, 7099–7103; g) Y. N. Lebedev, I. Polishchuk, B. Maity, L. Cavallo, M. Rueping, *J. Am. Chem. Soc.* **2019**, *141*, 19415–19423; h) V. Vasilenko, C. K. Blasius, H. Wadepohl, L. H. Gade, *Chem. Commun.* **2020**, *56*, 1203–1206; i) W. Liu, J. Guo, S. Xing, Z. Lu, *Org. Lett.* **2020**, *22*, 2532–2536; j) for a recent review, see: L. Wenbo, L. Zhan, *Chin. J. Org. Chem.* **2020**, *40*, 3596–3604.

[5] a) T. Kull, R. Peters, *Angew. Chem. Int. Ed.* **2008**, *47*, 5461–5464; *Angew. Chem.* **2008**, *120*, 5541–5544; b) T. Kull, J. Cabrera, R. Peters, *Chem. Eur. J.* **2010**, *16*, 9132–9139; c) P. Meier, F. Broghammer, K. Latendorf, G. Rauhut, R. Peters, *Molecules* **2012**, *17*, 7121–7150.

[6] F. Broghammer, D. Brodbeck, T. Junge, R. Peters, *Chem. Commun.* **2017**, *53*, 1156–1159.

[7] a) D. Brodbeck, F. Broghammer, J. Meisner, J. Klepp, D. Garnier, W. Frey, J. Kästner, R. Peters, *Angew. Chem. Int. Ed.* **2017**, *56*, 4056–4060; *Angew. Chem.* **2017**, *129*, 4115–4119; b) D. Brodbeck, S. Álvarez-Barcia, J. Meisner, F. Broghammer, J. Klepp, D. Garnier, W. Frey, J. Kästner, R. Peters, *Chem. Eur. J.*

2019, *25*, 1515–1524; c) T. Junge, M. Titze, W. Frey, R. Peters, *ChemCatChem*, DOI: 10.1002/cctc.202001921R1.

[8] *Cooperative Catalysis—Designing Efficient Catalysts for Synthesis* (Ed.: R. Peters), Wiley-VCH, Weinheim, **2015**.

[9] For the cleavage of B-H Bonds by metal-ligand cooperation, see: T. Higashi, S. Kusumoto, K. Nozaki, *Chem. Rev.* **2019**, *119*, 10393–10402.

[10] Selected related polyfunctional catalysts developed by our group: a) V. Miskov-Pajic, F. Willig, D. M. Wanner, W. Frey, R. Peters, *Angew. Chem. Int. Ed.* **2020**, *59*, 19873–19877; b) F. Willig, J. Lang, A. C. Hans, M. R. Ringenberg, D. Pfeffer, W. Frey, R. Peters, *J. Am. Chem. Soc.* **2019**, *141*, 12029–12043; c) J. Schmid, T. Junge, J. Lang, W. Frey, R. Peters, *Angew. Chem. Int. Ed.* **2019**, *58*, 5447–5451; *Angew. Chem.* **2019**, *131*, 5501–5505; d) M. Mechler, R. Peters, *Angew. Chem. Int. Ed.* **2015**, *54*, 10303–10307; *Angew. Chem.* **2015**, *127*, 10442–10446; e) J. Schmid, W. Frey, R. Peters, *Organometallics* **2017**, *36*, 4313–4324; f) M. Mechler, W. Frey, R. Peters, *Organometallics* **2014**, *33*, 5492–5508; g) M. Mechler, K. Latendorf, W. Frey, R. Peters, *Organometallics* **2013**, *32*, 112–130.

[11] Non-enantioselective Al-catalyzed hydroboration of ketones: a) A. J. Woodside, M. A. Smith, T. M. Herb, B. C. Manor, P. J. Carroll, P. R. Rablen, C. R. Graves, *Organometallics* **2019**, *38*, 1017–1020; b) V. K. Jakhar, M. K. Barman, S. Nembenna, *Org. Lett.* **2016**, *18*, 4710–4713; c) D. Franz, L. Sirtl, A. Pöthig, S. Inoue, *Z. Anorg. Allg. Chem.* **2016**, *642*, 1245–1250; d) V. A. Pollard, S. A. Orr, R. McLellan, A. R. Kennedy, E. Hevia, R. E. Mulvey, *Chem. Commun.* **2018**, *54*, 1233–1236; e) L. E. Lemmerz, R. McLellan, N. R. Judge, A. R. Kennedy, S. A. Orr, M. Uzelac, E. Hevia, S. D. Robertson, J. Okuda, R. E. Mulvey, *Chem. Eur. J.* **2018**, *24*, 9940–9948; f) Z. Yang, M. Zhong, X. Ma, S. De, C. Anusha, P. Parameswaran, H. W. Roesky, *Angew. Chem. Int. Ed.* **2015**, *54*, 10225–10229; *Angew. Chem.* **2015**, *127*, 10363–10367; Al-catalyzed hydroboration of alkynes and/or alkenes: g) A. Bismuto, S. P. Thomas, M. J. Cowley, *Angew. Chem. Int. Ed.* **2016**, *55*, 15356–15359; *Angew. Chem.* **2016**, *128*, 15582–15585; h) F. Li, X. Bai, Y. Cai, H. Li, S. Q. Zhang, F. H. Liu, X. Hong, Y. Xu, S. L. Shi, *Org. Process Res. Dev.* **2019**, *23*, 1703–1708.

[12] Review on Al catalysts in reduction chemistry: G. I. Nikonov, *ACS Catal.* **2017**, *7*, 7257–7266.

[13] Under these conditions we also investigated the use of the corresponding C_2-symmetric ligand bearing two ammonium moieties. However, both yield (11%) and *ee* (18%) were poor.

[14] K. Mori, *Synlett* **1995**, 1097–1109.

[15] a) V. Mahadevan, Y. D. Y. L. Getzler, G. W. Coates, *Angew. Chem. Int. Ed.* **2002**, *41*, 2781–2784; *Angew. Chem.* **2002**, *114*, 2905–2908; b) M. Mulzer, W. C. Ellis, E. B. Lobkovsky, G. W. Coates, *Chem. Sci.* **2014**, *5*, 1928–1933; c) Y. D. Y. L. Getzler, V. Mahadevan, E. B. Lobkovsky, G. W. Coates, *J. Am. Chem. Soc.* **2002**, *124*, 1174–1175.

[16] For a KF catalyzed hydroboration, see: K. Kuciński, G. Hreczycho, *Eur. J. Org. Chem.* **2020**, 552–555.

[17] Deposition Number 2030886 contains the supplementary crystallographic data for this paper. These data are provided free of charge by the joint Cambridge Crystallographic Data Centre and Fachinformationszentrum Karlsruhe Access Structures service www.ccdc.cam.ac.uk/structures.

[18] a) M. S. Sigman, E. N. Jacobsen, *J. Am. Chem. Soc.* **1998**, *120*, 5315; b) J. K. Myers, E. N. Jacobsen, *J. Am. Chem. Soc.* **1999**, *121*, 8959.

[19] a) R. D. Baxter, D. Sale, K. M. Engle, J.-Q. Yu, D. G. Blackmond, *J. Am. Chem. Soc.* **2012**, *134*, 4600–4606; b) D. G. Blackmond, *J. Am. Chem. Soc.* **2015**, *137*, 10852–10866.

[20] [*i*PrOH] determined by ¹H-NMR for experiment 1 in Table 8 after 50% conversion is in good agreement with the calculated value used in Table 8.

[21] a) J. Burés, *Angew. Chem. Int. Ed.* **2016**, *55*, 16084–16087; *Angew. Chem.* **2016**, *128*, 16318–16321; b) C. D.-T. Nielsen, J. Burés, *Chem. Sci.* **2019**, *10*, 348–353.

[22] Also for catalyst **C4** lacking an onium moiety a first order kinetic dependence was found.

[23] For the BPin ester of **2a**, no accelerating effect was found.

[24] T. Satyanarayana, S. Abraham, H. B. Kagan, *Angew. Chem. Int. Ed.* **2009**, *48*, 456–494; *Angew. Chem.* **2009**, *121*, 464–503.

[25] J. Kästner, J. M. Carr, T. W. Keal, W. Thiel, A. Wander, P. Sherwood, *J. Phys. Chem. A* **2009**, *113*, 11856–11965.

[26] S. Metz, J. Kästner, A. A. Sokol, T. W. Keal, P. Sherwood, *Wiley Interdiscip. Rev.: Comput. Mol. Sci.* **2014**, *4*, 101–110. „Chem-Shell, a Computational Chemistry Shell" can be found under http://www.chemshell.org.

[27] „TURBOMOLE V7 2015, a development of the University of Karlsruhe and Forschungszentrum Karlsruhe GmbH, 1989–2007, TURBOMOLE GmbH, since 2007; can be found under http://www.turbomole.com.

[28] Y. Zhao, D. Truhlar, *Theor. Chem. Acc.* **2008**, *120*, 215–241.

[29] a) F. Weigend, R. Ahlrichs, *Phys. Chem. Chem. Phys.* **2005**, *7*, 3297–3305; b) F. Weigend, *Phys. Chem. Chem. Phys.* **2006**, *8*, 1057–1065.

[30] A. Klamt, G. Schüürmann, *J. Chem. Soc. Perkin Trans. 2* **1993**, 799–805.

[31] G. Knizia, *J. Chem. Theory Comput.* **2013**, *9*, 4834–4843.

3.4 Paper IV

Asymmetric Hydroboration of Ketones by Cooperative Lewis Acid–Onium Salt Catalysis: A Quantum Chemical and Microkinetic Study to Combine Theory and Experiment

J. Heitkämper, J. Herrmann, M. Titze, S. Bauch, R. Peters, and J. Kästner
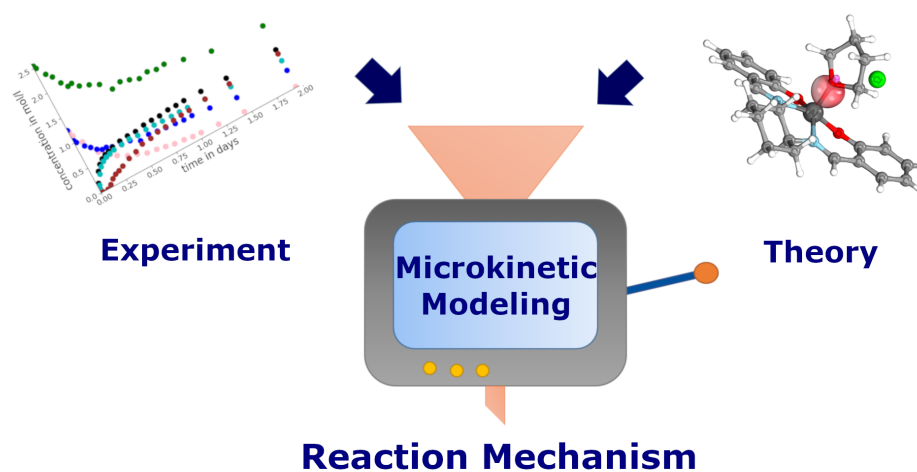
Own contributions:

- all quantum chemical calculations (major part of the manuscript)
- microkinetic modeling (major part of the manuscript)
- preparation of the computational part of the manuscript (major part) with J. Kästner

Asymmetric Hydroboration of Ketones by Cooperative Lewis Acid–Onium Salt Catalysis: A Quantum Chemical and Microkinetic Study to Combine Theory and Experiment

Juliane Heitkämper, Justin Herrmann, Marvin Titze, Soeren M. Bauch, René Peters, and Johannes Kästner*

ACCESS | Metrics & More | Article Recommendations | SI Supporting Information

ABSTRACT: We apply microkinetic modeling in homogeneous catalysis and show how it can be used to reveal important details of a complex mechanism and how this can lead to a direct comparison between theory and experiment. While regularly used in heterogeneous catalysis, its applications to organic chemistry or homogeneous catalysis are still comparatively scarce. This approach is exemplarily applied to the mechanism of the asymmetric hydroboration of acetophenone with a highly active cooperative Lewis acid−ammonium salt catalyst. In combination with density functional theory, it is a gateway to shed light into important mechanistic details. In our study, it reveals that the counterion of the ammonium salt of the catalyst facilitates the hydride transfer step of the cycle. Chloride replacing iodide speeds up the main reaction but simultaneously has the same effect on a side reaction that consumes the product. This observation is confirmed by experimental measurements of both the main catalytic cycle and the side reaction. A sensitivity analysis showed that the transition from the product complex to the hydride transfer is rate-limiting and that it determines the enantioselectivity. Based on this insight, an enantioselective kinetic model was applied, from which the difference of the Gibbs free energy barriers of the two pathways forming the two enantiomers can be extracted. The barriers are in fairly good agreement with the ones calculated by DFT, which reveal that the asymmetric backbone interacts with the reactant sterically to favor asymmetric product formation.

KEYWORDS: microkinetic modeling, homogeneous catalysis, density functional theory, hydroboration, sensitivity analysis, reaction mechanism
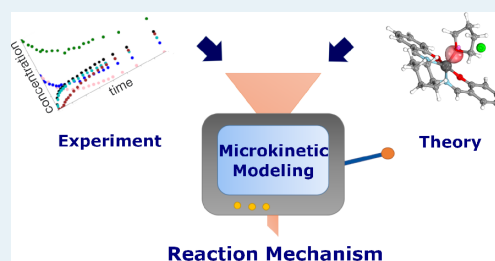
■ INTRODUCTION

In the present work, we study the hydroboration of acetophenone (**1**, 1-phenylethan-1-one) to 1-phenylethanol (**2**, 1-phenylethan-1-ol) by pinacolborane (HBPin) using a highly active cooperative Lewis acid−ammonium salt catalyst, see Figure 1, following our previous work.[1] Isopropanol (iPrOH) is used as proton source. The catalyst[2−7] provides exceptional catalytic turnover numbers and high enantioselectivity. The catalytic asymmetric reduction of ketones is an important reaction type producing enantioenriched secondary alcohols, which are valuable building blocks for the synthesis of bioactive compounds.[8−16] One of the most popular methods for catalytic asymmetric reductions is the enantioselective hydroboration.[17−33] Some years ago, Peters et al. introduced the concept of asymmetric bifunctional Lewis acid/aprotic onium salt catalysis, and since then, this concept has demonstrated its utility in various reaction classes such as formal [2 + 2] cycloadditions,[2−4] SN reactions,[5] and 1,2-additions.[6,7] In the highly enantioselective hydroborations of ketones, this concept allowed for unprecedented productivity.
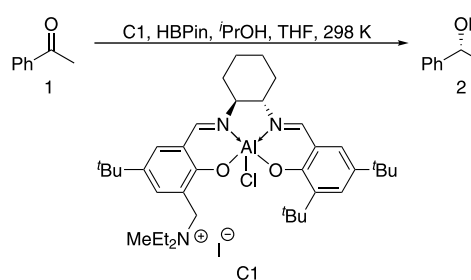
Figure 1. Overall reaction: reduction of acetophenone (**1**) by pinacolborane (HBPin) to 1-phenylethanol (**2**).
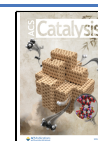
TONs up to 15 400 were achieved, whereas typical TONs in the literature are <100.[1]

Quantum chemical calculations have revealed that a solvent molecule (THF, tetrahydrofuran) plays a major role in the catalytic cycle. By coordinating to the Al center and replacing a chloride ligand, it increases the aluminum's Lewis acidity. The mechanism as it emerges from the present work is shown in Figure 2, where the chloride is replaced by an iodide in the

Figure 2. Reaction mechanism resulting from this study for the hydroboration of **1** by a Lewis acid−ammonium salt catalyst. Labels and structures in parentheses refer to **R4**.

catalytic cycle. In our above-mentioned study,[1] it was proposed that after forming the active catalyst, the hydride is transferred from HBPin to **1** in reaction **R2**, and simultaneously, the iodide at the onium group binds to the boron. In step **R3**, the Al-bound al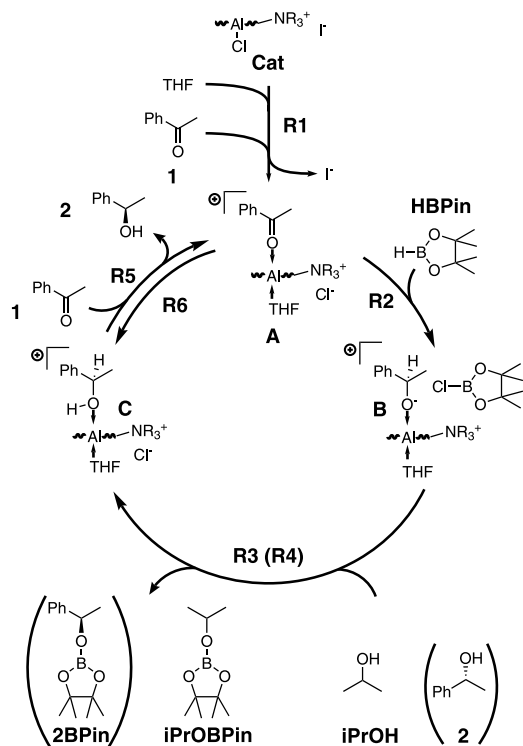coholate is protonated by iPrOH. Alternatively, the product alcohol **2** can serve as a proton source in reaction **R4**. Replacement of the product alcohol **2** by the reactant **1** closes the catalytic cycle in reaction **R5**. The catalyst is versatile and can reduce several ketone substrates,[1] but here, we restrict the study to **1**.

Besides the yield and the enantiomeric excess, time-resolved concentration profiles provide insight into the reaction mechanism from an experimental perspective.[34,35] DFT simulations provide reaction barriers and reaction enthalpies.

In the present work, we resolve the whole catalytic cycle by a combination of quantum chemical investigations and a microkinetic model, which provides concentration profiles to be compared directly with the experimental results. The enantioselectivity is included in the microkinetic model. A

sensitivity analysis reveals the rate-determining step and provides information on the accuracy of our numeric model.

■ RESULTS AND DISCUSSION

For the uncatalyzed reaction of HBPin, **1**, and iPrOH to iPrOBPin and **2**, a barrier of 137.1 kJ mol^{-1} with respect to the free reactants is obtained from DFT (**TS$_{uncat}$**). Herein, the hydride of HBPin and the proton of iPrOH are transferred simultaneously to **1** to reduce it. A cooperative Lewis acid−onium salt catalyst lowers the reaction barrier on the one hand and enables an enantioselective reaction on the other hand. We first discuss the catalytic cycle summarized in Figure 2 based on our DFT calculations. Then, these will be compared to the results from a kinetic model based on a measured concentration profile.

DFT Model. The catalyst **C1** as shown in Figure 1 is activated before becoming active in the reaction. A THF solvent molecule replaces the chloride ligand. The subsequent steps of the catalytic cycle could be envisaged with a chloride or a THF ligand at the Al site of the catalyst, but our previous study showed that barriers for the hydride transfer step are, with a bimolecular barrier of 165.2 kJ mol^{-1}, much higher than with a chloride ligand than with an THF ligand (118.0 kJ mol^{-1}).[1] Our DFT calculations show that simultaneously with the ligand exchange, the acetophenone (**1**) substrate coordinates to Al at the side opposite to THF in reaction **R1**. It is noted that **C1** is simplified in the quantum chemical calculations, as explained in the Computational Details, and therefore labeled as **Cat**. We found **R1** to possess a Gibbs free energy barrier of 91.3 kJ mol^{-1} (**TS1**) and to be endothermic by 42.7 kJ mol^{-1} using DFT. Note that all free enthalpies reported here and in the following refer to a reference state of a concentration of 1 M and refer to the bimolecular steps; see Computational Details, and therefore they may differ from values in our previous work.[1] **R1** results in the activated, substrate-bound catalyst **A** with the chloride ion still in the vicinity of the onium group and, thus, available for further reaction. Other coordinating agents, like **1**, could in principle replace the chloride ion. However, DFT calculations show that the THF-coordinated complex **A** is lower in energy by 32.5 kJ mol^{-1} than the corresponding complex with THF replaced by another ligand **1**. We, therefore, assume that **A** is the active form.

The first reaction inside the catalytic cycle, **R2**, transfers the hydride from HBPin to **1** to form an alcoholate and a B−Cl bond in state **B** in a concerted manner. As can be seen from Figure 2, this step is composed of a lose coordination of HBPin to **A**, endothermic by 56.9 kJ mol^{-1}, followed by the actual reaction. For the whole step **R2**, we found a reaction barrier of $\Delta G^{\ddagger} = 81.7$ kJ mol^{-1} by DFT. Since this step, with its transition state **TS2**, will be identified as rate-limiting below, a closer investigation is warranted. The step could take place with either iodide or chloride binding to boron. With iodide, however, we find a bimolecular DFT barrier of $\Delta G^{\ddagger} = 118.0$ kJ mol^{-1} (**AI → TS2I**), significantly higher than the value of $\Delta G^{\ddagger} = 81.7$ kJ mol^{-1} (**TS2**) obtained with chloride. Note that in ref 1, we presented unimolecular barriers for the reaction **AI → TS2I** only. The reaction with chloride possesses an earlier transition state **TS2** than with iodide. At the transition state, the B−H distance of 1.25 Å is still shorter using chloride than the 1.27 Å we found with iodide. Also, the C−H bond to be formed is still longer at the TS at 1.93 Å for chloride, while it is 1.64 Å for the iodide case.

Previously, we argued that the halide ion shifts electron density of the free electron pair toward the boron center to activate it.[1] Such an electron transfer can quantitatively be observed by intrinsic bond orbital analysis (IBO). The corresponding p-orbital of chloride in state **A+HBPin**, before any halogen−boron bond is formed, which is polarized toward the boron center, is shown in Figure 3. Already in state **A**
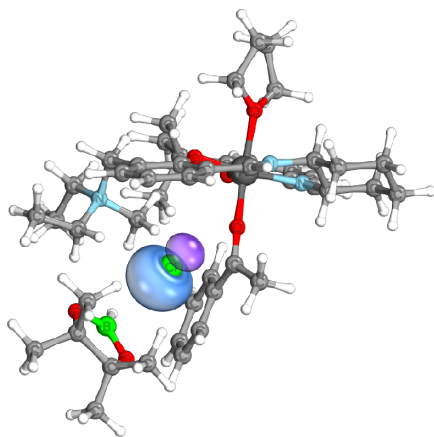
Figure 3. Complex of state **A+HBPin** with the p-electron pair of the chloride, which is polarized toward boron.

+HBPin, boron contributes 2.07% to the orbital of chloride, while it only contributes 1.62% to iodide, showing a higher degree of polarization toward the boron of chloride. This is in agreement with NMR studies that suggest a strength of the interaction between halide ions and HBPin in the order Cl⁻ > Br⁻ > I⁻.[1]

The next step in the catalytic cycle is the protonation of the alcoholate in **B** to form **C**, which contains the product alcohol **2**. With iPrOH as the proton source, the reaction is labeled **R3**, and we found a barrier of $\Delta G^{\ddagger} = 36.4$ kJ mol⁻¹ by DFT. However, alternatively, the product alcohol **2** can serve as a proton source in reaction **R4**. In that case, the barrier was found to be $\Delta G^{\ddagger} = 32.8$ kJ mol⁻¹ by DFT. The reaction results in structure **C**, an adduct between the catalyst and product alcohol, which is the lowest state in the catalytic cycle. Experimental attempts in which the product alcohol was added stoichiometrically to the catalyst to detect this species by ¹H NMR spectroscopy were not successful.

The catalytic cycle is closed by replacement of the product **2** by the reactant **1** in reaction **R5**, for which we found a barrier of $\Delta G^{\ddagger} = 79.4$ kJ mol⁻¹ using DFT.

An overview of the Gibbs free energy along the catalytic cycle is given in Figure 4. Step **R2**, the hydride transfer, is found to be slightly exothermic by 19.6 kJ mol⁻¹ using DFT, while the proton transfer from iPrOH, **R3**, is strongly exothermic by 116.0 kJ mol⁻¹. The exchange of **2** by **1**, reaction **R5**, is found to be slightly endothermic by 16.0 kJ
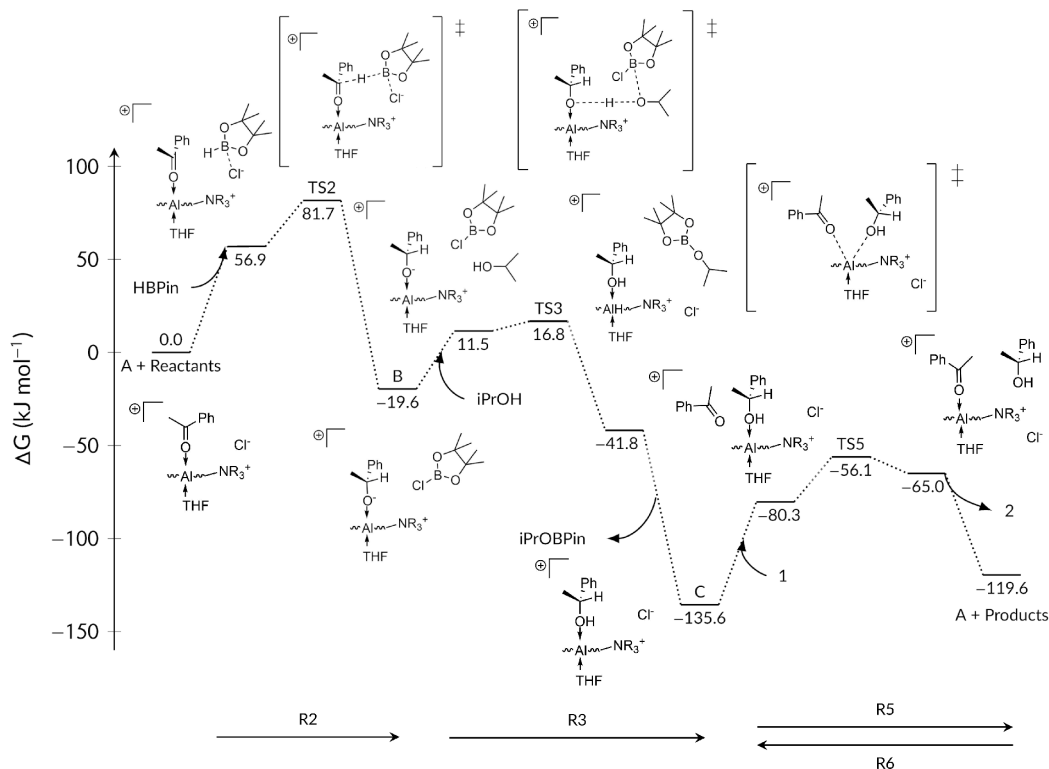
Figure 4. Gibbs free energy diagram for the main reaction cycle. Reactants refer to **1**, HBPin, and iPrOH, while products refer to **2** and iPrOBPin. The barriers are resolved into bimolecular steps under coordination of a reactant to form a prereactive complex and unimolecular steps, which represent the actual reaction.

mol^{-1} with DFT, resulting in an overall exothermic reaction by 119.6 kJ mol^{-1}. So far, we have discussed the main elementary reactions to explain the activation of the catalyst and the catalytic cycle. Several side reactions are possible. Before their DFT investigations are discussed, we now focus on the comparison to experiment via kinetic data.

Kinetic Model. A direct comparison between our Gibbs free energy from DFT and experimental kinetic data is possible via a kinetic model. Measured concentration profiles over time are illustrated in Figure 5, which also contains the results of our
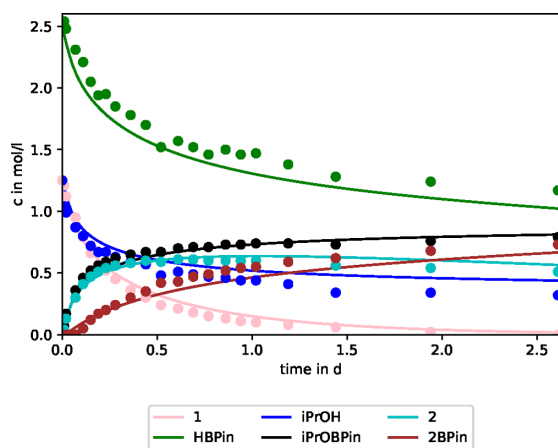
Figure 5. Measured concentration profiles (dots) vs results from our kinetic model (lines). The initial concentrations are 2.5 M (2 equiv) for HBPin, 1.25 M (1 equiv) for iPrOH, 1.25 M (1 equiv) for **1**, and 0.10 mol % of **C1**. The reaction was carried out at 298 K in THF as solvent.

kinetic model. The kinetic model contains barriers, and rate constants derived from these barriers, for each elementary reaction. In principle, the barriers from DFT can be used. However, we optimized these barriers as free parameters to fit the experimental concentrations. Using such an approach, the reaction barriers from DFT can be compared to those from the kinetic model to arrive at an overall picture of the catalytic cycle.

A full kinetic model is rarely used in organic chemistry. In our case, we feel it is necessary to go all the way to a kinetic model, especially because of the case that the product **2** is consumed by the reaction. The decrease of the concentration of **2** over time is clearly visible in Figure 5 both in the experimental data and in the results of our model. The model is, in principle, not unique and other reaction networks might be able to reproduce the experimental concentration profiles as well. However, our model is also consistent with DFT calculations, which pose a severe restriction to the generalization. Additionally, a kinetic model is able to not only consider barriers of elementary steps but also the different concentrations of every species. As an example for this important aspect, the different dynamics of **iPrOBPin** and **2BPin** are highlighted. The concentration of **iPrOBpin** is higher than that of **2Bpin** throughout the reaction even though the DFT calculations suggest similar barriers for both formation pathways. This is because at the beginning the concentration of iPrOH is high, while **2** is absent. At the start of the reaction, **iPrOBPin** is formed very fast, as the rate

depends on the concentrations not only on the barriers. Since **iPrOBPin** is not consumed by any reaction, it remains present. The longer the process proceeds, the less new **iPrOBPin** is formed. If the reaction is continued for more than 2.5 days, the concentration of **2BPin** approaches the concentration of **iPrOBPin** (see Figure S32 of the Supporting Information).

Comparison of DFT results with the kinetic measurement shows that **R2** indeed has to be activated by chloride rather than iodide. A microkinetic model using a barrier of $\Delta G^{\ddagger}$ = 118.0 kJ mol^{-1} for **R2**, the DFT value obtained for iodide, indicates that no reaction takes place (see Figure S2 of the Supporting Information). Fitting the barrier for **R2** to the experimental concentration profile with 118.0 kJ mol^{-1} as the initial value results in a barrier close to the one obtained for chloride with $\Delta G^{\ddagger}$ = 81.7 kJ mol^{-1}.

The measured concentrations show a decrease of the product (**2**) concentration at reaction times beyond 1 day; see Figure 5. While **2** serving as a proton source in reaction **R4** described above consumes **2**, it also produces the same amount of **2** after reaction **R5** and, thus, can not explain the net decrease in **2**. However, the alcohols **2** and iPrOH can directly react with HBPin to form the boron esters **2BPin** and **iPrOBPin** in side reactions **R7** and **R8**. These, and all other reactions included in our kinetic model, are listed in Table 1. **R8** explains the net decrease of the concentration of **2**. We investigated several more side reactions by DFT, which will be discussed below.

Table 1. Elementary Reactions Used to Model the Full Catalytic Cycle and the Corresponding Gibbs Free Energy Barriers Obtained from DFT Calculations ($\Delta G^{\ddagger}_{\text{DFT}}$) and from the Microkinetic Modeling ($\Delta G^{\ddagger}_{\text{KM}}$)

label	reaction	$\Delta G^{\ddagger}_{\text{DFT}}$	$\Delta G^{\ddagger}_{\text{KM}}$
		kJ mol^{-1}	
	catalyst generation		
R1	Cat + THF + **1** → A + Cl$^-$	91.3	91.2
	reaction		
R2	A + HBPin → B	81.7	77.5
R3	B + iPrOH → C + iPrOBPin	36.4	34.8
R4	B + **2** → C + 2BPin	32.8	34.4
	catalyst regeneration		
R5	C + **1** → **2** + A	79.4	75.3
R6	**2** + A → C + **1**	63.4	67.4
	side reactions		
R7	iPrOH + HBPin $\xrightarrow{\text{Cl}^-}$ iPrOBPin + H$_2$	98.8	92.7
R8	**2** + HBPin $\xrightarrow{\text{Cl}^-}$ 2BPin + H$_2$	95.8	89.8

Additionally to the forward reactions, their backward reactions should be considered in a kinetic model. This is done for **R5**, resulting in **R6**. The reactions **R3** and **R4** from **B** to **C** have low barriers and are strongly exothermic so that their reverse reactions can safely be ignored. Similarly, the back reaction of **R2** from **B** back to **A** can be ignored in the model, because it has a significantly larger barrier than both its competitors, **R3** and **R4**. Additionally, it is conceivable that another THF molecule instead of **1** coordinates to Al in an alternative to **R5**, inhibiting the reaction. However, coordination of THF resulted in a barrier of 115.1 kJ mol^{-1}, significantly higher than 79.4 kJ mol^{-1} for **R5**, and is therefore

neglected in the kinetic model. Thus, we arrived at the set of reactions listed in Table 1 for our kinetic model.

We fitted the barriers $\Delta G_{KM}^{\ddagger}$ that enter the kinetic model to match the experimental concentration profiles, as explained in the Computational Details. Thus, $\Delta G_{KM}^{\ddagger}$ values may be considered as reaction barriers resulting from experiment and compared to the DFT data. Overall, we obtain a satisfactory agreement between the concentration profiles from experiment and from our kinetic model; see Figure 5. The largest difference in barriers between DFT and the kinetic model is 6.1 kJ mol^{-1}, found for **R7** (see Table 1). However, as discussed later, the kinetic model is rather insensitive toward **R7**, so that $\Delta G_{KM}^{\ddagger}$ is not well-resolved for **R7**. The second-highest deviation between DFT and the kinetic model is 6.0 kJ mol^{-1} and is obtained for **R8**, which can be reliably extracted with our kinetic model (see discussion below).

The fit was initialized with the DFT barriers $\Delta G_{DFT}^{\ddagger}$. However, the experimental concentration profile can be reproduced almost equally well with a certain variation in some of the barriers. For example, the squared error SE, our measure of the fit, changed by <0.01 mol^2 L^{-2} if the barriers for both reactions, **R3** and **R4**, were increased by up to 30 kJ mol^{-1}. Their relative height does change the quality of the fit, however. Thus, from experiment, we learn the difference in barrier height between **R3** and **R4** but not their absolute values. Similarly, the barrier for reaction **R7** can be decreased by up to 2 kJ mol^{-1} or raised arbitrarily high without changing the quality of the fit by more than 0.01 mol^2 L^{-2}. Thus, the value of $\Delta G_{KM}^{\ddagger}$ = 92.7 kJ mol^{-1} given for **R7** in Table 1 may be understood as a lower bound. Interestingly, this does not apply to **R8**, which is well-defined by the decrease of the product. The model is also rather insensitive to the barrier of the catalyst generation, **R1**, but this value is weakly coupled to the optimum values of some of the other reactions.

Side Reactions. The concentration of the product **2** decreases during the course of the reaction as mentioned above and is visible from Figure 5. Experiments on the esterification of isopropanol with HBpin under standard catalysis conditions estimate that HBPin is consumed in a non-negligible amount due to the side reaction over the course of the catalytic reaction (see Figure S33 in the Supporting Information). One way to explain that is to consider a direct reaction between **2** and HBPin to form H$_2$ and **2BPin**; see **SR1** in Table 2. **SR1** is consistent with the observation of gas production during the experiment. An equivalent reaction is conceivable with iPrOH instead of **2**, denoted **SR2**. The structure of the associated prereactive complex is shown in Figure 6(a). Quantum chemical calculations, however, result in barriers for the bimolecular barrier with respect to the free reactants of 162.0 kJ mol^{-1} for **SR1** and 165.9 kJ mol^{-1} for **SR2**, too high to be of relevance at room temperature.

SR1 might be facilitated by the Al catalyst, starting from state **C**, where **2** is already coordinated to the catalyst. However, in **C**, the oxygen atom of **2**, coordinated to Al, has a lower intrinsic atomic orbital charge (IAO) of −0.49 in comparison to a value of −0.57 for the free alcohol **2**. Therefore, the nucleophilic attack to the boron of HBPin is weaker, which results in a barrier of 212.7 kJ mol^{-1} for **SR1Cat**, even higher than for the noncatalyzed case. All side reactions studied by DFT are listed in Table 2.

An alternative path to consume **2** by HBPin is a reaction similar to **SR4**. The formed adduct **HBAlt** is shown for **SR4** in Figure 6(b), but the same reaction is possible with **2**. The

Table 2. Side Reactions and Their Barriers as Obtained from DFT[a]

label	reaction	$\Delta G_{DFT}^{\ddagger}$ kJ mol^{-1}
SR1	2 + HBPin → 2BPin + H$_2$	162.0
SR1Cat	2 + HBPin $\xrightarrow{\text{Cat}}$ 2BPin + H$_2$	212.7
SR2	iPrOH + HBPin → iPrOBPin + H$_2$	165.9
SR3	1 + HBPin → 2BPin	147.1
SR3Cat	1 + HBPin $\xrightarrow{\text{Cat}}$ 2BPin	170.5
SR4	iPrOH + HBPin → HBAlt	115.0
SR5	HBAlt → iPrOH + HBPin	72.9
SR6	iPrOH + HBPin → H$_2$ + C$_3$H$_6$ + PinBOH	238.8
SR7Cl	iPrOH + HBPin $\xrightarrow{\text{Cl}^-}$ iPrOBPin + H$_2$	98.8
SR7I	iPrOH + HBPin $\xrightarrow{\text{I}^-}$ iPrOBPin + H$_2$	166.9
SR8Cl	2 + HBPin $\xrightarrow{\text{Cl}^-}$ 2BPin + H$_2$	95.8

[a]All barriers are with respect to the free reactants.

adduct contains an alcohol and a hydride functional group and, therefore, is in principle capable of donating a hydride or proton in the main reaction. However, **SR4** is endothermic, and still has a sizable barrier of 115.0 kJ mol^{-1}, still too high to be relevant at room temperature according to our kinetic model.

We considered catalysis of a reaction between **2** and HBPin by a halide ion, similar to our findings for **R2** of the main cycle. The halide could push electron density toward the boron to activate it. However, the calculations show that such a contribution is impeded sterically. Neither chloride nor iodide has the possibility to approach the boron atom close enough. However, our DFT calculations revealed that a halide ion can catalyze the reaction by acting as a proton shuttle from the alcohol to the hydride of HBPin. Thus, we arrive at the same net reaction as **SR2** but catalyzed by iodide (**SR7I**) or chloride (**SR7Cl**). While the effect of iodide is weak, chloride reduces the barrier to 98.8 kJ mol^{-1}. The transition state of **SR7Cl** is illustrated in Figure 6(c). The H−Cl distance has a minimum value of 1.31 Å during the course of the reaction and is close to the bond distance of 1.28 Å for isolated hydrogen chloride calculated at the same level of theory. A similar lowering of the barrier is found for the reaction of **2** with HBPin, **SR8Cl** catalyzed by chloride. The finding of similar barriers for **SR7Cl** and **SR8Cl** is supported by experiments on the catalytic reaction under standard conditions of HBPin with the enantiomerically pure **2** or iPrOH, which show that the two alcohols are converted at virtually the same rate (see Figure S29 of the Supporting Information). The reactions **SR7Cl** and **SR8Cl** are included in our catalytic model as **R7** and **R8**, respectively. Our analysis of possible side reactions shows that the presence of chloride enables these unwanted reactions, which reduce the yield. However, chloride also accelerates the main reaction as a major constituent of state **B** and is, thus, unavoidable in the reaction mixture.

Experimental Investigations. In our previous studies, we noticed that in the presence of a "non"-nucleophilic counterion like PF$_6^-$ still a noticeable productivity remained, which was explained by the generation of a cationic Al center thus releasing a nucleophilic chloride that could activate the borane reagent.[1] Since reactivity was lower than with the correspond-
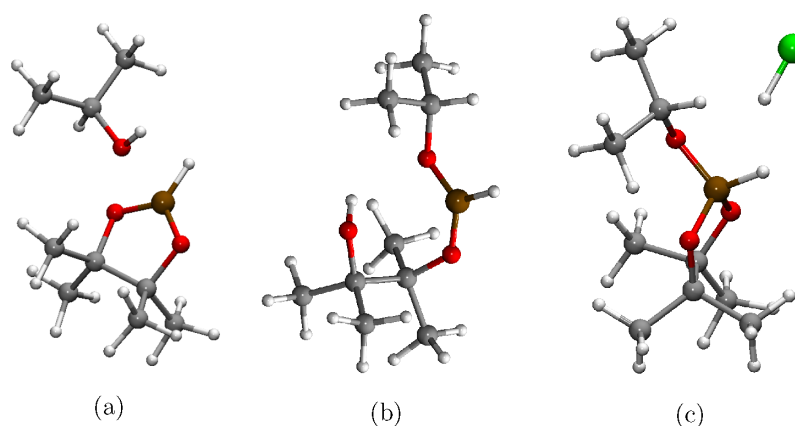
Figure 6. (a) Prereactive complex of **SR2**. (b) Adduct **HBAlt**. (c) The transition state of **SR7Cl**, the reaction of iPrOH (top) and HBPin (bottom) catalyzed by a chloride ion. Boron atoms are shown in brown, oxygen is shown in red, and chloride is shown in green.

ing catalyst bearing an iodide counterion, we speculated that iodide might more efficiently activate the borane than chloride.

However, investigation of additional Al−Cl-based catalysts with other non-nucleophilic counterions revealed a similar activity and enantioselectivity as for our standard catalyst **C1** (see Table 3). This data suggests that chloride does efficiently activate the borane reagents like the above-described calculations suggest.

Table 3. Study of the Impact of Different Counterions in Catalysts C1

C1 (0.05 mol%), c(**1**) = 1 mol/L,
HBPin (2.0 equiv.), iPrOH (1.0 equiv.),
THF, 25 °C, 22 h
then 1 M HCl

C1: X = I
C1-Cl: X = Cl
C1-OTf: X = OTf
C1-BAr^F: X = BAr^F

catalyst	yield[a] [%]	ee[b] [%]	source
C1	99	97	1
C1−Cl	67	93	1
C1−OTf	87	94	this work
C1−BAr^F	91	95	this work

[a]Yield determined by ¹H−NMR of the crude product using an internal standard. [b]The enantiomeric excess was determined by GC.

Because the calculations also suggest that Cl⁻ promotes the consumption of HBPin and both alcohols, iPrOH and **2**, faster than iodide by a dehydrogenative borate ester formation, these background processes were studied experimentally using 0.1 mol % of the corresponding tetrabutyl ammonium salts (TBA) (see Figure 7). More details about the reaction conditions are given in the Supporting Information. Continuous monitoring by ¹H−NMR over 24 h reveals that there is nearly no reaction
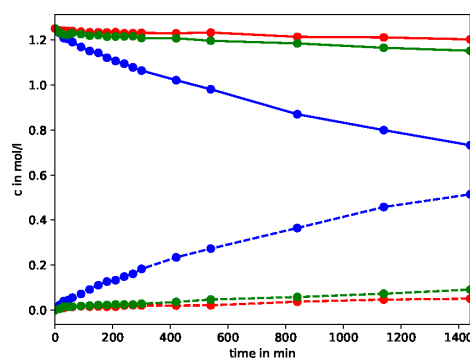
Figure 7. Dehydrogenative esterification using HBPin and **2**. Dotted lines refer to the concentration of **2BPin**, and solid lines refer to the concentration of **2**. Red: no catalyst was used; green: ⁿBu₄NI was used as the catalyst; blue: ⁿBu₄NCl was used as the catalyst. The graphs show the most rapid reaction in the presence of the chloride salt.

between both components in the absence of the halide salts. In contrast, in the presence of the halide salts, HBPin decomposition continues with both alcohols and proceeds significantly more rapidly in the case of Cl⁻.

If as a result of the inherently higher Cl⁻ amount the undesired consumption of HBPin and iPrOH (**SR8Cl**) is the reason for the lower activity of **C1−Cl** compared to **C1**, this effect should be negligible at the start of the reaction, when almost no HBPin has reacted yet. Moreover, these two catalysts should behave significantly differently in contrast to **C1−I**, in which no chloride ion is present. We thus compared the reaction profiles of these three catalysts. In Figure 8, the comparison for the consumption of **1** is shown. The structures of the corresponding catalysts are shown in Figure 8(b), and the reaction conditions and the monitoring of the other compounds in the reaction mixture are shown in Figures S22− S27 of the Supporting Information. As predicted, in the first few minutes, the reactions proceed similarly fast with **C1** and **C1−Cl** and differ from the profile of **C1−I**, suggesting that the latter possesses a different mechanistic aspect. However, also **C1** and **C1−Cl** diverge after about 2 h, probably because the

(a)   (b)
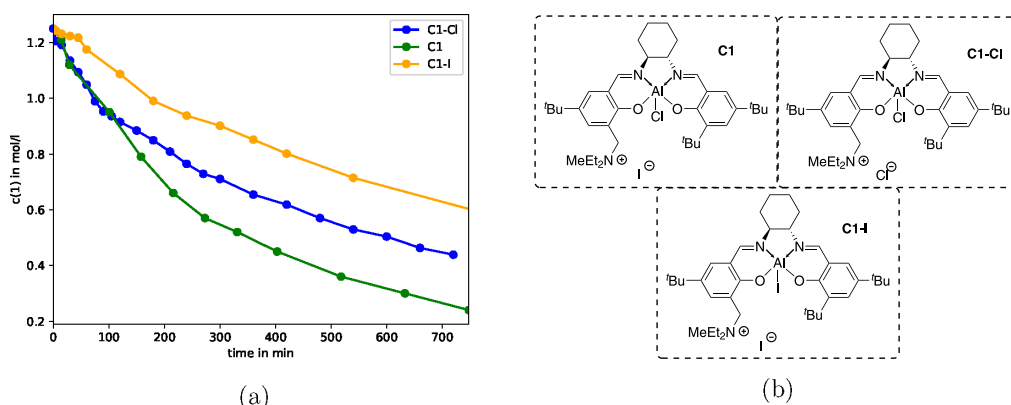
Figure 8. (a): Concentration of **1** when using the standard catalyst **C1** (green curve), **C1−Cl** (blue curve), and **C1−I** (orange curve). (b) Structures of the different catalysts used in (a).

HBPin and isopropanol concentrations more rapidly decrease by the undesired pathways.

Sensitivity Analysis. A sensitivity analysis of a microkinetic model reveals two factors: first, it provides information on the reaction steps or states that dominate the reaction to point out the mechanism's bottleneck, which controls the rate or the enantioselectivity of a reaction. Second, it provides insight into how accurately the Gibbs free energy barriers can be extracted via a fit to measured concentrations. Only if the concentration−time course of a set of reactions is sensitive to a particular barrier can that barrier be extracted reliably.

The concept of a rate-determining step, meaning the slowest step of the reaction, is well-established,[36] but its consequential validity is disputed.[37−40] However, for complex reaction networks, in which species with different concentrations are involved, this concept has drawbacks, as the reaction rate is dependent on both the rate constants and the concentrations. Therefore, a more complete concept for sensitivity analysis is provided by Campbells' concept of rate control.[39] It has been applied in many cases for heterogeneous catalysis,[41,42] but applications in homogeneous catalysis[43,44] are less common. Within this concept, a reaction constant scaled sensitivity RCSS is defined as

$$\text{RCSS} = \frac{k_i}{r}\left(\frac{dr}{dk_i}\right) \tag{1}$$

where r represents the overall rate and k_i represents the rate constant of reaction i. The RCSS is defined for each reaction i and is time-dependent. There are different definitions possible for the overall rate r in our case. While the rate of (**2**) formation may feel intuitive, it turned out to be less informative in our case, because the rate of formation of **2** vanishes during the course of our reaction, leading to a divergence of RCSS. Thus, we choose the rate of reactant (**1**) destruction as r.

The RCSS analysis is given in Figure 9. A positive value indicates that the overall rate is increased by a higher rate constant (lower barrier) of the respective reaction. As can be seen there, accelerating reactions **R2** and **R5** accelerates the overall reaction, while accelerating **R6** slows the overall reaction down in quite exactly a reverse manner as the effect of **R5**. The latter is not surprising, since **R6** is the back-reaction of **R5**.
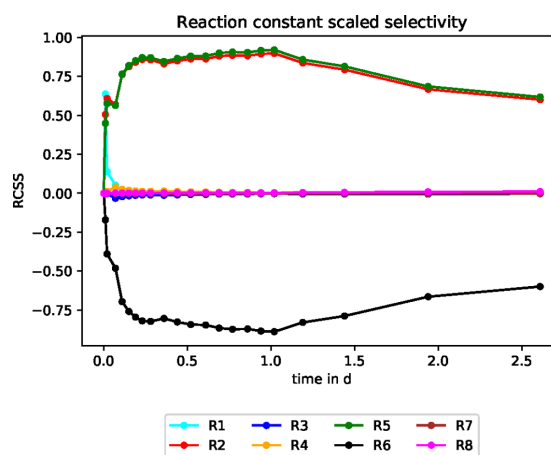
Figure 9. RCSS for each reaction shows a high sensitivity of the overall rate, the destruction of **1**, on **R2**, **R5**, and **R6**.

It is also apparent from Figure 9 that the overall rate is hardly sensitive to the rate constants of **R1**, **R3**, and **R4** and almost totally insensitive to the rate constant of **R7**. It can be expected that **R1** influences the reaction only at the beginning, since it represents the catalyst generation. The insensitivity of the overall kinetics to **R7** was already discussed above. **R3** and **R4** are so fast that the overall rate is independent of them. In the RCSS analysis, any sensitivity to the relative rates of **R3** and **R4** with respect to each other is not visible. The relative rate influences the amounts of **2** and iPrOH consumed as proton sources. These can be measured by the concentration profiles but do not influence the consumption of **1**.

The sensitivity analysis clearly shows that the overall rate is determined by three elementary steps, namely **R2**, **R5**, and **R6**. Such a situation was described previously by the energetic span model.[40] It states that the overall rate, or the turnover frequency (TOF), is determined by two states, rather than by merely *one* reaction step that possesses all the kinetic information. These two states are the TOF-determining intermediate and the TOF-determining transition state. They are picked to maximize the energetic span along the reaction cycle; see Figure 4. In our conditions, the TOF-determining

intermediate is state **C**, and the TOF-determining transition state is **TS2** of **R2**. The activation barrier is the energy difference between them. Since in our mechanism, the TOF-determining intermediate is after the TOF-determining transition state, the Gibbs reaction free energy must be added, resulting in an overall Gibbs free energy barrier of the cycle of $\Delta G_{\text{total}}^{\ddagger} = 97.7$ kJ mol^{-1}. That corresponds to the barrier from **C** to **TS2** of the next cycle. It determines the TOF and the selectivity.

The maximal energetic span between **C** to **TS2** is consistent with our sensitivity analysis, since the energetic span is precisely the sum of the barriers for **R2** and **R5** minus the barrier for **R6**, directly matching the sensitivities found.

Enantioselectivity. The overall reaction shows a high degree of enantioselectivity,[1] which we have not taken into account so far. All energetics were calculated for the main product enantiomer. In the following, species related to the minor enantiomer will be indicated by a prime (**C′**, **TS2′**, ...). As discussed above, the state **TS2** defines the enantioselectivity. As a consequence, the enantiomeric excess can be predicted from DFT data via

$$ee = \frac{1 - \exp\left(-\frac{\Delta\Delta G_{\text{DFT}}^{\ddagger}}{RT}\right)}{1 + \exp\left(-\frac{\Delta\Delta G_{\text{DFT}}^{\ddagger}}{RT}\right)} \qquad (2)$$

with $\Delta\Delta G_{\text{DFT}}^{\ddagger}$ being the difference of the Gibbs free energy between **TS2** and **TS2′**. Herein, R is the gas constant, and T is the temperature. With $\Delta\Delta G_{\text{DFT}}^{\ddagger} = 6.55$ kJ mol^{-1}, the enantiomeric excess predicted by DFT is 86.7%. In comparison, the experimental value of 97% results in $\Delta\Delta G_{\text{exp}}^{\ddagger} = 10.37$ kJ mol^{-1} using eq 2. The enantiomeric excess can, however, be extracted directly from the kinetic model, for which additional reactions were added to consider the formation of the minor enantiomer **2′** (for details, see Supporting Information). Figure 10 shows a very good
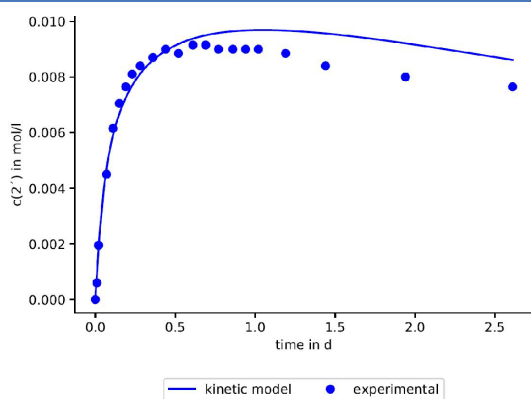
Figure 10. Measured concentration profile (dots) vs results from our kinetic model (line) of the minor enantiomer **2′**.

agreement between experimental values and the kinetic model for $\Delta\Delta G_{\text{KM}}^{\ddagger} = 10.37$ kJ mol^{-1}, which is in fairly good agreement with the DFT values if chemical accuracy is considered.

The reason for the higher Gibbs free energy of **TS2′** compared to **TS2** is illustrated in Figure 11. For **TS2**, the
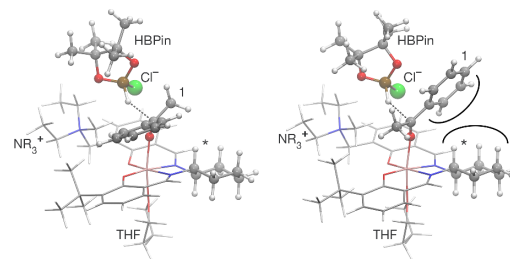
Figure 11. Left: **TS2** to form the main enantiomer, right: **TS2′** to form the minor enantiomer. The stereocenter of the catalyst is marked with an asterisk.

phenyl ring lies nearly flat over the catalyst in order to allow an almost perpendicular attack of the hydride to the electrophilic center (approximately 100°). The stereocenter prevents this in the geometry of **TS2′** as the phenyl ring is sterically hindered by upward facing axial hydrogen atoms of the cyclohexane backbone.

■ CONCLUSION

We have reported a combined quantum chemical, micro-kinetic, and experimental study to investigate the full mechanistic cycle exemplified by the hydroboration of acetophenone with a highly active cooperative Lewis acid–ammonium salt catalyst. We showed that this approach is a powerful tool to investigate important mechanistic details in organic chemistry. We gained consistent Gibbs free energy barriers for the quantum chemical and kinetic model considering a mechanism in which a chloride, released from the catalyst during its activation, instead of an iodide ion, activates the hydride transfer **R2**. **R2** is followed by a fast protonation by either isopropanol (**R3**) or the product alcohol **2** (**R4**) and a subsequent slow exchange of the product by a new reactant (**R5**). In order to explain the decrease of the product concentration during the course of the reaction, we investigated possible side reactions between the product alcohol **2** and HBPin, both quantum mechanically and experimentally. The results show that no reaction is observed between the two components. The side reaction becomes feasible at room temperature by the catalytic activity of chloride, acting as a proton shuttle. We conclude that chloride ions accelerate the main reaction but also facilitate the side reaction **R8** that consumes the product. Considering this interplay of the main catalytic cycle and the side reaction, we obtain agreement between quantum chemical and experimental results via our full microkinetic model.

The microkinetic model was also used to perform a sensitivity analysis, which reveals that the exchange of the product **2** by a new reactant **1** followed by the hydride transfer (**R2**) are rate-determining. **R2** is also the enantiodiscriminating step. We implemented an enantioselective kinetic model from which we directly extracted the $\Delta\Delta G^{\ddagger}$ between paths leading to the two enantiomers. It is in fairly good agreement with the values calculated by DFT, which reveal that the steric hindrance of the asymmetric backbone with the reactant cause an enantioselective reaction.

Overall, we have shown that microkinetic modeling allows to directly combine theory and experiment, which on their own both give limited insight into the catalytic system. Whereas computational investigations allow the study of reaction

barriers, experiments provide the concentrations of each species during the course of the reaction. A full microkinetic model combines the two to reveal important insight in mechanistic details.

COMPUTATIONAL DETAILS

Quantum Chemical Calculations. The structure of the catalyst **C1**, shown in Figure 1, was simplified such that the *t*Bu groups in the *para*-position to the oxygen were removed, as they are assumed not to influence the reaction significantly. All calculations were preformed in the singlet state; all structures of the main catalytic cycle, i.e., **A**, **B**, **C** carry a charge of +1.

To account for the structural complexity of the catalyst (especially of the ammonium moiety), the Conformer—Rotamer Ensemble Sampling Tool[45] has been applied, and the energetically lowest structures by DFT have been used for further investigations.

Molecular geometries for minima and transition states were optimized with the DL-FIND[46] optimization library in ChemShell.[47,48] The program package Turbomole V7.4.1[49] was used for the electronic structure calculations. Geometry optimization and subsequent frequency calculations were performed with density functional theory (DFT), the M06-2X functional,[50] and the def2-SVP basis set.[51,52] The reliability of gas-phase structures has been benchmarked (see Supporting Information). All transition structures were verified to possess only a single mode with imaginary frequency. IRC (internal reaction coordinate) calculations starting from the transition structures were performed to verify their connections to the reactants and products. For TS5, an IRC calculation was not possible. A converged NEB (nudged elastic band) calculation[53] verified the transition state.

At converged geometries, the electronic energy was calculated using the def2-TZVP basis set,[51,52] and the solvent effects were accounted for with the conductor-like screening model (COSMO)[54] using a dielectric constant of $\epsilon = 7.39$ for THF at 298.15 K. For the atomic radii in the cavity, the default values for COSMO were used. Numerical integration was carried out on an m4 grid, and SCF energies were converged for an energy difference of less than 10^{-8} atomic units.

The Gibbs free energy G was calculated at 298.15 K within the RRHO (rigid rotor harmonic oscillator) approximation. Vibrational frequencies less than 100 cm^{-1} were raised to this threshold. It is important to note that bimolecular barriers $\Delta G^{\ddagger,1M}$ are presented according to a reference state of 1 M in the liquid phase. Standard quantum chemical packages usually print Gibbs free energies $\Delta G^{\ddagger,1atm}$ for a reference state of a pressure of 1 atm in the phase. The need to be converted for bimolecular reactions using[55,56]

$$\Delta G^{\ddagger,1M} = \Delta G^{\ddagger,1atm} - RT\ln(V_m c_0) \qquad (3)$$

with the molar volume V_m and the standard concentration c_0.

Intrinsic bond orbitals (IBOs)[57] were calculated based on orbitals of the M06-2X/def2-TZVP level of theory with an exponent of 2 in the localization method. The visualization of the IBOs was realized using the IboView program by Knizia (http://www.iboview.org/).

Microkinetic Modeling. A kinetic model, i.e., a set of ordinary differential equations, was constructed to include all reactions listed in Table 1. It relates the rate of each reaction to the rate constants and the concentrations of each reactant. The set of specific differential equations is given in the Supporting Information. Rate constants were calculated from Gibbs free energy barriers via transition state theory using the Eyring equation

$$k_i = \frac{k_B T}{h} \exp\left(\frac{-\Delta G^{\ddagger}_{KM,i}}{RT}\right) \qquad (4)$$

with the Boltzmann constant k_B and the Planck constant h.

The numerical integration of the kinetic model was performed using the fourth-order Runge–Kutta method with a time step of 0.1 s in an in-house code. The initial concentrations provided by experiment[1] were used.

As the reactions **R3** and **R4** are very fast compared to the others, they cause numerical issues. Even with a time step as small as 10^{-5} s, negative concentrations are received. However, since the preceding step **R2** is comparably slow, the steady-state approximation for [B], d[B]/dt = 0, can be expected to be accurate. It results in

$$[B] = \frac{k_{R2}[A][HBPin]}{k_{R3}[iPrOH] + k_{R4}[2]} \qquad (5)$$

where [.] denotes the concentration of the respective species. Numerical tests with very short time steps showed that the use of the steady-state approximation for B has a negligible influence on the concentrations.

The kinetic model is intended to provide barriers that fit the experimental concentration profile. Thus, we modified $\Delta G^{\ddagger}_{KM}$ for each reaction until the concentrations predicted by our model match the experimentally measured concentrations along the time of the measurements. The deviation is measured by the squared error SE

$$SE = \sum_{n=1}^{N_{Exp}} \left(c_{Exp,n} - c_{KM,n}\right)^2 \qquad (6)$$

where n enumerates the time steps at which measurements were taken, N_{Exp} is the number of measurements, $c_{Exp,n}$ is the measured concentration, and $c_{KM,n}$ is the concentration predicted by the kinetic model.

The fit of the kinetic model is achieved by varying $\Delta G^{\ddagger}_{KM,i}$ in order to minimize SE. This is performed by calculating the derivative of SE with respect to all $\Delta G^{\ddagger}_{KM,i}$ by finite differences and performing a steepest descent minimization. Minimization was continued until ΔSE between two consecutive optimization cycles was less than $5.0 \cdot 10^{-4}$ mol^2 L^{-2}. Many different local minima can be found. In fact, SE is quite independent of some barriers, as discussed above. In order to arrive at a minimum of SE, which is chemically reasonable, we initiated the optimization from the barriers obtained by DFT. With that, a fit with a remaining SE = 0.96 mol^2 L^{-2} was obtained. The resulting barriers and concentration profiles are given in Table S1 of the Supporting Information. This fit shows a too weak decrease of the product (**2**) concentration, compared to experiment. In order to test if we find a better fit, the initial barriers for **R7** and **R8** were reduced by 6 kJ mol^{-1}, and the fitting procedure was repeated. Indeed, this resulted in a model with a lower SE of SE = 0.73 mol^2 L^{-2}, which was used in the subsequent analysis, in Table 1, and in Figure 5. Obviously, it is impossible to guarantee that the global minimum was found. However, a decent fit to the experimental concentrations was obtained. It should be noted that the remaining deviation is partially caused by noise in the experimental data. For example, the sum of all concentrations containing boron should, at any

point in time, correspond to the initial concentration of HBPin, 2.5 M in our case. However, the measured values are generally higher and deviate by up to 2.76 M from that value, while the kinetic model reproduced that sum accurately.

For the sensitivity analysis, the RCSS was calculated using eq 1 and using a finite-difference gradient $\frac{dr}{dk_i}$ with a step width of 1% of the respective rate constant. The rate $r = \frac{d[1]}{dt}$ was also calculated by finite differences between two points where measurements exist. In this time interval, the course of concentration **1** was propagated with the given barriers, set back to the initial concentration, and propagated with the slightly reduced and increased barriers, respectively, to evaluate the gradient. For the next time interval, the concentration was set back to the numerically evaluated values for the given barrier, and the procedure was repeated.

ASSOCIATED CONTENT

⑤ℐ Supporting Information

The Supporting Information is available free of charge at https://pubs.acs.org/doi/10.1021/acscatal.1c05440.

Differential equations and local minimum of the kinetic model, details about the enantioselective kinetic model, experimental details about the catalyst synthesis and kinetic measurements, *xyz* coordinates of DFT structures (PDF)

AUTHOR INFORMATION

Corresponding Author

Johannes Kästner − *Institute for Theoretical Chemistry, University of Stuttgart, 70569 Stuttgart, Germany;* ⊙ orcid.org/0000-0001-6178-7669; Phone: +49 (0)711 685-64473; Email: kaestner@theochem.uni-stuttgart.de

Authors

Juliane Heitkämper − *Institute for Theoretical Chemistry, University of Stuttgart, 70569 Stuttgart, Germany*

Justin Herrmann − *Institute of Organic Chemistry, University of Stuttgart, 70569 Stuttgart, Germany*

Marvin Titze − *Institute of Organic Chemistry, University of Stuttgart, 70569 Stuttgart, Germany*

Soeren M. Bauch − *Institute for Theoretical Chemistry, University of Stuttgart, 70569 Stuttgart, Germany*

René Peters − *Institute of Organic Chemistry, University of Stuttgart, 70569 Stuttgart, Germany;* ⊙ orcid.org/0000-0002-6668-4017

Complete contact information is available at:
https://pubs.acs.org/10.1021/acscatal.1c05440

Notes

The authors declare no competing financial interest.

REFERENCES

(1) Titze, M.; Heitkämper, J.; Junge, T.; Kästner, J.; Peters, R. Highly Active Cooperative Lewis Acid—Ammonium Salt Catalyst for the Enantioselective Hydroboration of Ketones. *Angew. Chem., Int. Ed.* **2021**, *60*, 5544−5553.

(2) Kull, T.; Peters, R. Contact ion pair directed Lewis acid catalysis: asymmetric synthesis of trans-configured beta-lactones. *Angew. Chem., Int. Ed.* **2008**, *47*, 5461−5464.

(3) Kull, T.; Cabrera, J.; Peters, R. Catalytic asymmetric synthesis of trans-configured beta-lactones: cooperation of Lewis acid and ion pair catalysis. *Chem. Eur. J.* **2010**, *16*, 9132−9139.

(4) Meier, P.; Broghammer, F.; Latendorf, K.; Rauhut, G.; Peters, R. Cooperative Al(salen)-pyridinium catalysts for the asymmetric synthesis of trans-configured *β*-lactones by 2 + 2-cyclocondensation of acylbromides and aldehydes: investigation of pyridinium substituent effects. *Molecules* **2012**, *17*, 7121−7150.

(5) Broghammer, F.; Brodbeck, D.; Junge, T.; Peters, R. Cooperative Lewis acid−onium salt catalysis as tool for the desymmetrization of meso-epoxides. *Chem. Commun.* **2017**, *53*, 1156−1159.

(6) Brodbeck, D.; Broghammer, F.; Meisner, J.; Klepp, J.; Garnier, D.; Frey, W.; Kästner, J.; Peters, R. An Aluminum Fluoride Complex with an Appended Ammonium Salt as an Exceptionally Active Cooperative Catalyst for the Asymmetric Carboxycyanation of Aldehydes. *Angew. Chem., Int. Ed.* **2017**, *56*, 4056−4060.

(7) Brodbeck, D.; Álvarez-Barcia, S.; Meisner, J.; Broghammer, F.; Klepp, J.; Garnier, D.; Frey, W.; Kästner, J.; Peters, R. Asymmetric Carboxycyanation of Aldehydes by Cooperative AlF/Onium Salt Catalysts: from Cyanoformate to KCN as Cyanide Source. *Chem. Eur. J.* **2019**, *25*, 1515−1524.

(8) Noyori, R.; Ohkuma, T. Asymmetric Catalysis by Architectural and Functional Molecular Engineering: Practical Chemo- and Stereoselective Hydrogenation of Ketones. *Angew. Chem., Int. Ed.* **2001**, *40*, 40−73.

(9) Noyori, R.; Koizumi, M.; Ishii, D.; Ohkuma, T. Asymmetric hydrogenation via architectural and functional molecular engineering. *Pure Appl. Chem.* **2001**, *73*, 227−232.

(10) Ohkuma, T.; Kitamura, M.; Noyori, R. Ligand design for catalytic asymmetric reduction. *New Frontiers in Asymmetric Catalysis* **2006**, 1−32.

(11) Zaidlewicz, M.; Pakulski, M. M. In *Science of Synthesis, Stereoselective Synthesis*; de Vries, J. G., Molander, G. A., Evans, P. A., Eds.; Thieme, 2011; Vol. 2, pp 59−131.

(12) Arai, N.; Ohkuma, T. In *Science of Synthesis, Stereoselective Synthesis*; de Vries, J. G., Molander, G. A., Evans, P. A., Eds.; Thieme, 2011; Vol. 2, pp 9−57.

(13) Gröger, H.; Borchert, S.; Krausser, M.; Hummel, W. In *Encyclopedia of Industrial Biotechnology*; Flickinger, M., Ed.; 2010; Vol. 3, pp 2094−2110.

(14) Shende, V. S.; Singh, P.; Bhanage, B. M. Recent trends in organocatalyzed asymmetric reduction of prochiral ketones. *Catal. Sci. Technol.* **2018**, *8*, 955−969.

(15) Yang, Z.-H.; Zeng, R.; Yang, G.; Wang, Y.; Li, L.-Z.; Lv, Z.-S.; Yao, M.; Lai, B. Asymmetric reduction of prochiral ketones to chiral alcohols catalyzed by plants tissue. *J. Ind. Microbiol. Biotechnol.* **2008**, *35*, 1047.

(16) Chen, B.-S.; Ribeiro de Souza, F. Z. Enzymatic synthesis of enantiopure alcohols: current state and perspectives. *RSC Adv.* **2019**, *9*, 2102−2115.

(17) Cho, B. T. Recent development and improvement for boron hydride-based catalytic asymmetric reduction of unsymmetrical ketones. *Chem. Soc. Rev.* **2009**, *38*, 443−452.

(18) Shegavi, M. L.; Bose, S. K. Recent advances in the catalytic hydroboration of carbonyl compounds. *Catal. Sci. Technol.* **2019**, *9*, 3307−3336.

(19) Brown, H. C.; Ramachandran, P. V. Asymmetric reduction with chiral organoboranes based on α-pinene. *Acc. Chem. Res.* **1992**, *25*, 16−24.

(20) Ramachandran, P. V.; Brown, H. C. Recent Advances in Asymmetric Reductions with B-Chlorodiisopinocampheylborane. *Reductions in organic synthesis* **1996**, *641*, 84−97.

(21) Kaur, P.; Khatik, G. L.; Nayak, S. K. A Review on Advances in Organoborane-Chemistry: Versatile Tool in Asymmetric Synthesis. *Curr. Org. Synth.* **2017**, *14*, 665−682.

(22) Hall, D. G. *Boronic Acids: Preparation, Applications in Organic Synthesis and Medicine*, 1st ed.; John Wiley & Sons, 2006.

(23) DeFrancesco, H.; Dudley, J.; Coca, A. Boron Chemistry: An Overview. *Boron reagents in synthesis* **2016**, *1236*, 1−25.

(24) Guo, J.; Chen, J.; Lu, Z. Cobalt-catalyzed asymmetric hydroboration of aryl ketones with pinacolborane. *Chem. Commun.* **2015**, *51*, 5725−5727.

(25) Vasilenko, V.; Blasius, C. K.; Wadepohl, H.; Gade, L. H. Mechanism-Based Enantiodivergence in Manganese Reduction Catalysis: A Chiral Pincer Complex for the Highly Enantioselective Hydroboration of Ketones. *Angew. Chem., Int. Ed.* **2017**, *56*, 8393−8397.

(26) Blasius, C. K.; Vasilenko, V.; Gade, L. H. Ultrafast Iron-Catalyzed Reduction of Functionalized Ketones: Highly Enantioselective Synthesis of Halohydrins, Oxaheterocycles, and Aminoalcohols. *Angew. Chem., Int. Ed.* **2018**, *57*, 10231−10235.

(27) Vasilenko, V.; Blasius, C. K.; Gade, L. H. One-Pot Sequential Kinetic Profiling of a Highly Reactive Manganese Catalyst for Ketone Hydroboration: Leveraging σ-Bond Metathesis via Alkoxide Exchange Steps. *J. Am. Chem. Soc.* **2018**, *140*, 9244−9254.

(28) Magre, M.; Maity, B.; Falconnet, A.; Cavallo, L.; Rueping, M. Magnesium-Catalyzed Hydroboration of Terminal and Internal Alkynes. *Angew. Chem., Int. Ed.* **2019**, *58*, 7025−7029.

(29) Lebedev, Y.; Polishchuk, I.; Maity, B.; Dinis Veloso Guerreiro, M.; Cavallo, L.; Rueping, M. Asymmetric Hydroboration of Heteroaryl Ketones by Aluminum Catalysis. *J. Am. Chem. Soc.* **2019**, *141*, 19415−19423.

(30) Vasilenko, V.; Blasius, C. K.; Wadepohl, H.; Gade, L. H. Borohydride intermediates pave the way for magnesium-catalysed enantioselective ketone reduction. *Chem. Commun.* **2020**, *56*, 1203−1206.

(31) Liu, W.; Guo, J.; Xing, S.; Lu, Z. Highly Enantioselective Cobalt-Catalyzed Hydroboration of Diaryl Ketones. *Org. Lett.* **2020**, *22*, 2532−2536.

(32) Liu, W.; Lu, Z. Application of Pinacolborane in Catalytic Enantioselective Hydroboration of Ketones and Imines. *Chin. J. Org. Chem.* **2020**, *40*, 3596.

(33) Wang, R.; Park, S. Recent Advances in Metal-Catalyzed Asymmetric Hydroboration of Ketones. *ChemCatChem.* **2021**, *13*, 1898−1919.

(34) Blackmond, D. G. Kinetic Profiling of Catalytic Organic Reactions as a Mechanistic Tool. *J. Am. Chem. Soc.* **2015**, *137*, 10852−10866.

(35) Nielsen, C. D.-T.; Burés, J. Visual kinetic analysis. *Chem. Sci.* **2019**, *10*, 348−353.

(36) Murdoch, J. R. What is the rate-limiting step of a multistep reaction? *J. Chem. Educ.* **1981**, *58*, 32.

(37) Laidler, K. J. Rate controlling step: A necessary or useful concept? *J. Chem. Educ.* **1988**, *65*, 250.

(38) Boyd, R. K. Some common oversimplifications in teaching chemical kinetics. *J. Chem. Educ.* **1978**, *55*, 84.

(39) Campbell, C. T. The Degree of Rate Control: A Powerful Tool for Catalysis Research. *ACS Catal.* **2017**, *7*, 2770−2779.

(40) Kozuch, S.; Shaik, S. How to conceptualize catalytic cycles? The energetic span model. *Acc. Chem. Res.* **2011**, *44*, 101−110.

(41) Agarwal, N.; Sanchez-Castillo, M. A.; Cortright, R. D.; Madon, R. J.; Dumesic, J. A. Catalytic Cracking of Isobutane and 2-Methylhexane over USY Zeolite: Identification of Kinetically Significant Reaction Steps. *Ind. Eng. Chem. Res.* **2002**, *41*, 4016−4027.

(42) Dix, S. T.; Scott, J. K.; Getman, R. B.; Campbell, C. T. Using degrees of rate control to improve selective n-butane oxidation over model MOF-encapsulated catalysts: sterically-constrained Ag3Pd(111). *Faraday Discuss.* **2016**, *188*, 21−38.

(43) Brezny, A. C.; Landis, C. R. Development of a Comprehensive Microkinetic Model for Rh(bis(diazaphospholane))-Catalyzed Hydroformylation. *ACS Catal.* **2019**, *9*, 2501−2513.

(44) Ho, M.-H.; Rousseau, R.; Roberts, J. A. S.; Wiedner, E. S.; Dupuis, M.; DuBois, D. L.; Bullock, R. M.; Raugei, S. Ab Initio-Based Kinetic Modeling for the Design of Molecular Catalysts: The Case of H_2 Production Electrocatalysts. *ACS Catal.* **2015**, *5*, 5436−5452.

(45) Pracht, P.; Bohle, F.; Grimme, S. Automated exploration of the low-energy chemical space with fast quantum chemical methods. *Phys. Chem. Chem. Phys.* **2020**, *22*, 7169−7192.

(46) Kästner, J.; Carr, J. M.; Keal, T. W.; Thiel, W.; Wander, A.; Sherwood, P. DL-FIND: an open-source geometry optimizer for atomistic simulations. *J. Phys. Chem. A* **2009**, *113*, 11856−11865.

(47) Sherwood, P.; et al. QUASI: A general purpose implementation of the QM/MM approach and its application to problems in catalysis. *J. Mol. Struct.* **2003**, *632*, 1−28.

(48) Metz, S.; Kästner, J.; Sokol, A. A.; Keal, T. W.; Sherwood, P. ChemShell—a modular software package for QM/MM simulations. *Wiley Interdiscip. Rev. Comput. Mol. Sci.* **2014**, *4*, 101−110.

(49) *TURBOMOLE*, V7.4, 2019, a development of University of Karlsruhe and Forschungszentrum.

(50) Zhao, Y.; Truhlar, D. G. The M06 suite of density functionals for main group thermochemistry, thermochemical kinetics, non-covalent interactions, excited states, and transition elements: two new functionals and systematic testing of four M06-class functionals and 12 other functionals. *Theor. Chem. Acc.* **2008**, *120*, 215−241.

(51) Weigend, F.; Ahlrichs, R. Balanced basis sets of split valence, triple zeta valence and quadruple zeta valence quality for H to Rn: Design and assessment of accuracy. *Phys. Chem. Chem. Phys.* **2005**, *7*, 3297−3305.

(52) Weigend, F. Accurate Coulomb-fitting basis sets for H to Rn. *Phys. Chem. Chem. Phys.* **2006**, *8*, 1057−1065.

(53) Henkelman, G.; Uberuaga, B. P.; Jónsson, H. A climbing image nudged elastic band method for finding saddle points and minimum energy paths. *J. Chem. Phys.* **2000**, *113*, 9901−9904.

(54) Klamt, A.; Schüürmann, G. COSMO: a new approach to dielectric screening in solvents with explicit expressions for the screening energy and its gradient. *J. Chem. Soc., Perkin trans. 2* **1993**, 799−805.

(55) Besora, M.; Maseras, F. Microkinetic modeling in homogeneous catalysis. *WIREs Comput. Mol. Sci.* **2018**, *8*, No. e1372.

(56) Harvey, J. N.; Himo, F.; Maseras, F.; Perrin, L. Scope and Challenge of Computational Methods for Studying Mechanism and Reactivity in Homogeneous Catalysis. *ACS Catal.* **2019**, *9*, 6803−6813.

(57) Knizia, G. Intrinsic Atomic Orbitals: An Unbiased Bridge between Quantum Theory and Chemical Concepts. *J. Chem. Theory Comput.* **2013**, *9*, 4834−4843.

4   Discussion

Contemporary research practices often incorporate computational methods alongside experimental studies to advance the development of novel reactions. These methods extend the experimental investigation of reaction performance by providing a comprehensive insight into the reaction mechanism on a molecular scale. While computational protocols have been mainly limited to academic research in the last decade, they are increasingly becoming an integral part of industrial research. This calls for reliable and generalizable methods. Recent reviews by the references 18, 20, and 77 present both the current state-of-the-art and the challenges within this dynamic research field. Also, the present thesis aims to contribute to the discussion of how computational chemistry can reliably investigate chemical reactivity in homogeneous catalysis, and which methodologies can be employed to maximize the utility of these calculations.

This thesis employs computational methods to investigate three catalytic reactions, which are summarized in Figure 4.1. The results, discussed in Chapter 3, serve as a foundation for the subsequent chapter's exploration of the challenges, opportunities, and constraints within computational homogeneous catalysis.

4.1   Studying the Potential Energy Landscape

One unique characteristic of catalytic reactions is the repetitive nature of the potential energy surface (PES). The overall reaction usually breaks down into multiple consecutive elementary steps that start over again after rebuilding the catalyst. As a result, the cyclic nature characteristic of catalytic reactions appears. For an arbitrary reaction, the consequence is illustrated in Figure 4.2. Note that the Gibbs free energy, discussed in Section 2.1.2 in more detail, is plotted. This quantity is used in homogeneous catalysis instead of electronic energy as it is a measure of the driving force of a reaction at constant pressure. Assuming a non-catalytic reaction A $\rightarrow$ C, the step from A to TS$_B$ is the bottleneck, or rate determining step (RDS),[78] of the reaction. It is noted that the consequential validity of one rate-determining step due to oversimplification is
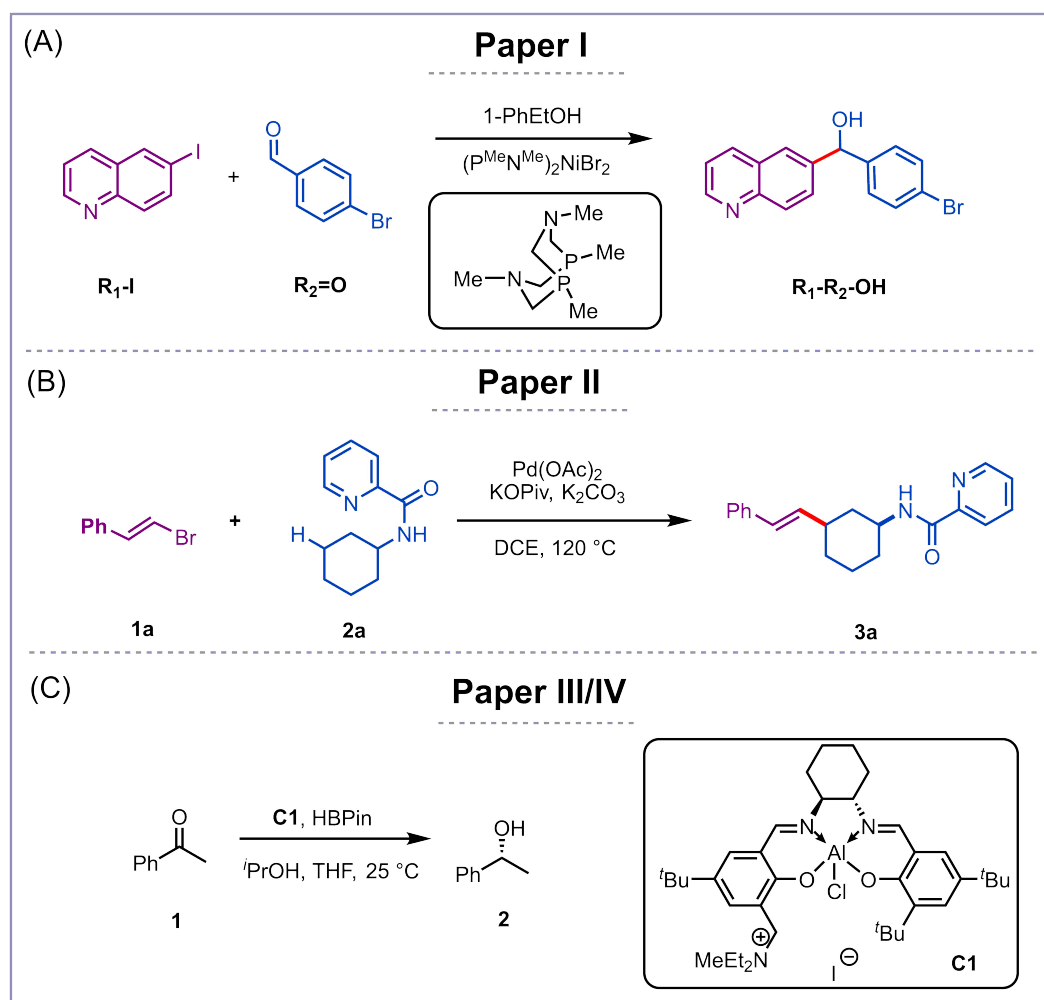
Figure 4.1: Overview of the reactions examined in this thesis. (A) Ni-catalyzed aldehyde arylation reaction facilitated by a 1,5-diaza-3,7-diphosphacyclooctane ligand,[5] (B) directed palladium-catalyzed γ-C(sp^3)-H alkenylation of (aza and oxa) cyclohexanamines with bromoalkenes,[7] (C) cooperative Lewis acid and ammonium salt catalyst for the enantioselective hydroboration of ketones.[10,11]

disputed in the literature.[41,79,80] This is particularly true for catalytic reactions. Closing the catalytic cycle by releasing the product from C and binding a new reactant results in the re-formation of A, shifted by the reaction energy ΔG_R. Overall, TS$_B$ has to be reached from C rather than from A. To account for that, Kozuch *et al.* introduced an energetic span δG to conceptualize catalytic cycles.[81] It includes that the overall rate, or the turnover frequency (TOF), is determined by two independent states rather than one reaction step. As shown in Figure 4.2, they are chosen such that they maximize the energetic span along the reaction cycle and are termed TOF-determining intermediate

(TDI) and TOF-determining transition state (TDTS).
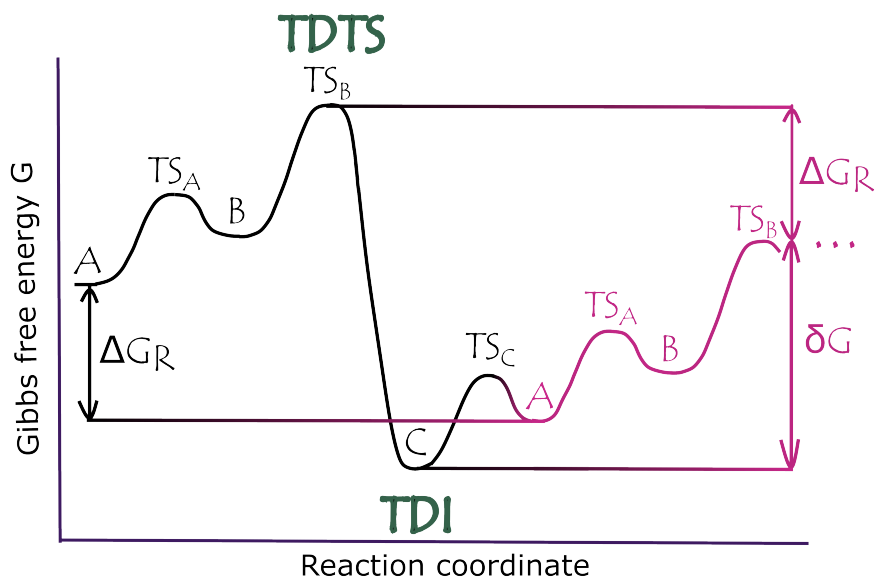
Figure 4.2: Gibbs free energy profile (at standard conditions) of a catalytic reaction with a reaction energy ΔG_R and an energetic span δG. The first catalytic cycle is drawn in black and the second in pink.

As demonstrated by the energetic span concept, the multi-step character and cyclic nature of the reactions require examining the TDI and TDTS of the overall reaction. They can be part of different mechanistic steps. This complexity is evident in all three reactions investigated within this thesis. It's crucial to exercise caution when solely focusing on individual reaction steps, a practice often undertaken to explore specific aspects such as the stereoselectivity of a reaction. To accurately grasp the states governing chemical reactivity, a comprehensive study of the entire mechanism is indispensable.

This point is underscored by the investigation of the Pd-catalyzed γ-C(sp^3)-H alkenylation of cyclohexylamine with 1-bromoalkenes (see Figure 4.1(B)). Pd-catalyzed C-H bond functionalizations emerge as an important tool to form carbon–carbon bonds. However, the utilization of alkenyl halides as reagents poses particular challenges. These reactions typically require superstoichiometric halide scavenging silver reagents. Furthermore, they are typically confined to alkenyl iodides, which are both more costly and less readily accessible compared to alkenyl bromides. Replacing silver salts from the reaction protocols, for instance, with potassium salts, is desirable. Potassium salts are more abundant, cost-effective, and generate less waste owing to their lower molec-

ular weight.[7] The publication incorporated into this thesis introduces a novel and efficient silver-free reaction protocol utilizing alkenyl bromides. This work was published together with experimental collaborators Karthik Gadde, Narendraprasad Reddy Bheemireddy, and Prof. Bert Maes from the University of Antwerp. Quantum chemical calculations from the author of this thesis are employed to elucidate why these reactants are particularly challenging and why silver salts are unnecessary in this alkenylation protocol.

As shown in Figure 4.3 and discussed in Section 3.2 in more detail, the reaction follows a Pd(II)/Pd(IV) pathway. An examination of the energetic span reveals that the transition state of the $C(sp^3)$-H activation, $\mathbf{TSI_{OPiv}}$, is rate-determining. This state remains unaffected by substituents on the 1-bromoalkenes. However, this is not the case for the resting state $\mathbf{V_{Br,3a}}$, where the palladium center strongly coordinates with the reaction products containing the C=C bond of the utilized alkenes. The stability of this state is highly dependent on substituents at the bromoalkenes. Comparing the energetic stabilities of resting states across different reactants revealed that this state is destabilized for ethenyl groups with electron-withdrawing groups. These groups reduce the electron density at the double bond, resulting in a weaker interaction between Pd(II) and the double bond. Consequently, electron-donating substituents result in lower conversions, aligning with the observed trend in the experimental performance of various substituents.

The overall remarkable stability of this sink, partly attributed to the interaction between the double bond and the palladium center, could potentially pose challenges in the utilization of alkenyl bromides and call the need of silver halide scavengers. Also in the present study, the resulting energetic span exceeds the appropriate range for the given temperature. However, the calculations unveil the pivotal role of co-catalyst KOPiv and the solvent DCE. In the presence of a catalytic amount of KOPiv, a bromide ligand in the resting state is exchanged by a pivalate to form $\mathbf{V_{OPiv,3a}}$. This destabilizes this complex and decreases the energetic span. At the same time, KBr precipitates, enabling this endergonic reaction step. This insight prompted the screening of greener solvents than the utilized toxic DCE, with a key criterion being the insolubility of KBr. Experimentally it was found that 1,4-dioxane and t-amyl alcohol are potentially suitable solvents, but DCE proved to be a more general solvent for a wider range of reactants.

Yet, the effectiveness of a reaction isn't solely defined by the sheer magnitude of the energetic span, but also by the intricate balance between competing reaction pathways. This aspect is exemplified by the DFT study of the catalytic reaction between aryl
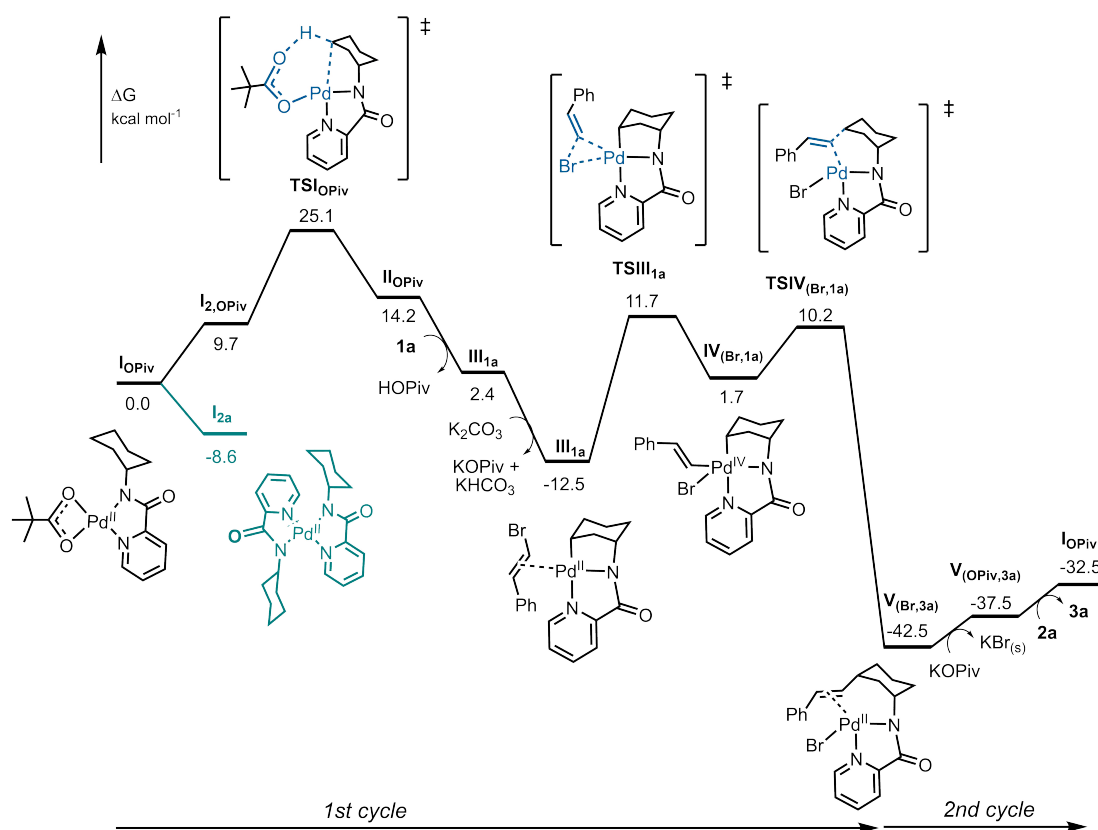
Figure 4.3: Energy diagram for the γ-C(sp^3)-H alkenylation of N-picolinoylcyclohexanamine (**2a**) with (E)-β-bromostyrene (**1a**). Reprinted from reference 7.

iodides and aldehydes, catalyzed by a metal catalyst that combines nickel and a 1,5-diaza-3,7-diphosphacyclooctane ligand (see Figure 4.1(A)). The energy profile and important structures are shown in Figure 4.4. For a comprehensive overview of the reaction mechanism and the computational details, the reader is referred to Section 3.1. The findings challenge the proposed mechanism in the literature[6] that involves a Ni(0) species. Instead, a direct path was discovered, taking shortcuts following the course of Ni(II) (see Figure 4.4, blue line). Additionally, an alternative pathway has been unveiled in which the ligand is not innocent but actively involved in the transfer of a hydride (see Figure 4.4, black line). Unexpectedly, this alternative mechanism also involves a Ni(0) intermediate. A critical factor influencing the reaction's performance was identified as a competitive side reaction, forming the stable product **R$_1$-H** from **R$_1$-I** (see Figure 4.4, red line). This reaction channel results in a decreased conversion towards the desired product. Considering all reactions, the yield of the reaction is influenced by the interplay among the various pathways.

Identifying the energetic span of the overall reaction offers an efficient approach to exploring the experimental performance of different ligands by examining their influence on the relevant states, as shown in Figure 4.5 for the two ligands $P^{Cy}NAr^{CF3}$ and $P^{Cy}NAr^{OMe}$. With this approach, it's unnecessary to recompute the entire mechanism with different ligands; only the states that determine the energetic span need to be analyzed, namely intermediate **VI** and transition state **TS$_{II}$**. As depicted in Figure 4.5, certain ligands slightly favor the side reaction, while others promote the main reaction. This highlights the importance of ensuring that all reaction pathways or side reactions are discovered and considered. The automated reaction discovery, which is elaborated on later in Section 4.5, would help prevent the overlooking of crucial reaction channels.

4.2 Orbital Localization Methods

Various methods are available to address different aspects of chemical reactivity. First-principles electronic structure theory, or DFT in the present thesis, is used to explore the energy landscape of the reaction. This gives fundamental insights into the relevant elementary steps and competing reactions of a complex reaction mechanism as discussed in the previous section. In addition to exploring the PES, quantum chemical tools such as localization methods aid in extracting chemical information from the calculated wave function of key intermediates. This can assist in quantitatively unraveling important interactions. The theoretical principles of the localization methods are covered in Section 2.3.3.

For the Pd-catalyzed γ-C(sp^3)-H alkenylation of N-picolinoylcyclohexanamine (see Figure 4.1(B)), for which the energy diagram of the mechanism is shown in Figure 4.3, the TDI is a highly stable sink.

The natural bond orbitals (NBO) localization method[70,71] has been further used to study this crucial intermediate. Orbitals akin to those illustrated in Figure 4.6 emerge, revealing a π donation from the ligand to the d orbital of the metal center and a back donation from the metal center to a π^* orbital of the ligand. Indeed, it's fascinating how fundamental qualitative concepts from inorganic chemistry, such as assessing the stabilities of complexes based on their ability to donate electron density from the coordination center to ligands and vice versa, naturally emerge from the calculated wavefunction. This highlights the role of localization methods as a bridge between
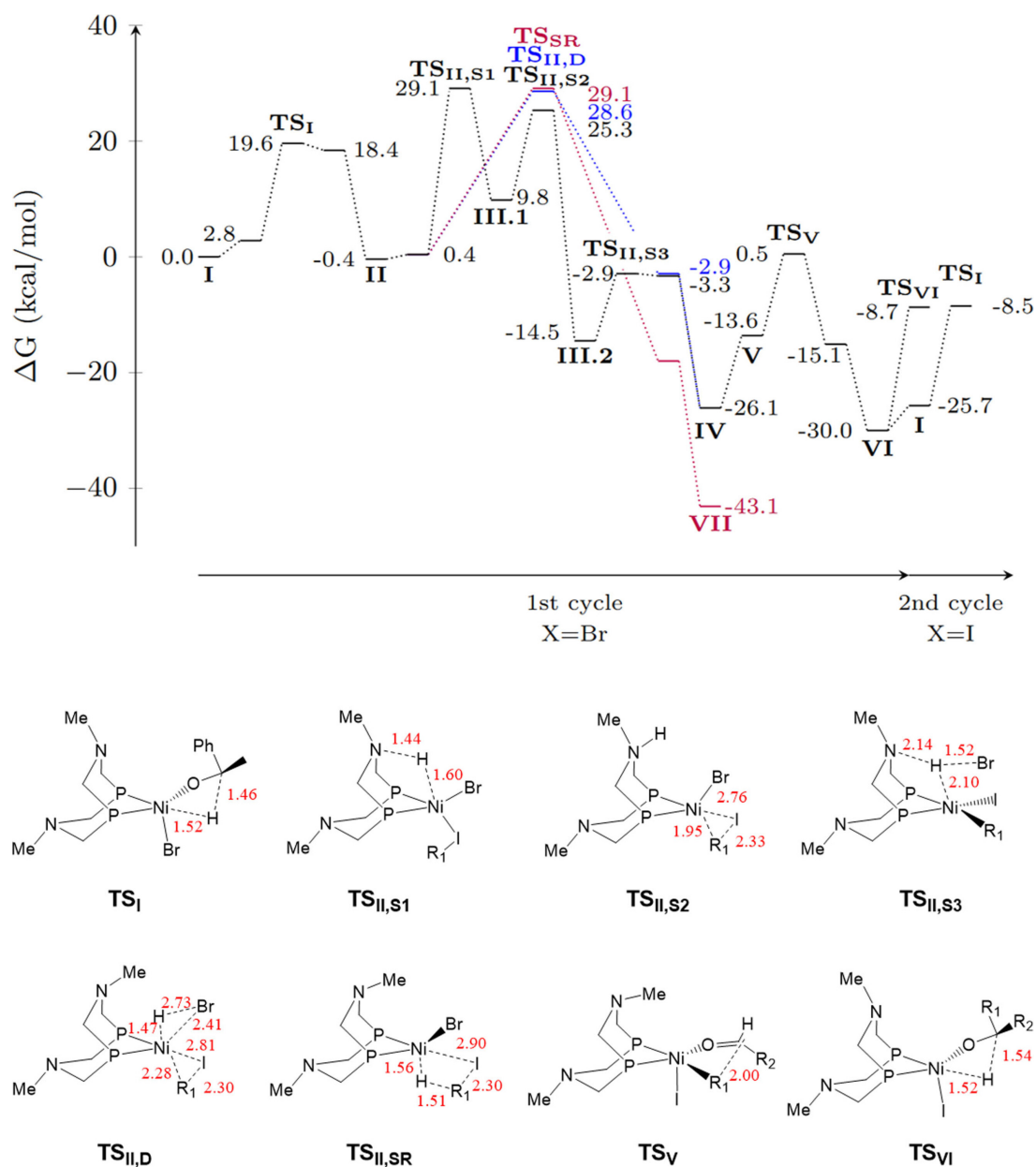
Figure 4.4: Energy diagram of the investigated Ni-catalytic aldehyde arylation reaction facilitated by a 1,5-diaza-3,7-diphosphacyclooctane ligand (above) and structures of the transition states (below). Relative Gibbs energies are given in kcal mol^{-1} and selected distances in red are given in Å. Reprinted from reference 5.

computational techniques and established concepts in inorganic chemistry.

Moreover, the NBO method provides a quantitative approach for calculating the interaction energies between the ligand and the coordination center (see Section 2.3.3), shedding light on the individual ligands' roles. Examination of the Pd(IV) species $\mathbf{IV_{Br,1a}}$ of the reaction reveals that the interaction between the amide ligand and
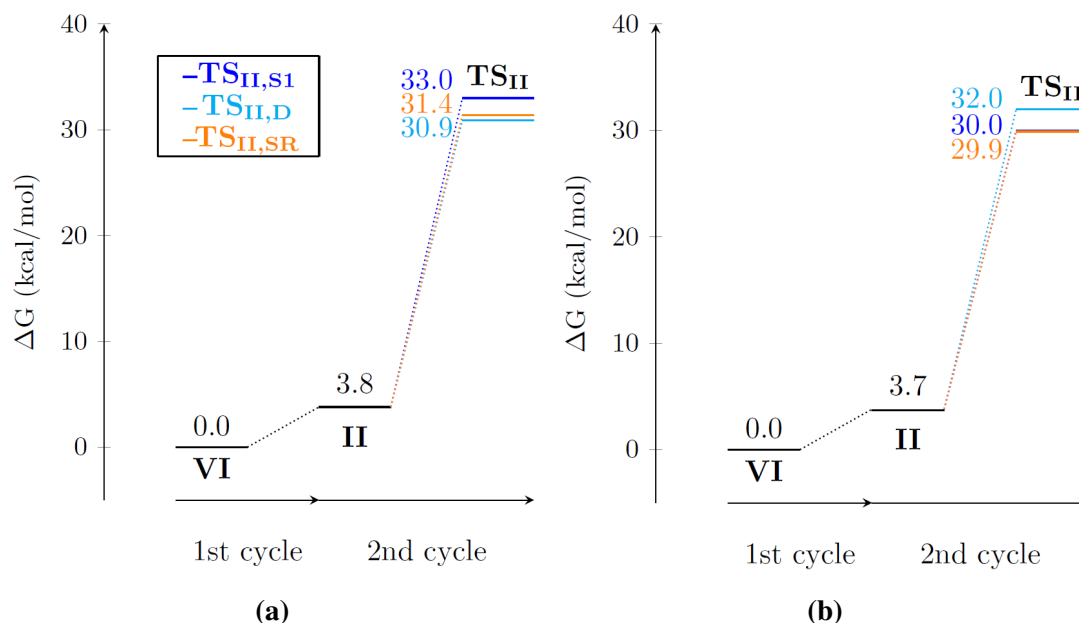
Figure 4.5: Energetic span for the Ni-catalytic aldehyde arylation reaction facilitated by a 1,5-diaza-3,7-diphosphacyclooctane ligand using (a) the $P^{Cy}NAr^{CF3}$ catalyst and (b) the $P^{Cy}NAr^{OMe}$ catalyst. Relative Gibbs energies are given in kcal mol^{-1}. Reprinted from reference 5.

palladium center significantly surpasses the strength of other interactions. For instance, this interaction, characterized by a σ donation of the amide ligand to the palladium center, exhibits a substantial stabilization energy of 117.5 kcal mol^{-1}. In contrast, the stabilization energy for the σ donation of pyridine was determined to be 38.1 kcal mol^{-1}. This analysis suggests that the amide group plays a crucial role as a ligand, facilitating a Pd(II)/Pd(IV) mechanism despite the typically high instability of Pd(IV) intermediates.

Localization methods also play a pivotal role in uncovering the dual activation in the study of the asymmetric hydroboration of ketones by a cooperative Lewis acid–onium salt catalyst (see Figure 4.1(C)). Experiments to investigate this reaction were carried out by Marvin Titze and Prof. Peters from the Institute of Organic Chemistry at the University of Stuttgart. The energy landscape has been calculated within this thesis to elucidate possible reaction mechanisms and competitive side reactions (see Section 3.3 and Section 3.4 for details). It was revealed that the hydride transfer from the borane to the ketone, constituting the actual reduction, is rate-determining. Simultaneously to the hydride transfer, the borane binds to the free iodide, illustrated in Figure 4.7.

(a) **(b)**
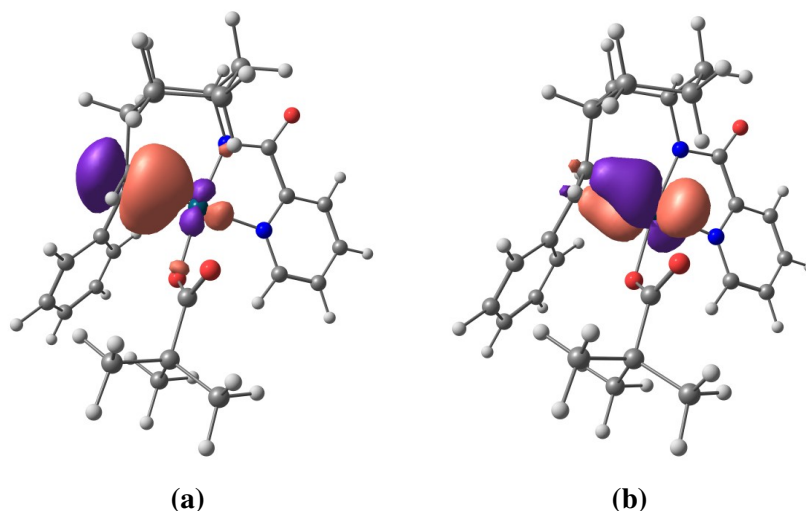
Figure 4.6: Exemplary natural bond orbitals (NBO) involved in the (a) π donation of a C-C double bond to a d orbital of Pd and (b) back donation of a d orbital of palladium to the π^* orbital of a C-C double bond. Reprinted from reference 7.
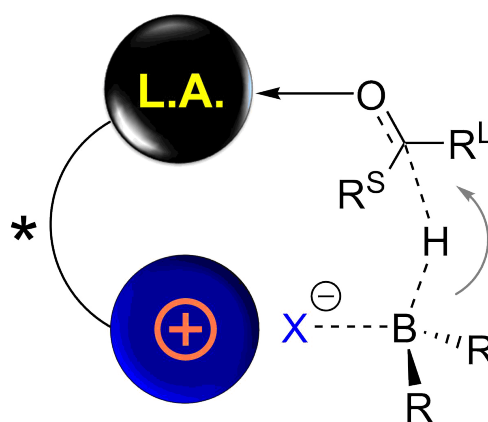
Figure 4.7: Visualization of the envisaged dual activation of the Lewis acid and ammonium salt catalyst (L.A.). Reprinted from reference 10.

As shown in this figure, the catalyst has been designed by the experimentalists with dual activation in mind: the Lewis acid center (L.A.) coordinates the ketone. A strong Lewis acidity withdraws electron density from the ketone, enhancing the electropositive character at the carbonylic carbon group and thereby facilitating the hydride transfer. Simultaneously, the iodide (X^-), situated in the vicinity of the onium moiety, likely donates electron density towards the boron to activate it.

To study this effect, the IBO localization method[74] has been conducted. As shown in

Figure 4.8, the electron density of one orbital that relates to the free electron pair at the iodide, is polarized towards the borane according to the IBO method. This gives evidence that indeed an electron-pushing effect of the halogenide could activate the boron center. A quantitative analysis of the contributions of the boron to the p orbital of the halide indicates that chloride exhibits a higher degree of polarization toward the boron compared to iodide. This is in agreement with NMR studies to investigate the strength of the interaction between halide ions and HBPin, which were performed by the experimental collaborators. Further discussion on the importance of corroborating computational results with experimental control experiments can be found in Section 4.4.
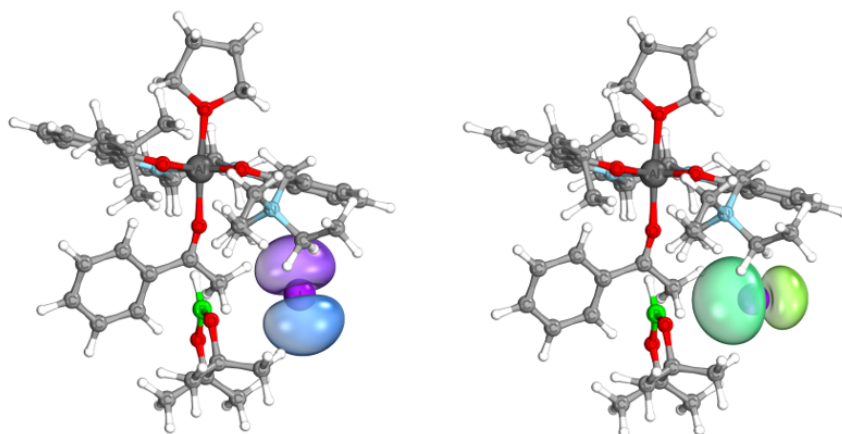
Figure 4.8: IBOs that relate to the p electron pairs of the chloride. One p orbital (right) is polarized towards the borane. Reprinted from reference 10.

4.3 Limitations in Computational Homogeneous Catalysis

In addition to the typical limitations in computational chemistry stemming from the fact that the Schrödinger equation of many-body-systems can not be solved exactly (see Section 2.3), applications in homogeneous catalysis encounter specific challenges.
The molecular systems under investigation are typically quite large. Therefore, scientists must strike a balance between employing electronic structure methods that are as accurate as possible and managing computational time efficiently. In computational

catalysis, density functional theory (DFT) has been proven to be a good trade-off in this respect.[20,77] However, it comes with the risk of large and unsystematic errors due to the parametrized nature of this method. The choice of the best functional remains an open question. Homogeneous catalysis often (but not exclusively) involves transition metal complexes. Their partially occupied d shells require a careful choice of quantum chemical methods that can be applied due to a possible multi-reference character.[82] There is literature benchmarking functionals to accurate theoretical or experimental references (see e.g. references 83–85); however, the performance of a functional is very much dependent on the specific system, the target properties, and the type of atoms involved. A comprehensive study is given in reference 83, which benchmarks various density functionals for applications aiming at basic properties, reaction energies, or non-covalent interactions.

Even within DFT, chemical systems have to be simplified to a minimum to optimize computing time. For example, homogeneous catalysis reactions are experimentally carried out in a solvent, but the explicit treatment of solvent molecules is too costly. Yet, polar solvents usually heavily influence reactivity and must be included in computational investigations explicitly in some cases. The investigation of the enantioselective hydroboration of ketones with a Lewis acid–ammonium salt catalyst within this thesis (Figure 4.1(C)) emphasizes this aspect. The calculations reveal that replacing chloride by a solvent molecule THF in the catalyst is necessary to form the active catalyst. This finding aligns with the experimental observation that THF is required for the reaction. As a consequence of the exchange, the unimolecular barrier of the hydride transfer step from the borane to the ketone decreases from 102 kJ mol^{-1} to 62 kJ mol^{-1}. Again, localized IBOs were conducted to study structurally simplified (SS) complexes of the active ($C1_{SS}^{+}$) and the original ($C1_{SS}$) catalyst, see Figure 4.9. The IBO corresponding to the interaction between the aluminum center and the THF ligand is located at aluminum by only 12%. In the corresponding Al-Cl bond of $C1_{SS}$, 19% of the bond charge is located at aluminum. Consequently, the aluminum center carries a higher IBO charge in $C1_{SS}$ than in $C1_{SS}$ (+1.19 *versus* +1.08). Therefore, the Lewis acidity of the aluminum is enhanced by the exchange of chloride with THF.

Apart from explicit solvent participation, solvation effects due to electrostatic interactions with the environment can be treated with implicit continuum methods that describe the solvent as a homogeneous, polarisable medium.[27,28] The molecule is placed in a cavity of the appropriate shape in the continuum, and stabilizing and destabilizing interactions at the contact surface are evaluated.
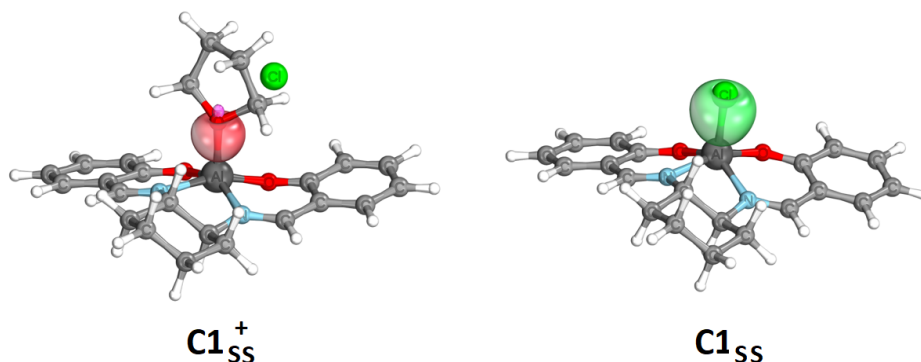
Figure 4.9: The binding IBO for the coordination of the ligand to the aluminum center for the simplified model catalysts $C1_{SS}^+$ (left) and $C1_{SS}$ (right). Reprinted from reference 10.

Surrounding solvent molecules affect not only the energy itself but also the entropy. One reason is that many different arrangements between the solute and the solvent arise; another reason is that the ideal gas expression to calculate the entropy is no longer valid. The entropy calculation is still an unsolved issue that is discussed in Section 2.1.2 in more detail. In summary, with the methods currently available, it is customary, and also employed in this thesis, to compute the thermal contribution to the Gibbs free energy using the rigid-rotor-harmonic-oscillator (RRHO) approximation and incorporate solvation Gibbs energies through continuum solvent models.[20] However, it has to be kept in mind that (partially) anharmonicities and configurational contributions are neglected completely and that the approximation of an ideal gas can achieve only limited accuracy for solvated systems.

Finally, it should be mentioned that electronic structure calculations usually lead to a large consumption of computing power, which is rarely addressed within the scientific community. An open-source tool to evaluate the resulting CO_2 equivalent emission of computational calculations was published in 2021 in *Advanced Science*[86] and is available online[i]. In this thesis, the search for transition states and a subsequent frequency calculation at the DFT level was generally carried out on about 24 CPU cores with 64 GB of memory and took about one day on average. Performing this calculation in 2022 on servers in a German high-performance data center consumes 8.17 kWh electricity, which results in an emission of 2.77 kg CO_2 equivalent and is comparable to driving 15.81 km by car or 6% of a flight Paris-London for one

---

[i]http://www.green-algorithms.org/

passenger. Within the investigation of a full catalytic cycle of a reaction, there are typically many geometry optimizations, accounting for conformational complexity and failed convergence for transition states. One improvement is establishing protocols that pre-optimize roughly estimated input structures with cheap semi-empirical methods, such as the semi-empirical geometry, frequency, noncovalent, extended tight-binding (GFN2-xTB) method,[87] to save optimization steps with higher-level methods.

4.4   How to Bridge the Gap to Experiments

Due to the limited accuracy of electronic structure calculations discussed above, results must be carefully evaluated and interpreted. Therefore, the combination of computational and experimental results is auspicious for comprehensive mechanistic insights. Directly comparing results from both approaches is, however, not trivial.

One approach is to establish a synergy between calculations and experiments. This strategy was applied to study the Pd-catalyzed γ-C(sp^3)-H alkenylation of cyclohexylamine with 1-bromoalkenes (Figure 4.1(B)). The computational calculations, which are part of this thesis, were used to give an insight into the reaction on a molecular level. For example, the calculations indicated that the C(sp^3)-H bond cleavage is rate-limiting and not the oxidative addition of the organobromide to form a Pd(II) complex. Furthermore, as discussed above, the precipitation of KBr in the solvent was found to be crucial in forming a less stable resting state and decreasing the energetic span. Following the proposal of a comprehensive reaction mechanism with the aforementioned details, control experiments were conducted by the experimental collaborators to validate the proposed catalytic cycle. For example, kinetic isotope effect experiments supported that indeed the γ-C(sp^3)-H activation step is rate-limiting. Moreover, the determination of the reaction order of zero for 1-bromoalkene also suggests that this compound is not involved in the rate-determining step. Also, the insolubility of KBr in the solvent DCE was experimentally verified.

This synergy results in a constructive loop of mutual verification or falsification of experimental and computational results, eventually converging to a reliable and detailed insight into the mechanism. It is noteworthy that this approach necessitates excellent cooperation and communication skills from both parties to effectively adapt established terminology and concepts from one field to another.

Also, for the enantioselective hydroboration of ketones with a cooperative Lewis acid–ammonium salt catalyst (Figure 4.1(C)), control experiments were carried out by the experimental collaborators, Justin Herrmann and Prof. Peters from the Institute of Organic Chemistry at the University of Stuttgart. The aim was to enlighten the impact of the active participation of a solvent molecule, shown in Figure 4.9. Calculations indicate that chloride ions, released after a ligand exchange by a solvent molecule, speed up the main reaction but also a side reaction that consumes the product. This side reaction occurs between HBPin and an alcohol molecule, for which the transition state is shown in Figure 4.10a. Chloride ions act as a hydride shuttle and catalyze the formation of a borester and hydrogen. Figure 4.10b shows the results of an experiment in which the concentrations of a mixture of the product alcohol and the reactant HBPin, in the presence of tetrabutyl ammonium salts (TBA) of iodide and chloride, have been measured as a function of time. This experiment supports that in the presence of the halide salts, a reaction between the product alcohol and HBPin occurs, which is more efficiently catalyzed by chloride than by iodide ions.

The examples above illustrate the importance of carefully designing control experiments tailored to address the specific questions at hand. Therefore, a synergetic approach leads to a significant overhead of elaborately designed experiments. Evidence supporting or refuting a proposed mechanism can be provided through control experiments, but a direct comparison to the quantum chemical results is not possible. This is illustrated in Figure 4.12. Computational studies provide energy diagrams of the reaction mechanism, including all elementary steps. Unfortunately, resolving a multi-step mechanism into its elementary steps is experimentally difficult. A reaction occurs on the time scale of picoseconds, which is too fast to be followed by standard equipment. Measurable are concentrations of reactants, stable intermediates, and products over time. A direct comparison between barriers of microscopic reaction steps and macroscopic time-dependent concentrations of the overall reaction is complex. Using chemical kinetics is promising to bridge the gap between these two approaches (see references 37 and 38 for a good review). This approach is rarely utilized in homogeneous catalysis and is not commonly incorporated into the computational exploration of reaction mechanisms. As shown in Figure 4.12 and explained in Section 2.2.1 in more detail, the idea is to set up a kinetic model encompassing all feasible reactions based on quantum chemical investigations. The kinetic model can be solved and the reaction barriers adjusted to generate a concentration-vs-time profile aligning

        (a)   **(b)**
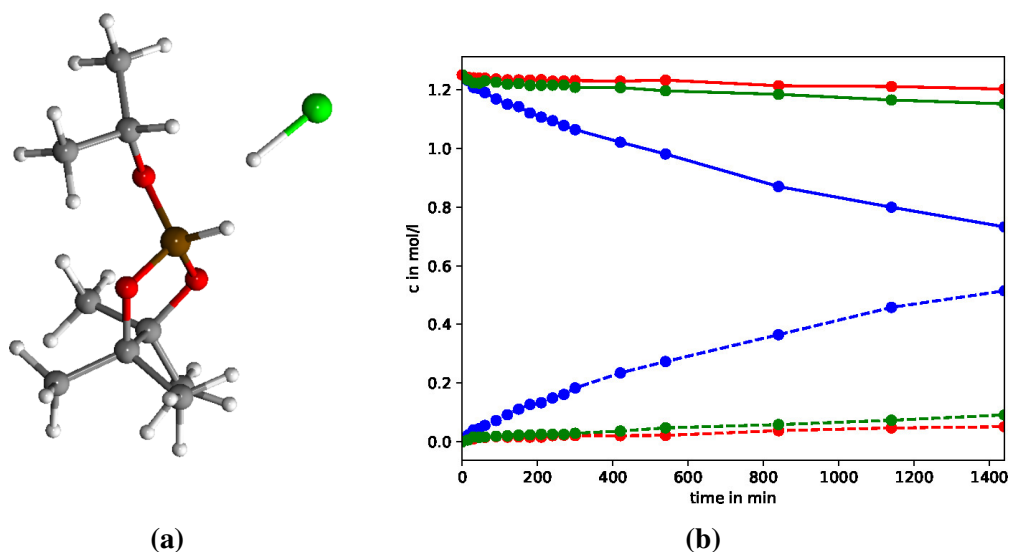
Figure 4.10: Control experiments to study the unwanted side reaction of the product alcohol and HBPin, catalyzed by halide ions in the enantioselective hydroboration of ketones with a cooperative Lewis acid–ammonium salt catalyst. (a) Geometry of the transition state. (b) Experimental concentration-vs-time profile for the reaction of HBPin and the product alcohol. Solid lines refer to the concentration of the product alcohol, and dotted lines refer to the concentration of the resulting product. Red: no catalyst was used; green: nBu_4NI was used as the catalyst; blue: nBu_4NCl was used as the catalyst. Reprinted from reference 11.

with experimental values. The fitted barriers represent the outcome of the kinetic model and can be seen as reaction barriers, extracted from experimental data. They can be directly compared to the values gained from quantum chemical calculations. This approach enables a direct comparison between barriers from quantum chemical calculations and barriers extracted from experiments. Additionally, kinetic modeling offers a comprehensive understanding of chemical reactivity that goes beyond the energy landscape to also consider the species' concentration.

This approach has been applied within the combined quantum chemical and microkinetic study of asymmetric hydroboration of ketones by cooperative Lewis acid and onium salt catalysis (see Figure 4.1(C)). Figure 4.12 shows, that consistent free enthalpy barriers for the quantum chemical and kinetic model have been gained. This was only possible for a mechanism considering that the counterion of the ammonium salt of the catalyst facilitates the hydride transfer step of the cycle but also influences the side reaction, discussed already above. Chloride replacing iodide speeds up the
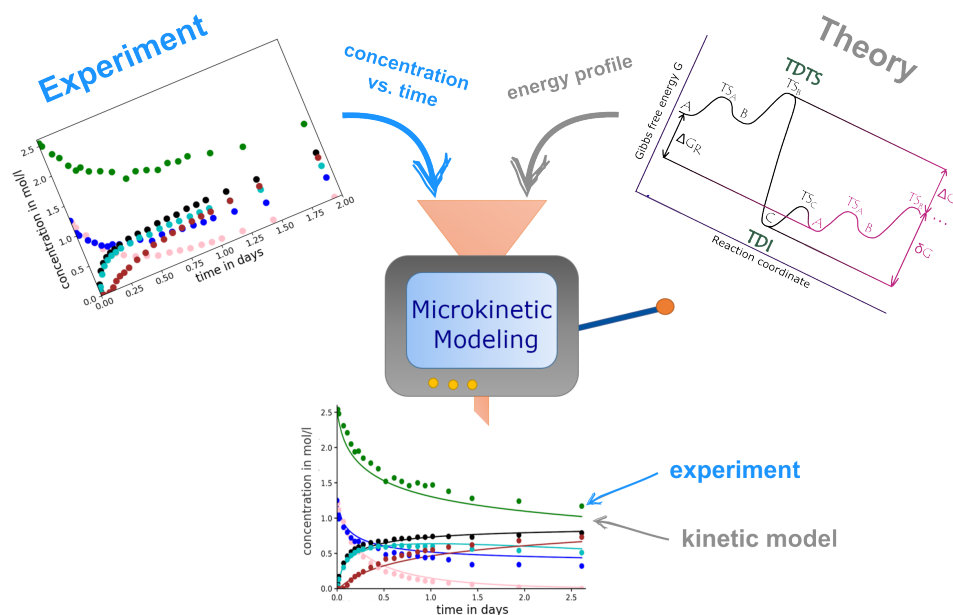
Figure 4.11: The idea of microkinetic modeling to combine theory and experiment in homogeneous catalysis.

main reaction but simultaneously has the same effect on a side reaction that consumes the product. A microkinetic sensitivity analysis has been used, showing that the hydride transfer step and the product release are rate-limiting. These reactions determine enantioselectivity.

4.5   The Future of Computational Catalysis

Nowadays, computational methods usually augment experimental studies to understand reactions for which experimental data already exist. However, the future goal is fully computing-based rational reaction design and discovering novel catalysts from first principles without prior experimental work. This would establish new roles in the interplay between computations and experiments, leading to the ultimate goal of designing novel reactions without needing trial-and-error experiments. This goal is currently not achieved, but is it realistic in the near future? A few recent reviews exist, tackling the question of which computational approaches will prevail in molecular computational catalysis in the future and how promising they are.[88–90]

A reaction-mechanism-based approach followed in the present thesis has high pre-
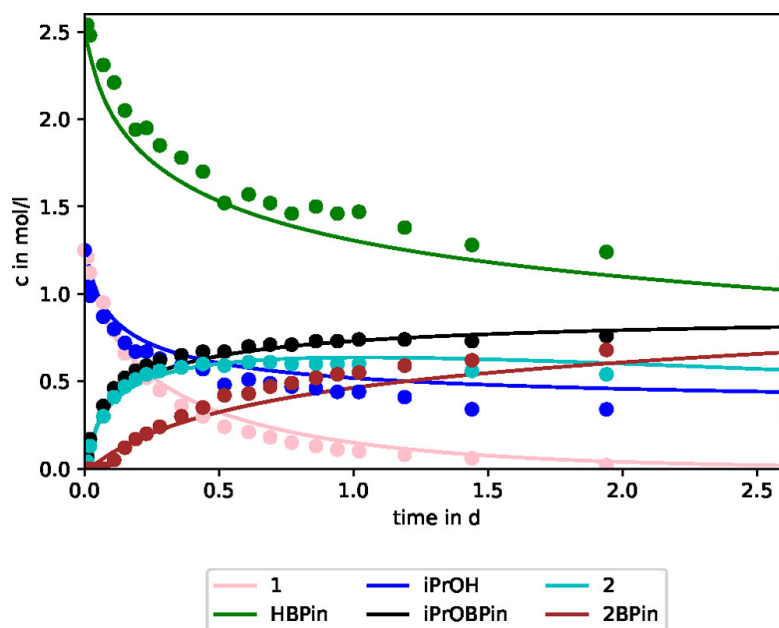
Figure 4.12: Measured concentration profiles (dots) vs results from the kinetic model (lines). Reprinted from reference 11.

dictive power. However, as discussed by reference 88, the complexity of the reaction mechanisms in homogeneous catalysis provides many challenges, including several competing pathways and the consideration of conformational complexity of each single transition state and intermediate. This is, to date, done manually resulting in a high human workload and a bias defined by the chemical knowledge and intuition of the investigating scientist.

Moving from manual to automated methods would mean a big step towards predictive reaction discovery (see reference 91 for the latest review on automated reaction discovery). With this unbiased approach, unexpected discoveries are waiting to be explored.

Martinez and co-workers pioneered the automated reaction discovery to explore reaction mechanisms independent of pre-defined ideas of the reaction with their *ab-initio* nanoreactor.[92] It uses *ab-initio* molecular dynamics (MD) under high pressure. MD simulations evolve the chemical system in time using Newton's equations of motion for the nuclei and take snapshots while doing so. A huge number of MD steps is necessary to observe a reaction as it is a rare event that the system escapes the (local) minimum to pass a transition state. For typical applications, this comes with an unfeasible computation time. The high pressure applied compresses the system, accelerating the

MD and increasing the probability of atomic collisions to enhance reactivity. However, *ab-initio* MD comes with a high computational cost for large systems. Grimme developed the so-called conformer–rotamer ensemble sampling tool (CREST) algorithm that combines the fast semi-empirical tight-binding method geometry, frequency, non-covalent, extended tight-binding (GFN2-xTB)[87] with meta-dynamics simulations.[93,94] The latter method follows the simple idea of adding history-dependent bias potentials over time to the potential energy that fills the minimum and promotes escaping from it.[95,96] However, choosing appropriate collective variables needed for meta-dynamics simulations is a significant challenge in unsupervised exploratory studies and can potentially introduce bias.[91] Also, the GFN2-xTB method has many limitations due to its strong approximations and parametrization. In the present work, this method is extensively used for conformer search. The sampling of the conformation or reaction space is usually done manually; the generation of different possible structures or the exploration of a pre-defined mechanism by a user relies on their experience and creativity, carrying the risk of missing important structures and reaction paths. The error bar associated with conformer choice can be as high as 10 kcal mol^{-1} if bulky ligands are involved,[20] and overlooking a more favorable reaction path can change a story completely.

A somewhat different approach is to quantify relationships between descriptors from electronic or steric effects and the catalytic performance.[88] This reveals trends among similar catalysts; for example, yields, rates, and selectivity can be related to steric and electronic descriptors of ligand properties.[97] For this analysis, data-driven machine-learning approaches are suitable.[98] They need no human workload or bias apart from the generation and selection of the input data set. However, descriptor-based methods are mainly used to fine-tune catalysts for which a reaction mechanism is already known, and for example, different ligands are screened. The transferability between different reactions is only given as long as similar systems are part of the training set. Insights into the reaction mechanism must be already known, as this is necessary to choose an appropriate descriptor variable. Also, it is highlighted that it is difficult to interpret machine learning methods. Due to the lack of a physical foundation, the results of such models may not hold any chemical meaning or might get the right answers, but maybe for the wrong reasons.[88] However, the field of data-driven methods in homogeneous catalysis is very young, with the potential to grow rapidly.[88,98]

Of course, faster and more accurate algorithms are needed to push quantum chemical calculations forward and achieve more predictive power. Unfortunately, classical

computers are unable to treat highly correlated quantum systems efficiently. For an exact treatment (within a basis set limit), the dimension of the wave function grows exponentially with the number of molecular orbitals (so-called "curse of dimensionality"). It is conceivable that after several decades of research we begin to reach the limits of classical computing.

In 1982, Feynman pioneered a completely new computation paradigm and suggested to use quantum systems as a platform to simulate nature, that follows the same laws of quantum mechanics. The essence of the idea is that for accurately simulating a quantum system, it's optimal to employ another quantum system that can be manipulated and controlled to represent the initial one. This takes advantage of their unique and non-classical characteristics such as superposition and entanglement, which are highly suitable properties to describe highly correlated (or entangled) many-body electronic structure problems. This way, quantum systems that are represented by a wave function that scales exponentially with system size is ideally mapped onto a number of logical qubits that scale only linearly with the system size. This allows an exponential advantage of quantum computers over classical computers for the simulation of chemistry. Selected reviews about the quantum computing era in quantum chemistry are provided by the references 99–102.

Similar to classical computers, which execute consecutive logical operations on a bit, a quantum computation can be broken down into controlled unitary operations (quantum gates) on a quantum bit (qubit). Promising physical realizations of such a qubit are especially, but not exclusively, ion traps, superconducting systems, photonic systems, nitrogen vacancy centers, nuclear magnetic resonance, and neutral atoms. However, present quantum hardware has shown bad performance in reliable controllability and in maintaining the coherence of the qubits long enough to execute relevant quantum algorithms. This is to date the main limiting factor for quantum computing to reach its enormous potential and it is still an open question, if and which technology can accomplish the breakthrough in the near future.

In parallel to quantum hardware, quantum algorithms are developed extensively. The quantum phase estimation (QPE) is a promising method to achieve quantum advantage. It allows the computation of eigenvalues for an eigenstate of an observable with tunable precision. A controllable error is highly desirable and would be a big advantage over very unforeseeable errors in classical quantum chemistry. Unfortunately, this type of

algorithm results in many consecutive quantum gates, and therefore in long quantum circuits, the so-called depth of a quantum circuit. Current qubits can not remain its coherence long enough to perform these circuits. This emphasizes the strong coupling between the development of quantum hardware and quantum algorithms that hinders the fast development of this technology significantly. Therefore, applications are to date limited to toy problems or small chemical systems that can already be solved with classical methods.

As QPE algorithms are currently beyond reach, resource estimates are provided to assess the capabilities of quantum algorithms. Reiher *et al.* published such an estimate for elucidating reaction mechanisms in 2017, driven by the recognition that fast and accurate quantum simulations of chemical processes such as fertilizer production or clean energy processes would have a high potential to impact economic and social aspects.[103] The authors propose a workflow for how quantum computers can support the study of reaction mechanisms in the near future. Herein, quantum simulations are used to calculate energies of intermediates and transition states to obtain accurate activation energies. Still, the quantum simulations just augment established classical methods, which are used to obtain e.g. geometries or thermal corrections. The authors state that even considering an overhead of qubits due to error correction, this methodology is not beyond reach in the near future.

Whereas research on QPE has been based on theoretical analyses mainly, methods have been developed to deal with the current shortcomings of a low number of noisy qubits. In this so-called noisy intermediate-scale quantum (NISQ) era, hybrid quantum-classical methods, like the variational quantum eigensolver (VQE) algorithm, are implemented to obtain approximate solutions. The integration of classical optimization steps within the variational framework leads to the necessity for shorter quantum circuits, making them feasible on modern quantum hardware. For example, the electrocatalytic oxygen reduction reaction in a fuel cell has been studied with the VQE algorithm on a real quantum device.[104] The applied approach included both, the preprocessing of geometries and the incorporation of dynamics correlation with classical methods, and the strong static correlation using a complete active space approach run on real quantum hardware.

In contrast to the QPE algorithm, it has been proven that the VQE approach is not scalable.[99] It has to be kept in mind that classical algorithms that have been developed for several decades now, become more and more efficient, which makes it increasingly

hard to compete with these traditional approaches. However, it is a pivotal intermediate method to pave the way for showcasing the high potential of quantum computers to reach their full maturity one day.

The development of homogeneous catalysis toward predictive discovery remains a dream to date. It is exciting to see if and which method will achieve this ultimate goal.

5 Summary

This thesis explores the chemical reactivity and mechanistic details of three reactions in homogeneous catalysis with computational methods.

A density functional theory (DFT) study of a catalytic reaction to access secondary alcohols from aryl iodides has been reported. The reaction is catalyzed by a metal catalyst that combines nickel and a 1,5-diaza-3,7-diphosphacyclooctane ligand. An alternative to the proposed catalytic pathway in the literature has been discovered. Herein, the ligand is not innocent but actively involved in the transfer of a hydride. The results call into question the existence of a Ni(0) species intermediate proposed in the initial mechanism for this cross-coupling reaction and contribute to the long-standing question of the oxidation state of nickel in such reactions. Unexpectedly, this alternative mechanism also includes uncommon Ni(0) intermediates.

Identifying the energetic span provides an efficient approach to investigating the experimental performance of different ligands by studying their influence on the involved states. The discovery of a competitive side reaction reveals that the yield of the reaction is defined by the interplay between different pathways. Some ligands favor the side reaction slightly, and some the main reaction. The mechanistic study also unveils the role of the base, which is indispensable for the reaction but, in some cases inhibiting the reaction by preventing the formation of an indispensable intermediate. The insights help to improve the reaction conditions experimentally.

For the Pd-catalyzed γ-C(sp^3)-H alkenylation of cyclohexylamine with 1-bromoalkenes the quantum chemical calculations enabled an comprehensive insight into the reaction mechanism and aspects that drive the reaction. The reaction follows a Pd(II)/Pd(IV) pathway, in which the transition state of the oxidative addition to form a Pd(IV) species is not rate-determining, but rather the C(sp^3)-H activation. This transition state determines the overall energy barrier together with the resting state, which is the palladium center that strongly coordinates to the reaction products containing a C=C bond. This very stable sink explains why alkenylation reactions have been particularly challenging to develop and required silver halide scavengers. Addition of a catalytic

amount of KOPiv is pivotal for the reaction as a bromide ligand in the resting state is exchanged by a pivalate, destabalizing this complex and turning it to a more reactive intermediate. At the same time, KBr precipitates, enabling this endergonic reaction step. This shows the value of the mechanistic insight towards the choice of the solvents. Precipitation of KBr in a suitable solvent avoids the use of superstoichiometric metal reagents, which are known for its role to scavenge halide ions. A detailed investigation of the resting state with different substituents revealed that it is destabilized for ethenyl featuring electron withdrawing groups that lower the electron density at the double bond resulting in a weaker interaction between the Pd(II) and the double bond. As a consequence, electron donating substituents provide a poorer conversion, which is exactly the observed trend in the experimental performance of the different substituents.

Finally, a combined quantum chemical and microkinetic study of the asymmetric hydroboration of ketones by a cooperative Lewis acid–onium salt catalyst has been reported. The energy landscape has been calculated to shed light on possible reaction mechanisms and competitive side reactions. Localization methods have been used to investigate the envisaged dual activation of the catalyst and the role of the solvent, co-ordinating with the metal center and increasing the Lewis-acidity of the reactive center. Additionally, microkinetic modeling has been applied to account for both energetics and concentration effects. Varying the reaction barriers of the proposed mechanism to yield a concentration-vs-time profile that fits the experimental values. This makes it possible to directly compare barriers from quantum chemical calculations to barriers extracted from experiments. Consistent free enthalpy barriers for the quantum chemical and kinetic model have been gained for a mechanism considering that the counterion of the ammonium salt of the catalyst facilitates the hydride transfer step of the cycle but also influences the side reaction. Chloride replacing iodide speeds up the main reaction but simultaneously has the same effect on a side reaction that consumes the product. A microkinetic sensitivity analysis has been used, showing that the hydride transfer step and the product release are rate-limiting. These reactions determine enantioselectivity.

Bibliography

[1] J. Hagen: *Industrial catalysis: A practical approach.* Wiley-VCH, Weinheim, third edition (2015)

[2] Y. Li, X. Wei, L. Chen, and J. Shi: *Electrocatalytic Hydrogen Production Trilogy.* Angewandte Chemie (International ed. in English) **60** (36), 19550–19571 (2021)

[3] J. Artz, T. E. Müller, K. Thenert, J. Kleinekorte, R. Meys et al.: *Sustainable Conversion of Carbon Dioxide: An Integrated Review of Catalysis and Life Cycle Assessment.* Chemical reviews **118** (2), 434–504 (2018)

[4] R. M. Peltzer, J. Gauss, O. Eisenstein, and M. Cascella: *The Grignard Reaction - Unraveling a Chemical Puzzle.* Journal of the American Chemical Society **142** (6), 2984–2994 (2020)

[5] J. Heitkämper, S. Posada-Pérez, S. Escayola, M. Solà, J. Kästner et al.: *A Non Expected Alternative Ni(0) Species in the Ni-Catalytic Aldehyde and Alcohol Arylation Reactions Facilitated by a 1,5-Diaza-3,7-diphosphacyclooctane Ligand.* Chemistry: A European Journal **29** (28), e202300193 (2023)

[6] E. S. Isbrandt, A. Nasim, K. Zhao, and S. G. Newman: *Catalytic Aldehyde and Alcohol Arylation Reactions Facilitated by a 1,5-Diaza-3,7-diphosphacyclooctane Ligand.* Journal of the American Chemical Society **143** (36), 14646–14656 (2021)

[7] K. Gadde, N. R. Bheemireddy, J. Heitkämper, A. Nova, and B. U. W. Maes: *Directed Palladium-Catalyzed γ-C(sp 3)–H Alkenylation of (Aza and Oxa) Cyclohexanamines with Bromoalkenes: Bromide Precipitation as an Alternative to Silver Scavenging.* ACS Catalysis **14** (2), 1157–1172 (2024)

[8] C. He, W. G. Whitehurst, and M. J. Gaunt: *Palladium-Catalyzed C(sp3)–H Bond Functionalization of Aliphatic Amines.* Chem **5** (5), 1031–1058 (2019)

[9] K. J. Bonney and F. Schoenebeck: *Experiment and computation: a combined approach to study the reactivity of palladium complexes in oxidation states 0 to IV.* Chemical Society reviews **43** (18), 6609–6638 (2014)

[10] M. Titze, J. Heitkämper, T. Junge, J. Kästner, and R. Peters: *Highly Active Cooperative Lewis Acid—Ammonium Salt Catalyst for the Enantioselective Hydroboration of Ketones.* Angewandte Chemie (International ed. in English) **133** (10), 5604–5613 (2021)

[11] J. Heitkämper, J. Herrmann, M. Titze, S. M. Bauch, R. Peters et al.: *Asymmetric Hydroboration of Ketones by Cooperative Lewis Acid–Onium Salt Catalysis: A Quantum Chemical and Microkinetic Study to Combine Theory and Experiment*. ACS Catalysis **12** (2), 1497–1507 (2022)

[12] A. Szabo and N. S. Ostlund: *Modern Quantum Chemistry: Introduction to Advanced Electronic Structure Theory*. Courier Corporation (2012)

[13] W. Koch and M. C. Holthausen: *A chemist's guide to density functional theory*. Wiley-VCH, Weinheim, second edition (2015)

[14] F. Jensen: *Introduction to computational chemistry*. Wiley, Chichester, West Sussex and Hoboken, NJ and Oxford, third edition (2017)

[15] B. R. Brooks, D. Janezic, and M. Karplus: *Harmonic analysis of large systems. I. Methodology*. Journal of Computational Chemistry **16** (12), 1522–1542 (1995)

[16] C. Y. Lin, A. T. B. Gilbert, and P. M. W. Gill: *Calculating molecular vibrational spectra beyond the harmonic approximation*. Theoretical Chemistry Accounts **120** (1-3), 23–35 (2008)

[17] D. A. McQuarrie: *Statistical thermodynamics*. Harper's chemistry series. Harper Row, New York (1973)

[18] S. Grimme and P. R. Schreiner: *Computational Chemistry: The Fate of Current Methods and Future Challenges*. Angewandte Chemie (International ed. in English) **57** (16), 4170–4176 (2018)

[19] K. N. Houk and F. Liu: *Holy Grails for Computational Organic Chemistry and Biochemistry*. Accounts of Chemical Research **50** (3), 539–543 (2017)

[20] J. N. Harvey, F. Himo, F. Maseras, and L. Perrin: *Scope and Challenge of Computational Methods for Studying Mechanism and Reactivity in Homogeneous Catalysis*. ACS Catalysis **9** (8), 6803–6813 (2019)

[21] A. Hellweg and F. Eckert: *Brick by brick computation of the gibbs free energy of reaction in solution using quantum chemistry and COSMO–RS*. AIChE Journal **63** (9), 3944–3954 (2017)

[22] P. Pracht and S. Grimme: *Calculation of absolute molecular entropies and heat capacities made simple*. Chemical science **12** (19), 6551–6568 (2021)

[23] S. Grimme, F. Bohle, A. Hansen, P. Pracht, S. Spicher et al.: *Efficient Quantum Chemical Calculation of Structure Ensembles and Free Energies for Nonrigid Molecules*. The Journal of Physical Chemistry A **125** (19), 4039–4054 (2021)

[24] G. H. Findenegg and T. Hellweg: *Statistische Thermodynamik*. Springer Berlin Heidelberg, zweite edition (2015)

[25] Z. Liu, C. Patel, J. N. Harvey, and R. B. Sunoj: *Mechanism and reactivity in the Morita-Baylis-Hillman reaction: the challenge of accurate computations*. Physical Chemistry Chemical Physics **19** (45), 30647–30657 (2017)

[26] M. Besora, P. Vidossich, A. Lledós, G. Ujaque, and F. Maseras: *Calculation of Reaction Free Energies in Solution: A Comparison of Current Approaches*. The Journal of Physical Chemistry A **122** (5), 1392–1399 (2018)

[27] C. J. Cramer and D. G. Truhlar: *Implicit Solvation Models: Equilibria, Structure, Spectra, and Dynamics*. Chemical reviews **99** (8), 2161–2200 (1999)

[28] J. Tomasi, B. Mennucci, and R. Cammi: *Quantum mechanical continuum solvation models*. Chemical Reviews **105** (8), 2999–3093 (2005)

[29] D. Suárez and N. Díaz: *Direct methods for computing single-molecule entropies from molecular simulations*. WIREs Computational Molecular Science **5** (1), 1–26 (2015)

[30] E. Dzib, J. L. Cabellos, F. Ortíz-Chi, S. Pan, A. Galano et al.: *Eyringpy : A program for computing rate constants in the gas phase and in solution*. International Journal of Quantum Chemistry **119** (2), e25686 (2019)

[31] P. L. Houston: *Chemical kinetics and reaction dynamics*. McGraw-Hill, Boston (2001)

[32] J. I. Steinfeld, J. S. Francisco, and W. L. Hase: *Chemical kinetics and dynamics*. Prentice Hall, Upper Saddle River, NJ, second edition (1999)

[33] P. Stoltze: *Microkinetic simulation of catalytic reactions*. Progress in Surface Science **65** (3-4), 65–150 (2000)

[34] A. H. Motagamwala and J. A. Dumesic: *Microkinetic Modeling: A Tool for Rational Catalyst Design*. Chemical reviews **121** (2), 1049–1076 (2021)

[35] B. W. J. Chen, L. Xu, and M. Mavrikakis: *Computational Methods in Heterogeneous Catalysis*. Chemical reviews **121** (2), 1007–1048 (2021)

[36] W. Xie, J. Xu, J. Chen, H. Wang, and P. Hu: *Achieving Theory-Experiment Parity for Activity and Selectivity in Heterogeneous Catalysis Using Microkinetic Modeling*. Accounts of chemical research **55** (9), 1237–1248 (2022)

[37] M. Besora and F. Maseras: *Microkinetic modeling in homogeneous catalysis*. WIREs Computational Molecular Science **8** (6) (2018)

[38] G. Sciortino and F. Maseras: *Microkinetic modelling in computational homogeneous catalysis and beyond*. Theoretical Chemistry Accounts **142** (10), 2547 (2023)

[39] C. Runge: *Ueber die numerische Auflsung von Differentialgleichungen*. Mathematische Annalen **46** (2), 167–178 (1895)

[40] W. Kutta: *Beitrag zur Naherungsweisen Integration Totaler Differentialgleichungen*. Zeitschrift für angewandte Mathematik und Physik **46**, 435–453 (1901)

[41] C. T. Campbell: *The Degree of Rate Control: A Powerful Tool for Catalysis Research*. ACS Catalysis **7** (4), 2770–2779 (2017)

[42] N. Agarwal, M. A. Sanchez-Castillo, R. D. Cortright, R. J. Madon, and J. A. Dumesic: *Catalytic Cracking of Isobutane and 2-Methylhexane over USY Zeolite: Identification of Kinetically Significant Reaction Steps*. Industrial & Engineering Chemistry Research **41** (16), 4016–4027 (2002)

[43] S. T. Dix, J. K. Scott, R. B. Getman, and C. T. Campbell: *Using degrees of rate control to improve selective n-butane oxidation over model MOF-encapsulated catalysts: sterically-constrained Ag3Pd(111)*. Faraday discussions **188**, 21–38 (2016)

[44] A. C. Brezny and C. R. Landis: *Development of a Comprehensive Microkinetic Model for Rh(bis(diazaphospholane))-Catalyzed Hydroformylation*. ACS Catalysis **9** (3), 2501–2513 (2019)

[45] M.-H. Ho, R. Rousseau, J. A. S. Roberts, E. S. Wiedner, M. Dupuis et al.: *Ab Initio-Based Kinetic Modeling for the Design of Molecular Catalysts: The Case of H 2 Production Electrocatalysts*. ACS Catalysis **5** (9), 5436–5452 (2015)

[46] H. Eyring: *The Activated Complex in Chemical Reactions*. The Journal of Chemical Physics **3** (2), 107–115 (1935)

[47] M. G. Evans and M. Polanyi: *Some applications of the transition state method to the calculation of reaction velocities, especially in solution*. Transactions of the Faraday Society **31**, 875 (1935)

[48] H. Eyring: *The Activated Complex and the Absolute Rate of Chemical Reactions*. Chemical Reviews **17** (1), 65–77 (1935)

[49] E. Wigner: *The transition state method*. Transactions of the Faraday Society **34**, 29 (1938)

[50] J. Meisner and J. Kästner: *Atom Tunneling in Chemistry*. Angewandte Chemie (International ed. in English) **55** (18), 5400–5413 (2016)

[51] J. L. Bao and D. G. Truhlar: *Variational transition state theory: theoretical framework and recent developments*. Chemical Society reviews **46** (24), 7548–7596 (2017)

[52] B. H. Mahan: *Activated complex theory of bimolecular reactions*. Journal of Chemical Education **51** (11), 709 (1974)

[53] F. A. Lindemann, S. Arrhenius, I. Langmuir, N. R. Dhar, J. Perrin et al.: *Discussion on "the radiation theory of chemical action"*. Transactions of the Faraday Society **17** (0), 598–606 (1922)

[54] O. K. Rice and H. C. Ramsperger: *Theories of unimolecular gas reactions at low pressures*. Journal of the American Chemical Society **49** (7), 1617–1629 (1927)

[55] L. S. Kassel: *Studies in Homogeneous Gas Reactions. II. Introduction of Quantum Theory*. The Journal of Physical Chemistry **32** (7), 1065–1079 (1928)

[56] R. A. Marcus and O. K. Rice: *The Kinetics of the Recombination of Methyl Radicals and Iodine Atoms*. The Journal of Physical Chemistry **55** (6), 894–908 (1951)

[57] R. A. Marcus: *Unimolecular Dissociations and Free Radical Recombination Reactions*. The Journal of Chemical Physics **20** (3), 359–364 (1952)

[58] W. H. Miller: *Tunneling corrections to unimolecular rate constants, with application to formaldehyde*. Journal of the American Chemical Society **101** (23), 6810–6814 (1979)

[59] T. Baer and W. L. Hase: *Unimolecular reaction dynamics: Theory and experiments*. The international series of monographs on chemistry. Oxford University Press, New York (1996)

[60] E. E. Aubanel, D. M. Wardlaw, L. Zhu, and W. L. Hase: *Role of angular momentum in statistical unimolecular rate theory*. International Reviews in Physical Chemistry **10** (3), 249–286 (1991)

[61] A. Martín-Sómer, M.-P. Gaigeot, M. Yáñez, and R. Spezia: *A RRKM study and a DFT assessment on gas-phase fragmentation of formamide–M 2+ (M = Ca, Sr)*. Physical Chemistry Chemical Physics **16** (28), 14813–14825 (2014)

[62] C. Puzzarini: *Gas-phase Chemistry in the Interstellar Medium: The Role of Laboratory Astrochemistry*. Frontiers in Astronomy and Space Sciences **8** (2022)

[63] S. Nandi, B. Ballotta, S. Rampino, and V. Barone: *A General User-Friendly Tool for Kinetic Calculations of Multi-Step Reactions within the Virtual Multifrequency Spectrometer Project*. Applied Sciences **10** (5), 1872 (2020)

[64] J. Heitkämper, S. Suchaneck, J. La García de Concepción, J. Kästner, and G. Molpeceres: *The reactivity of pyridine in cold interstellar environments: The reaction of pyridine with the CN radical*. Frontiers in Astronomy and Space Sciences **9** (2022)

[65] P. Hohenberg and W. Kohn: *Inhomogeneous Electron Gas*. Physical Review **136** (3B), B864–B871 (1964)

[66] W. Kohn and L. J. Sham: *Self-Consistent Equations Including Exchange and Correlation Effects.* Physical Review **140** (4A), A1133–A1138 (1965)

[67] S. Grimme, J. Antony, S. Ehrlich, and H. Krieg: *A consistent and accurate ab initio parametrization of density functional dispersion correction (DFT-D) for the 94 elements H-Pu.* The Journal of Chemical Physics **132** (15), 154104 (2010)

[68] S. F. Boys: *Construction of Some Molecular Orbitals to Be Approximately Invariant for Changes from One Molecule to Another.* Reviews of Modern Physics **32** (2), 296–299 (1960)

[69] J. M. Foster and S. F. Boys: *Canonical Configurational Interaction Procedure.* Reviews of Modern Physics **32** (2), 300–302 (1960)

[70] J. P. Foster and F. Weinhold: *Natural hybrid orbitals.* Journal of the American Chemical Society **102** (24), 7211–7218 (1980)

[71] A. E. Reed, R. B. Weinstock, and F. Weinhold: *Natural population analysis.* The Journal of Chemical Physics **83** (2), 735–746 (1985)

[72] A. E. Reed, L. A. Curtiss, and F. Weinhold: *Intermolecular interactions from a natural bond orbital, donor-acceptor viewpoint.* Chemical Reviews **88** (6), 899–926 (1988)

[73] F. Weinhold and C. R. Landis: *Natural bond orbitals and extensions of localized bonding concepts.* Chemistry Education Research and Practice **2** (2), 91–104 (2001)

[74] G. Knizia: *Intrinsic Atomic Orbitals: An Unbiased Bridge between Quantum Theory and Chemical Concepts.* Journal of Chemical Theory and Computation **9** (11), 4834–4843 (2013)

[75] L. Nunes Dos Santos Comprido, J. E. M. N. Klein, G. Knizia, J. Kästner, and A. S. K. Hashmi: *The Stabilizing Effects in Gold Carbene Complexes.* Angewandte Chemie (International ed. in English) **54** (35), 10336–10340 (2015)

[76] J. Pipek and P. G. Mezey: *A fast intrinsic localization procedure applicable for abinitio and semiempirical linear combination of atomic orbital wave functions.* The Journal of Chemical Physics **90** (9), 4916–4926 (1989)

[77] F. Studt: *Grand Challenges in Computational Catalysis.* Frontiers in Catalysis **1**, 016105 (2021)

[78] J. R. Murdoch: *What is the rate-limiting step of a multistep reaction?* Journal of Chemical Education **58** (1), 32 (1981)

[79] K. J. Laidler: *Rate controlling step: A necessary or useful concept?* Journal of Chemical Education **65** (3), 250 (1988)

[80] R. K. Boyd: *Some common oversimplifications in teaching chemical kinetics.* Journal of Chemical Education **55** (2), 84 (1978)

[81] S. Kozuch and S. Shaik: *How to Conceptualize Catalytic Cycles? The Energetic Span Model.* Accounts of Chemical Research **44** (2), 101–110 (2011)

[82] M. Bursch, J.-M. Mewes, A. Hansen, and S. Grimme: *Best–Practice DFT Protocols for Basic Molecular Computational Chemistry.* Angewandte Chemie (International ed. in English) **61** (42) (2022)

[83] L. Goerigk and S. Grimme: *A thorough benchmark of density functional methods for general main group thermochemistry, kinetics, and noncovalent interactions.* Physical Chemistry Chemical Physics **13** (14), 6670–6688 (2011)

[84] C. A. Jiménez-Hoyos, B. G. Janesko, and G. E. Scuseria: *Evaluation of range-separated hybrid and other density functional approaches on test sets relevant for transition metal-based homogeneous catalysts.* The Journal of Physical Chemistry A **113** (43), 11742–11749 (2009)

[85] M. M. Quintal, A. Karton, M. A. Iron, A. D. Boese, and J. M. L. Martin: *Benchmark study of DFT functionals for late-transition-metal reactions.* The Journal of Physical Chemistry A **110** (2), 709–716 (2006)

[86] L. Lannelongue, J. Grealey, and M. Inouye: *Green Algorithms: Quantifying the Carbon Footprint of Computation.* Advanced science **8** (12), 2100707 (2021)

[87] C. Bannwarth, S. Ehlert, and S. Grimme: *GFN2-xTB – An Accurate and Broadly Parametrized Self-Consistent Tight-Binding Quantum Chemical Method with Multipole Electrostatics and Density-Dependent Dispersion Contributions.* Journal of Chemical Theory and Computation **15** (3), 1652–1671 (2019)

[88] A. Soyemi and T. Szilvási: *Trends in computational molecular catalyst design.* Dalton transactions **50** (30), 10325–10339 (2021)

[89] I. Funes-Ardoiz and F. Schoenebeck: *Established and Emerging Computational Tools to Study Homogeneous Catalysis—From Quantum Mechanics to Machine Learning.* Chem **6** (8), 1904–1913 (2020)

[90] D. Claudino: *The basics of quantum computing for chemists.* International Journal of Quantum Chemistry **122** (23), 182 (2022)

[91] A. Baiardi, S. A. Grimmel, M. Steiner, P. L. Türtscher, J. P. Unsleber et al.: *Expansive Quantum Mechanical Exploration of Chemical Reaction Paths.* Accounts of chemical research **55** (1), 35–43 (2022)

[92] L.-P. Wang, A. Titov, R. McGibbon, F. Liu, V. S. Pande et al.: *Discovering chemistry with an ab initio nanoreactor.* Nature chemistry **6** (12), 1044–1048 (2014)

[93] S. Grimme: *Exploration of Chemical Compound, Conformer, and Reaction Space with Meta-Dynamics Simulations Based on Tight-Binding Quantum Chemical Calculations.* Journal of Chemical Theory and Computation **15** (5), 2847–2862 (2019)

[94] P. Pracht, F. Bohle, and S. Grimme: *Automated exploration of the low-energy chemical space with fast quantum chemical methods.* Physical Chemistry Chemical Physics **22** (14), 7169–7192 (2020)

[95] T. Huber, A. E. Torda, and W. F. van Gunsteren: *Local elevation: a method for improving the searching properties of molecular dynamics simulation.* Journal of computer-aided molecular design **8** (6), 695–708 (1994)

[96] A. Laio and M. Parrinello: *Escaping free-energy minima.* Proceedings of the National Academy of Sciences of the United States of America **99** (20), 12562–12566 (2002)

[97] D. J. Durand and N. Fey: *Computational Ligand Descriptors for Catalyst Design.* Chemical reviews **119** (11), 6561–6594 (2019)

[98] W. Yang, T. T. Fidelis, and W.-H. Sun: *Machine Learning in Catalysis, From Proposal to Practicing.* ACS omega **5** (1), 83–88 (2020)

[99] Y. Cao, J. Romero, J. P. Olson, M. Degroote, P. D. Johnson et al.: *Quantum Chemistry in the Age of Quantum Computing.* Chemical reviews **119** (19), 10856–10915 (2019)

[100] B. Bauer, S. Bravyi, M. Motta, and G. Kin-Lic Chan: *Quantum Algorithms for Quantum Chemistry and Quantum Materials Science.* Chemical reviews **120** (22), 12685–12717 (2020)

[101] S. McArdle, S. Endo, A. Aspuru-Guzik, S. C. Benjamin, and X. Yuan: *Quantum computational chemistry.* Reviews of Modern Physics **92** (1) (2020)

[102] H. Liu, G. H. Low, D. S. Steiger, T. Häner, M. Reiher et al.: *Prospects of quantum computing for molecular sciences.* Materials Theory **6** (1), 5162 (2022)

[103] M. Reiher, N. Wiebe, K. M. Svore, D. Wecker, and M. Troyer: *Elucidating reaction mechanisms on quantum computers.* Proceedings of the National Academy of Sciences of the United States of America **114** (29), 7555–7560 (2017)

[104] C. Di Paola, E. Plekhanov, M. Krompiec, C. Kumar, F. Du et al.: *Applicability of Quantum Computing to Oxygen Reduction Reaction Simulations.* arXiv:2307.15823 (2023)